PWM and Model Predictive MRAS based Estimators for Sensorless Control of PMSM

Saleh B Shlimet

A thesis submitted for the degree of Doctor of Philosophy

School of Electrical and Electronic Engineering

The University of Sheffield

Sheffield, S1 3JD

United Kingdom

December 2023

ABSTRACT

A novel sensorless rotor position and speed estimator is presented in this thesis. The method is based on the measurement of the current response to conventional space-vector pulse width modulation (SV-PWM) for sensorless PMSM drives applications. Model-Reference Adaptive Systems (MRAS) estimators are frequently used for sensorless angle estimate. They are typically based on the comparison of two stator flux estimations based on current and voltage models. The voltage model uses integration of stator voltages to calculate the stator flux. The integration process, however, results in phase delays. The proposed method uses oversampling and averaging over a switching SV-PWM cycle, eliminating the need for integrators. Extensive experiments are provided to assess the effectiveness of the proposed estimator. The results of the experiments demonstrate good performance at various speeds and under various load circumstances, in both motoring and regenerating mode. The proposed method also shows robustness to changes in motor parameters.

This thesis also introduces an innovative predictive model reference adaptive system position and speed estimators for Permanent Magnet Synchronous Machines. The speed estimator is based on the finite control set model predictive control (FCS-MPC) principle. A search method is utilized to find the best estimated speed at each sampling interval that produces the smallest speed tuning error signal. Consequently, the need for a PI controller in MRAS estimators is eliminated. The problem with a fixed PI controller is that it is unable to maintain optimal performance under all different operation conditions. Therefore, an adaptive PI controller is required for a satisfactory performance, however, this is a difficult process that takes time and effort. In contrast to MRAS methods based on PI controllers, the suggested approach eliminates the need for gain tuning, simplifying the process and ensuring optimal performance. The

experimental testing of the proposed estimator demonstrates enhanced performance compared to the PI-based MRAS method.

ACKNOWLEDGEMENTS

I would like to extend my heartfelt appreciation to my supervisor, Dr. Antonio Griffo, for his invaluable comments, suggestions, and unwavering support throughout the entirety of this work.

I would also like to dedicate this work to the memory of my father, Bashir Hamed, who taught me the true essence of life. I extend my heartfelt thanks and affection to my mother, Aisha, for her steadfast dedication and support, which have played a crucial role in my accomplishments.

I express my gratitude to my wife for her understanding and support. Completing this project would not have been possible without her support.

Moreover, I wish to express appreciation for the support offered by Neville Gillott, Tom, and Andy within my department. Their contributions have been invaluable in facilitating the smooth progress of this project.

Table of contents

List of figures

Chapter 1: Introduction and Thesis Scope

1.1 Introduction

Controlled AC drives have gained significant popularity in various high-performance industrial applications. Traditionally, DC drives were preferred due to their simple structure. However, AC motors offer several advantages over DC motors, including affordability, compact size, robustness, and reduced maintenance requirements [1]. Recent advancements in power electronics, control technology, and signal processing have contributed to the remarkable growth of AC drives.

In applications requiring rapid dynamic response, permanent magnet synchronous motors (PMSM) are increasingly replacing conventional DC motors [1]. The improved performance and efficiency of PMSM, coupled with the advancements in control systems, make them a favourable choice in a wide range of applications.

Permanent magnet synchronous motors (PMSM) utilize permanent magnets instead of electromagnets to generate the magnetic field in the air gap. This design choice offers numerous advantages, such as high efficiency, a favourable torque-to-inertia ratio, lightweight construction, and a straightforward structure. These benefits have led to the widespread adoption of PMSM motors in diverse applications, including robotic automation and electric vehicles [2], [3, 4].

Speed control of PMSM can be achieved through various techniques, including scalar control, vector control, or field-oriented control (FOC). For applications such as pumps and fans where precise speed control is not critical, scalar control can provide satisfactory dynamic performance [5]. However, scalar control poses a challenge as the motor flux and torque are interdependent. On the other hand, vector control allows separate control of torque and flux, enabling more precise control of PMSM. This technique facilitates the matching of dynamic performance with that of a DC machine drive [6]. By employing vector control, the PMSM can be effectively controlled to achieve the desired performance characteristics.

The fundamental principle behind FOC is to transform the three stator currents that are represented by a three-coordinate reference frame into two fixed currents on rotating reference frames [1, 5]. The motor voltage command, which is the output of the current control, is then transformed back from the rotating to stationary reference frame and instructs the voltage inverter to create the sinusoidal voltages that are supplied to the motor.

The fundamental principle of field-oriented control (FOC) involves transforming the three-phase stator currents, represented in a three-coordinate stationary reference frame, into two fixed currents in rotating reference frames [1, 5]. These transformed currents serve as the control input. The resulting motor voltage command, which is the control output, is then transformed back and used to generate sinusoidal voltages through the voltage inverter. These voltages are subsequently supplied to the motor for operation.

Field-oriented control (FOC) of PMSMs traditionally relies on knowledge of the rotor position. This information is commonly obtained through the use of shaft encoders, resolvers, or Hall sensors. However, incorporating such position sensors can compromise the overall robustness and reliability of the drive system, increase costs, and add weight. Moreover, in compact assembly spaces and demanding operating environments characterized by vibrations and high temperatures, installing and maintaining position sensors can present challenges.

As a result, significant efforts have been dedicated to developing position-sensorless control systems for estimating the rotor position and speed of PMSMs, particularly within the last decade [7-11]. These sensorless control systems aim to overcome the limitations associated with position sensors, offering a cost-effective and reliable alternative for precise control and operation of PMSMs without the need for additional sensors.

1.2 Sensorless techniques

As mentioned previously, obtaining precise shaft position in a high-performance PMSM control system is essential. However, using position sensors can lead to increased costs, larger motor volume, and decreased system reliability [2]. To overcome these challenges, position sensorless control strategies are suggested with the goal of eliminating the necessity for position sensors. By adopting sensorless methods, the cost of encoders can be eliminated, and the overall system reliability can be enhanced. Sensorless techniques have undergone extensive development and are classified into saliency-based and model-based approaches, as illustrated in Figure 1.1.

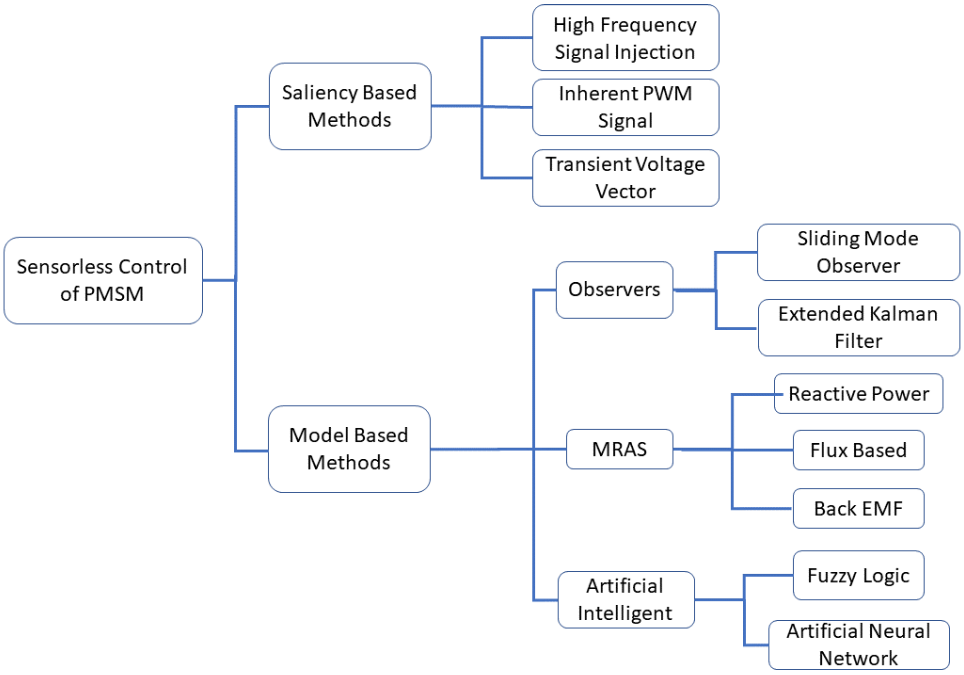

Figure 1.1 Sensorless control techniques

1.2.1 Model-based Sensorless Strategies

These sensorless methods rely on the assumption of a sinusoidal flux distribution across the air gap. These approaches employ the mathematical model of the machine, integrating measurements of stator voltages and/or currents to predict both the rotor position and speed [11]. Model-based techniques are well-suited for accurately estimating motor position [1]. However, they face challenges at very low speeds due to increased sensitivity to variations in machine parameters, inverter nonlinearity, low signal-to-noise ratio, and non-observability of the back-EMF signal [1, 7, 12].

Among the model-based sensorless strategies, MRAS (Model-Reference Adaptive Systems) methods are widely used due to their simplicity and performance. These techniques encompass reactive power-based MRAS [13-16], back EMF-based MRAS [17], and flux-based MRAS [18]. Figure 1.2 illustrates the overall configuration of a model-based sensorless control drive system.

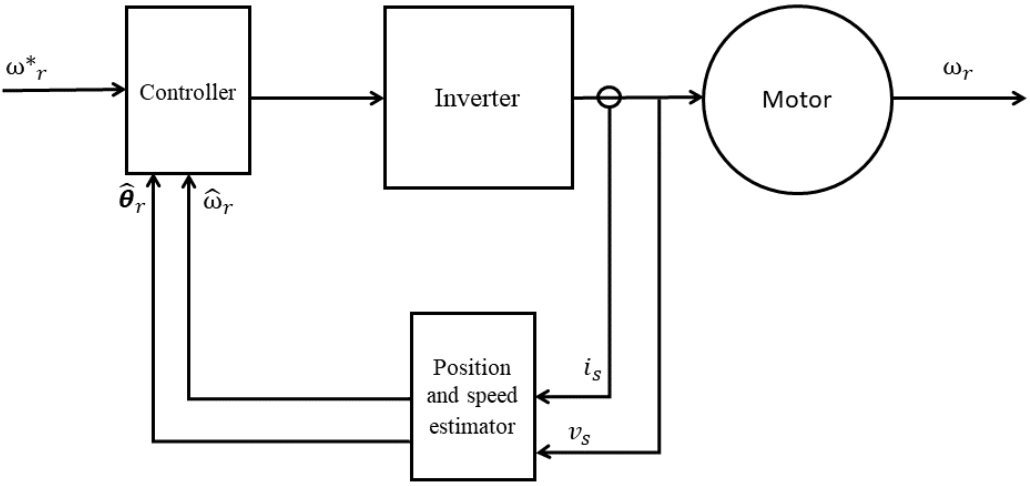

+

Figure 1.2 Illustration of model-based sensorless drive

1.2.2 Saliency-based Sensorless Schemes

In PMSMs, saliency emerges due to the uneven distribution of air gap permeance, leading to asymmetrical magnetic pathways for the q-axis and d-axis armature responses. In this sensorless strategy, high-frequency signals are injected into the machine windings. These signals contain rotor-related information, which is then processed to determine the rotor position [19]. The amplitude of saliency (or saliency inductance amplitude) remains unaffected by the rotor speed, enabling precise position estimate even at zero speed [20].

However, it's important to note that these saliency-based methods may introduce some drawbacks. They can potentially induce torque variations, generate audible noise, and result in vibrations on the rotor [21].

1.2.3 Predictive Sensorless Control

Predictive control (PC) has emerged as an alternative to conventional PI controllers in power electronics and electric drive applications [22]. Initially, the application of PC was limited due to its high computational demands [23, 24]. However, recent advancements in microcontrollers have mitigated this issue [25]. As a result, PC has become increasingly popular for implementing sensorless control in electrical drives [26-29].

The utilization of predictive control has demonstrated improved performance in sensorless drive systems. It enhances robustness against motor parameter variations [30] and enables fast transient response and accurate tracking response [29]. These advantages make predictive control an appealing choice for achieving high-performance sensorless control in electric drive systems.

1.3 Thesis Scope and Innovation

This thesis introduces an innovative flux-based Model-Reference Adaptive System (MRAS) for the estimation of both position and speed. Unlike the classical flux-based method, the proposed technique does not rely on integrators, leading to improved performance at low speeds compared to the traditional approach. Additionally, the new method exhibits stability in all four operating quadrants.

The performance of the proposed estimator was evaluated through extensive experimental testing, utilizing a 2.1-kW Permanent Magnet Synchronous Motor with FOC scheme as the control technique. The experiments showcased the estimator's good performance across various speeds and load conditions. The suggested approach also exhibited resilience to variations in motor parameters.

Furthermore, a comprehensive comparison was conducted between the novel method and the conventional flux MRAS estimator, providing insights into the advantages and improvements offered by the novel approach.

Finally, this study presents a novel speed estimator for Permanent Magnet Synchronous Motors (PMSMs) based on Finite Control Set Model Predictive Control (FCS-MPC). The adaptation mechanism of this estimator aims to minimize the error signal in speed across a finite range of rotor speeds. To ensure optimal speed estimation at each sampling time, a rotor speed search algorithm is employed.

The performance of the proposed estimator is evaluated through experimental testing. Additionally, a comparison is conducted between the proposed FCS-MPC-based estimator and the classical PI-based Flux MRAS estimator.

1.4 Objectives of the thesis

1. Develop a novel flux-based Model-Reference Adaptive System (MRAS) position estimator for sensorless control of Permanent Magnet Synchronous Motors (PMSM) that does not rely on integrators, distinguishing it from classical flux-based MRAS methods.

2. Evaluate the performance and effectiveness of the novel position estimator through simulation and experimental analysis, considering various speeds and loading conditions, and compare it to the classical method.

3. Design and develop a novel Finite Control Set Model Predictive Control (FCS-MPC) -based speed estimator for PMSM, aiming to replace the Proportional-Integral (PI) controller used in the classical MRAS method.

4. Conduct experimental investigations on the proposed predictive estimator to assess its performance in terms of estimated speed and position error, considering different speeds and loading conditions.

1.5 Thesis Layout

The organization of the thesis is as follows:

Chapter 1: Introduction

This chapter provides the background information for the thesis, highlighting the importance and significance of the study. It also outlines the research objectives that will be addressed.

Chapter 2: Literature Review

In this chapter, various sensorless estimation schemes, particularly focusing on MRAS-based estimators, are reviewed. The chapter provides an overview of the existing research and developments in the field.

Chapter 3: PMSM Modelling and MRAS

Chapter 3 delves into the modelling of Permanent Magnet Synchronous Motors (PMSM) and explains the principles of vector control. Additionally, the chapter covers the details of the flux-based MRAS model, which is relevant to the proposed estimation schemes.

Chapter 4: Proposed Flux-Based MRAS Estimator

In this chapter, a comprehensive description of the proposed flux-based Model-Reference Adaptive System (MRAS) estimator is provided. The chapter includes details of the methodology, simulation setup, and experimental implementation. Both simulation and experimental results are presented and analysed to evaluate the performance and effectiveness of the proposed estimator. Furthermore, the chapter includes a comparative analysis between the classical MRAS estimator and the proposed estimator.

Chapter 5: Proposed Predictive Observer

This chapter provides a comprehensive description of the proposed predictive observer. The chapter provides an in-depth explanation of the methodology and implementation of the observer. Additionally, it covers the experimental results obtained from the implementation of the proposed predictive observer. Furthermore, a comparative analysis is conducted between the proposed predictive observer and the PI-based estimator.

Chapter 6: Conclusion and Future Work

Chapter 6 serves as the conclusion of the thesis, summarizing the key findings, contributions, and implications of the research conducted. It provides a comprehensive overview of the main results obtained from the proposed estimators. The conclusion chapter also highlights the limitations of the proposed methods and discusses potential areas for future research. It identifies possible improvements, extensions, and directions that can be explored to enhance the performance and applicability of the proposed techniques.

Chapter 2: Literature Review on Model Reference Adaptive Systems for Position Estimator

Saliency-based approaches and model-based methods are among the numerous sensorless techniques that have been extensively developed. The saliency-based technique relies on the anisotropic property of PMSMs and is particularly reliable at zero and low speeds, as it is independent of speed. However, its effectiveness diminishes at high speeds attributed to the reduced signal-to-noise ratio of the signal.

On the other hand, model-based methods demonstrate good performance in the medium to high-speed range. This is because these methods ultimately rely on the detection of the rotor flux-induced back-EMF which is proportional to speed. By leveraging the accurate machine model, model-based techniques can accurately predict the rotor position, enabling reliable sensorless control.

In the following sections, a brief review of various model-based position estimators utilized for sensorless techniques is provided, and a focus is given to the MRAS-based observers.

2.1 Model-Based Speed and Position Estimators

Model-based speed and position estimators utilize the mathematical model of the machine to estimate the rotor speed and position. These estimators can be categorized into open-loop estimators, which are sensitive to variations in machine parameters [31], and closed-loop estimators, which offer improved performance and robustness by minimizing the error between measured and estimated quantities [32].

Closed loop estimators can be further classified into the extended Kalman filter (EKF) [33, 34], MRAS estimators [13-18], sliding mode (SM) estimators [35-38], artificial neural network [39] and Fuzzy Logic [40].

The Extended Kalman Filter (EKF) [41] is a widely used estimation algorithm for systems that involve nonlinear dynamics. It's an extension of the standard Kalman Filter (KF), which is designed for linear systems. The EKF handles nonlinearities by linearizing the system dynamics at each sample point and takes care of model inaccuracies and measurement noise in a system. Kalman-filter-based methods are known for their robustness to noise. However, these methods are sensitive to parameter variation and require significant computational demands. Furthermore, the tuning process involves trial and error to choose the optimal values for the covariance matrices, which can be challenging and time consuming.

A comparative study investigating the performance of three different observer methods—MRAS, SM, and EKF—for controlling Permanent Magnet Synchronous Motors (PMSMs) has been conducted in [42]. The study encompassed a diverse range of conditions for testing. Notably, MRAS exhibited a notable advantage over the other two methods in terms of performance.

Firstly, the dynamic response analysis demonstrated that MRAS achieved the fastest response dynamics among the three methods. Regarding fluctuation analysis, the findings indicated that MRAS exhibited the least amount of fluctuation, indicating its inherent stability and its ability to maintain smoother motor operation. In contrast, SM demonstrated the highest level of fluctuation.

In the evaluation of speed error, MRAS showcased the smallest error, particularly during transient speed variations. This suggests that MRAS is adept at minimizing speed errors during periods of rapid speed changes. On the other hand, Sliding Mode (SM) exhibited the largest speed error, this is because the presence of chattering. But when changing speeds, the EKF produces a larger error than SM observer. Furthermore, the observer methods were subjected to tests involving variations in motor parameters. Notably, all three methods demonstrated low sensitivity to variations in motor resistance. However, with changes in motor inductance, the Sliding Mode (SM) method displayed sensitivity, particularly to reductions in inductance.

The comparison was extended to torque mode testing, revealing that SM exhibited more pronounced torque ripples compared to the other methods. In contrast, MRAS showcased the lowest level of torque ripples, further solidifying its superiority in terms of minimizing undesirable torque fluctuations.

Table 2. 1 Comparison between MRAS, SM and EKF observers [42]

Observers	MRAS	SM	EKF
Speed error at steady state operation	0.42%	2%	0.5%
Speed error at transient operation	0.42%	4.2%	4.5%<error<6.5
Robustness to resistance change	Not sensitive	Not sensitive	Not sensitive
Robustness to inductance change	Not sensitive	Not sensitive	Sensitive
Robustness to load change	Error 0.8%	Error 10.4%	Error 4.2%

[43] and [44] reviewed various sensorless speed control techniques for Permanent Magnet Synchronous Machines, and a summarized comparison of these techniques are shown in table 2. 2.

Table 2. 2 Comparison between Open loop and close loop methods

Methods	Types	Advantages	Disadvantages
Open loop methods	Flux Linkage-Based Methods	Suitable for high and medium speeds, robust	Not accurate at low speeds, contains integrator
	Inductance-Based Methods	Work at very low speeds and standstill	Highly affected by measurement noise, poor performance for non-salient motor
Close loop methods	Extended Kalman Filter	Less sensitive to noise	High computational requirements, poor at low speeds
	Sliding-Mode Observers	Insensitivity to parameter variations	Chattering issues, Inefficient at low speeds
	MRAS-Based Methods	High speed of adaptation	Sensitive to motor parameters
	Extended EMF	Improved robustness against external disturbances	The accuracy is slightly affected by parameter variations

2.2 Model Reference Adaptive Systems

Model Reference Adaptive Systems (MRAS) have gained popularity in electric motor applications due to their performance and simplicity in parameter estimation. The block representation of a typical MRAS is depicted in Figure 2.1. The MRAS consists of two models: the reference model (a voltage model) and the adaptive model (a current model).

The two models utilise different methods to estimate the same state vector $\hat{Y}$, which is used to estimate the needed value of the state vector Y. As a result of a comparison of their outputs, an error is generated. This error is then used to drive an adaptation process, which modifies the parameters of the adjustable model until the error is minimized to zero.

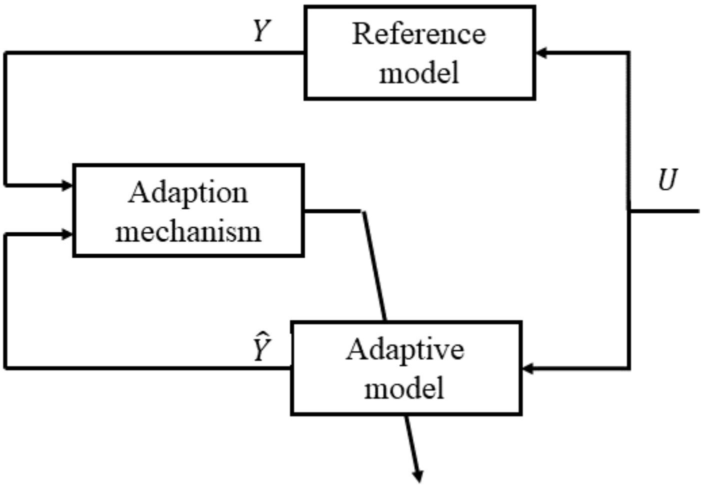

Figure 2.1 Illustration of MRAS observer.

Several variations of MRAS estimators have been developed, including back EMF-based MRAS [17], flux-based MRAS [18], power-based MRAS [13-16] and Model Predictive MRAS estimator.

2.2.1 Power-based MRAS position Estimator

In [45], a proposed method based on the Model Reference Adaptive System (MRAS) is introduced to estimate the rotor speed and position using the reactive power equation. The method utilizes the reference model to obtain the instantaneous reactive power, which is independent of speed. On the other hand, the adaptive model calculates the same quantity but as a function of speed.

The voltage equations of a Permanent Magnet Synchronous Motor (PMSM) represented in the rotating dq-reference frame are expressed as follows:

$$v_d = L_d \frac{di_d}{dt} + R_s i_d - wL_q i_q \tag{2.1}$$

$$v_q = R_s i_q + L_q \frac{di_q}{dt} + w(L_d i_d + \psi_m) \tag{2.2}$$

where v_d , v_q , i_d , i_q are dq-axis voltages and currents, respectively; L_d, L_q, are the dq-axis inductances, R_s is the stator resistance, ω is the rotor speed, and ψ_m is the rotor PM flux linkage.

At steady state and for vector controlled PMSM drive i_d = 0, rearranging the equations (2.1) and (2.2) to become as:

$$v_d = -\omega L_q i_q \tag{2.3}$$

$$v_q = R_s i_q + \omega \psi_m \tag{2.4}$$

The instantaneous reactive power q_r, which is used in the reference model, is expressed as:

$$q_r = v_q * i_d - v_d * i_q \tag{2.5}$$

Substituting (2.3) and (2.4) in (2.5),

$$q_r = \omega L_q {i_q}^2 \tag{2.6}$$

The reactive power in (2.6) is dependent on the speed, so it will be used in the adaptive model. The speed tuning error is determined by the difference between the reference and adjustable models, as follows:

$$\epsilon = (v_q * i_d - v_d * i_q) - \omega L_q {i_q}^2 \tag{2.7}$$

The estimated speed is obtained by passing the error in (2.7) to a PI controller and integrating to obtain the estimated position, as shown in Figure. 2.2.

While the method described is simple and has no integrator or stator resistance in the reference model and offer improved performance at low speeds compared to the flux-based and back-

EMF-based techniques, it is important to note that it has a drawback related to instability at certain operation points [13, 14]. And the accuracy may decrease at high speeds. Although a new formula has been proposed to overcome stability issues, it cannot guarantee stability in the presence of large disturbances [15, 16].

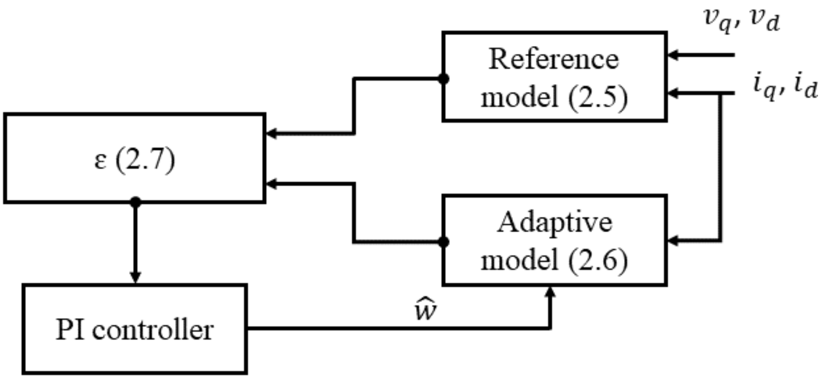

Figure 2.2 Illustration of power-based MRAS observer

2.2.2 Back EMF-based MRAS Estimator

The back electromotive force (EMF) of the PMSM in the stationary reference frame for the α-axis and β-axis can be expressed as [46]

$$e_\alpha = v_\alpha - L_s \frac{di_\alpha}{dt} - R_s i_\alpha \tag{2.8}$$

$$e_\beta = v_\beta - R_s i_\beta - L_s \frac{di_\beta}{dt} \tag{2.9}$$

Where v_α, v_β are the stator voltages, i_α, i_β represent the stator currents, R_s is the stator resistance and L_s donates the stator inductance.

The estimated back-EMFs in the stationary reference frame can be expressed as

$$\hat{e}_\alpha = -\hat{w} k_e \sin \hat{\theta} \tag{2.10}$$

$$\hat{e}_\beta = \hat{w} k_e \cos \hat{\theta} \tag{2.11}$$

Where $\hat{w}$ and $\hat{\theta}$ are the estimated speed and position respectively. k_e is the back-EMF constant.

The speed tuning signal for the back EMF based method which is used to estimate the speed is expressed as

$$\epsilon = e_\beta * \hat{e}_\alpha - e_\alpha * \hat{e}_\beta \tag{2.12}$$

Although the back EMF estimation method is very common method for sensorless PMSM control, and showing great performance at medium and high speeds, it has a poor performance and stability issue at low speeds. This is ultimately due to the fact that, as shown in (2.10-2.11) back electromotive force (EMF) is directly proportional to the speed and therefore these signals become unobservable as the speed approaches zero. Moreover, Due to the differentiation term in the reference model, it is sensitive to measurement noise.

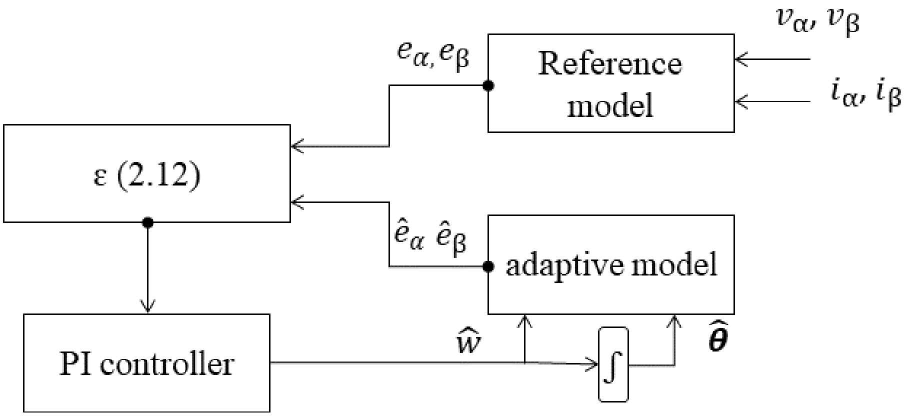

Figure 2.3 Block diagram of the MRAS estimator based on back EMF.

2.2.3 Flux-Based MRAS Estimation Method

The initial introduction of the first flux-based estimator was documented in [47]. Flux-based MRAS observers have undergone extensive research over the past two decades, demonstrating superior performance across a broad range of speeds.

Nevertheless, this method encounters several challenges, particularly at low speeds. These challenges include the pure integration problem, measurement errors and the MRAS adaptation mechanism problem [6]. In the subsequent chapter, a detailed examination of this observer will be conducted, focusing on these issues, and exploring potential solutions.

2.2.4 Model Predictive MRAS Estimator

Model Predictive-based Controllers (MPCs) with sensorless applications have gained significant attention recently, and they can be categorized into two types: classical MPCs and finite control set-model predictive controllers (FCS-MPCs) [48]. In classical MPCs, the controller generates a continuous voltage vector that is then applied to the inverter through a modulator. On the other hand, in FCS-MPCs, the controller directly generates the switching state of the inverter.

Sensorless induction machine control systems with predictive current controllers have been proposed in [30], which enhance robustness against changes in motor parameters. Similarly, in [29], speed and current predictive controllers for a sensorless Permanent Magnet Synchronous Motor (PMSM) drive system were introduced, achieving fast transient responses and accurate tracking responses. Comparative studies have shown that the proposed predictive current control method in [49] outperforms Pulse Width Modulation (PWM) and hysteresis current controls.

Furthermore, in [50], a sensorless Induction Motor (IM) drive system is utilized with predictive torque control (PTC) combined with sliding mode feedback. By combining the proposed prediction model with a sliding mode full-order observer, a robust sensorless PTC is achieved, which is stable even at very low speeds and does not require parameter estimation.

Finite Control Set Model Predictive Control (FCS-MPC) has gained popularity in various applications due to its user-friendliness and flexibility to accommodate different performance specifications [51-53]. It has been successfully employed in different fields and industries.

In [54], Finite Control Set Model Predictive Control (FCS-MPC) was employed to operate an Induction Motor (IM) to improve system performance. Similarly, in [27], a control scheme based on the predictive deadbeat algorithm was proposed for a sensorless vector-controlled Permanent Magnet Synchronous Generator (PMSG). The scheme demonstrated excellent performance and robustness against parameter variations.

Furthermore, in [55], a sensorless system for an Induction Motor based on FCS-Predictive Torque Control (FS-PTC) was introduced. This method incorporated an Extended Kalman Filter (EKF) to enhance speed accuracy, and the estimated stator currents were utilized instead of the measured currents to improve current Total Harmonic Distortion (THD).

In contrast to the previously mentioned methods, [56] presents a novel approach that utilizes Finite Set Model Predictive Control (FS-MPC) for position estimation in an Induction Motor (IM). Unlike traditional approaches where prediction principles are applied to the design of the controller, this approach applies prediction principles directly to the design of the position estimator.

In this approach, a rotor position search algorithm is employed to discretize the rotor position into a finite number of positions. At each sampling time, the cost function is evaluated for each of these positions, and the optimal position corresponding to the minimum cost function is determined to remove the requirement for PI controller.

Figure 2.4 presents the flow chart of the search algorithm, while Figure 2.5 displays the block diagram of the predictive Model Reference Adaptive System (MRAS) estimator. The process begins by computing the voltage model outputs $\psi_{\alpha v}$ and $\psi_{\beta v}$ using the stator voltages and currents as inputs.

To discretize the rotor position, the 360º search space is divided into j sectors. The algorithm then identifies the sector that yields the minimum cost function. Subsequently, this sector is further subdivided, and the search process is iteratively repeated. In this search, eight sectors and eight iterations are employed, resulting in a resolution of 0.35° for each search result.

The displacement angle ($\Delta\theta_i$) is calculated as follows:

$$\Delta\theta_i = 45° \cdot 2^{-i} \tag{2.13}$$

Where i is the order of the iteration.

The displacement of the base position within each iteration is performed to obtain eight discrete rotor positions. This process is carried out as follows:

$$\theta_{i,j} = \theta_b + \Delta\theta_i . (j - 4) \tag{2.14}$$

Where j is the order of the displacement $= 1 \dots 8$ and θ_b is initialised as the rotor angle from the previous time step.

In the first iteration, a displacement of $\Delta\theta_0 = 45°$ is applied with a base position $\theta_b = 0$. By applying Equation (2-14), eight discrete positions are obtained: $0°$, $45°$, $90°$, $135°$, $180°$, $-45°$, -90°, $-135°$.

For each of these discrete positions, the adaptive model outputs are calculated. This allows for the determination of eight different cost functions, each corresponding to a specific angle. The cost functions capture the discrepancy between the reference and adaptive model outputs for each angle, providing an assessment of the estimation accuracy.

In the study conducted by [18], the predictive method described above was implemented on the previously mentioned flux-based method. As a result, the error ($\varepsilon_{i,j}$) is computed for each estimated position using the following:

$$\varepsilon_{i,j} = \psi_{\alpha v}\psi_{\beta i,j} - \psi_{\beta v}\psi_{\alpha i,j} \tag{2.15}$$

The angle associated with the minimum error is selected as the base angle $\theta_{b,1}$ for the next iteration.

In subsequent iterations ($i = 1$), the angular displacement is reduced to $\Delta\theta_0 = 45° \cdot 2^{-1} = 22.5°$. The second iteration of the search begins from the updated angle $\theta_{b,1}$ to identify the position that yields the smallest error.

In [18], the number of sectors was set to 8, and the number of iterations was set to 13. These parameters were chosen to achieve an angle with an error of 0.005° for each search result. The estimated speed was obtained by utilizing a phase-locked loop (PLL), which calculates the speed based on the estimated position. This method produces a speed estimation with less noise compared to the differentiation method used in [56]. This technique shows fluctuations in the estimated rotor speed. To address these variations an adaptive low-pass filter is implemented.

In practice, the search time can be effectively reduced by setting the initial value of the algorithm output to be the algorithm output at the last sampling instant, $\theta_{b,7}$, instead of starting from the zero angle in each sampling period. This approach is based on the observation that the rotor angle does not undergo substantial changes between two consecutive time samples.

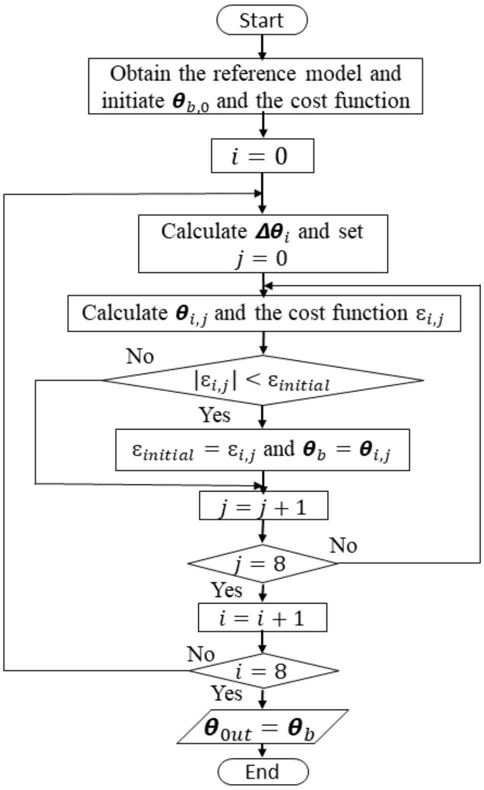

Figure 2.4 Flowchart of the algorithm for searching the rotor position.

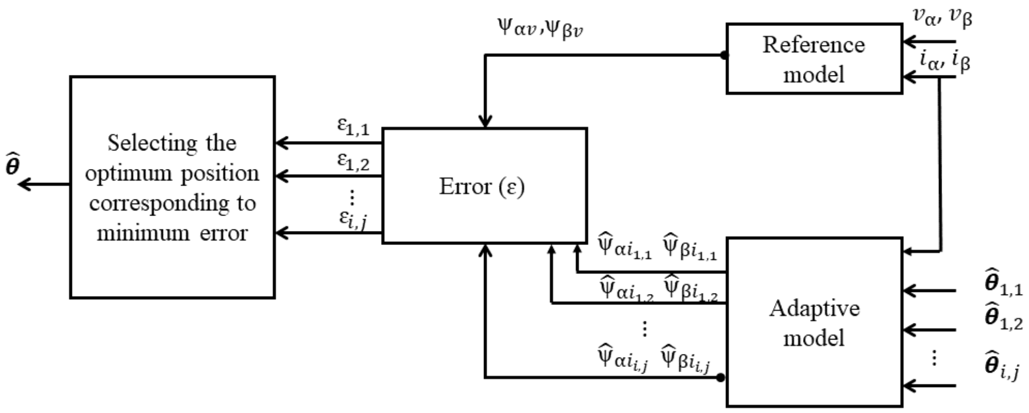

Figure 2.5 Block diagram of the MP-MRAS observer.

This method has been simulated using Matlab/Simulink and applied to a PMSM with the following parameters: Pole-pairs = 3, stator resistance = 2.2 ohms, PM flux = 0.356 V/Hz, d- inductance = 12.5 mH, q-inductance = 15 mH and inertia = 0.00077 Kg.m^2

Fig 2.6 shows the simulation results for MP-MRAS estimator compared to the classical estimator. The reference speed is initially set to 20 rad/s and then increased to 80 rad/s at the time instant 2s at no load. The results show the superiority of MP-MRAS. During the transient phase, the estimated speed for both approaches tracks the reference speed, and it takes about 0.3s to get to steady state. It is notable that the cost function in the MP-MRAS remains very small even during transient operations, in contrast to 0.04 observed in the conventional MRAS case. Moreover, the MP-MRAS has more accurate estimated position during the transient operation compared to the classical method.

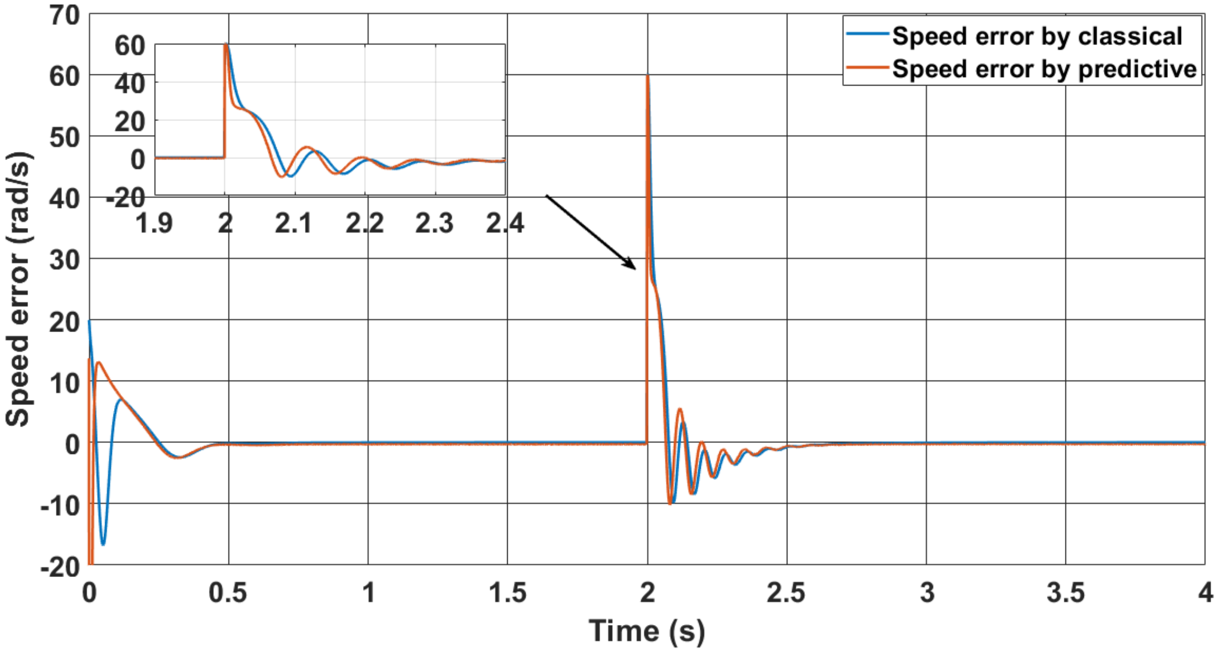

(a)

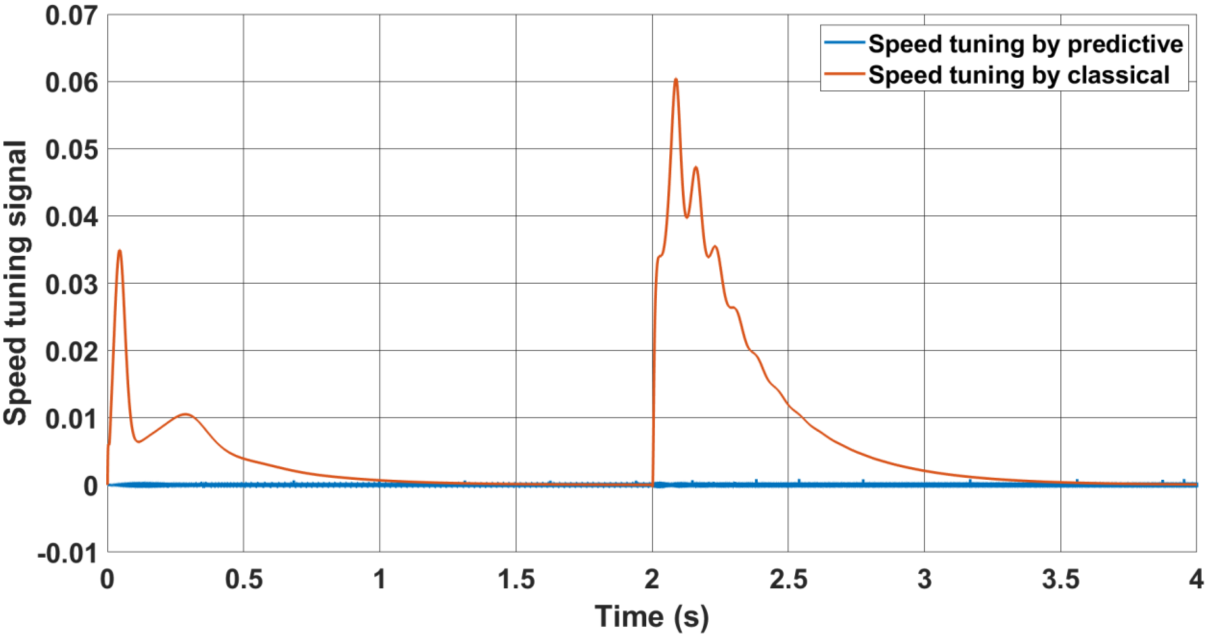

(b)

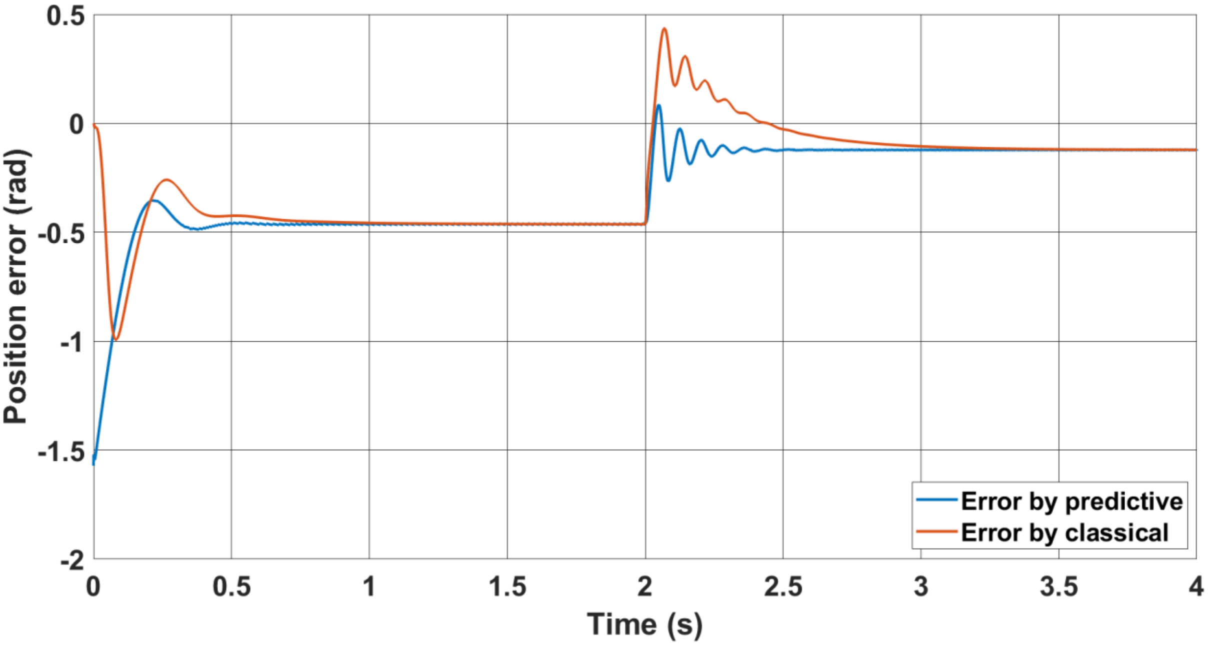

(c)

Fig 2.6 Simulation results of MP-MRAS and classical estimators (a) estimated speeds (b) speed tuning signals (c) position errors.

2.3 Conclusion

This chapter provides various sensorless methods utilized for position estimation in PMSM drives, including Extended Kalman Filter (EKF), Sliding Mode methods, and MRAS-based methods. The chapter has concentrated on MRAS-based schemes, offering a detailed explanation of these methods with their advantages and disadvantages. A Model Predictive-MRAS based method has been introduced and compared to the classical MRAS based method. It was tested in simulation and the results showed the superiority of this method compared to the classical method.

Chapter 3: Modelling and Model Reference Adaptive Systems for Vector Control PMSM

PMSM (Permanent Magnet Synchronous Motor) can be categorized into two types based on rotor structures: Surface Mounted PMSM (SPMSM) and Interior PMSM (IPMSM) [57].

In SPMSM, the permanent magnets are mounted on the surface of the rotor. Due to the similarity in relative permeability between the permanent magnets and air, the active air gap in SPMSM is roughly equal to the sum of the air gap length and the magnet radial thickness. As a result, the stator windings in SPMSM have low and equal inductances along the dq-axes.

On the other hand, in IPMSM, the permanent magnets are located inside the rotor structure. In these machines, there is a saliency effect, which means that the inductance along the d-axis (L_d) is lower than the inductance along the q-axis (L_q). This difference in inductance is a result of the d-axis flux traveling through a higher reluctance path compared to the q-axis flux.

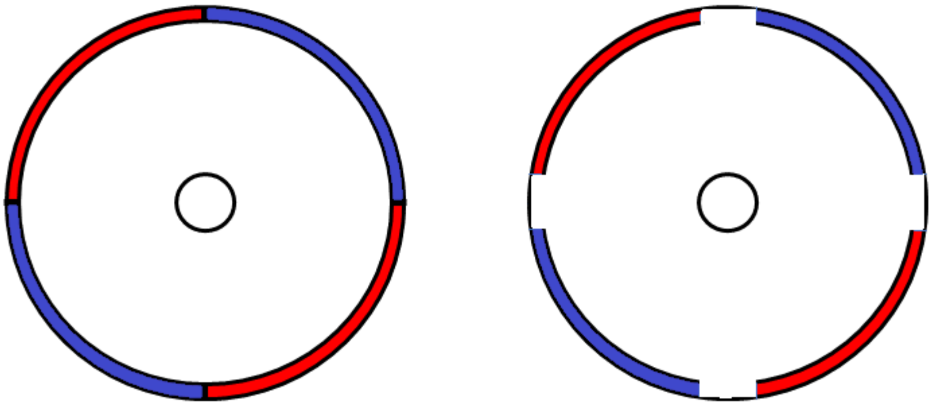

a. SPMSM b. IPMSM

Figure 3.1 Rotor topologies of PMSM

Based on the type of back-EMF, PMSM can be categorized into two types: brushless DC machines (BLDC) and brushless AC machines (BLAC) [58, 59]. BLDC machines have a trapezoidal back-EMF waveform and fed by square-wave currents. On the other hand, BLAC machines have a sinusoidal back-EMF waveform and are fed by sinusoidal stator currents.

BLDC drives are commonly used in low-cost applications where high-resolution position sensors are not required. In certain cases where the dynamic response of the speed is not critical, even the current sensor can be eliminated. BLDC drives offer simplicity and cost-effectiveness in such applications.

In contrast, BLAC motors are employed in applications that demand low torque ripple and fast torque response. Compared to BLDC motors, BLAC motors generate smoother torque due to their sinusoidal back-EMF waveform [60]. This makes them suitable for applications where precise control of torque and speed is crucial.

In this thesis, the focus will be on the control system of BLAC motors, which involves achieving low torque ripple and fast response in various applications.

To achieve high-performance control of PMSM, the field-oriented control (FOC) technique is utilized. FOC allows for the independent control of torque and flux, enabling the attainment of a similar dynamic performance as that of a DC machine drive [3]. In FOC, the three-phase time and rotor position-dependent model of the PMSM is transformed into a two-coordinate (d and q) time and position-invariant model. This transformation involves shifting from a stationary frame (such as the stator reference frame a, b, c or the orthogonal reference frame α-β) to a rotating frame (d-q) that rotates at the synchronous speed.

In the rotating frame, the d-axis is aligned with the rotor flux. This enables the independent control of flux and torque by manipulating the d and q components of the stator currents [61]. Accurate modelling of the PMSM is crucial for both FOC and MRAS sensorless control.

Therefore, this chapter presents the modelling of PMSM along with a flux-based MRAS estimator.

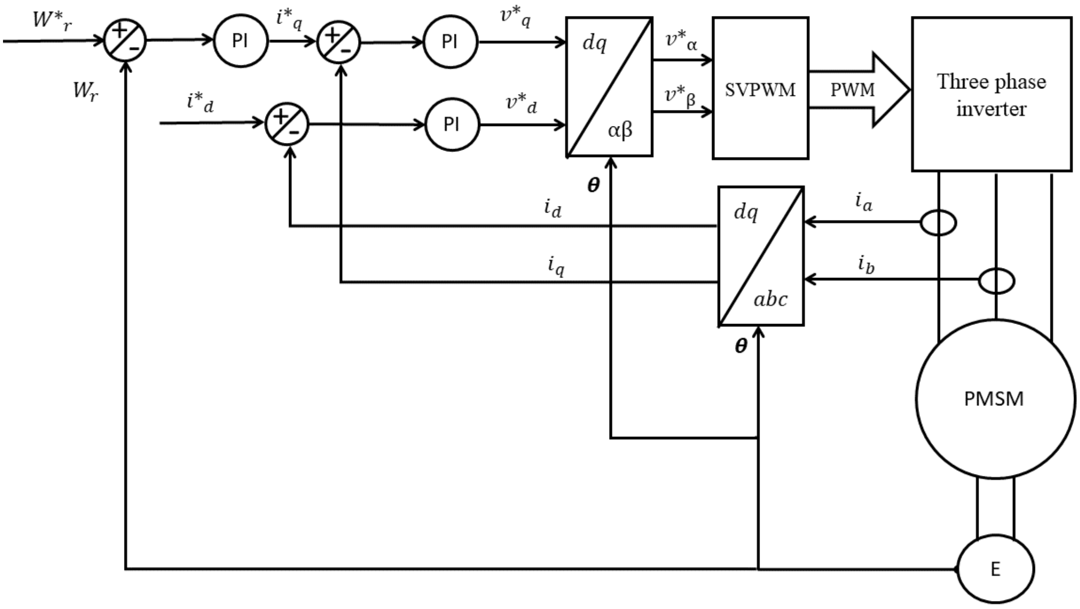

Figure 3.2 FOC control of PMSM

3.1 The Dynamic Model of PMSM

In a three-phase PMSM, the space vector of the stator current in the stationary reference frame is represented as:

$$i_s = \frac{2}{3}(i_a + a i_b + a^2 i_c) \tag{3.1}$$

Here, i_a, i_b and i_c denote the phase currents, The variable ' a ' represents the complex exponential term $a = e^{j\frac{2\pi}{3}}$, where j is the imaginary unit.

To obtain the two orthogonal components (αβ) of the stator current vector, the value of 'a' in equation (3.1) is substituted. The α component represents the real part, while the β component represents the imaginary part. This substitution leads to the following expressions:

$$i_\alpha = \frac{2}{3} i_a - \frac{1}{3} i_b - \frac{1}{3} i_c \tag{3.2}$$

$$i_\beta = \frac{1}{\sqrt{3}} (i_b - i_c) \tag{3.3}$$

This can be represented in a matrix as:

$$\begin{bmatrix} i_\alpha \\ i_\beta \end{bmatrix} = \frac{2}{3} \begin{bmatrix} 1 & -\frac{1}{2} & -\frac{1}{2} \\ 0 & \frac{\sqrt{3}}{2} & -\frac{\sqrt{3}}{2} \end{bmatrix} \begin{bmatrix} i_a \\ i_b \\ i_c \end{bmatrix} \tag{3.4}$$

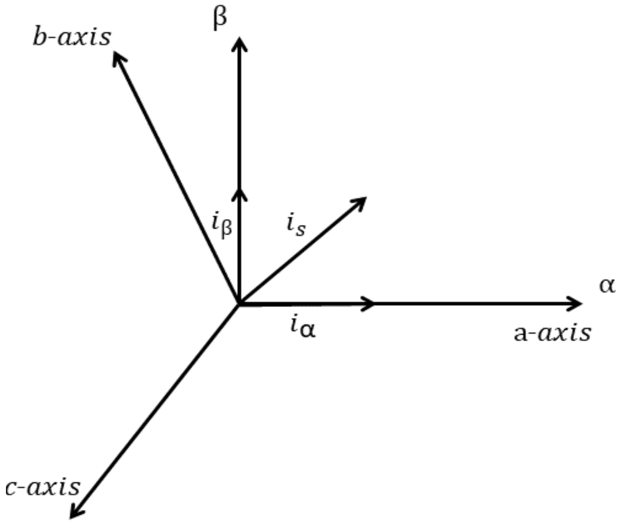

Figure 3.3 The space vector of the stator current

The current vector can be easily converted from $(\alpha\beta)$ frame to the three-phase frame by inversing the above matrix and multiplying it by $\alpha\beta$ components as following:

$$\begin{bmatrix} i_a \\ i_b \\ i_c \end{bmatrix} = \begin{bmatrix} 1 & 0 \\ -\frac{1}{2} & \frac{\sqrt{3}}{2} \\ -\frac{1}{2} & -\frac{\sqrt{3}}{2} \end{bmatrix} \begin{bmatrix} i_\alpha \\ i_\beta \end{bmatrix} \tag{3.5}$$

The d-q components of the phase current vector in the rotating frame can be obtained from the (αβ) components in the stationary frame using the following equation:

$$i_d + ji_q = (i_\alpha + ji_\beta)e^{-j\theta} \tag{3.6}$$

This transformation can be represented in matrix form, known as the Park transformation matrix, as follows:

$$\begin{bmatrix} i_d \\ i_q \end{bmatrix} = \begin{bmatrix} cos\theta & sin\theta \\ -sin\theta & cos\theta \end{bmatrix} \begin{bmatrix} i_\alpha \\ i_\beta \end{bmatrix} \tag{3.7}$$

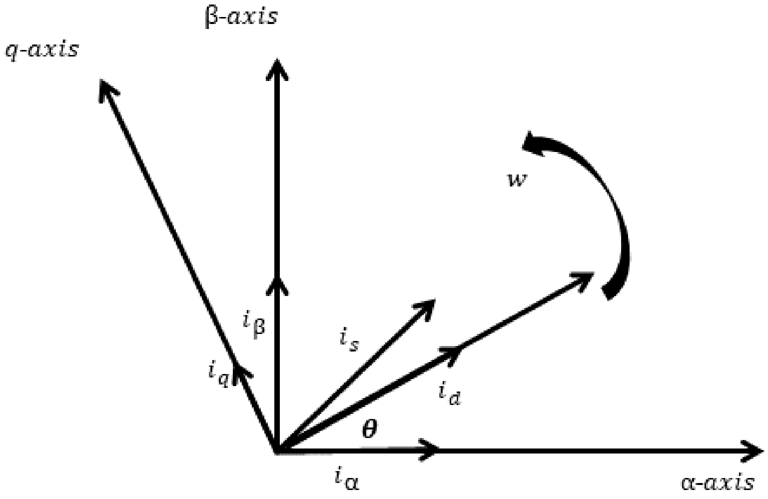

Figure 3.4 Park transformation

Similarly, the $(\alpha\beta)$ components can be obtained from the d-q components using the Inverse Park transformation as:

$$\begin{bmatrix} i_\alpha \\ i_\beta \end{bmatrix} = \begin{bmatrix} cos\theta & -sin\theta \\ sin\theta & cos\theta \end{bmatrix} \begin{bmatrix} i_d \\ i_q \end{bmatrix} \tag{3.8}$$

For a 3-phase brushless AC motor with a PM rotor, the 3-phase voltages can be calculated as:

$$\begin{bmatrix} v_a \\ v_b \\ v_c \end{bmatrix} = R_s \begin{bmatrix} i_a \\ i_b \\ i_c \end{bmatrix} + \rho \begin{bmatrix} \psi_a \\ \psi_b \\ \psi_c \end{bmatrix} \tag{3.9}$$

Where v_a, v_b, v_c, i_a, i_b, i_c, ψ_a, ψ_b and ψ_c are the phase voltages, currents and flux-linkages, Rs the stator resistance, and $\rho = \frac{d}{dt}$.

(3.9) can be written in $\alpha\beta$ frame as:

$$\begin{bmatrix} v_\alpha \\ v_\beta \end{bmatrix} = R_s \begin{bmatrix} i_\alpha \\ i_\beta \end{bmatrix} + \rho \begin{bmatrix} \psi_\alpha \\ \psi_\beta \end{bmatrix} \tag{3.10}$$

By left-multiplying equation (3.10) with the Park transformation matrix on both sides, the equation can be expressed as follows:

$$\begin{bmatrix} cos\theta & sin\theta \\ -sin\theta & cos\theta \end{bmatrix} \begin{bmatrix} v_\alpha \\ v_\beta \end{bmatrix} = R_s \begin{bmatrix} cos\theta & sin\theta \\ -sin\theta & cos\theta \end{bmatrix} \begin{bmatrix} i_\alpha \\ i_\beta \end{bmatrix} + \begin{bmatrix} cos\theta & sin\theta \\ -sin\theta & cos\theta \end{bmatrix} \rho \begin{bmatrix} \psi_\alpha \\ \psi_\beta \end{bmatrix} \tag{3.11}$$

$$\begin{bmatrix} v_d \\ v_q \end{bmatrix} = R_s \begin{bmatrix} i_d \\ i_q \end{bmatrix} + \begin{bmatrix} cos\theta & sin\theta \\ -sin\theta & cos\theta \end{bmatrix} \rho \begin{bmatrix} \psi_\alpha \\ \psi_\beta \end{bmatrix} \tag{3.12}$$

The flux term in (3.12) can be expressed as:

$$\begin{bmatrix} cos\theta & sin\theta \\ -sin\theta & cos\theta \end{bmatrix} \rho \begin{bmatrix} \psi_\alpha \\ \psi_\beta \end{bmatrix} = \rho \left(\begin{bmatrix} cos\theta & sin\theta \\ -sin\theta & cos\theta \end{bmatrix} \begin{bmatrix} \psi_\alpha \\ \psi_\beta \end{bmatrix} \right) - \rho \begin{bmatrix} cos\theta & sin\theta \\ -sin\theta & cos\theta \end{bmatrix} \begin{bmatrix} \psi_\alpha \\ \psi_\beta \end{bmatrix}$$

$$= \rho \begin{bmatrix} \psi_d \\ \psi_q \end{bmatrix} - w \left(\begin{bmatrix} -sin\theta & cos\theta \\ -cos\theta & -sin\theta \end{bmatrix} \begin{bmatrix} \psi_\alpha \\ \psi_\beta \end{bmatrix} \right)$$

$$= \rho \begin{bmatrix} \psi_d \\ \psi_q \end{bmatrix} - w \begin{bmatrix} \psi_q \\ -\psi_d \end{bmatrix} \tag{3.15}$$

Therefore, based on equation (3.15), equation (3.12) can be written as follows:

$$\begin{bmatrix} v_d \\ v_q \end{bmatrix} = R_s \begin{bmatrix} i_d \\ i_q \end{bmatrix} + \begin{bmatrix} \rho\psi_d - w\psi_q \\ \rho\psi_q + w\psi_d \end{bmatrix} \tag{3.16}$$

For salient PMSM, the fluxes can be expressed as:

$$\psi_d = (L_d i_d + \psi_m) \tag{3.17}$$

$$\psi_q = (L_q i_q) \tag{3.18}$$

By substituting (3.17) and (3.18) in (3.16), it yields the following:

$$\begin{bmatrix} v_d \\ v_q \end{bmatrix} = R_s \begin{bmatrix} i_d \\ i_q \end{bmatrix} + \begin{bmatrix} L_d \rho i_d - w L_q i_q \\ L_q \rho i_q + w(L_d i_d + \psi_m) \end{bmatrix} \tag{3.19}$$

For non-salient PMSMs drive, the maximum torque per unit current operation is obtained by setting i_d = 0. In this case, rearranging equation (3.19), we can express it as follows:

$$\begin{bmatrix} v_d \\ v_q \end{bmatrix} = R_s \begin{bmatrix} 0 \\ i_q \end{bmatrix} + \begin{bmatrix} -wL_q i_q \\ L_q \rho i_q + w\psi_m \end{bmatrix} \tag{3.20}$$

The electromagnetic torque can be expressed as:

$$T_e = \frac{3}{2} p(\psi_d i_q - \psi_q i_d) = \frac{3}{2} p \psi_m i_q \tag{3.21}$$

From equation (3.21), it can be observed that the torque is independently controlled by the q-axis current (i_q), similar to that of DC machines.

3.2 Flux-based MRAS Position and Speed Estimators

In the flux-based MRAS estimation method for PMSM, the estimated speed is determined by taking the magnitude of the cross product (error) between the estimated stator flux linkage obtained from integrating the back electromotive force (EMF) (equation 3.22) and the stator flux linkage derived from the magnet flux and current (equation 3.23). This error is then passed through a proportional-integral (PI) controller, and the integrated output is used to obtain the estimated position.

$$\begin{bmatrix} \psi_{\alpha v} \\ \psi_{\beta v} \end{bmatrix} = \int \left(\begin{bmatrix} v_\alpha \\ v_\beta \end{bmatrix} - R_s \begin{bmatrix} i_\alpha \\ i_\beta \end{bmatrix} \right) dt \tag{3.22}$$

$$\begin{bmatrix} \psi_{di} \\ \psi_{qi} \end{bmatrix} = \begin{bmatrix} L_d & 0 \\ 0 & L_q \end{bmatrix} \begin{bmatrix} i_d \\ i_q \end{bmatrix} + \begin{bmatrix} \psi_m \\ 0 \end{bmatrix} \tag{3.23}$$

Equation (3.23) is transformed to the stationary reference frame by employing the Clarke to Park transform as:

$$\begin{bmatrix} \psi_{\alpha i} \\ \psi_{\beta i} \end{bmatrix} = \begin{bmatrix} \cos\hat{\theta} & -\sin\hat{\theta} \\ \sin\hat{\theta} & \cos\hat{\theta} \end{bmatrix} \begin{bmatrix} \psi_{di} \\ \psi_{qi} \end{bmatrix} \tag{3.24}$$

The magnitude of the cross product of the two estimated fluxes can be calculated using the following equation:

$$\varepsilon = \psi_{\alpha v}\psi_{\beta i} - \psi_{\beta v}\psi_{\alpha i} \tag{3.25}$$

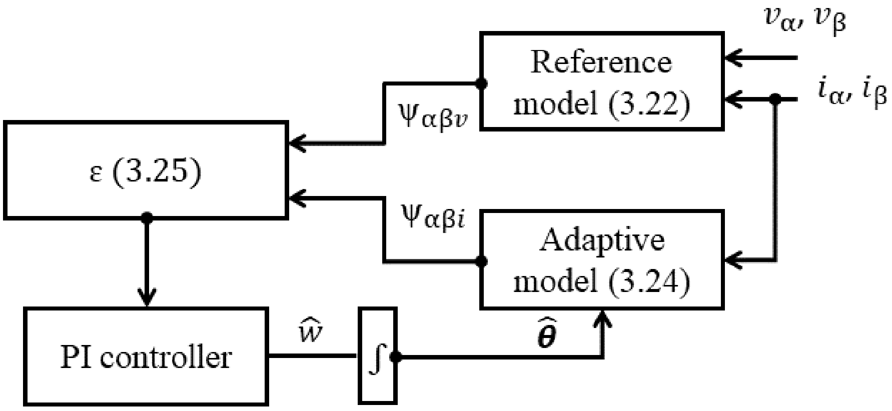

Figure 3.5 Illustration of the flux-based MRAS method.

The error calculated in equation (3.25) is subsequently input into a proportional-integral (PI) controller. The PI controller processes the error and generates an estimation of the rotor speed. This speed estimation is then integrated to obtain the estimated position of the rotor.

As depicted in Figure 3.5, the estimated position is fed back to the current model, where it is utilized to drive the error to zero.

The actual and estimated fluxes can be expressed as:

$$\begin{gathered}\psi_d = \psi \cos(\theta) \\ \psi_q = \psi \sin(\theta) \\ \hat{\psi}_d = \hat{\psi} \cos(\hat{\theta}) \\ \hat{\psi}_q = \hat{\psi} \sin(\hat{\theta})\end{gathered} \tag{3.26}$$

Substituting (3.26) into (3.25) yields:

$$\epsilon = \psi\hat{\psi}\sin(\theta - \hat{\theta}) \approx \psi\hat{\psi}(\theta - \hat{\theta}) \tag{3.27}$$

It can be noticed that the relationship is sinusoidal between the error ϵ and the position error. And the error ϵ is approximately proportional to the position error when the estimated position is nearly equal to the actual position. Figure 3.6 shows the close loop transfer function of the classical estimator.

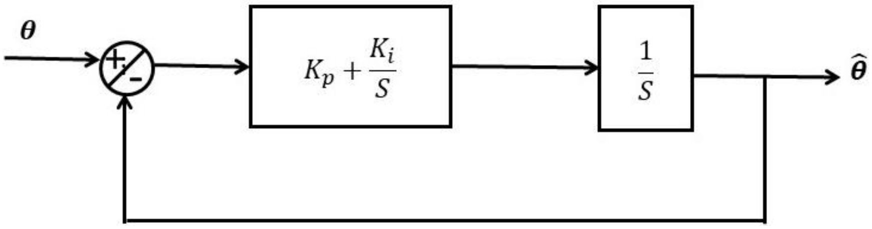

Figure 3.6 the close loop transfer function of the classical estimator

To tune the PI controller, the pole placement method, which involves placing the poles of the closed-loop transfer function at desired locations to achieve the desired performance is used as following.

The characteristic equation for the system can be written as

$$S^2 + k_pS + k_i = S^2 + 2\zeta\omega_nS + {\omega_n}^2 \tag{3.28}$$

Where ζ, ω_n are the damping ratio and the natural frequency, respectively.

By choosing $\zeta = 0.7, \omega_n = 30\ rad/s$, the gains are obtained from equation 3.28 as

$k_p = 2\zeta\omega_n = 2 * 0.7 * 30 = 42\ rad\ V^{-2}\ s^{-3}$, $k_i = {\omega_n}^2 = 900\ rad\ V^{-2}\ s^{-3}$

3.3 The Problems for flux-based MRAS method

The traditional flux-based MRAS estimator encounters several challenges that restrict their effectiveness, particularly at low speeds. Here, a summary of these problems:

3.3.1 The Issue of Pure Integration

According to [6], the flux-based MRAS speed estimation method demonstrates superior performance over a wide range of speeds. However, the presence of a pure integrator in the voltage model (3.22) poses a significant disadvantage, specifically at low speeds, as it degrades the performance of the estimation.

The pure integrator used in the voltage model has infinite gain at zero frequency, which can be problematic as it amplifies small offsets in current sensors and initial conditions. To mitigate this issue, a low pass filter (LPF) is commonly employed in place of the pure integrator. The LPF has a similar frequency response as the pure integrator above its cross-over frequency but possesses a finite DC gain at zero frequency. This allows the LPF to attenuate any offset and bring initial conditions to zero.

However, at low frequencies, the LPF and integrator exhibit different responses, leading to significant amplitude and phase errors. Figure 3.7 presents a comparative view of the frequency responses of the ideal integrator and various approximations achieved through distinct first-order transfer functions using three-time constants: $10s$, $1s$, and $0.1s$. An integrator's frequency response leads to a linear decrease in magnitude with increasing frequency, which causes significant attenuation of high-frequency components. The integrator introduces a consistent 90-degree phase shift across all frequencies. Conversely, a low-pass filter's frequency response entails gradual attenuation of higher frequencies beyond a defined cut-off point. The filter introduces a variable phase shift that becomes minimal at frequencies significantly lower than the cut-off. Longer time constants offer an enhanced approximation of the integrator's behaviour. However, this advantage comes at the cost of a slower transient response, resulting in a reduced ability to swiftly attenuate undesired initial conditions.

Fig. 3.8 provides an illustrative example of how the LPF affects the amplitude and angle of the flux in comparison to the integrator. It can be observed that the angle error obtained with the LPF decreases as the speed increases. In contrast, the amplitude and angle accuracy remain unaffected when using the integrator.

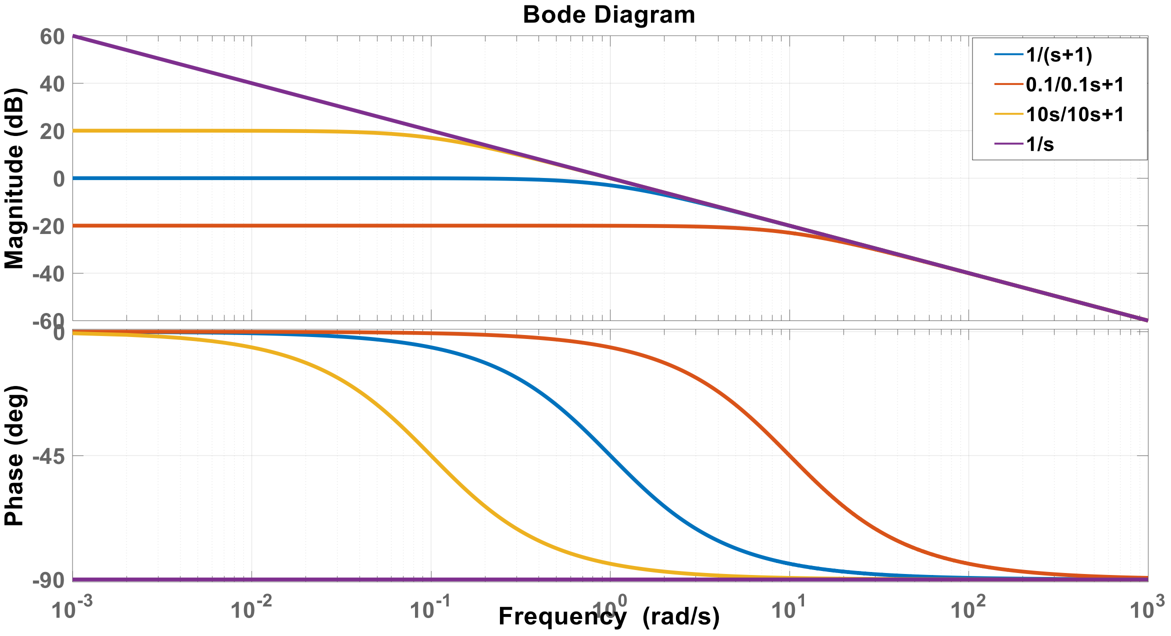

0

Figure 3.7 Frequency responses of the low pass filters for different values of time constants compared with the response of the integrator.

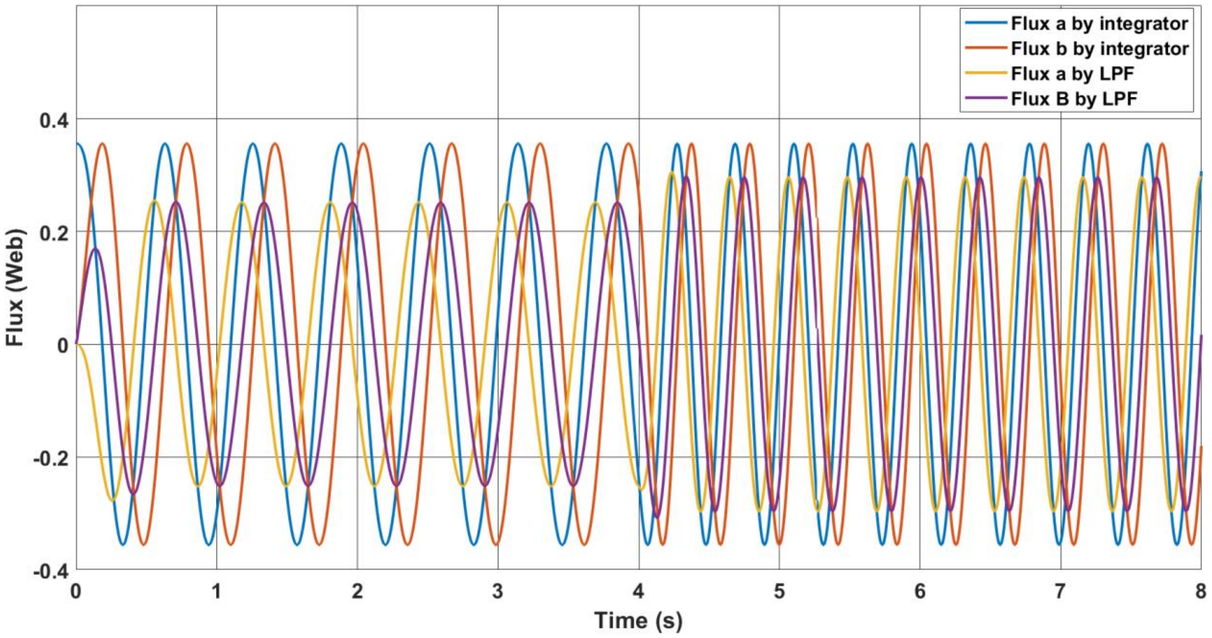

(a)

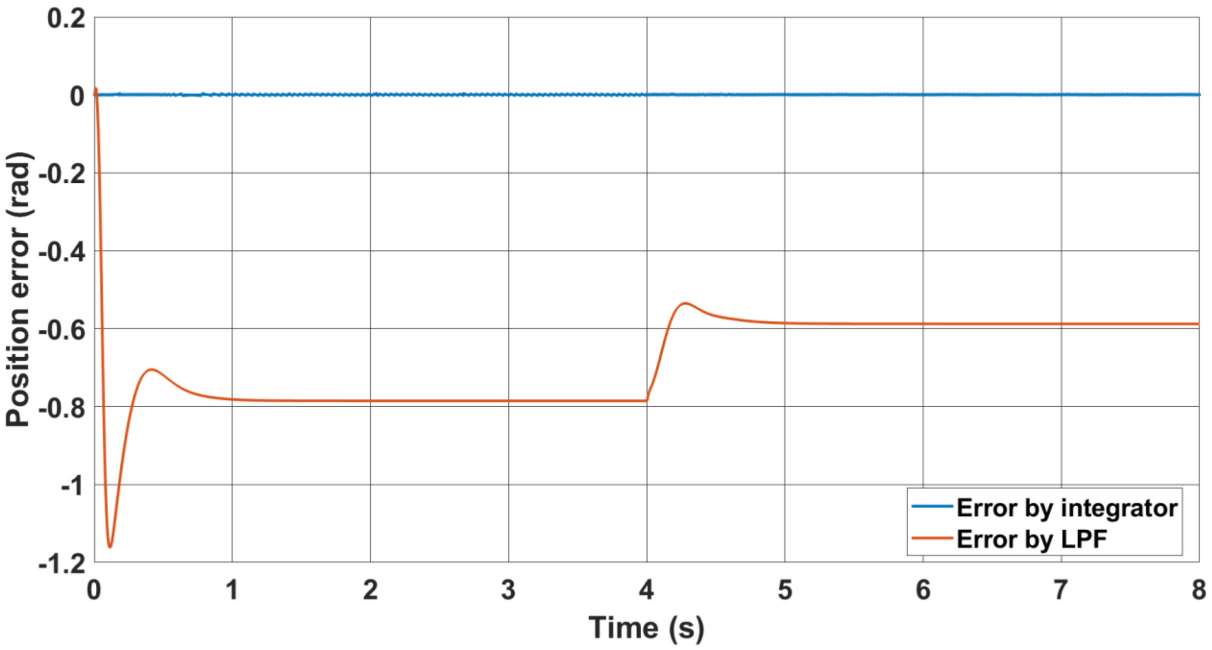

(b)

Figure 3.8 Simulation results of LPF effect on the amplitude and angle of flux compared with the integrator (a) flux, (b) flux angle error.

Some studies have attempted to address the DC offsets and drifts present in the motor back-EMFs by employing more intricate systems instead of a basic low-pass filter with a fixed cut-off frequency.

In [62], a new integration algorithm is introduced employing fixed cut-off low pass filters and feedback mechanisms to replicate the behaviour of pure integration. This approach involves significant computational demands. Furthermore, at lower speeds, the influence of DC offsets becomes more pronounced, leading to inaccuracies in the stator flux estimation.

Fig 3.10 shows the simulation results of the integration algorithm illustrated in figure 3.9 for sensorless control of PMSM. The cutoff frequency ω_c used in the LP filter is set to 10 rad/s. The reference speed was initially set to 2 rad/s and then increased to 7 rad/s at instant 15s. It can be seen that the DC offset in the estimated flux is obviously high at low speed and it reduces at higher speeds as shown in figure 3.10 (a). As a results, the speed becomes more fluctuated as it goes low as seen in figure 3.10 (b).

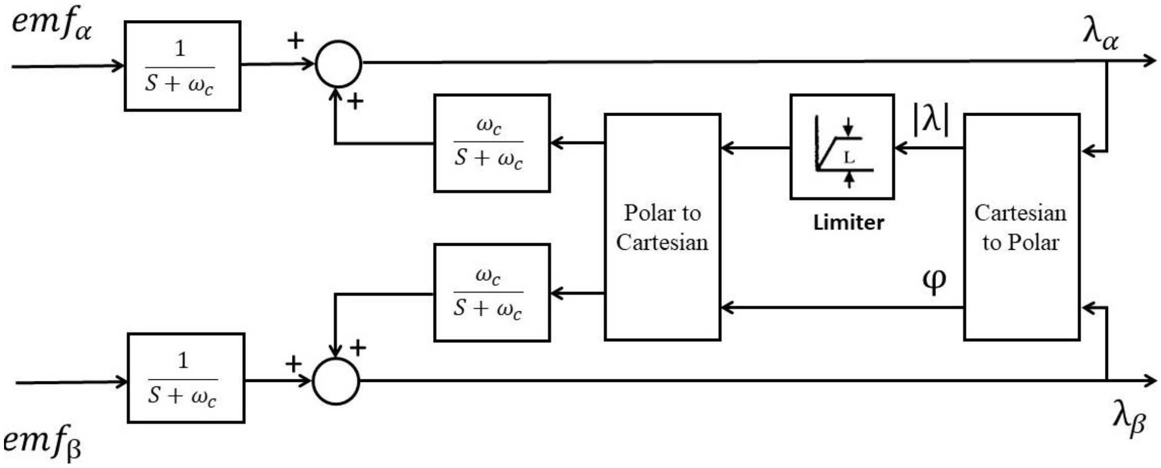

Figure 3.9 Block diagram of the integration algorithm

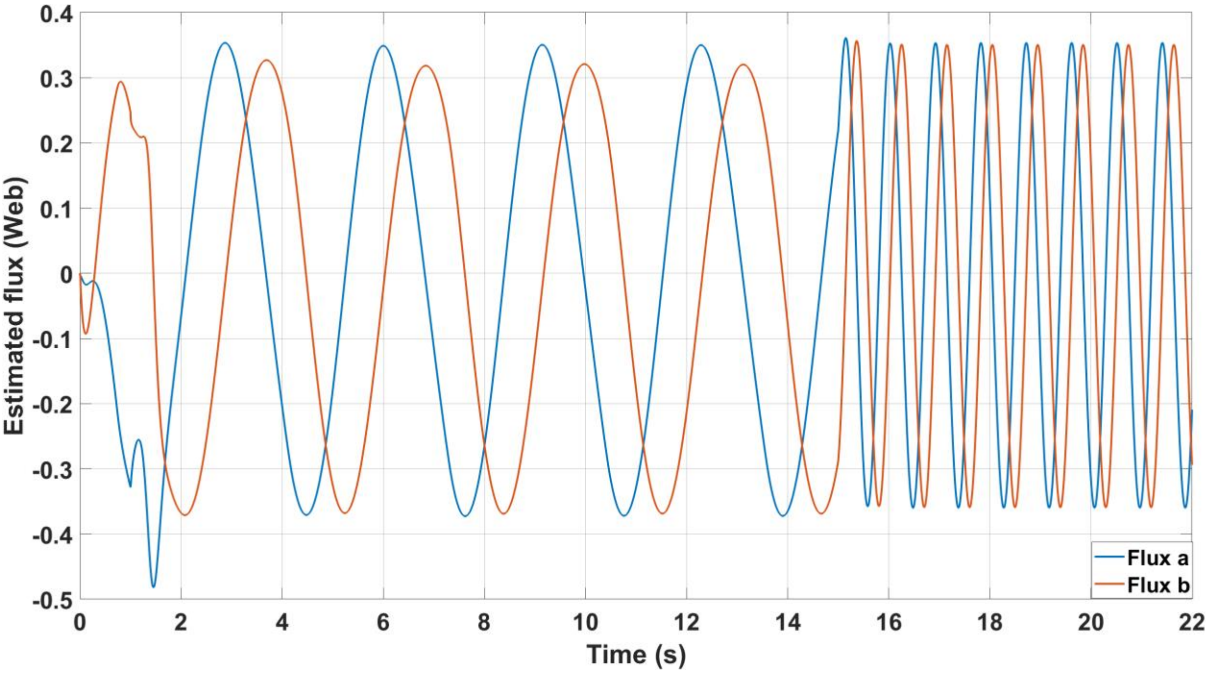
Estimated flux (Web)
0.4
0.3
0.2
0.1
0
-0.1
-0.2
-0.3
-0.4
-0.5
0
2
4
6
8
10
12
14
16
18
20
22
Time (s)
Flux a
Flux b

(a)

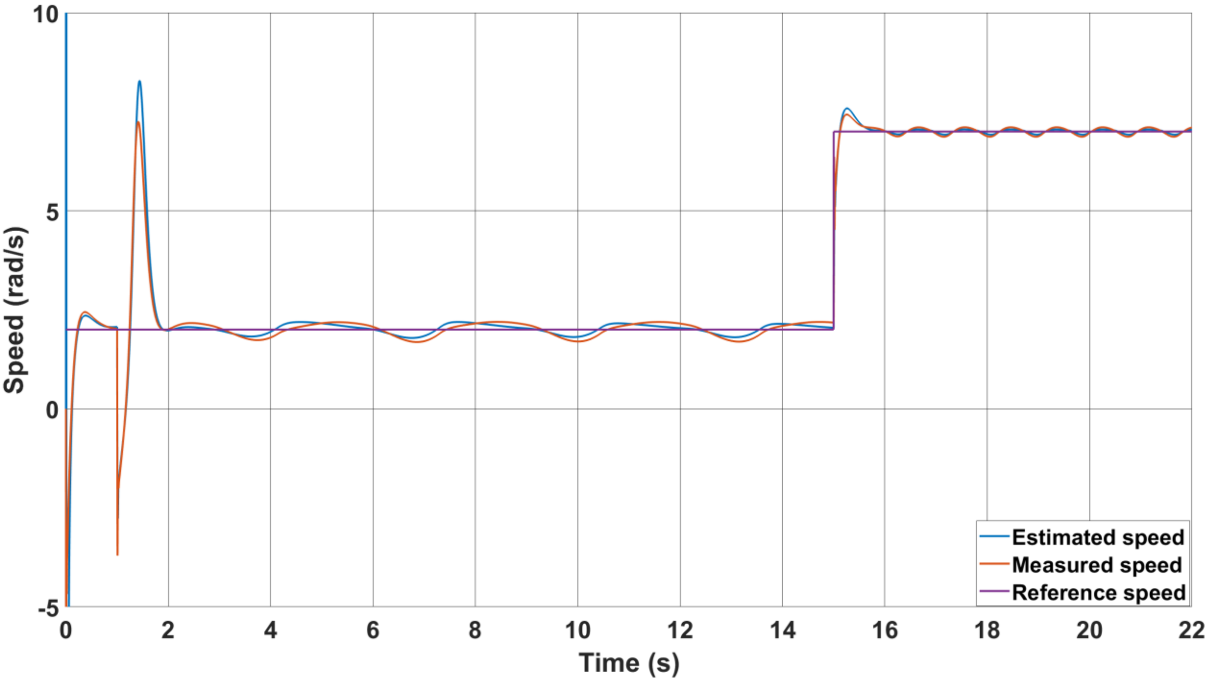
Speed (rad/s)
10
5
0
-5
0
2
4
6
8
10
12
14
16
18
20
22
Time (s)
Estimated speed
Measured speed
Reference speed

(b)

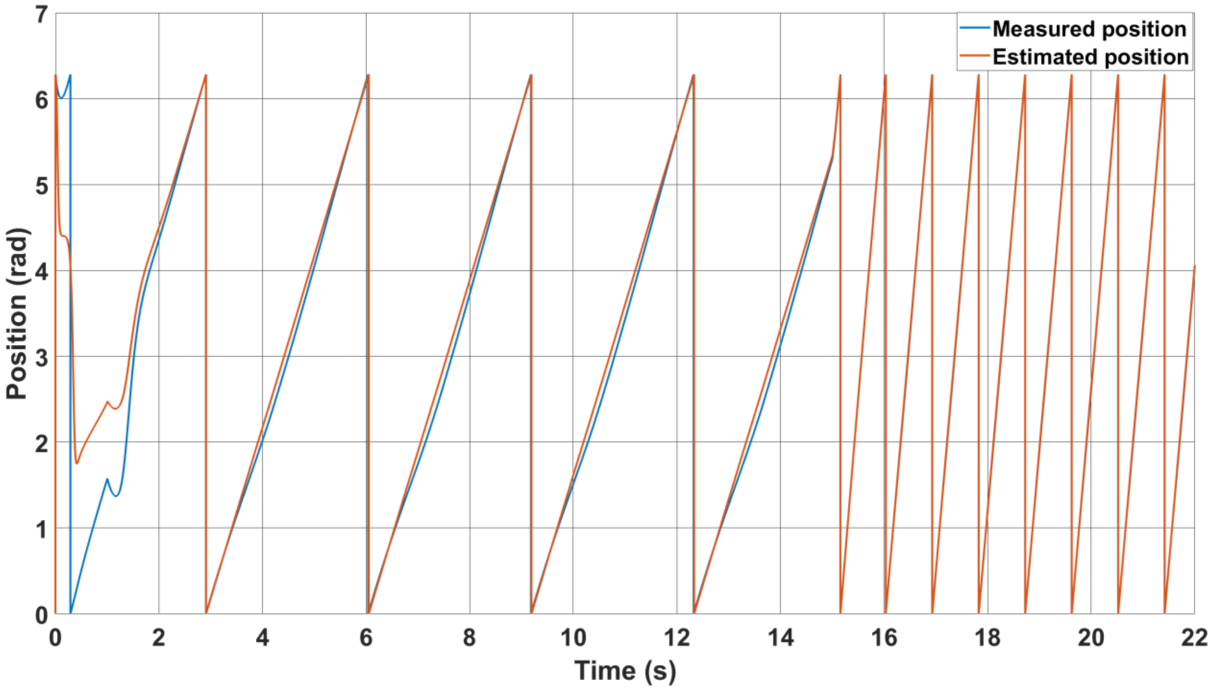

(c)

Figure 3.10 Simulation results of new integrator algorithm (a) estimated flux, (b) measured and estimated speeds (c) measured and estimated positions.

In [63], Programmable Low-Pass Filters are utilized for stator flux estimation. The αβ axis back-EMFs are passed through filters with adjustable cut off frequencies. The outputs are then aligned with the actual rotor position by a vector rotator, enhancing the accuracy of the estimation. It's important to highlight that accuracy is affected, particularly when operating at lower speeds, due to the presence of DC offsets, which introduce distortion into the fluxes.

Similarly, this method (illustrated in figure 3.11) is tested in simulation under the same operating conditions, and it showed similar results with the prior technique. As depicted in Figure 3.12, it becomes evident that as the DC offset gains prominence, the estimated speed displays heightened fluctuations, particularly at lower operational speeds.

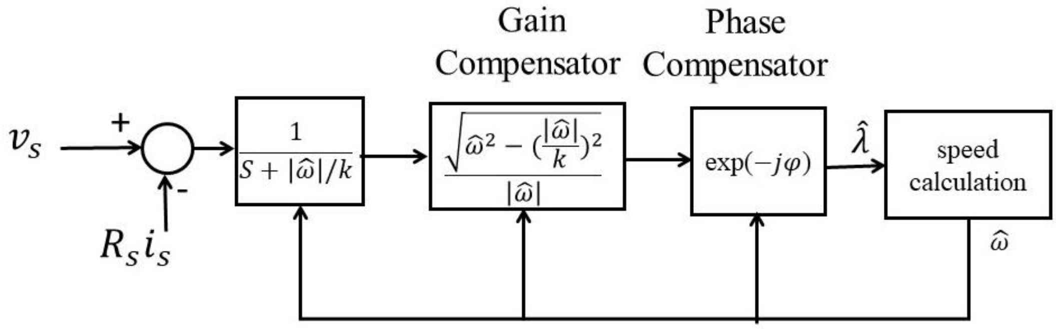

Figure 3.6 Block diagram of programmable low pass filter method

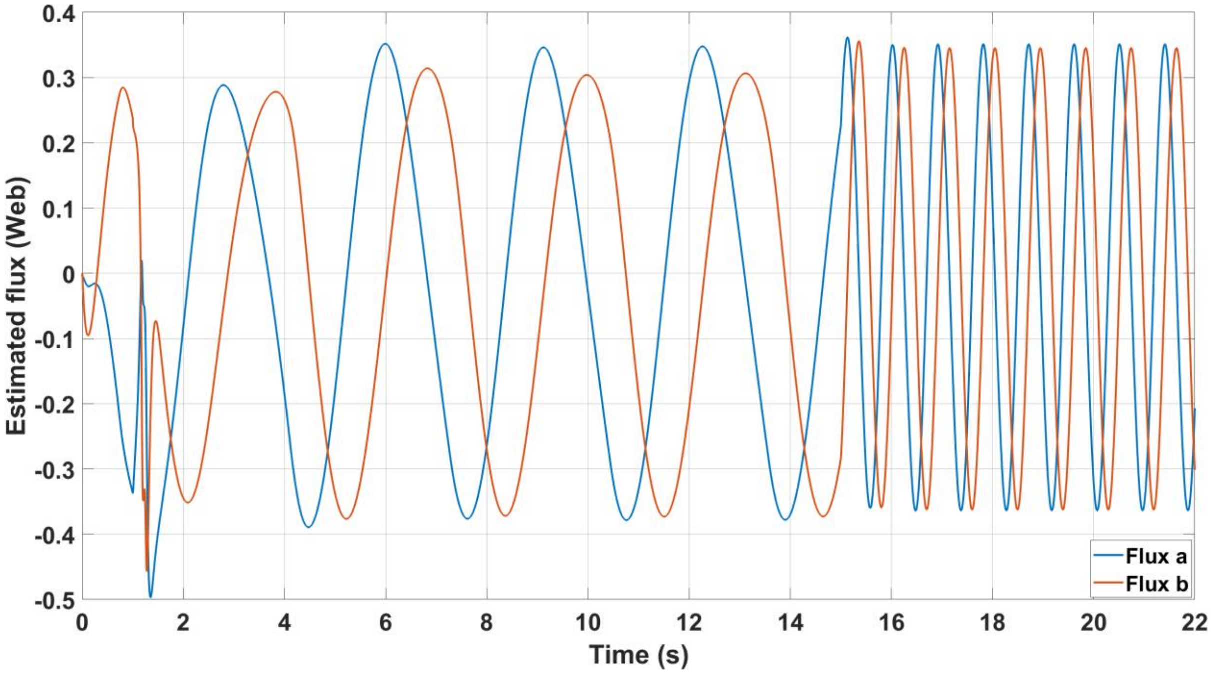

(a)

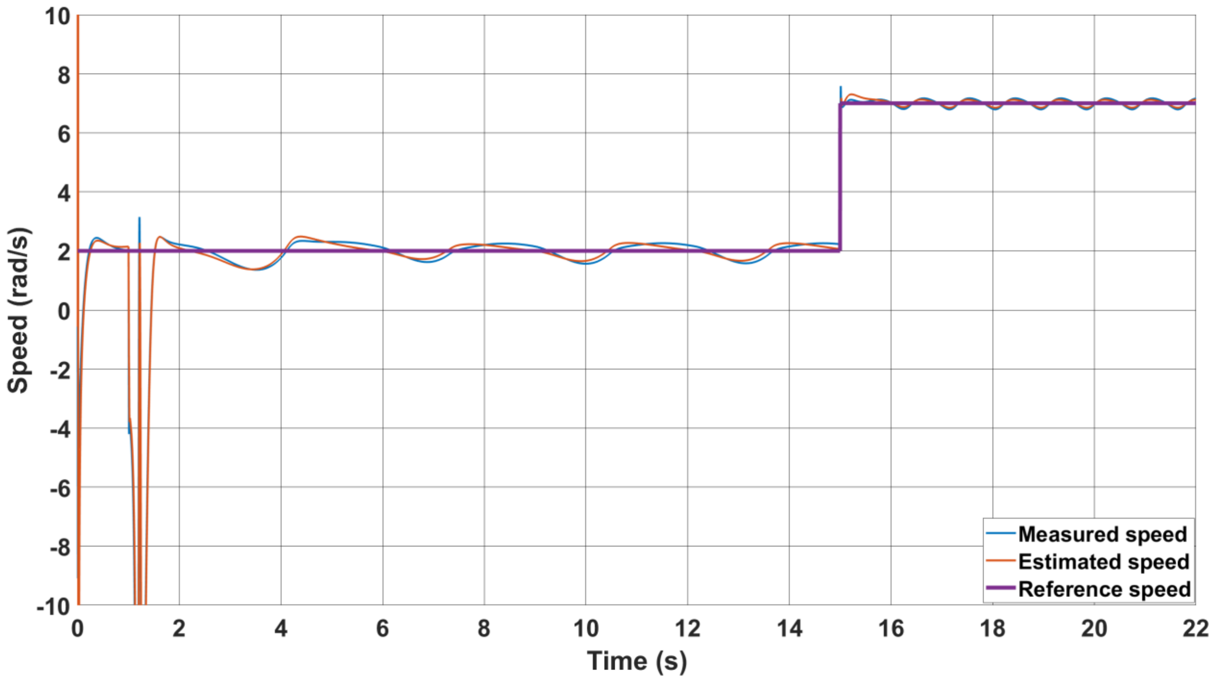

(b)

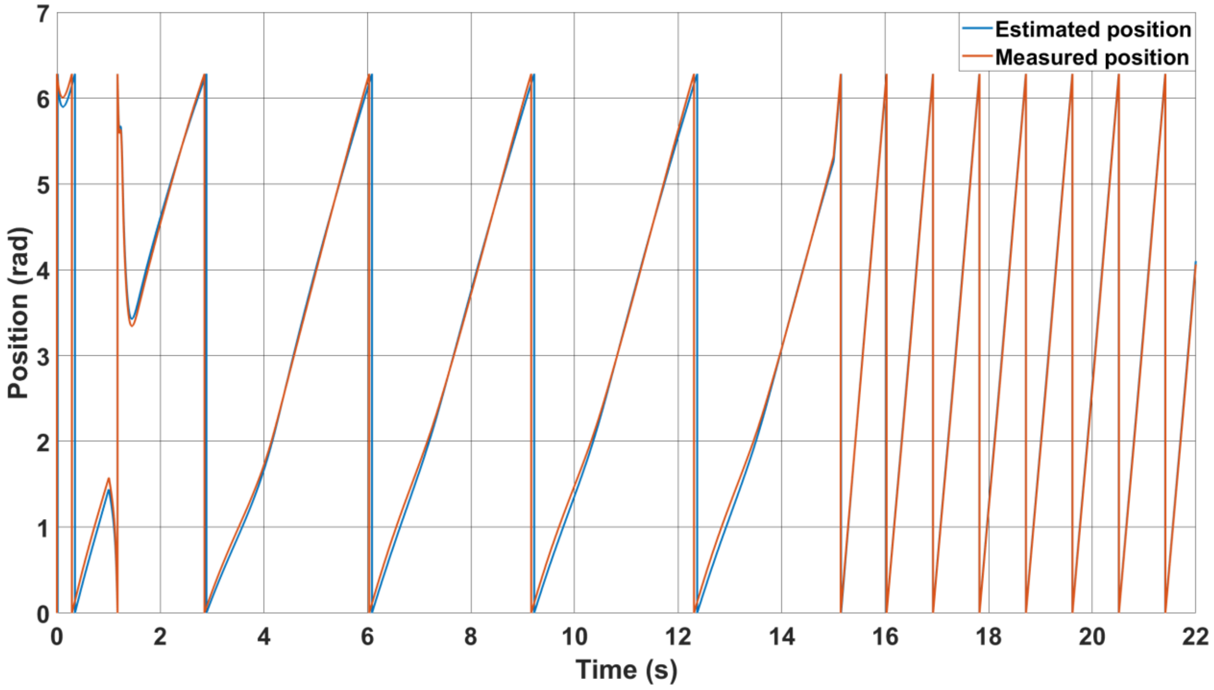

(c)

Figure 3.7 Simulation results of Programmable Low-Pass Filter (a) estimated flux, (b) measured and estimated speeds (c) measured and estimated positions.

Further research has aimed to improve Model Reference Adaptive System (MRAS) sensorless techniques. In [64], a proposed speed estimation method operates independently of the integrator and machine parameters. However, it is sensitive to speed error and stability cannot be guaranteed during significant changes in speed. In [65], the voltage model is replaced by a state observer model to eliminate the need for an integrator, albeit at the cost of increased complexity. Additionally, in [66], high-pass filters are employed in both voltage and current models to mitigate integrator issues. but the computational complexity of the fuzzy controller is the main drawback of this scheme, and it consumes time and effort to tune the three scaling factors.

Other sensorless techniques have been proposed to address the problems associated with conventional flux-based MRAS estimators. The full-order flux observers are well-known model-based methods utilized for sensorless controls. [67] proposed a design formulation aimed at enhancing performance and parameter robustness; however, it suffers from deteriorating performance and instability at low speeds due to a significant increase in feedback gain values. In response, [68] introduced a full-order flux observer to mitigate the issues identified in [67]. Nevertheless, accuracy of the observer is compromised at low speeds and by an inaccurate model. Furthermore, control complexity escalates, necessitating careful tuning of feedback gains considering system dynamics and operating conditions, as stability relies on these gains [69]. Due to the above disadvantages, full-order observers are not used for under -tested machines.

[70] presents a comparison of three adaptive full-order flux observers with different feedback gains: Proportional poles (PP), Left poles (LP), and Complete stability (CS). The first two observers showed instability in low-speed regenerative mode. Conversely, with slower sampling frequency the observer with complete stability feedback gains showed a larger speed

error compared to the other observers as the sampling frequency decreases further. Moreover, the speed error worsens as the load increases, particularly with CS feedback gains observer.

3.3.2 The Problem with the MRAS Adaptation Mechanism

Another issue related to the MRAS adaptation mechanism is the fixed PI controller's inability to maintain optimal performance under different operational conditions. Because of its simple construction and effective performance across a wide range of speed, the fixed PI control is commonly utilized in the adaptation process of MRAS schemes. However, at lower speeds, the fixed PI control may not provide the desired performance due to the increasing prevalence of variations in machine parameters and inverter nonlinearities. Furthermore, it is difficult to tune these PI gains.

To overcome this challenge, several solutions have been proposed to replace the conventional fixed Proportional-Integral (PI) controller with more advanced algorithms. In [35-38], a sliding mode (SM) algorithm was proposed as a replacement for the PI adaptation mechanism. This approach enhances the dynamic response of the estimator, but it can introduce a chattering issue in the speed. Low pass filters are typically employed to mitigate the chattering effect.

In [40], a fuzzy logic (FL)-based approach is recommended as a substitute for PI control, providing an enhancement in the performance of the estimator. However, it involves complex computations due to the inherent nature of fuzzy logic systems.

At low speeds, the PI gains must be tuned to small values to prevent significant increases in estimated speed oscillation. However, under transient operation conditions where sudden changes in load or speed occur, higher PI gains are necessary for smooth and satisfactory system operation. Achieving an adaptive PI controller that can provide satisfactory performance under various conditions is a challenging task that requires trial and error tuning.

The effect of PI gains on the speed was experimentally tested in [71]. The results demonstrated that using high PI gains increases the speed ripples but improves the dynamic performance and accelerates the system's response compared to using low PI gains.

Fig. 3.13 presents simulation results illustrating how the PI gains impact the system's performance in terms of speed oscillation and angle error. As depicted in Fig. 3.13(b), increasing the PI gains leads to higher speed oscillation. However, this results in a shorter settling time and reduced angle error during the transient period, indicating improved dynamic performance. The test was carried out with high, medium, and low PI gains. Where $k_p = 150\, rad\, V^{-2}\, s^{-3}$ and $k_i = 1500\ rad\, V^{-2}\, s^{-4}$ for high gains, $k_p = 60\ \ rad\, V^{-2}\, s^{-3}$ and $k_i = 600\ \ \ rad\, V^{-2}\, s^{-4}$ for medium gains and $k_p = 20\, rad\, V^{-2}\, s^{-3}$ and $k_i = 200$ $rad\, V^{-2}\, s^{-4}$ for low gains.

These findings highlight the trade-off between speed oscillation and system response speed. Higher PI gains enhance dynamic performance but introduce increased speed oscillation, while lower PI gains reduce speed oscillation but result in slower system response. Careful selection of PI gains is necessary to strike a balance between these factors based on the specific requirements and operating conditions of the system.

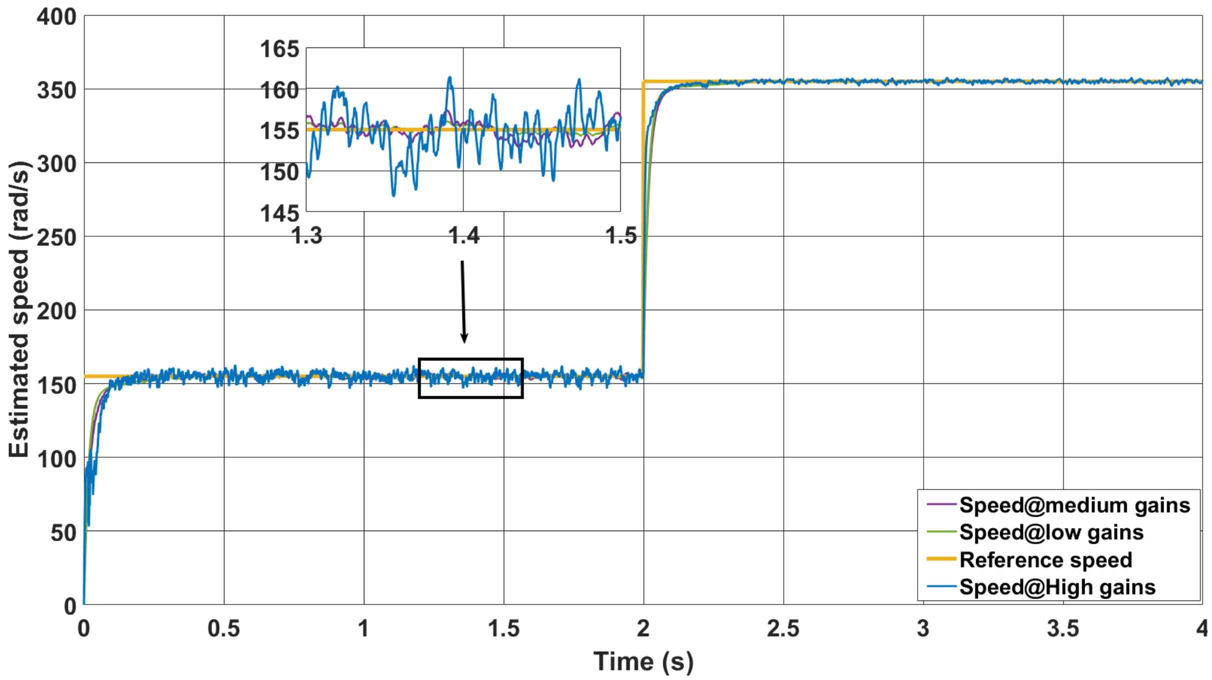

(a)

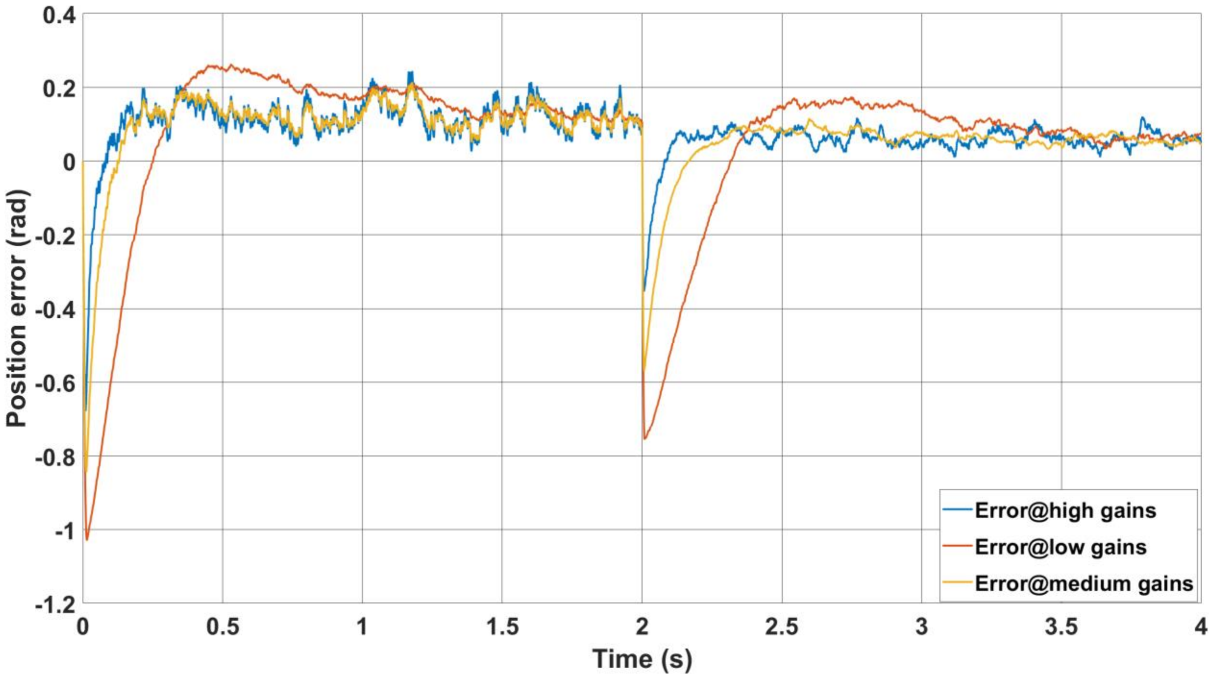

(b)

Figure 3.8 Simulation results depicting the impact of PI gains on the system performance (a) speed response (b) corresponding position error.

3.4 Conclusion

This chapter has presented the modelling of a three phase PMSM and the principle of vector control. It has also introduced the classical flux MRAS based observer and the issues influencing the performance of this observer particularly at low speeds such as the pure integration and the adaptation mechanism. Some methods have been introduced in this chapter to solve the problem of pure integration at low-speed operation. These methods were tested in simulation and the results showed an improvement in the performance, but the presence of the DC offset causes significant fluctuation in speed at low speed.

Chapter 4: PWM-based Speed and Position Estimations for Permanent Magnet Synchronous Machines

A novel sensorless rotor position and speed estimator is introduced in this chapter, focusing on its application in sensorless PMSM drives. The method relies on measuring the current response to conventional space-vector pulse width modulation (SV-PWM).

As discussed in Chapter 3, Model-Reference Adaptive Systems (MRAS) estimators are commonly employed for sensorless angle estimation. These estimators compare two stator flux estimations based on current and voltage models. The voltage model utilizes the integration of stator voltages to calculate the stator flux. However, this integration process introduces phase delays.

A new flux-based MRAS method is introduced in this chapter, offering an alternative approach to speed estimation. Unlike the classical flux-based method, the proposed technique eliminates the need for integrators, resulting in improved performance at low speeds. The key idea behind this method is to leverage oversampling and averaging over a switching period of the standard space-vector pulse-width modulation (SV-PWM).

By using oversampling and averaging techniques, the proposed method enables the computation of the rotor flux without the requirement of integration. This eliminates the potential drawbacks and phase delays associated with integrators, leading to enhanced speed estimation accuracy, especially at low speeds. The lack of an integrator in the novel method ensures that the position accuracy remains unaffected even in low-speed scenarios.

This chapter will provide a comprehensive explanation of the proposed flux-based MRAS method, including the underlying principles, mathematical formulation, and implementation details. Experimental tests and simulations will be conducted to assess the performance of the proposed method and compare it with the classical flux-based approach.

4.1 The Space Vector PWM for Inverter

The Space Vector Pulse Width Modulation (SVPWM) technique is widely utilized in drive applications due to its advantages over Sinusoidal Pulse Width Modulation (SPWM). SVPWM allows for a higher DC bus voltage and lower total harmonic distortion (THD) compared to SPWM [72].

The core concept of SVPWM revolves around representing the inverter output as space vectors that rotate at the fundamental frequency. These space vectors serve as a representation of the three-phase voltages, combining them into a single rotating vector. The definition of this space vector is provided in Equation (3.1).

Figure 4.1 illustrates a three-phase, two-level voltage source inverter with six power transistors. The upper and lower switches operate in a complementary manner. When the upper switch is active, the leg voltages $V_a, V_b,$ and V_c can attain the DC bus voltage V_{dc}, with reference to the negative of the DC link, while they reach 0V when the lower switch is active. This configuration allows for 8 possible outputs, as there are 2^3 combinations.

The active state vectors V_1 to V_6 (100, 110, 010, 011, 001, 101) while the zero vectors V_0 and V_7 (000, 111). In this representation, 1 signifies the upper switch being active, and 0 signifies the upper switch being inactive.

In Figure 4.2, the active vectors V_1 to V_6 form a hexagon, with each vector corresponding to a 60° sector. The rotating voltage vector $\overline{V}^*$ represents the voltage command and can be transformed into $\bar{V}_a$ and $\bar{V}_b$ components, as depicted in the figure. The magnitudes of these components designate the period for which the vectors are applied.

Equation (4.1) establishes the relationship between the phase-to-neutral voltage scalars and the switching states a, b, and c, which represent the upper switches of the inverter.

$$\begin{bmatrix} V_a \\ V_b \\ V_c \end{bmatrix} = \frac{V_{dc}}{3} \begin{bmatrix} 2 & -1 & -1 \\ -1 & 2 & -1 \\ -1 & -1 & 2 \end{bmatrix} \begin{bmatrix} a \\ \mathrm{b} \\ \mathrm{c} \end{bmatrix} \tag{4.1}$$

The switching vectors and the corresponding output phase voltages, are provided in Table 4.1

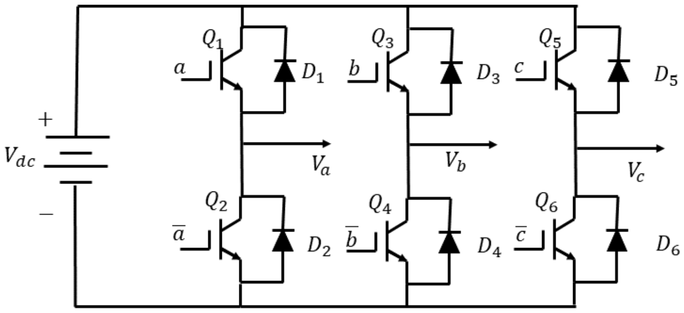

Figure 4.1 A three-phase voltage source inverter.

Table 4. 1 Switching vectors, output phase voltage scalars.

Voltage vector	Switching states			Phase-to-neutral voltage scalars		
	a	b	c	V_a	V_b	V_c
V_0	0	0	0	0	0	0
V_1	1	0	0	$2V_{dc}/3$	$-V_{dc}/3$	$-V_{dc}/3$

V_2	1	1	0	$V_{dc}/3$	$-V_{dc}/3$	$-2V_{dc}/3$
V_3	0	1	0	$-V_{dc}/3$	$2V_{dc}/3$	$-V_{dc}/3$
V_4	0	1	1	$-2V_{dc}/3$	$V_{dc}/3$	$V_{dc}/3$
V_5	0	0	1	$-V_{dc}/3$	$-V_{dc}/3$	$2V_{dc}/3$
V_6	1	0	1	$V_{dc}/3$	$-2V_{dc}/3$	$V_{dc}/3$
V_7	1	1	1	0	0	0

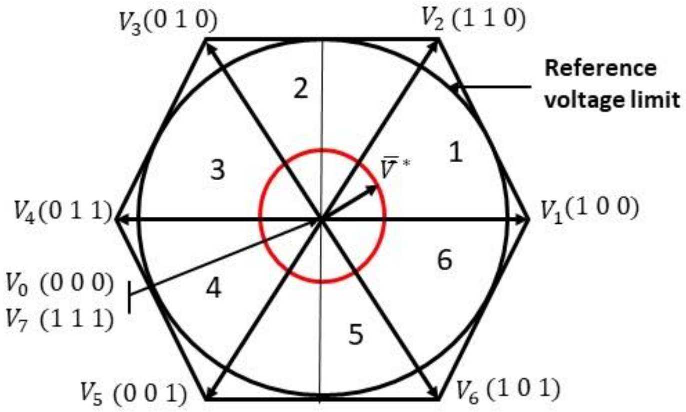

Figure 4.2 Reference voltage vector and switching states

4.1.1 Implementation of Space Vector PWM

In the implementation of SVPWM, the reference voltage is generated by utilizing two adjacent active vectors and zero vectors. The selection of the two active vectors depends on the position of the reference voltage. Once the active vectors are identified, the next step is to determine the duration, also known as the dwell time, for which each vector should be applied.

To determine the sector, the two orthogonal components (V_α, V_β) of the reference vector are obtained by converting from three-phase to two-phase applying the conversion shown in Figure

3.3. From these components, the amplitude and angle of the reference voltage vector can be calculated as:

$$V^* = \sqrt{{V_\alpha}^2 + {V_\beta}^2} \tag{4.2}$$

$$\alpha = \tan^{-1} \frac{V_\beta}{V_\alpha} \tag{4.3}$$

The "equal volt-second principle" is applied to calculate the dwell time. This principle assumes a constant reference voltage throughout the switching period. In accordance with this principle, the product of the applied voltage vectors and their respective time durations is equivalent to the product of the reference voltage and the switching time.

If the reference voltage vector ($\overline{V}^*$) is located in sector one, the two neighbouring active vectors are V_1 and V_2. The applied time for V_1 is denoted as t_a, and the applied time for V_2 is denoted as t_b. The dwell time, which represents the duration for which the vectors should be applied, can be calculated as follows:

$$\overline{V}^* T_s = V_1 t_a + V_2 t_b + V_0 t_0 \tag{4.4}$$

Where T_s is the switching time, and t_0 is the applied time for zero vectors.

$$\overline{V}^* = V^* e^{i\alpha} \quad V_1 = \frac{2V_{dc}}{3} \quad V_2 = \frac{2V_{dc}}{3} e^{i\frac{\pi}{3}} \quad V_0 = 0 \tag{4.5}$$

Substituting the expressions for ($\overline{V}^*$) , V_1, and V_2 into equation (4.4), we have:

$$T_s V^* \begin{bmatrix} \cos\alpha \\ \sin\alpha \end{bmatrix} = t_a \frac{2V_{dc}}{3} \begin{bmatrix} 1 \\ 0 \end{bmatrix} + t_b \frac{2V_{dc}}{3} \begin{bmatrix} \cos\frac{\pi}{3} \\ \sin\frac{\pi}{3} \end{bmatrix} \tag{4.6}$$

Separating the real (α-axis) and imaginary (β-axis) components, we get

$$T_s V^* \cos\alpha = t_a \frac{2V_{dc}}{3} + t_b \frac{2V_{dc}}{3} \cos\frac{\pi}{3} \tag{4.7}$$

$$T_s V^* \sin\alpha = t_b \frac{2V_{dc}}{3} \sin\frac{\pi}{3} \tag{4.8}$$

Solving equations (4.7) and (4.8) for t_a and t_b

$$t_a = \frac{\sqrt{3} T_s V^*}{V_{dc}} \sin(\frac{\pi}{3} - \alpha) \tag{4.9}$$

$$t_b = \frac{\sqrt{3} T_s V^*}{V_{dc}} \sin(\alpha) \tag{4.10}$$

In general, the dwell time for any sector can be calculated as following.

$$t_a = \frac{\sqrt{3} T_s V^*}{V_{dc}} \sin(\mathrm{k}\frac{\pi}{3} - \alpha) \tag{4.11}$$

$$t_b = \frac{\sqrt{3} T_s V^*}{V_{dc}} \sin(\alpha - (k-1)\frac{\pi}{3}) \tag{4.12}$$

$$t_0 = T_s - t_a - t_b \tag{4.13}$$

where $k = 1,2, \ldots .6$ is the sector number

Finally, to achieve optimum performance of SVPWM, a minimum number of switching operations is required for each switching period. This can be achieved by following a specific pattern. In the first half of the switching period, the zero vector V_0 is applied, followed by two neighbouring active vectors, and then the zero vector V_7.

To create a symmetrical SVPWM, the second half of the switching period should mirror the first half. This means that the sequence of applied vectors in the second half should be the reverse of the sequence in the first half.

The switching sequence for sector one follows a specific pattern. In the first half of the switching period, the zero vector V_0 is applied for a duration of $t_0/4$. This is followed by the application of V_1 and V_2, each for a duration of $t_a/2$ and $t_b/2$ respectively. Finally, the zero vector $V_7$is applied for $t_0/4$. In the second half of the switching period, this pattern is repeated. This switching sequence is depicted in Figure 4.3. It is important to note that similar switching patterns are used for all other sectors.8

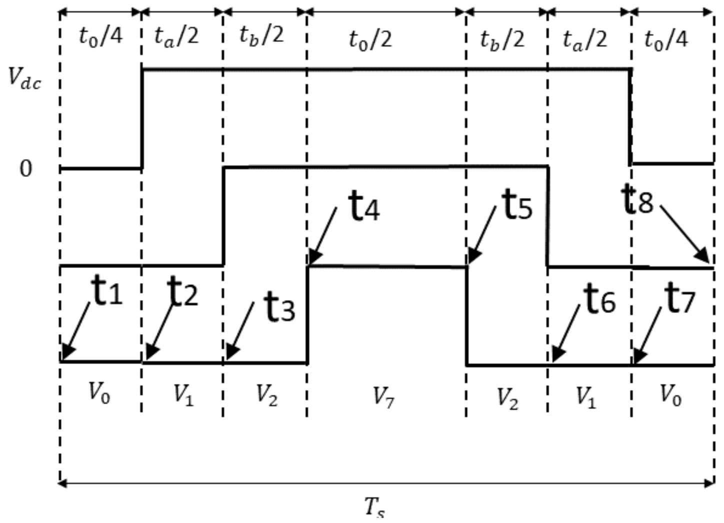

Figure 4.3 Switch pattern for SVPWM for sector one.

4.2 PWM-Based Speed Estimator

The voltage equations of a PMSM, when represented in the estimated dq frame can be formulated as follows:

$$L_d \frac{d\hat{\imath}_d}{dt} = \hat{v}_d - R_s\hat{\imath}_d + \widehat{w}\left(\widehat{\psi}_{m_q} + L_q\hat{\imath}_q\right) \tag{4.14}$$

$$L_q \frac{d\hat{\imath}_q}{dt} = \hat{v}_q - R_s\hat{\imath}_q - \widehat{w}(L_d\hat{\imath}_d + \psi_m) \tag{4.15}$$

Figure 4.4 illustrates a PWM switching cycle with three PWM gate signals controlling the upper three transistors in a two-stage inverter. It also shows the synchronous reference currents i_d and i_q, with a sampling frequency equal to 10 times the switching frequency.

Considering t_1, t_2, ..., t_8 as the time instants at which distinct voltage vectors are applied, and $\widehat{w}$ is constant during one switching period, equation (4.14) can be discretized with a sampling time Ts. The resulting relationships between two adjacent sampling points are given as follows:

$$\hat{v}_{d(t_1\sim(t_1+T_s)} = R_s\hat{\imath}_{d(t_1\sim(t_1+T_s))} + L_d\frac{d}{dt}\hat{\imath}_{d(t_1\sim(t_1+T_s)} - \widehat{w}L_q\hat{\imath}_{q(t_1\sim(t_1+T_s)} - \widehat{w}\widehat{\psi}_{m_q} \tag{4.16}$$

$$\begin{aligned}\hat{v}_{d((t_1+T_s)\sim(t_1+2T_s))} = R_s\hat{\imath}_{d((t_1+T_s)\sim(t_1+2T_s))} + L_d\frac{d}{dt}\hat{\imath}_{d((t_1+T_s)\sim(t_1+2T_s))} \\ -L_q\hat{\imath}_{q((t_1+T_s)\sim(t_1+2T_s))} - \widehat{w}\widehat{\psi}_{m_q}\end{aligned} \tag{4.17}$$

$$\vdots$$

$$\begin{aligned}\hat{v}_{d((t_1+(n-2)T_s)\sim t_8)} = R_s\hat{\imath}_{d((t_1+(n-2)T_s)\sim t_8)} + L_d\frac{d}{dt}\hat{\imath}_{d(t_1+(n-2)T_s)\sim t_8} \\ -\widehat{w}L_q\hat{\imath}_{q((t_1+(n-2)T_s)\sim t_8)} - \widehat{w}\widehat{\psi}_{m_q}\end{aligned} \tag{4.18}$$

where n is the integer number of sampling points in a switching cycle, calculated as n $=$ $1/(f_{sw} *$ Ts), where f_{sw} is the switching frequency. The time instant t_8 is defined as t_1 + $(n-$ 1) Ts.

The derivative term can be approximated by the following:

$$\frac{d}{dt}\hat{\imath}_d = (\hat{\imath}_{d(t_1+(k+1)T_s)} - \hat{\imath}_{d(t_1+kT_s)})/Ts \tag{4.19}$$

By multiplying each of the $n-1$ equations by Ts and then adding each equation to the next, we obtain the following result:

$$T_s\sum_{1}^{n-1}\hat{v}_{d(j)} = T_sR_s\sum_{1}^{n-1}\hat{\imath}_{d(j)} - t_s\widehat{w}_r\hat{\psi}_{m_q} - \widehat{w}_rT_sL_q\sum_{1}^{n-1}\hat{\imath}_{q(j)} + L_d\sum_{1}^{n-1}\hat{\imath}_{d(k+1)} - \hat{\imath}_{d(k)} \tag{4.20}$$

Here, $t_s = 1/f_{sw}$, k = 0,1 ⋯ n – 2 and j is the jth equation.

According to [73], the sum $T_s\sum_1^{n-1}\hat{v}_d(j)$ is equal to the average PWM voltage as:

$$(t_3-t_2)\hat{v}_{d(t_3-t_2)} + (t_4-t_3)\hat{v}_{d(t_4-t_3)} + (t_6-t_5)\hat{v}_{d(t_6-t_5)} + (t_7-t_6)\hat{v}_{d(t_7-t_6)} = T_s\sum_{1}^{n-1}\hat{v}_d(j) \tag{4.21}$$

Where $\hat{v}_{d(t_3-t_2)}$, $\hat{v}_{d(t_4-t_3)}$, $\hat{v}_{d(t_6-t_5)}$ and $\hat{v}_{d(t_7-t_6)}$ represent the estimated switching vectors on the estimated d-axis transformed from $\alpha\beta$ -reference frame. The time differences $(t_3-t_2) = (t_7-t_6) = t_a/2$ and $(t_4-t_3) = (t_6-t_5) = t_b/2$

Considering that the switching cycle contains two symmetrical switching combinations, it can be easily verified that:

$$(t_3-t_2)\hat{v}_{d(t_3-t_2)} = (t_7-t_6)\hat{v}_{d(t_7-t_6)} \tag{4.22}$$

$$(t_4 - t_3)\hat{v}_{d(t_4-t_3)} = (t_6 - t_5)\hat{v}_{d(t_6-t_5)} \tag{4.23}$$

Therefore, by rearranging equation (4.20), we can express $\hat{\psi}_{m_q}$ as follows:

$$\hat{\psi}_{m_q} = \frac{f_{sw}}{\hat{w}}[-2[(t_3 - t_2) * \hat{v}_{d(t_3-t_2)}+(t_4 - t_3) * \hat{v}_{d(t_4-t_3)}]+T_sR_s \sum_{1}^{n-1} \hat{\imath}_{d(j)} + L_d \sum_{1}^{n-1}[\hat{\imath}_{d(k+1)} - \hat{\imath}_{d(k)}] - \hat{w}T_sL_q \sum_{1}^{n-1} \hat{\imath}_{q(j)}] \tag{4.24}$$

The position of the voltage reference vector (figure 4.2) is utilized to compute the average PWM voltage at the start of a PWM switching cycle. Therefore, the voltage reference in the $\alpha\beta$ frame ($v^*{}_{\alpha}$, $v^*{}_{\beta}$) should be represented as a rotating space vector.

The actual reference magnet flux, ψ_m, lies along the real d-axis and is 0 on the q-axis. On the other hand, $\hat{\psi}_{m_q}$, the estimated flux along the estimated q-axis, is proportional to the sine of the angle estimation error. The vector product, ϵ, of these flux components (as shown in (4.25)), is then input into a PI controller, which generates the speed. Finally, the integration of the speed yields the position, as illustrated in Figure 4.5.

$$\epsilon = \psi_{m_d} \,.\, \hat{\psi}_{m_q} - \psi_{m_q} \,.\, \hat{\psi}_{m_d} = \psi_m \cdot \hat{\psi}_{m_q} \tag{4.25}$$

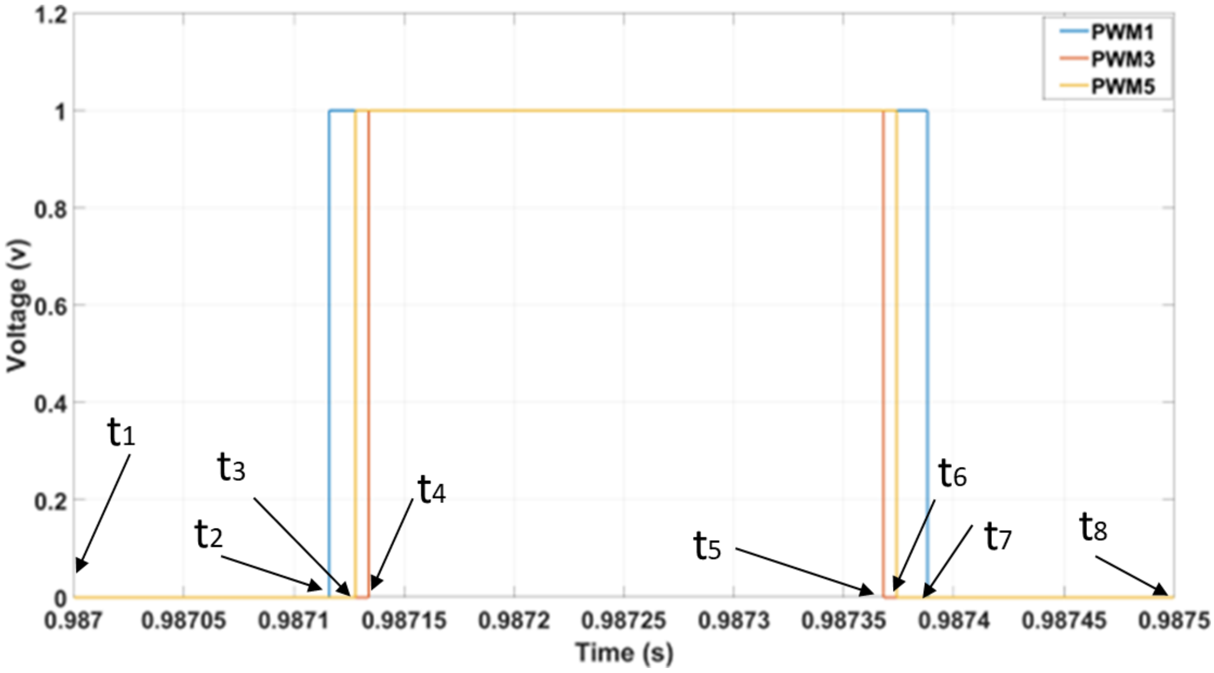

(a)

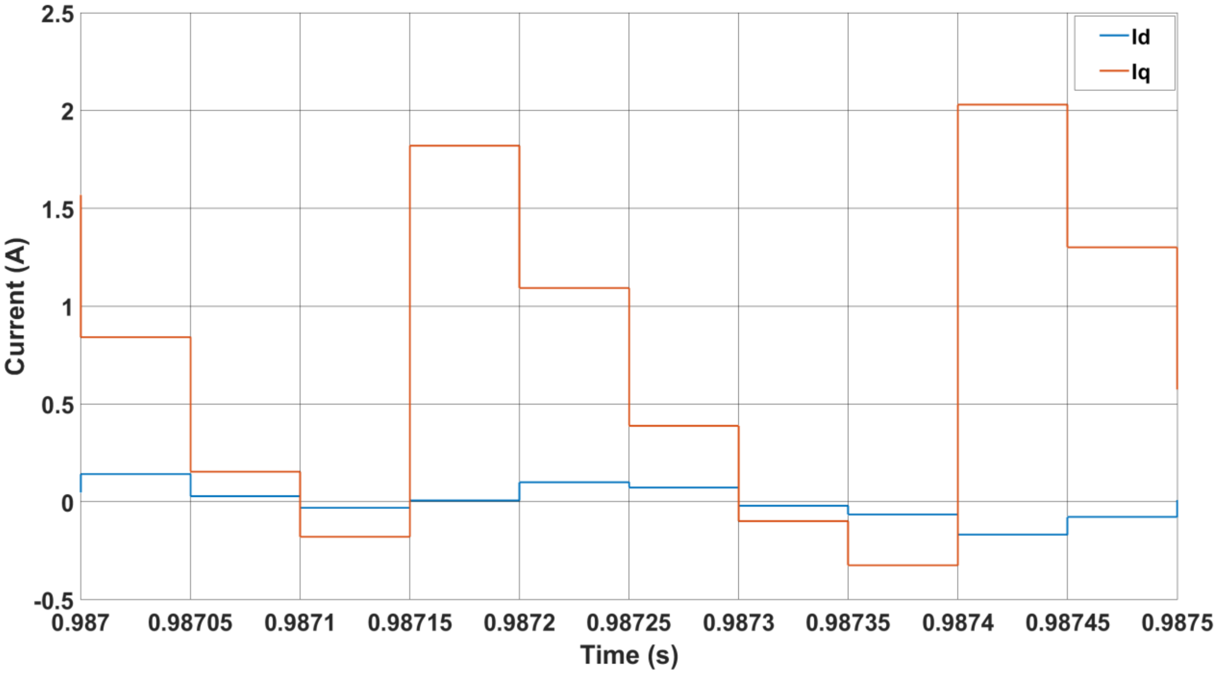

(b)

Figure 4.4 PWM signals with the corresponding q-d-currents in a switching cycle.

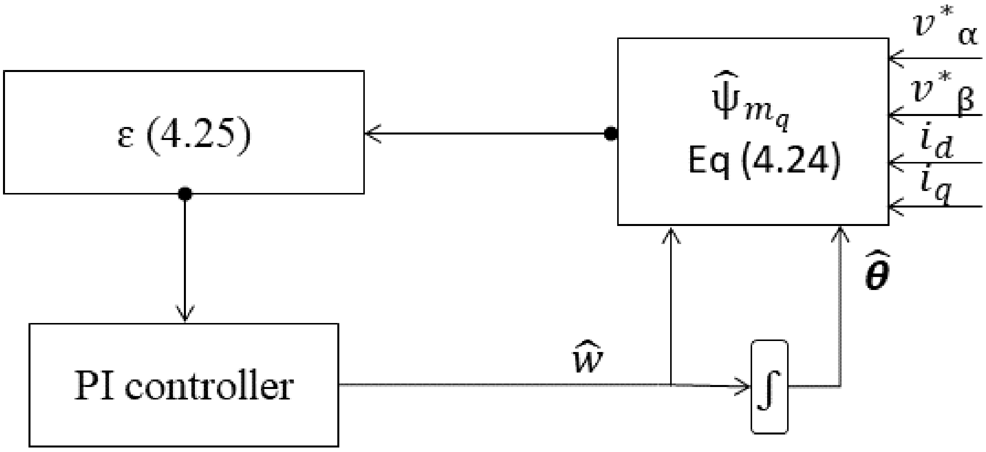

Figure 4.5 Block diagram of the PWM based estimator.

For vector controlled PMSM drive ($i_d = 0$), the equation 4.24 can be simplified as:

$$\hat{\psi}_{m_q} = \frac{f_{sw}}{\hat{w}}[-2[(t_3 - t_2) * \hat{v}_{d(t_3-t_2)} + (t_4 - t_3) * \hat{v}_{d(t_4-t_3)}] + -\hat{w}T_sL_q\sum_{1}^{n-1}\hat{\imath}_{q(j)}] \tag{4.26}$$

4.3 Simulation results

The proposed method was tested offline using MATLAB/Simulink. The control strategy, Field-Oriented Control (FOC), is implemented with a sampling frequency of 12.5 kHz to control a Permanent Magnet Synchronous Motor (PMSM) model. The PI controller of the estimator is executed with a sampling frequency of 12.5 kHz. The model parameters used in the simulation are listed in Table 4.2. It was assumed that the motor is fed directly from the reference voltage. Consequently, the nonlinearity of the inverter was not considered. Additionally, the current sensors were assumed to be ideal, neglecting factors such as DC-offset and inaccuracies in the current measurement calibration. It is worth noting that all speeds and positions in simulation and experimental results are electrical. All units for proportional and integral controller gains of the estimators are in $rad\ V^{-2}s^{-3}$ and $rad\ V^{-2}s^{-4}$ respectively.

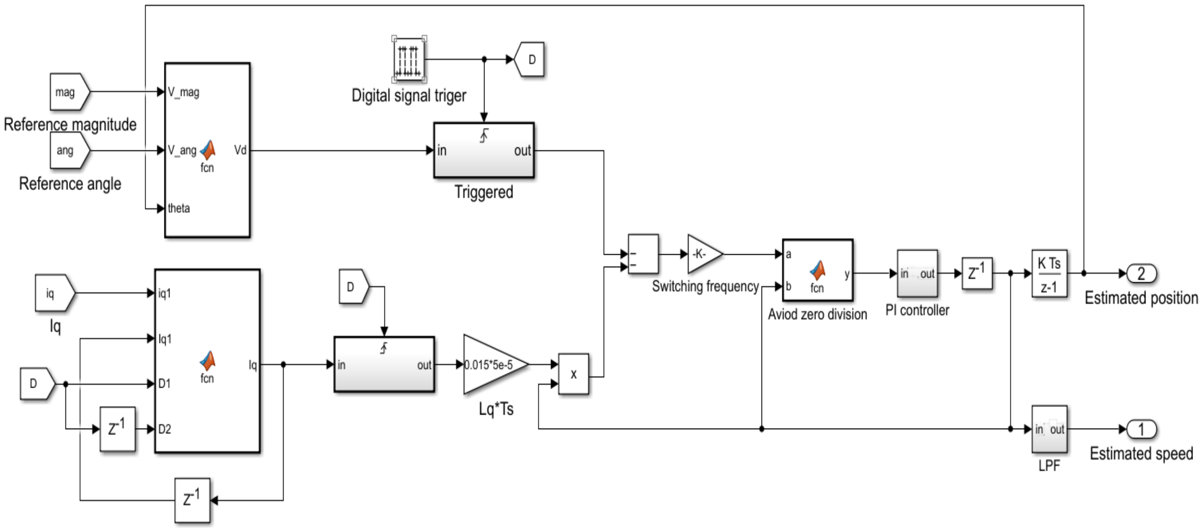

Figure 4.6 Simulink model for PWM-based estimator

Figures 4.7 and 4.8 depict the performance of both the proposed and conventional estimators under rated torque when the speed reference is changed from 40 rad/s to 80 rad/s. The test results demonstrate the superior performance of the proposed observer compared to the conventional method in terms of both speed signal and position accuracy during the transient period. Furthermore, from Fig. 4.7(b) and Fig. 4.8(b), it is evident that the position accuracy of the novel estimator remains unaffected by changes in speed, unlike the conventional estimator. It is worth noting that both methods were tested in sensorless mode from the beginning, starting at time 0s.

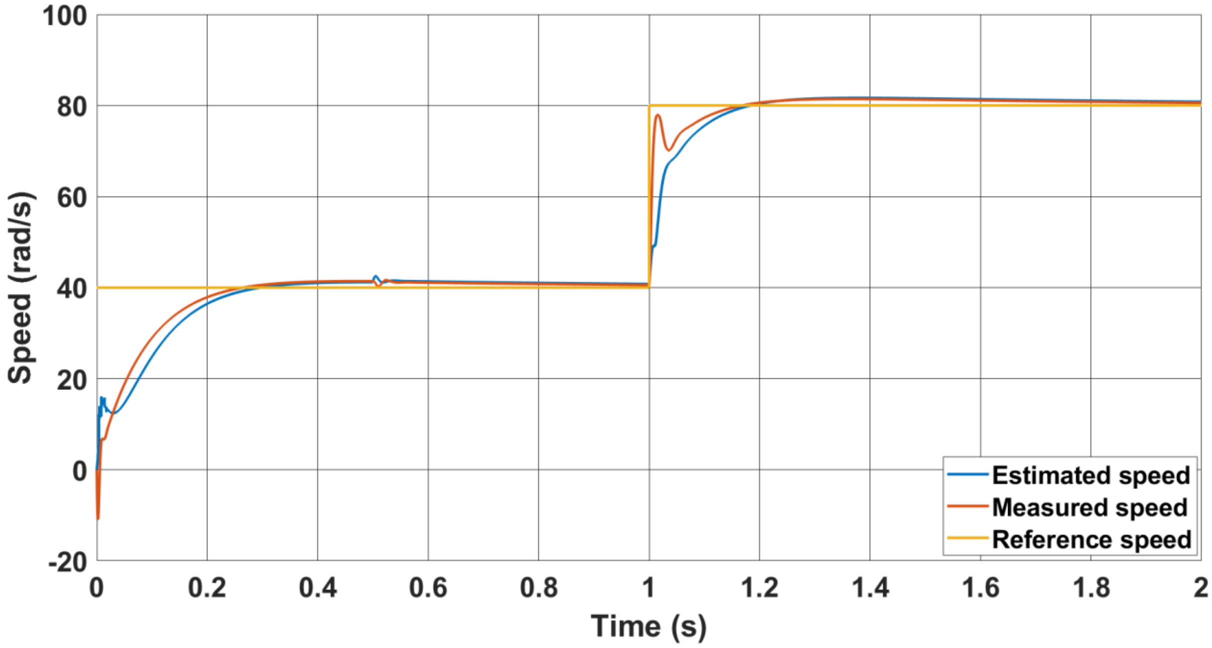

(a)

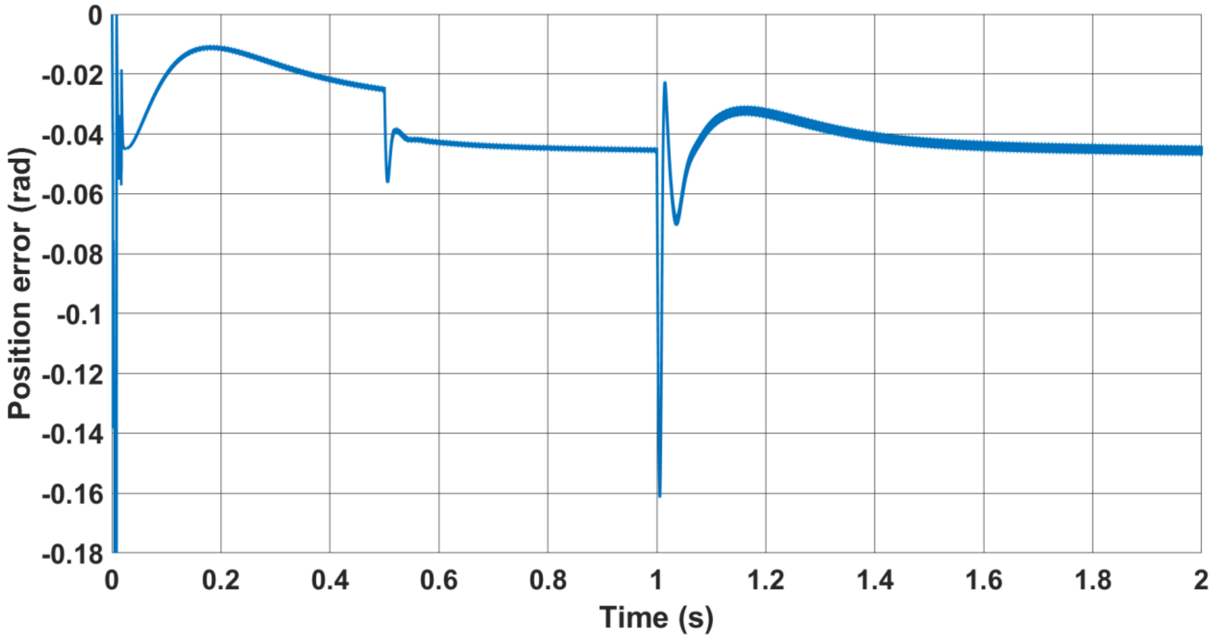

(b)

Figure 4.7 Sensorless performance for the PWM-based method, reference speed change from 40 to 80 rad/s at full load, (a) Speed response (b) Corresponding position error.

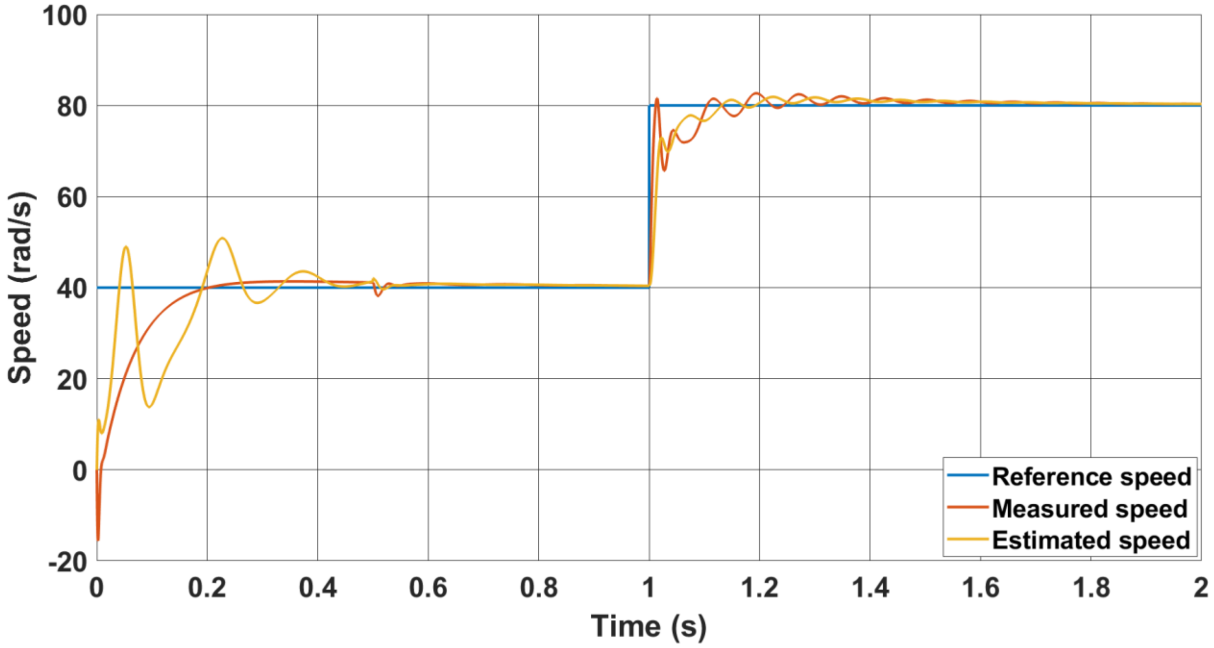

(a)

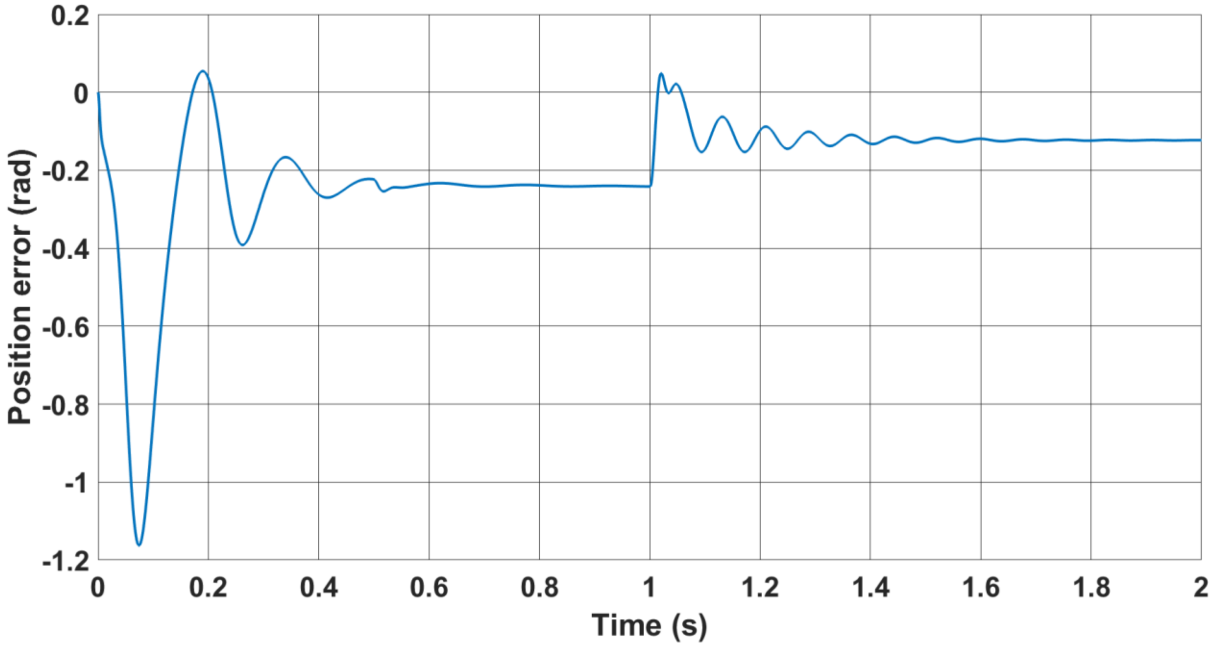

(b)

Figure 4.8 Sensorless performance for conventional method, reference speed change from 40 to 80 rad/s at full load, (a) Speed response (b) Corresponding position error.

In Figs. 4.9-4.10, the speed reference is set to 200 rad/s to test both methods under rated torque at medium speeds. Once again, the novel method shows a better performance in both speed and position accuracy during the transient period.

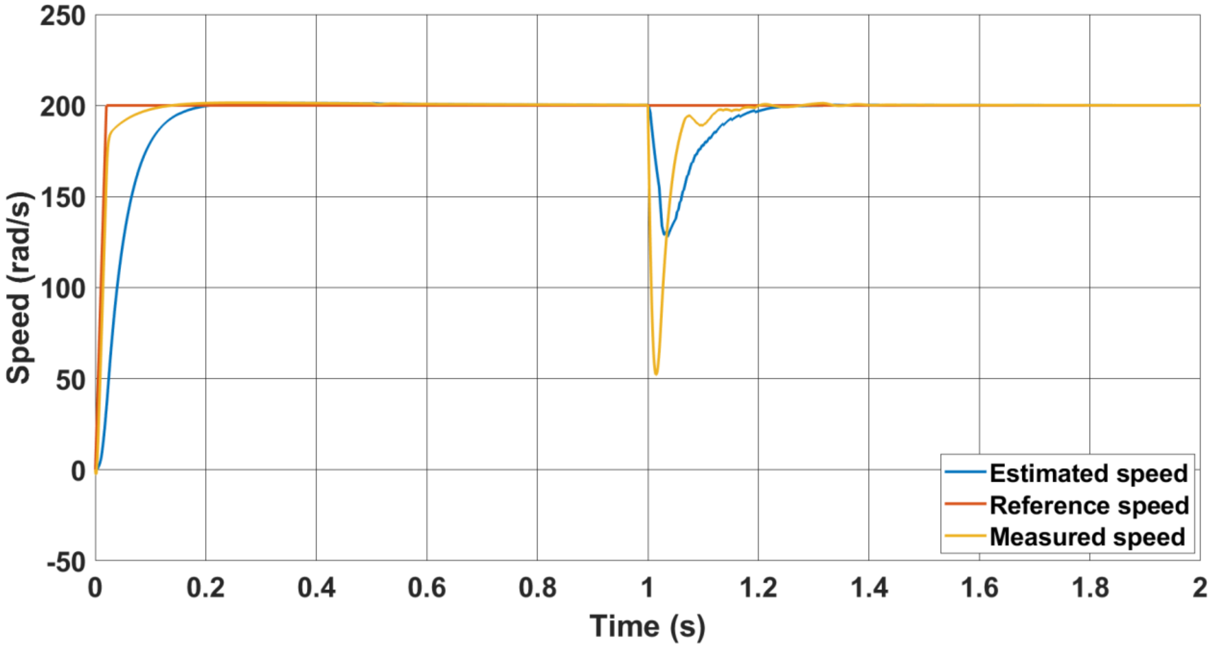

(a)

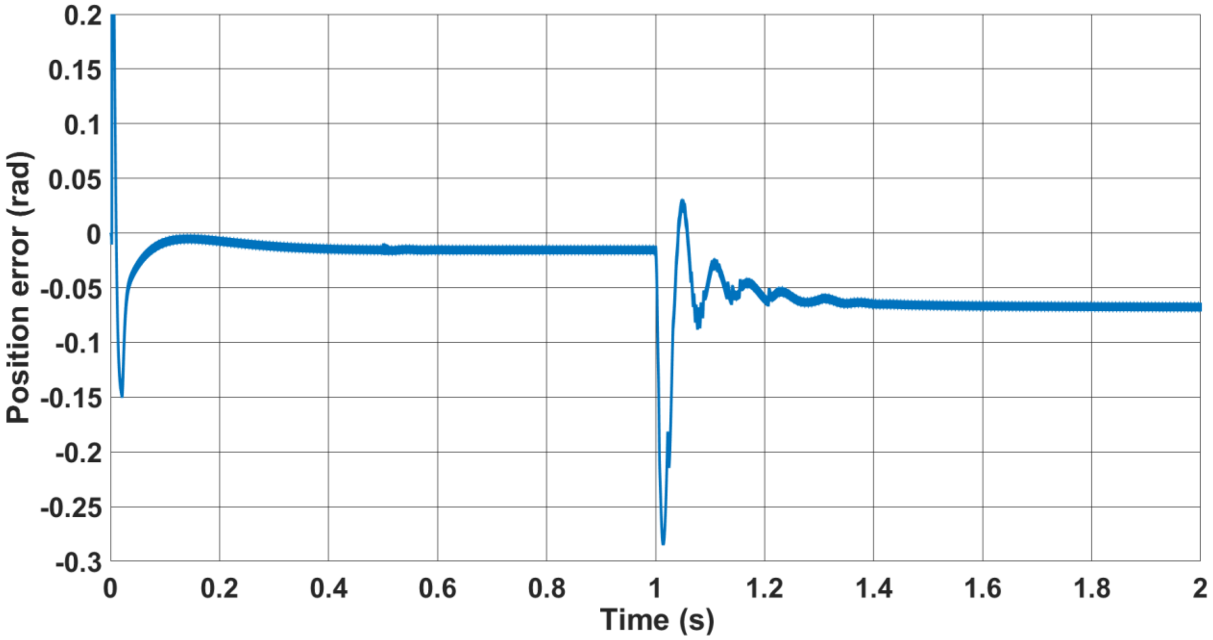

(b)

Figure 4.9 Sensorless operation for the novel method with rated torque, (a) Speed response, (b) Corresponding position error.

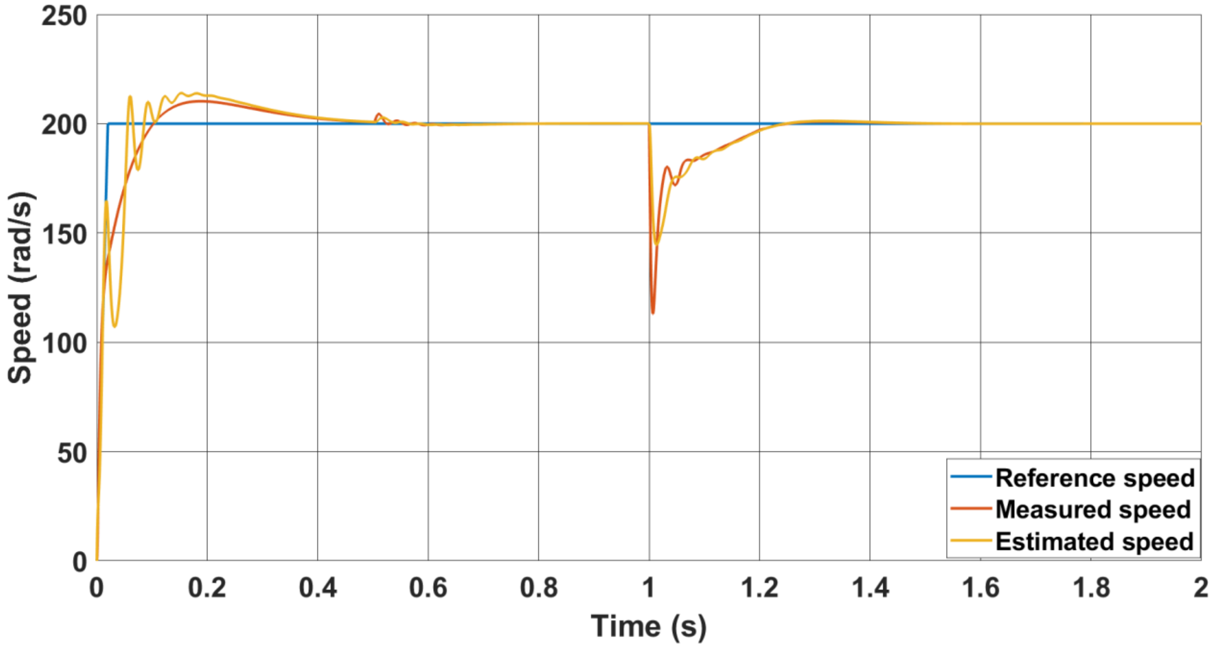

(a)

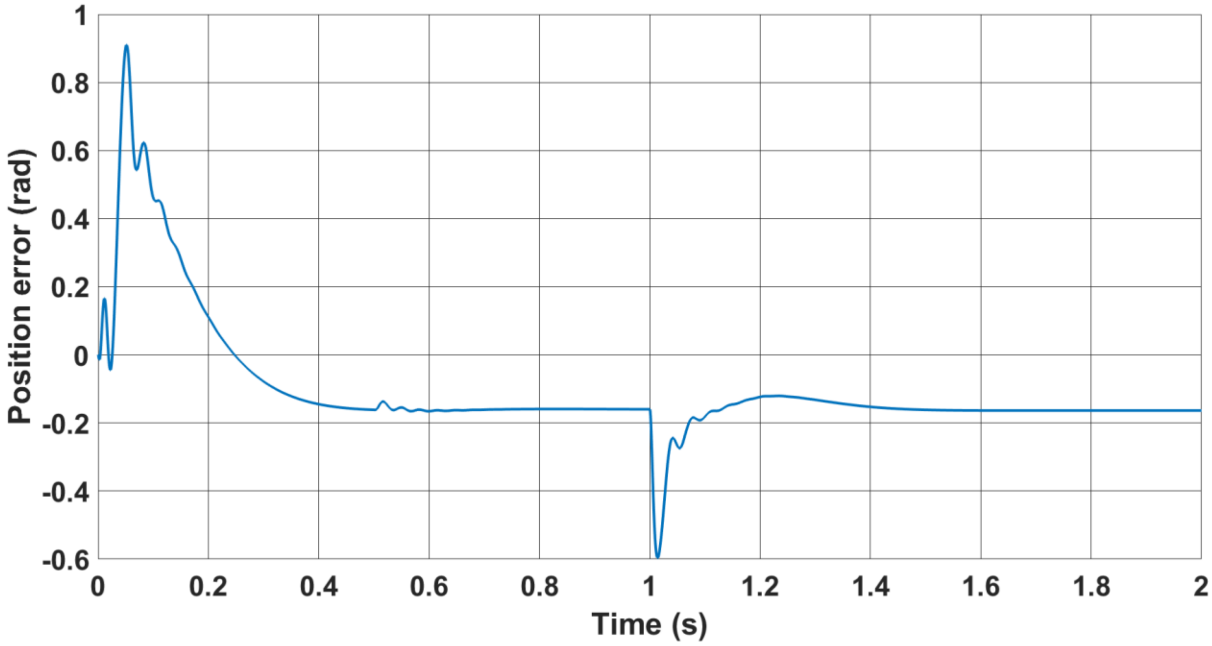

(b)

Figure 4.10 Sensorless operation for the classical method with rated torque, (a) Speed response, (b) Corresponding position error.

Figure 4-11 illustrates the sensorless performance of the proposed method at low speed under rated torque. The reference speed was set to 20 rad/s and the torque was initially set to 0, then the torque was set to the rated value at 1 s. It can be concluded that the position error slightly increases when the rated torque is applied. Regarding the transient period, it takes about 0.3 seconds for the estimated speed to start tracking the reference speed.

.

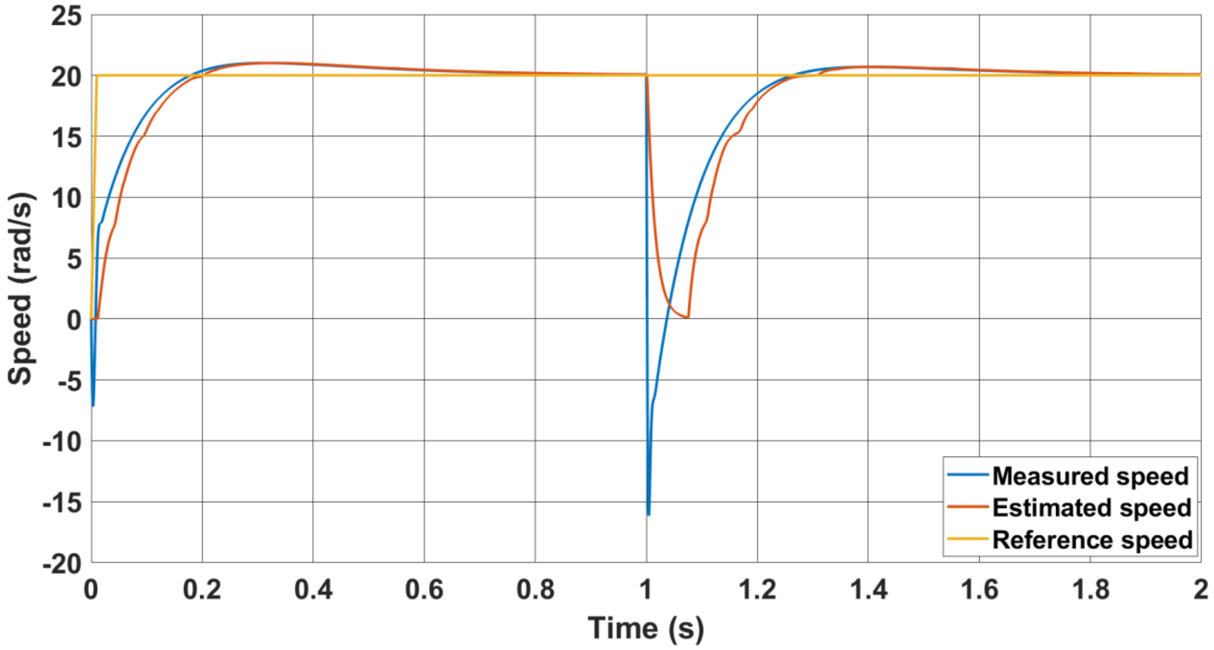

(a)

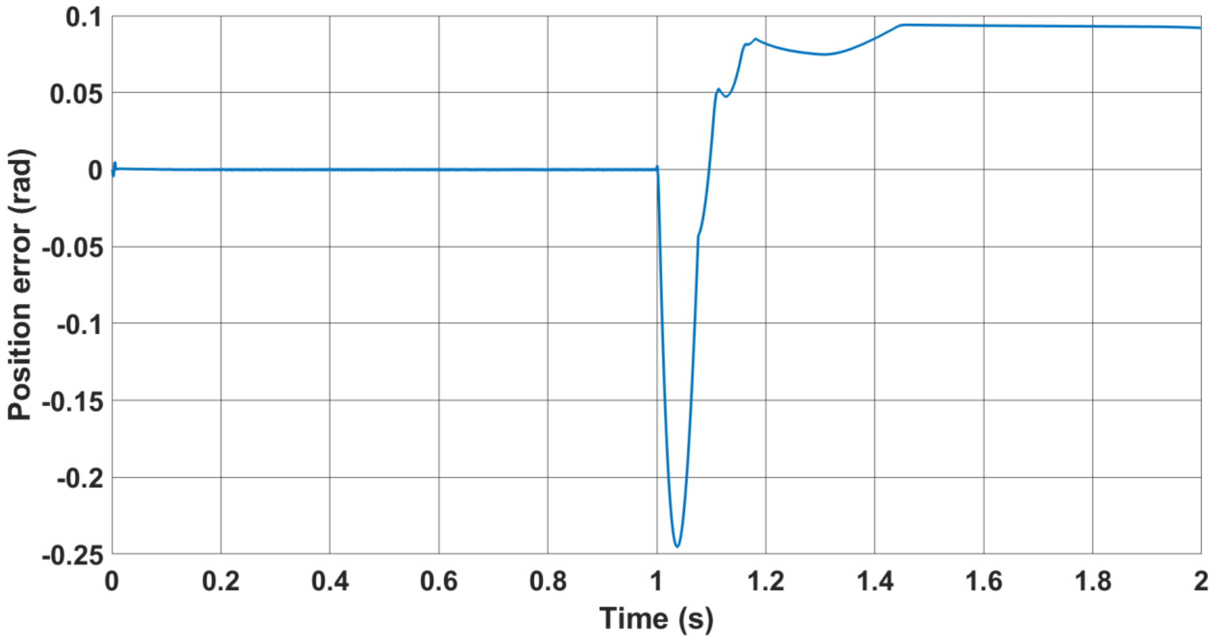

(b)

Figure 4.11: Sensorless performance of the novel method at 30 rad/s and rated torque, (a) speed response (b) corresponding position error

Figure 4.12 illustrates the performance of the classical estimator at low and rated torque. It is evident that the estimated speed is fluctuated compared to the novel method. Furthermore, the position error is significantly increased during the transient period.

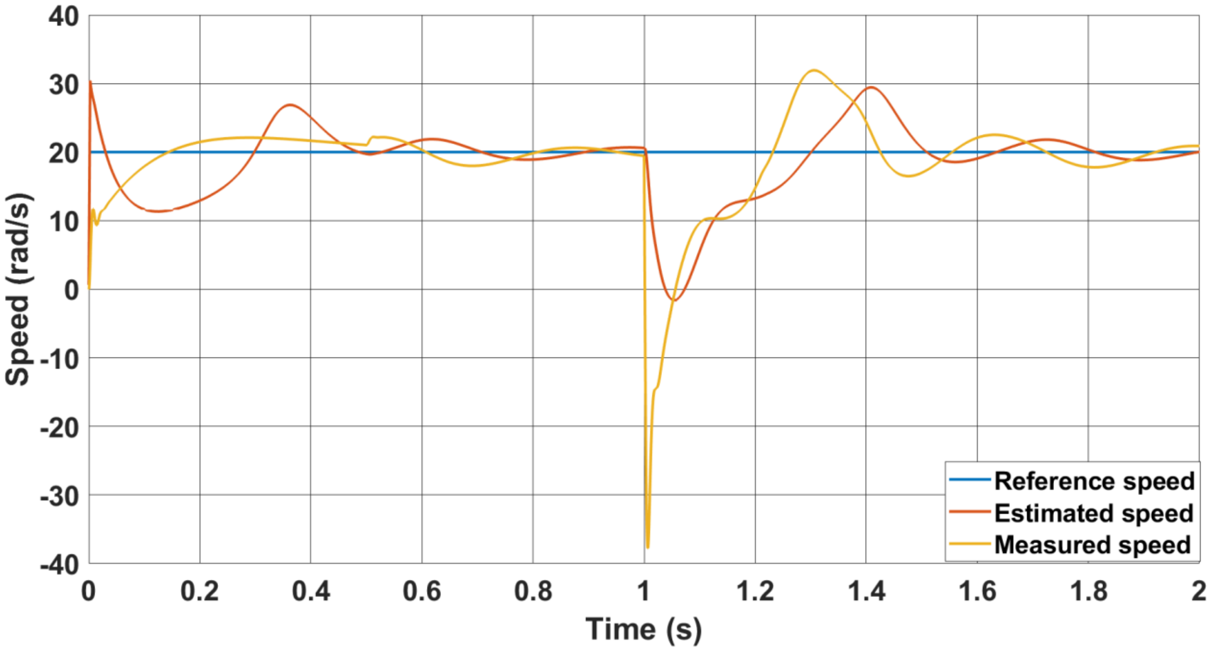

(a)

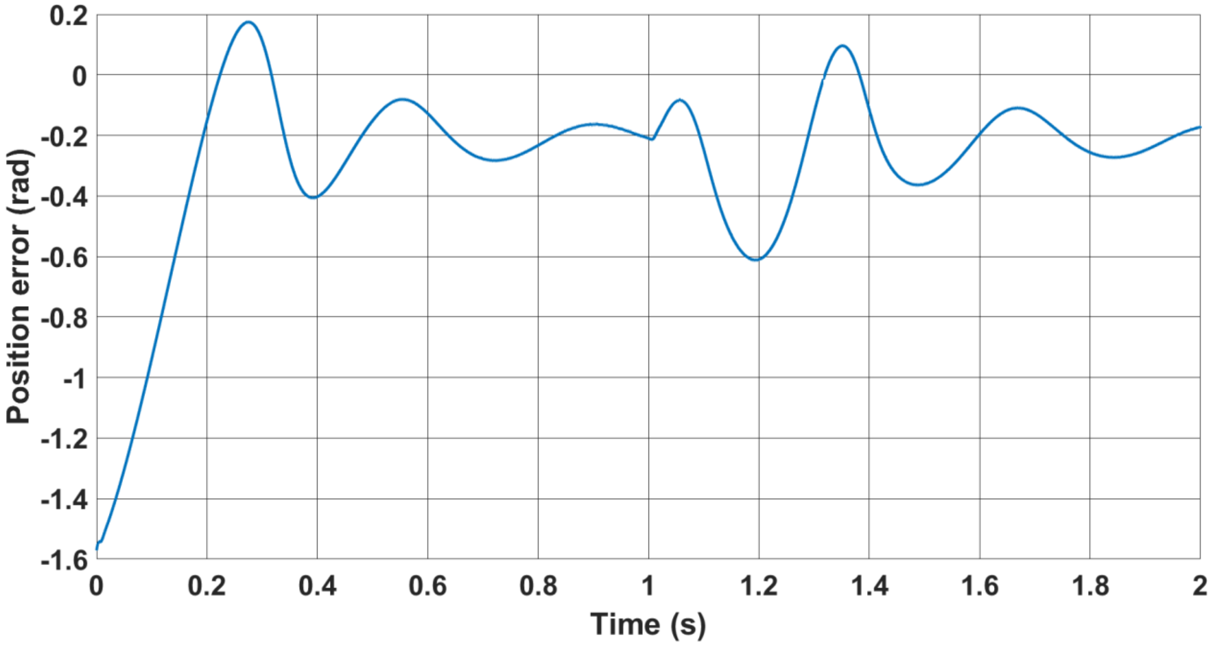

(b)

Figure 4.12 Sensorless performance of classical method at 30 rad/s and rated torque, (a) speed response (b) corresponding position error.

To assess the robustness of the proposed scheme against variations in motor parameters, two tests were conducted. In the first test (Fig. 4.13), the sensorless mode was activated at 1s, and at 3s, a 100% alteration was introduced to the stator resistance in the estimator models. In the second test (Fig. 4.14), the q-inductance in the estimator model was reduced by 50% at 3s. Notably, the novel method demonstrated remarkable robustness in the face of these changes in motor parameters.

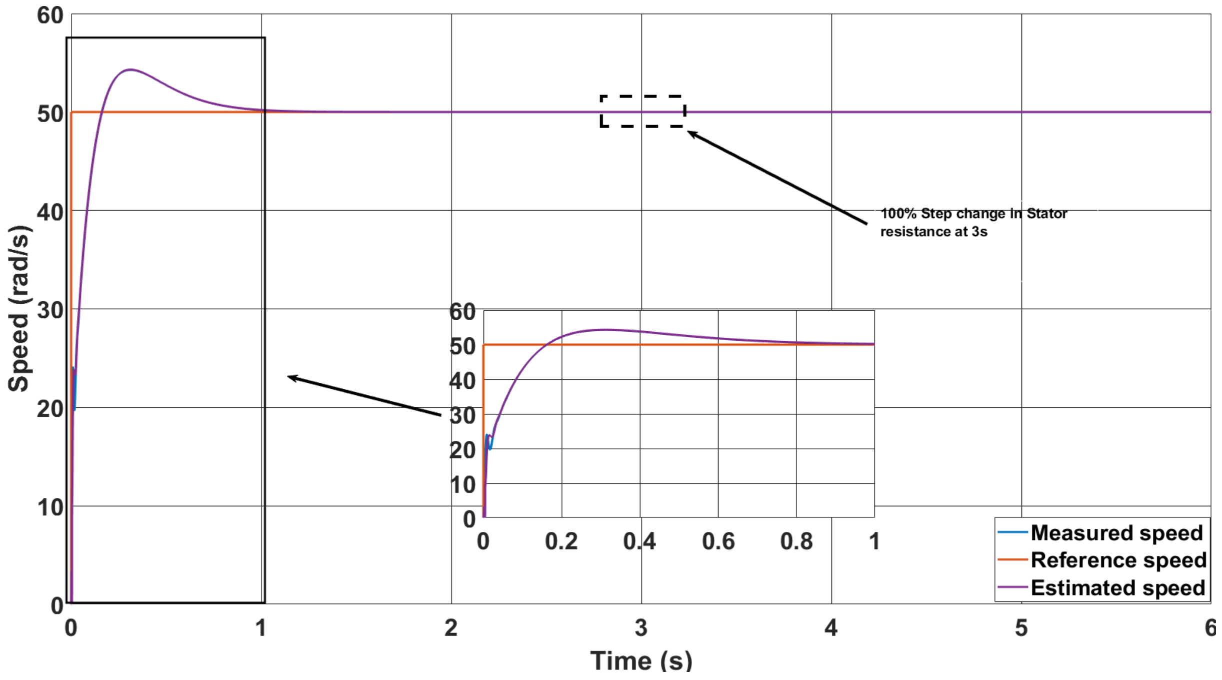
Speed (rad/s)
60
50
40
30
20
10
0
0
1
2
3
4
5
6
Time (s)
100% Step change in Stator resistance at 3s
60
50
40
30
20
10
0
0
0.2
0.4
0.6
0.8
1
Measured speed
Reference speed
Estimated speed

(a)

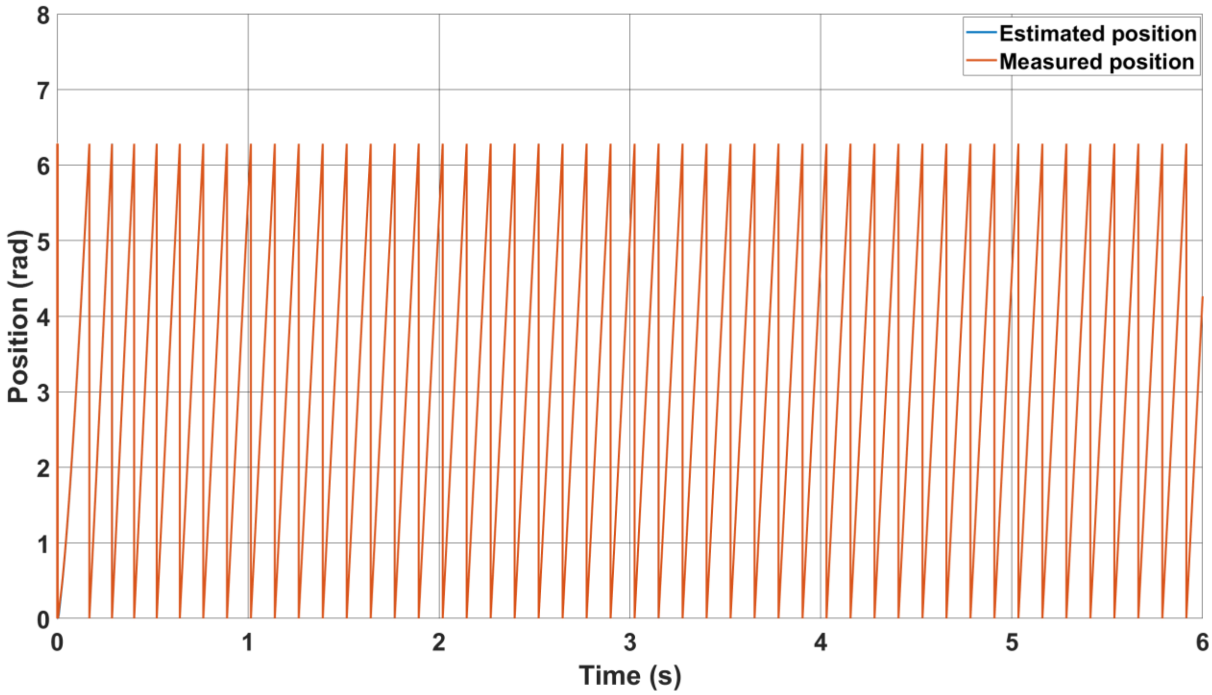
Position (rad)
8
7
6
5
4
3
2
1
0
0
1
2
3
4
5
6
Time (s)
Estimated position
Measured position

(b)

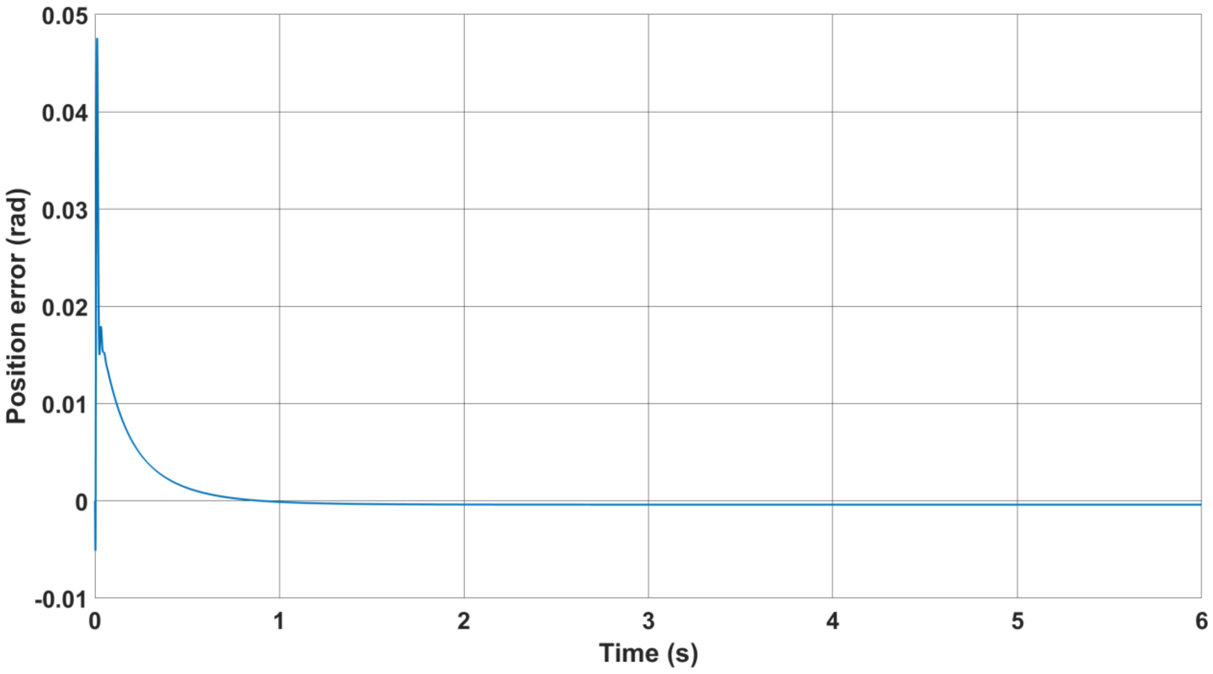

(c)

Figure 4.13 Effect of stator resistance change for the novel method, (a) Estimated speed response, (b) Corresponding estimated and measured positions (c) corresponding position error.

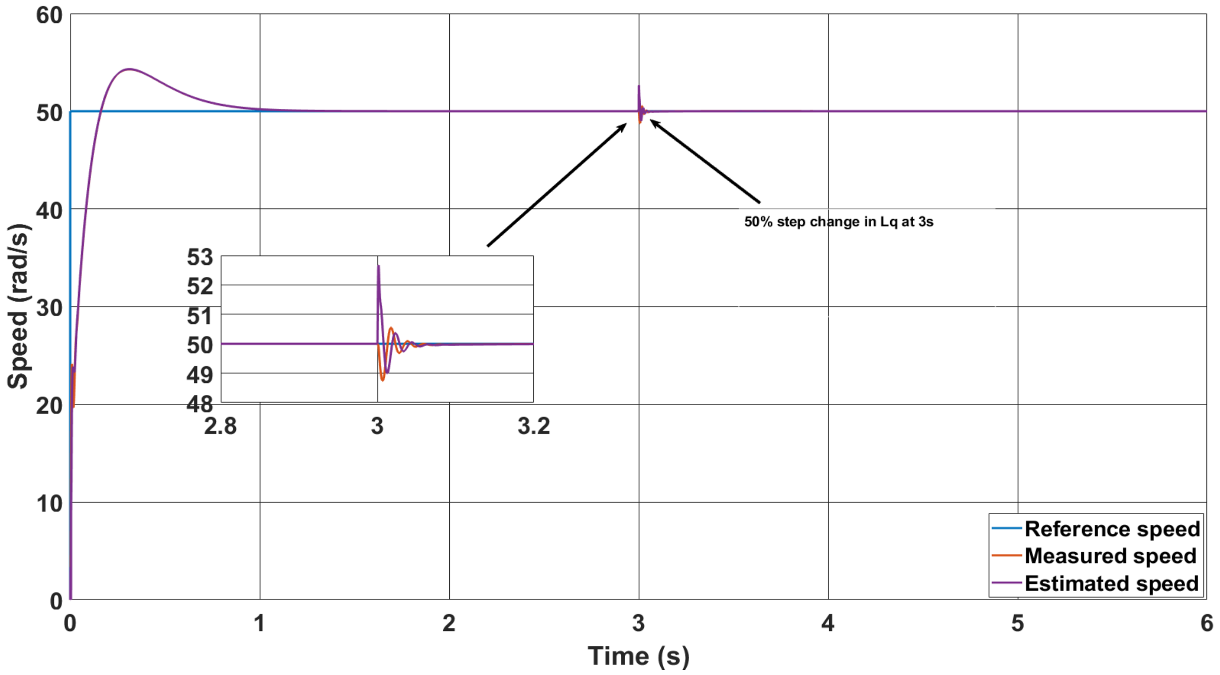

(a)

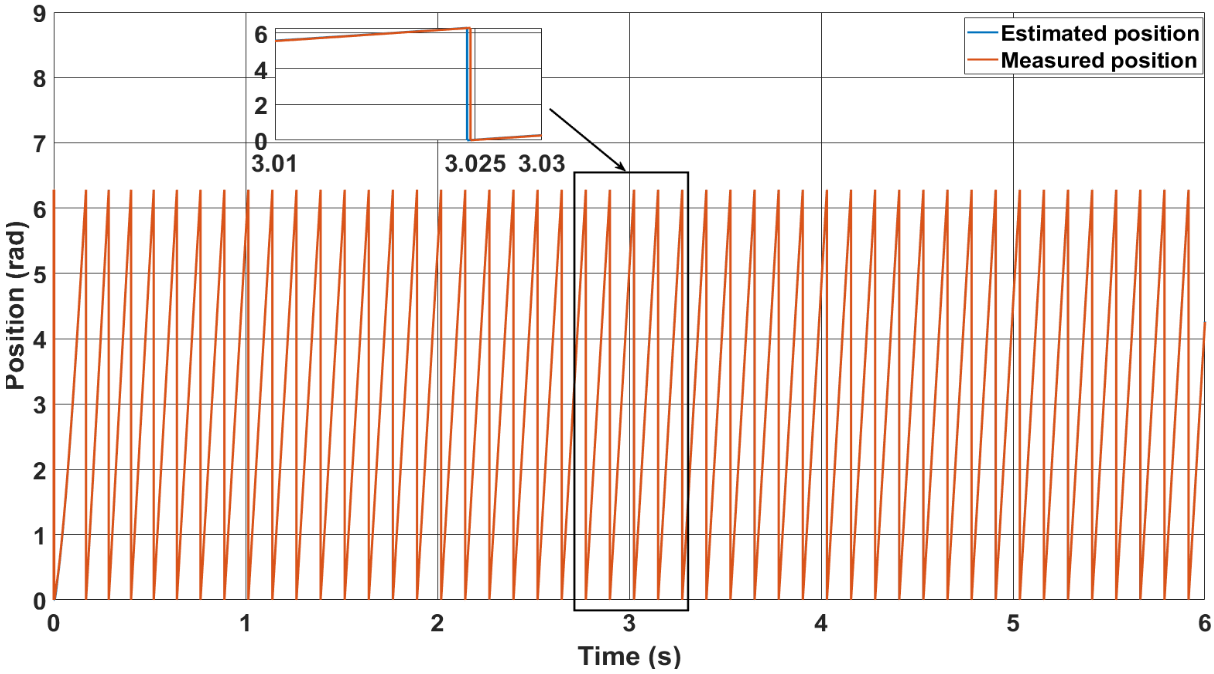

(b)

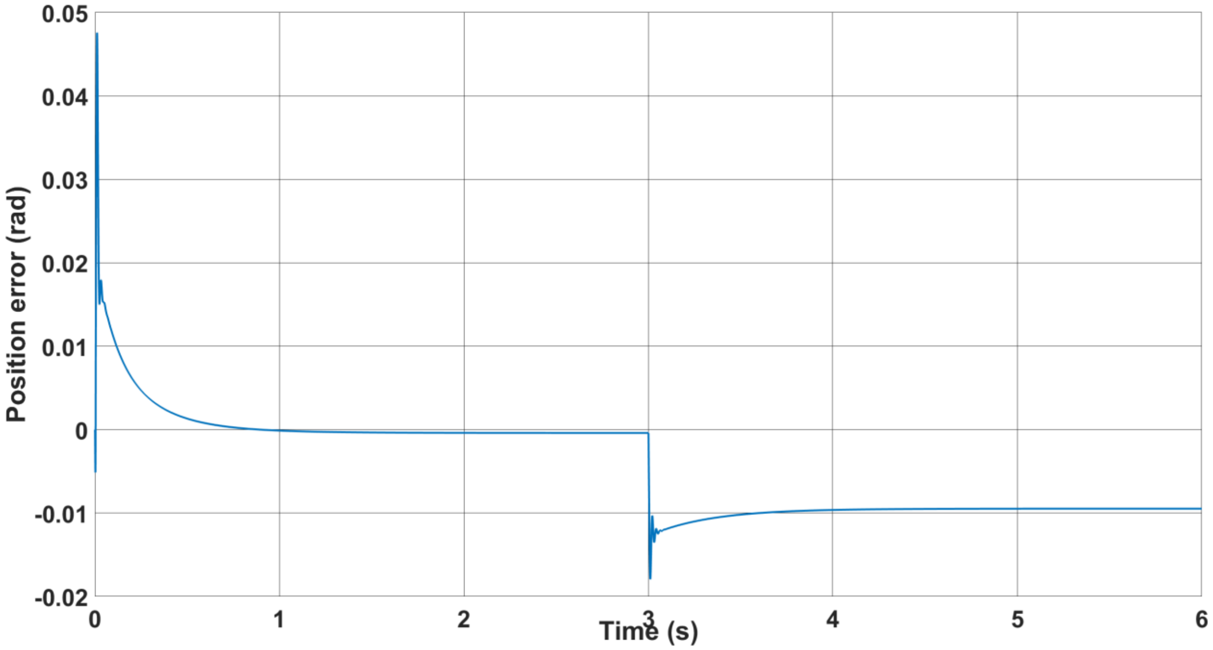

(c)

Figure 4.14 Effect of q-inductance change for the PWM based method, (a) Measured and estimated speed responses, (b) Corresponding estimated and measured positions, (c) corresponding position error.

The PWM based method is also tested for $i_d \neq 0$ and $i_q = 1.25$ A to investigate the effect of cancelling the terms $L_d d\hat{\imath}_d/dt$ and $R\hat{\imath}_d$ in (4.24) on the position accuracy. Fig. 4.15 shows the error resulting from setting the d-axis current to nonzero. Specifically, it is set to -0.5A and -1A at 2s and 4s respectively, and it is clearly shown that the accuracy is not significantly affected.

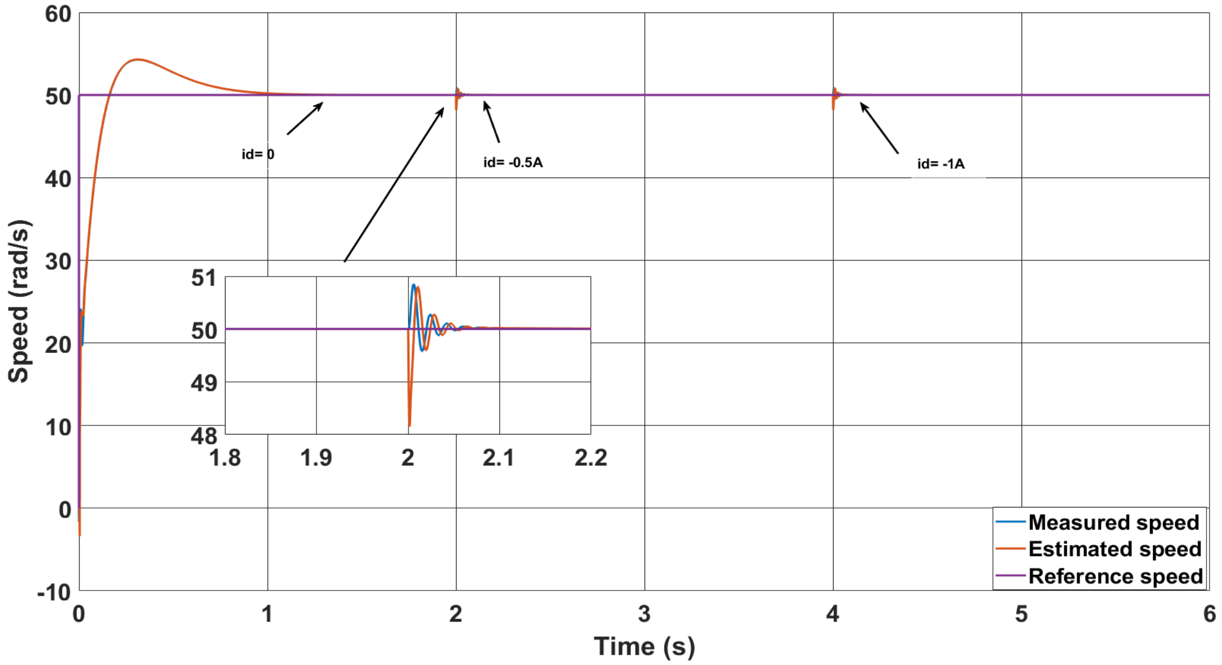

(a)

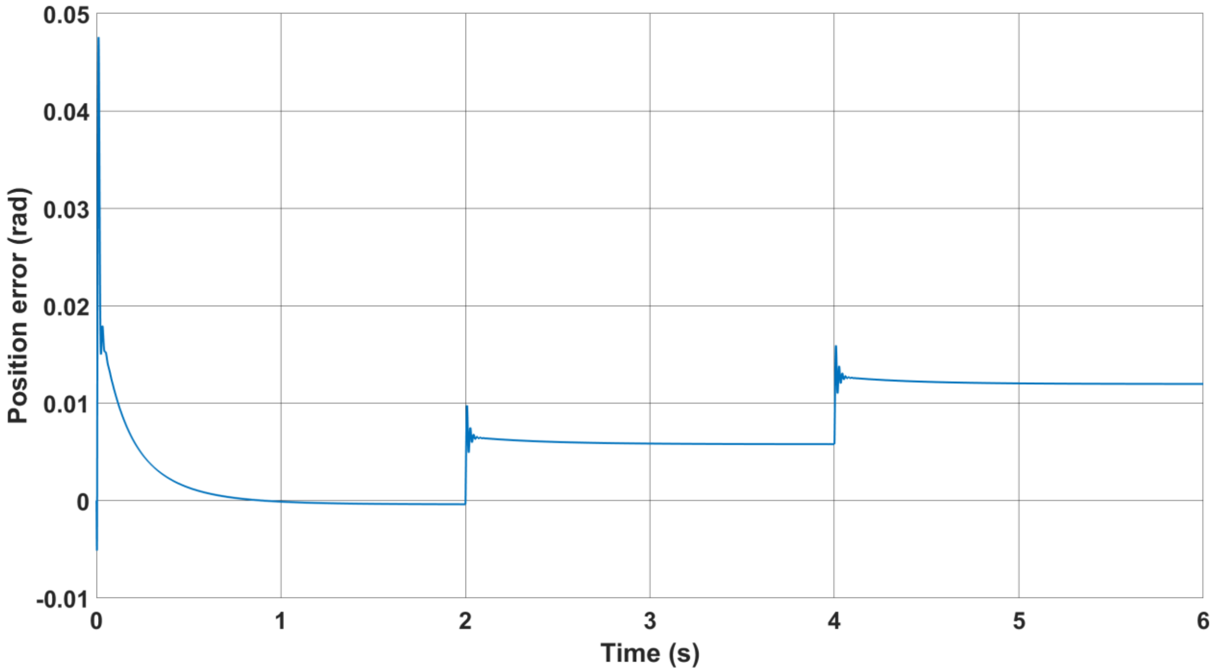

(b)

Figure 4.15 nonzero d-current effect on the novel method, (a) the speed response, (c) the error

The novel method is also tested for $i_d \neq 0$ to investigate the effect of resistance change on the accuracy. Fig. 4.16 shows the error resulting from setting the d current reference to -1A, and a 50% change was introduced to the stator resistance at 2s, then further increased to 100% at 4s. It is clearly shown that the accuracy is not affected.

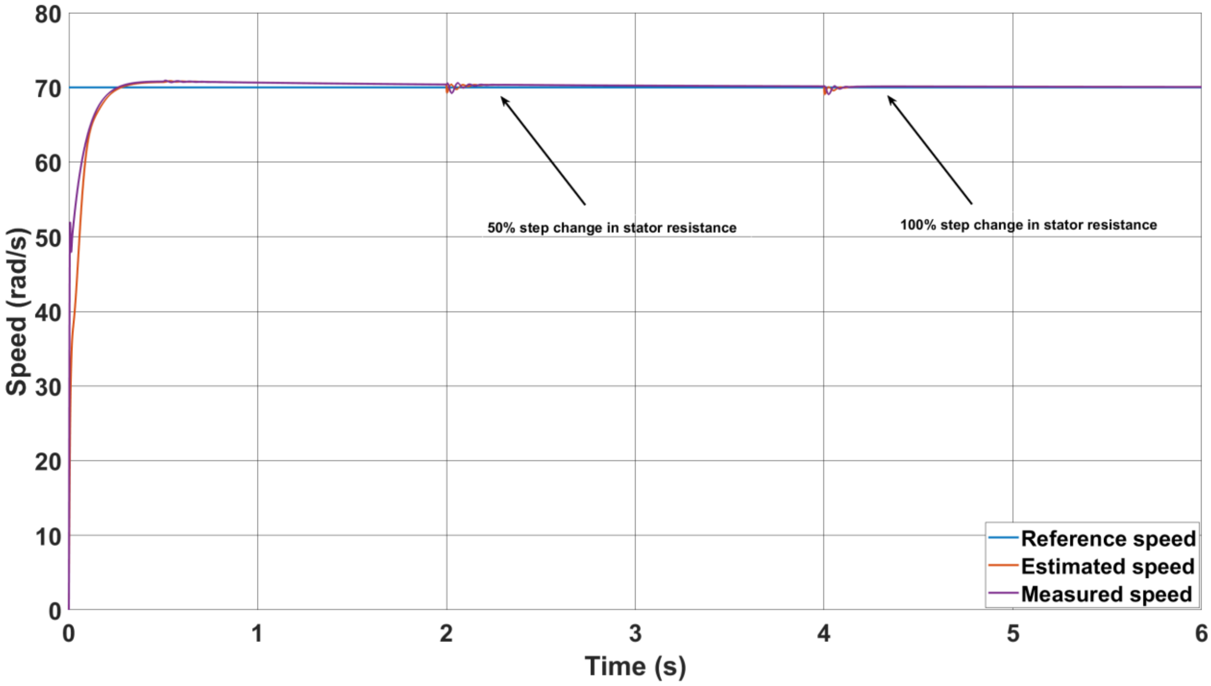

(a)

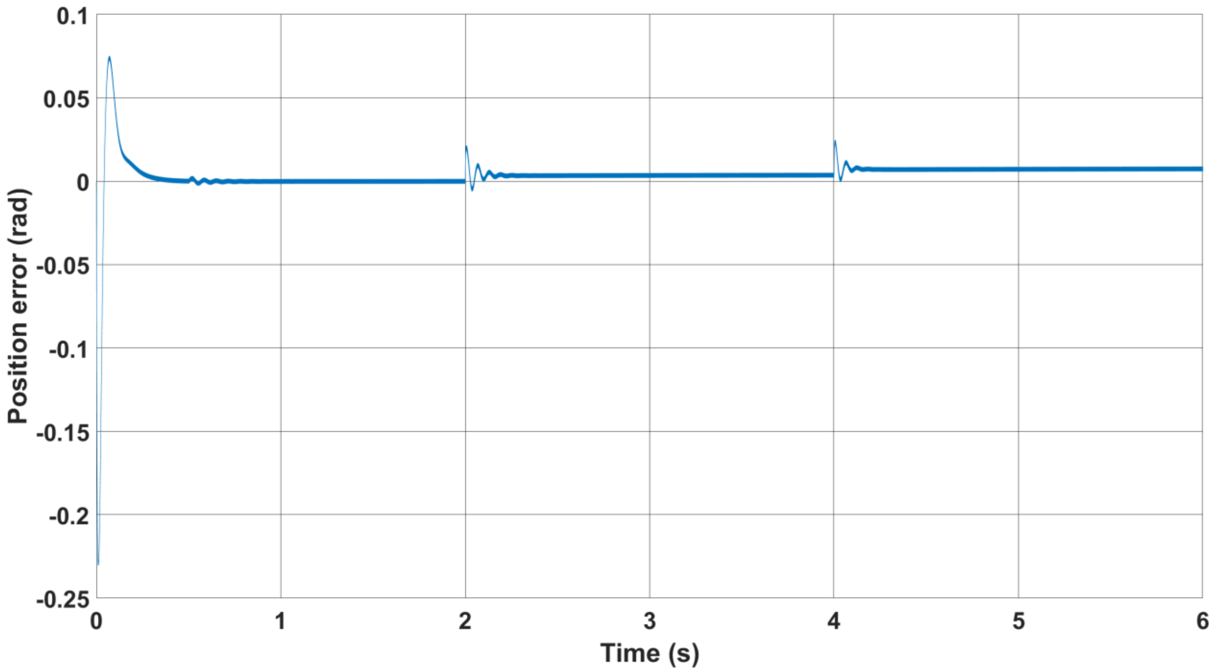

(b)

Fig 4.16 resistance change effect on the novel method for $i_d = -1$ (a) speed response (b) the corresponding position error.

Inverter dead-time effect on the estimated speed for the new method is tested in simulation. Dead-times $1\mu s$, $2\mu s$ and $4\mu s$, are applied between the three phase PWM and their complementary signals to simulate this effect. It is seen from Fig 4-17 that the fluctuation in the estimated speed increases as dead time increases, which is the reflection of the increasing difference between the actual voltages and the command voltages.

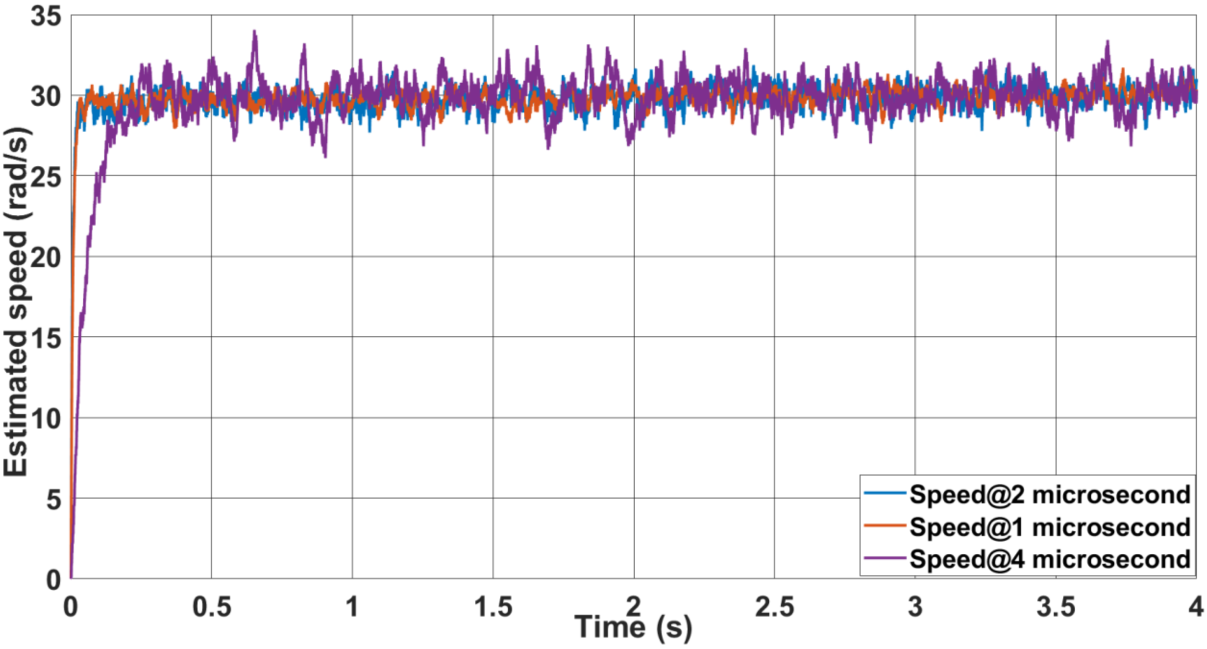

Fig. 4.17 Estimated speeds for the new method with, $1\mu s$, $2\mu s$, and $4\mu s$ dead times.

4.4 Experimental validation

4.4.1 Experimental setup

Figure 4.18 illustrates the block diagram of the experimental hardware, which comprises two distinct systems: the dynamometer and the Drive Unit Test (DUT). This integrated system allows for simultaneous operation in two different modes, with each system capable of functioning in either speed or torque mode. Moreover, the experimental rig is designed to facilitate both sensorless and open-loop operation.

Figures 4.19 and 4.20 show the experimental rig, which consists of two identical 2.1 kW PMSMs manufactured by Control Techniques. These motors are star connected and operate at 400V and 50 Hz. They are equipped with quadrature encoders offering a resolution of 4096 counts per revolution. The two motor shafts are mechanically joined by a rigid coupling.

The first motor, acting as a dynamometer, which is connected to a three-phase two-level inverter, which utilizes a Semikron IGBT module stack for control. This inverter is controlled by a Speedgoat real-time controller. On the other hand, the second motor, known as the Drive Unit, is controlled by a Nidec Unidrive 700M drive. The motor parameters are presented in Table 4.2

The 4096 counts/rev resolution quadrature encoder is used to measure the rotor position for verification purposes, and two TA189 current sensors are used for current phase measurements. The inverter switching frequency is set to 3.125 kHz with a dead time of 0.5 µs, and the control strategy FOC is implemented with sampling time of 80 µs. Hence, the ratio between the sampling and switching frequencies (the total number of the sampling points n in one switching period) is $= \frac{1}{3125*80*10^{-6}} = 4$, which is the optimum ratio that gives sufficiently accurate results without excessive computational burden. A lowpass filter with 3 Hz cut-off frequency is used in the classical method instead of the integrator to minimize problems associated with pure integration.

The trail-error method is used to tune the PI controller of the speed estimators for the classical and the proposed methods. The tuned gains for the classical method and the proposed method are $k_p = 700\, rad\, V^{-2}\, s^{-2}$, $k_i = 7000\, rad\, V^{-2}\, s^{-3}$ and $k_p = 1000\, rad\, V^{-2}\, s^{-2}$, $k_i = 8000\, rad\, V^{-2}\, s^{-3}$ respectively. The trail-error method is also used to tune the current controller gains, and these gains are $k_p = 30\, VA^{-1}$, $k_i = 400\, VA^{-1}\, s^{-1}$. The closed-loop bandwidth for the current loop is approximately calculated as $f_{BW} \approx \frac{k_p}{2*\pi*L} = \frac{30}{2*\pi*0.015} = 318$ Hz. The speed controller gains of the proposed method are tuned to be $k_p = 0.125\, A\, rad^{-1} s$, $k_i = 20\, A\, rad^{-1}\, s^2$, and the bandwidth can be approximated calculated as $w_B \approx \sqrt{\frac{k_i}{j}} = \sqrt{\frac{20}{0.00077}} = 161$ rad/s.

Where L and J are the inductance and the inertia of the motor respectively.

For sensorless control applications, a bandwidth of approximately 161 rad/s is generally suitable and can provide the necessary dynamic response and estimation accuracy for many industrial applications. However, it's important to ensure that the control algorithm is optimized to handle the computational load within the control loop cycle time, and validate the control performance under various operating conditions, including low-speed operation and load variations.

Regarding the computational power requirements of the proposed method, execution on the Speedgoat system takes approximately 8,2 µs to perform both the proposed sensorless algorithm and FOC, which includes Clarke and Park transformations, PI controllers, inverse transformations, and SVPWM calculation. This short execution time is due to the high clock speed (1.99 GHz) and potential hardware support for efficient trigonometric calculations. However, Speedgoat is a rapid control prototyping system and is not suitable for commercial products, where low-cost microcontrollers are more common. TMS320F28335 floating point microcontroller (150 MHz clock) is a low-cost microcontroller and can be used to implement the proposed method. The estimated execution time for the proposed method is approximately $\frac{8.2*1990}{150} = 109$ µs. By using efficient trigonometric approximations like lookup tables and simplified functions, the execution time can be reduced to under 26 µs. In a similar context, [61] discusses a more computationally intensive method implemented on the TMS320F28335 microcontroller, which achieved an execution time of 39 µs.

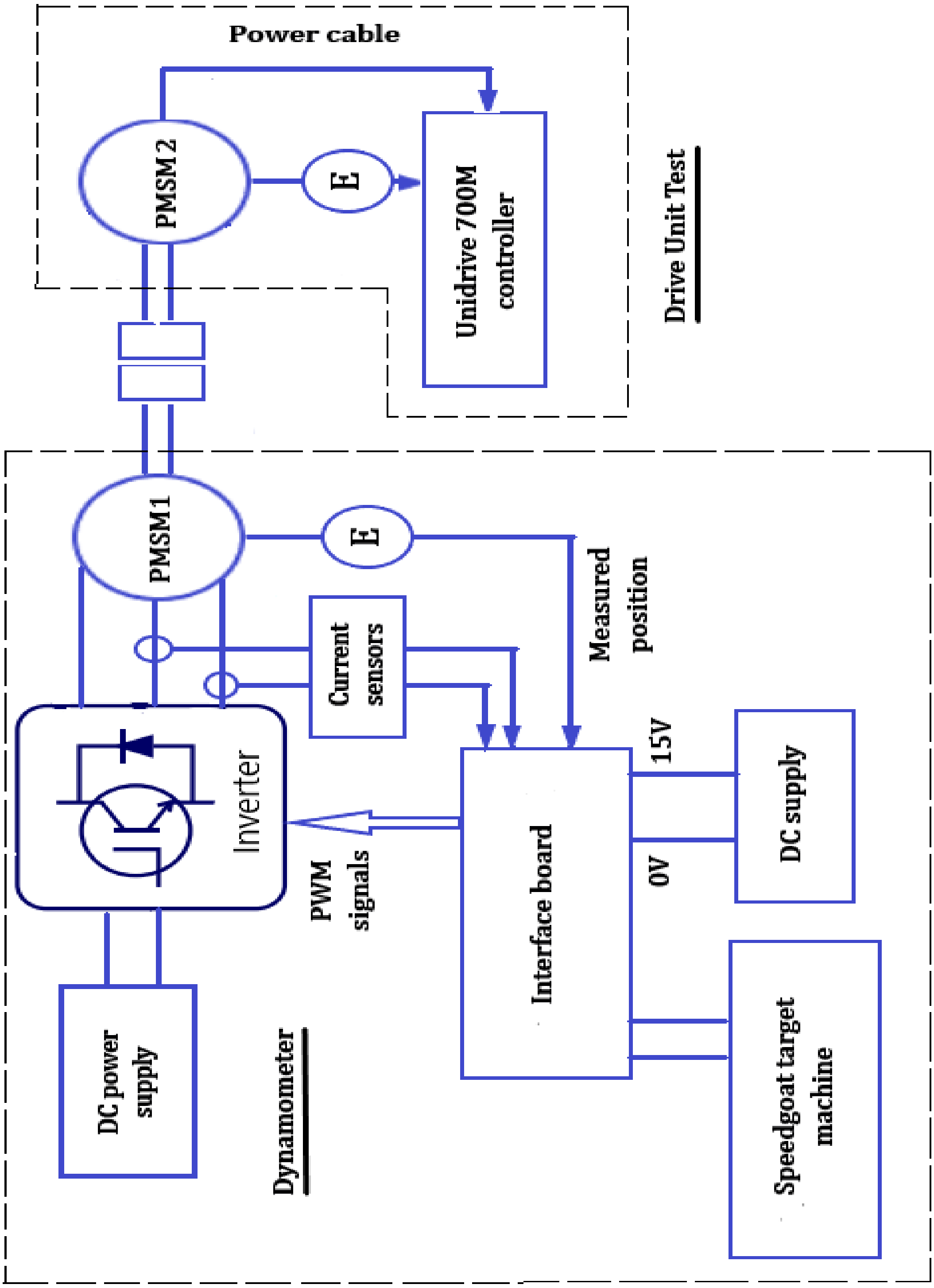

Figure 4.18 Illustration of the rig

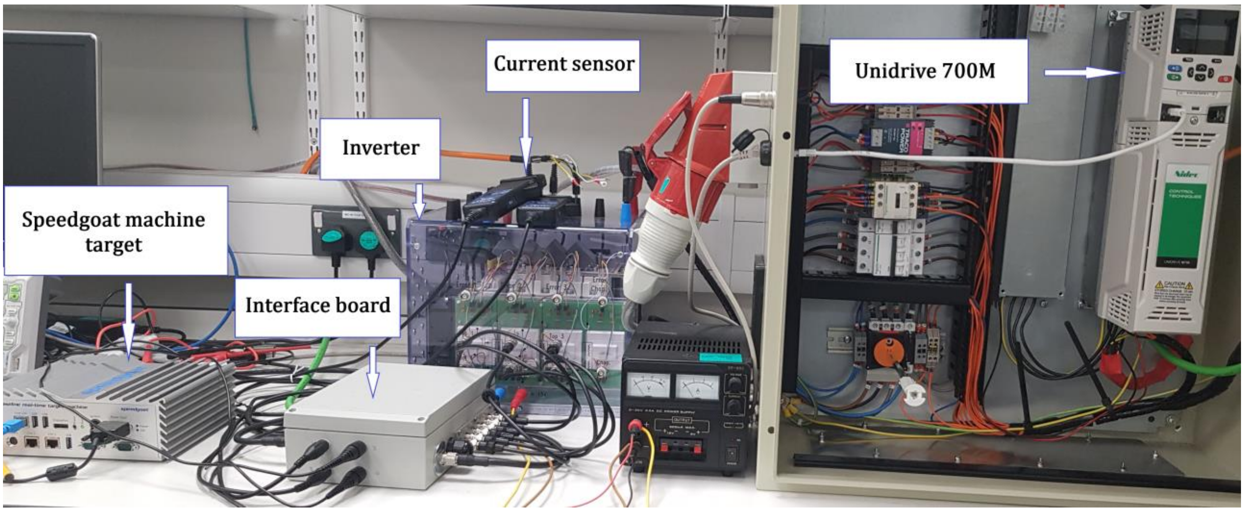

Figure 4.10 Laboratory photograph of the experimental hardware

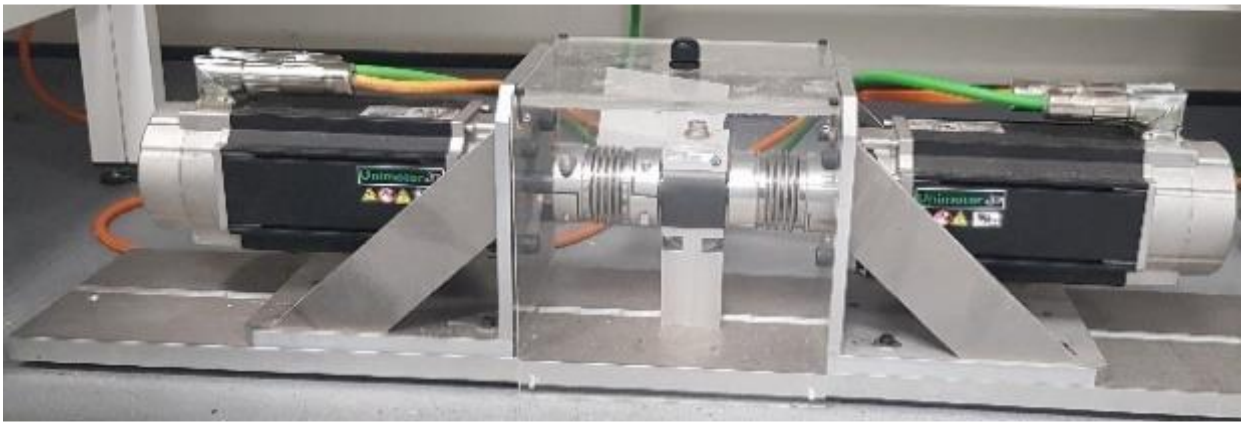

Figure 4.20 Laboratory photograph of the two identical PMSMs

To verify and align the zero position of a position sensor with the d-axis, certain steps need to be followed. Initially, PMSM is driven by a load machine at a low speed in the positive direction. The three-phase back-EMF of the PMSM is then measured and transformed into d-q components from the machine terminals. To set the reference position to zero at the beginning of a revolution, the index signal in the Speedgoat quadrature encoder block should be turned on. This facilitates the alignment process. While the motor is running, the alignment is achieved by selecting an angle that results in $v_d = 0$ and v_{qmax}. Figure 4.21 depicts the position aligned with the phase a back-EMF. Figure 4.21 shows the simulation results of the rotor position aligned against the Phase-A back-EMF. It is seen that the angle and phase-A back-emf are 180-degree phase-shifted because the machine operates as a generator.

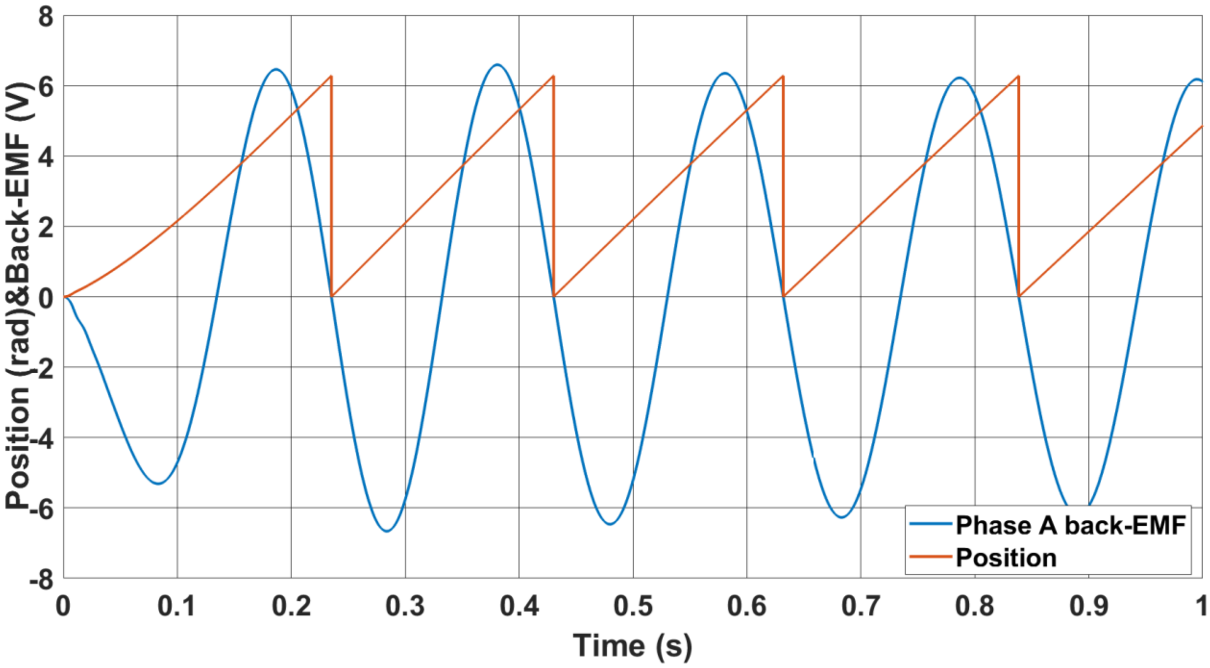

Figure 4.21 Rotor position alignment

Table 4.2 The PMSM parameters

Quantity	Unit	Value
Pole-pairs	--	3
Rated Power	kW	2.1
Stator resistance	ohms	2.19
Rated current	A	4.2
Base speed	rpm	3000
Rated torque	N.M	6.7
Torque constant	Nm/A	1.6
PM flux linkage	V/Hz	0.356
d-axis inductance	mH	12.5
q-axis inductance	mH	15
Inertia	$Kg.m^2$	0.00077

4.4.2 The Experimental Results

Extensive tests are performed in both open-loop and closed-loop operations, to assess both the novel and conventional flux-based MRAS schemes. Both estimators' performances are evaluated under various load and speed conditions.

4.4.2.1 Open Loop Operation

In this mode, the sensorless estimator is not used in feedback, and the FOC controller obtains the speed and position signals from the sensor. The PI gains for both the proposed and conventional MRAS estimators are set to Kp=1000, Ki=8000 for the proposed estimator, and Kp=700, Ki=7000 for the conventional MRAS estimator. These values are determined using the trial-and-error method to achieve optimal dynamic performance.

Figure 4.22 compares the performance of the classic and novel Model Reference Adaptive System (MRAS) estimators under no load conditions. The novel method exhibits reduced fluctuation in the speed compared to the classical method. Additionally, as the speed decreases to 50 rad/s, the position error (the difference between measured and estimated positions) increases in the classical method (approximately -0.2 rad), while it remains minimal (around 0 rad) in the novel method.

Moving on to Figure 4.23, it shows the performance of the classical and novel MRAS estimators in the motoring mode, where 25% of the rated load is employed to counter the speed direction. Subsequently, the load is increased to 50% of the rated load. Notably, the oscillation in the conventional method intensifies when the load is applied, whereas the novel speed estimation remains unaffected.

Furthermore, it can be observed that both methods experience a slight increase in position error as the load is augmented while maintaining a constant speed. In the novel method, the error progresses from -0.027 rad under no load to -0.06 rad at 50% of the rated torque. On the other hand, the classical method exhibits an error escalation from -0.107 rad under no load to -0.125 rad at 25% of the rated torque, further increasing to -0.133 rad at 50% of the rated torque. It is important to highlight that the error amplifies by approximately -0.02 rad per 25% increase in load for both methods.

Figure 4.24 illustrates the open-loop performance of the proposed and classical methods in a regenerative mode. In this case, 25% and 50% of the rated torque are applied to support the direction of rotation. The new method exhibits better performance with reduced oscillations in comparison to the conventional method.

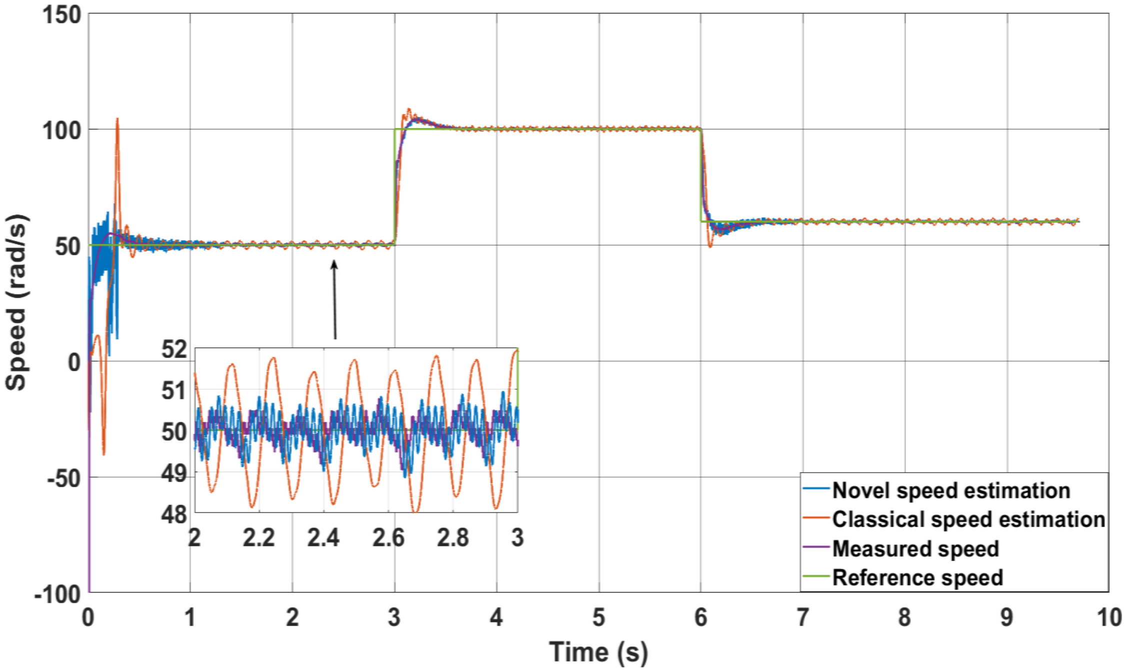

(a)

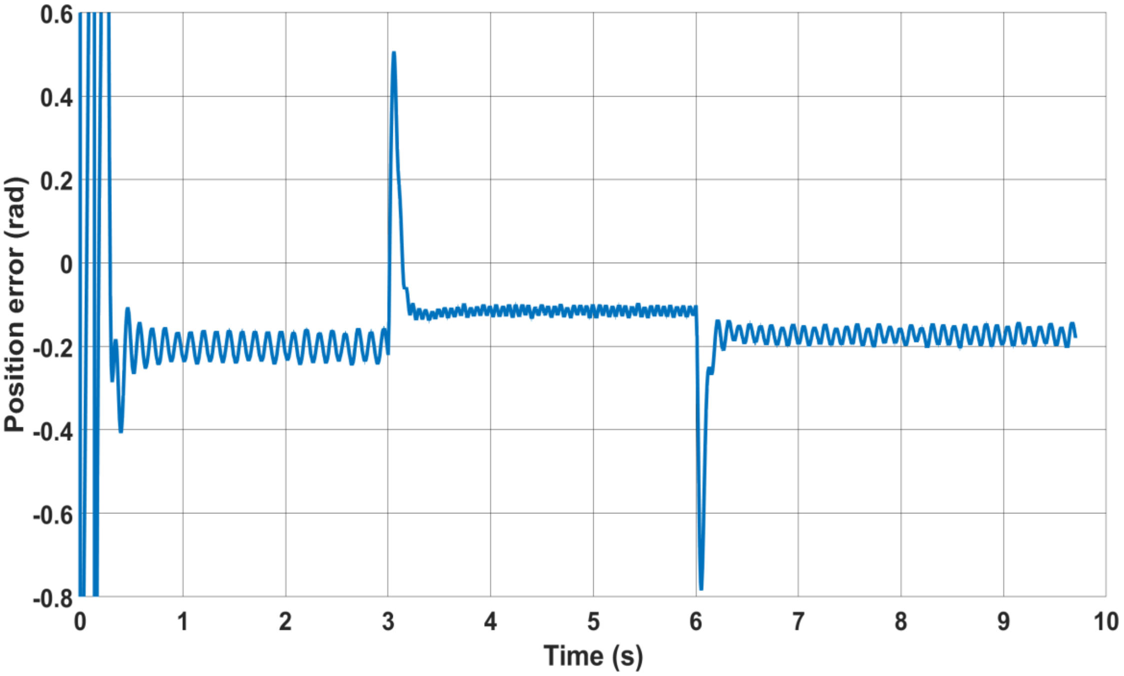

(b)

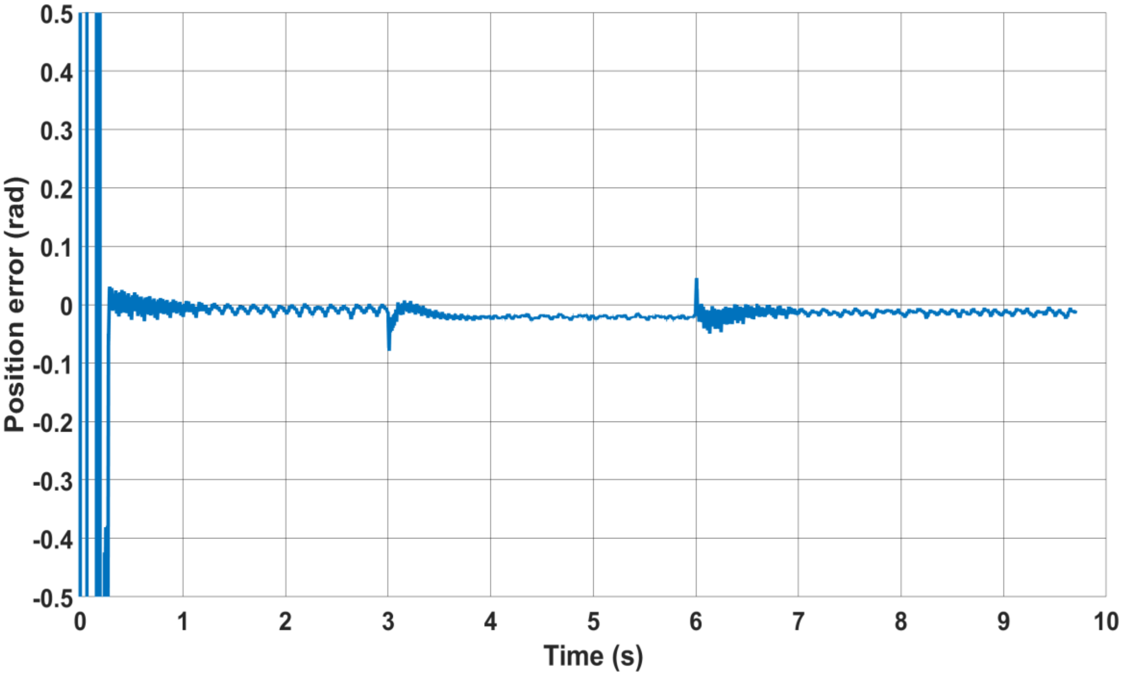

(c)

Figure 4.22 Open-loop response under no load, (a) Speed response for both methods, (b) Corresponding position error for the classical MRAS, (c) position error for the novel MRAS

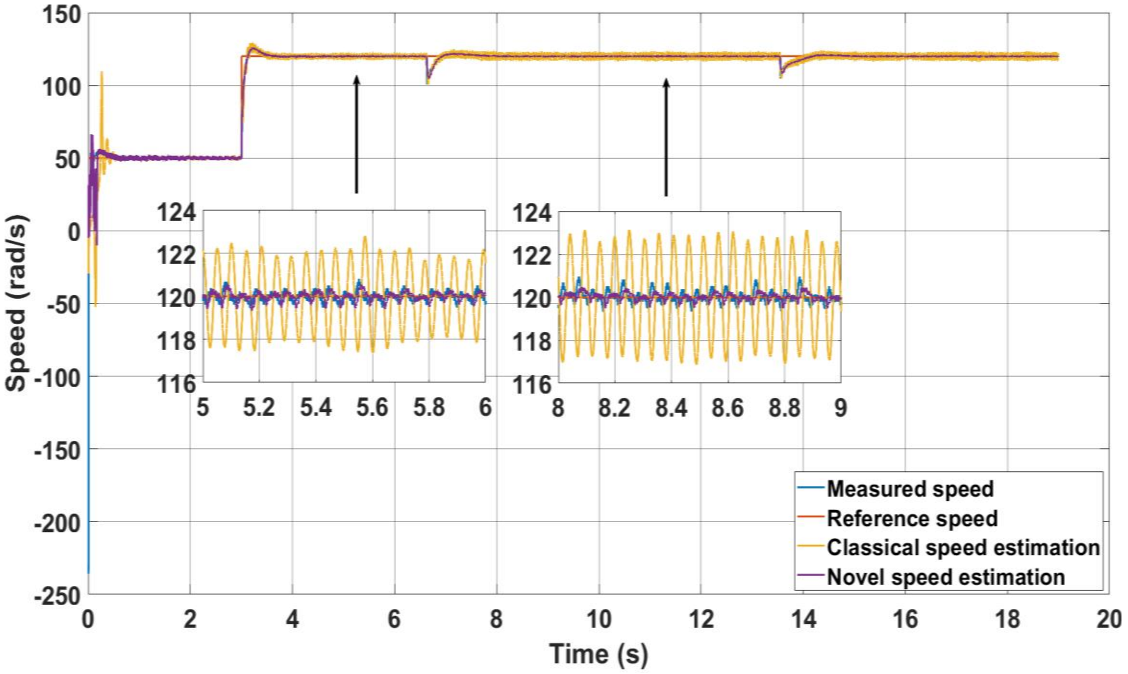
Speed (rad/s)
150
100
50
0
-50
-100
-150
-200
-250
0
2
4
6
8
10
12
14
16
18
20
Time (s)
124
122
120
118
116
5
5.2
5.4
5.6
5.8
6
8
8.2
8.4
8.6
8.8
9
Measured speed
Reference speed
Classical speed estimation
Novel speed estimation

(a)

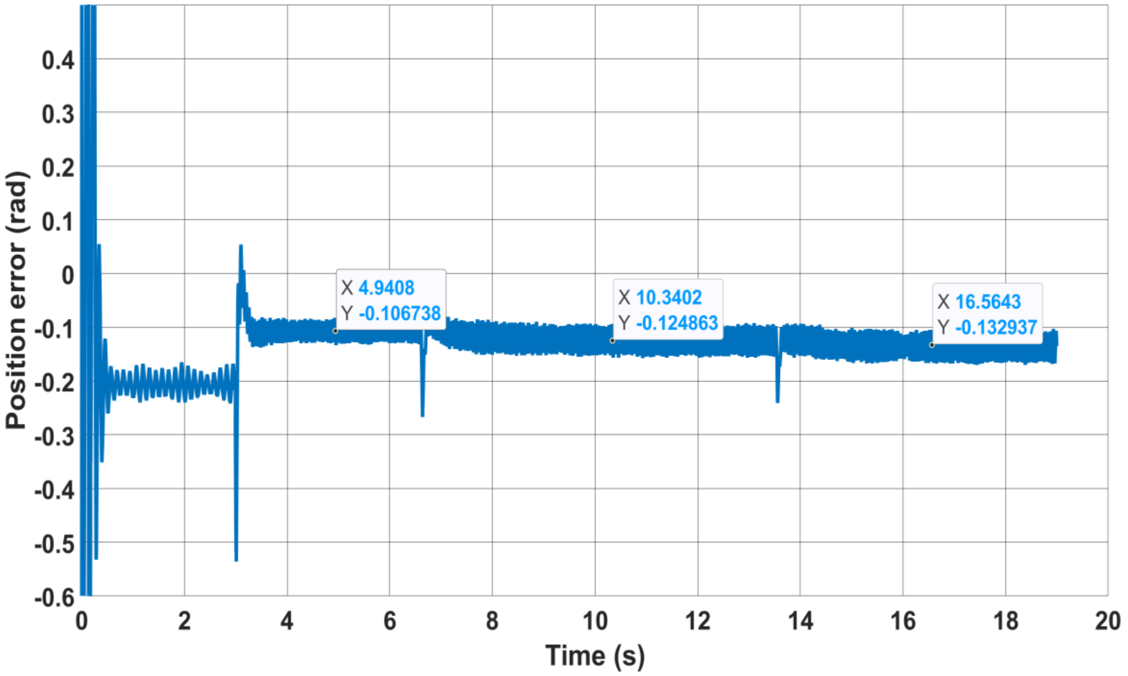
Position error (rad)
0.4
0.3
0.2
0.1
0
-0.1
-0.2
-0.3
-0.4
-0.5
-0.6
0
2
4
6
8
10
12
14
16
18
20
Time (s)
X 4.9408
Y -0.106738
X 10.3402
Y -0.124863
X 16.5643
Y -0.132937

(b)

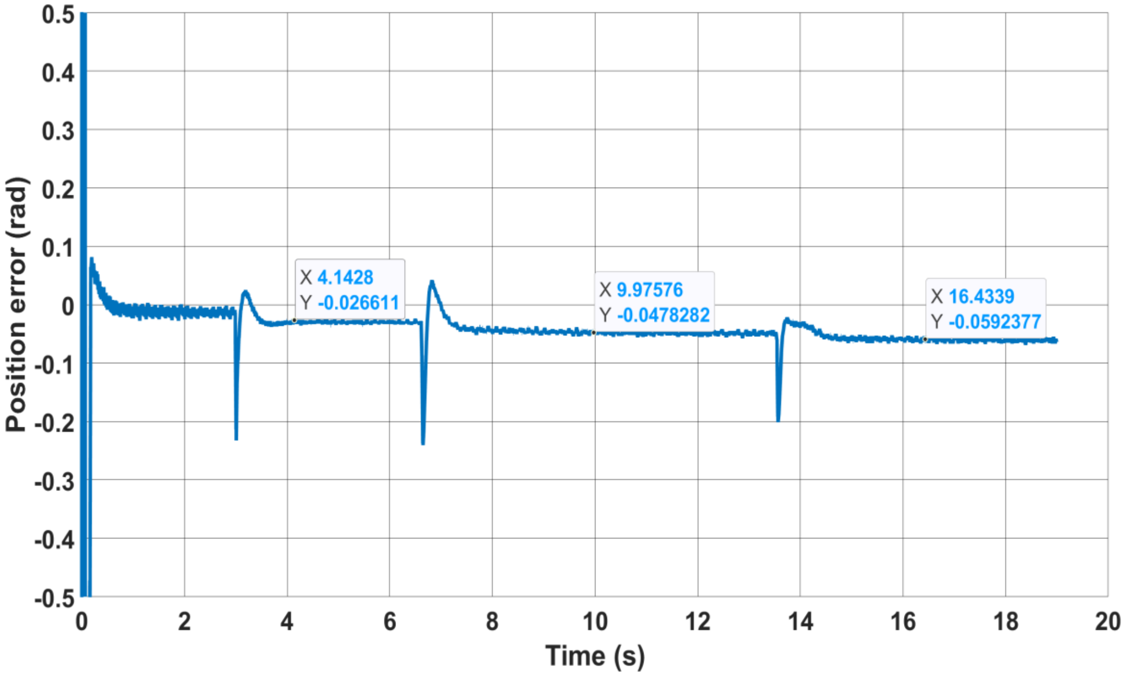

(c)

Figure 4.23 Open-loop response with motoring operation, (a) Speed response for both methods, (b) Corresponding position error for the classical MRAS, (c) position error for the novel MRAS

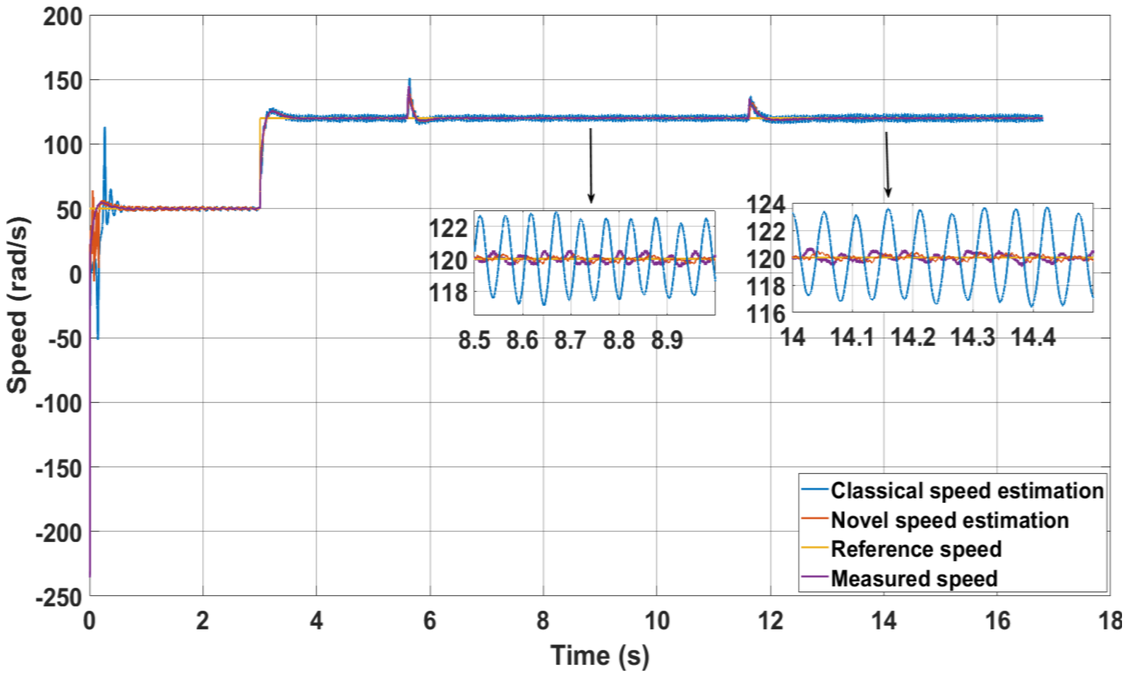

(a)

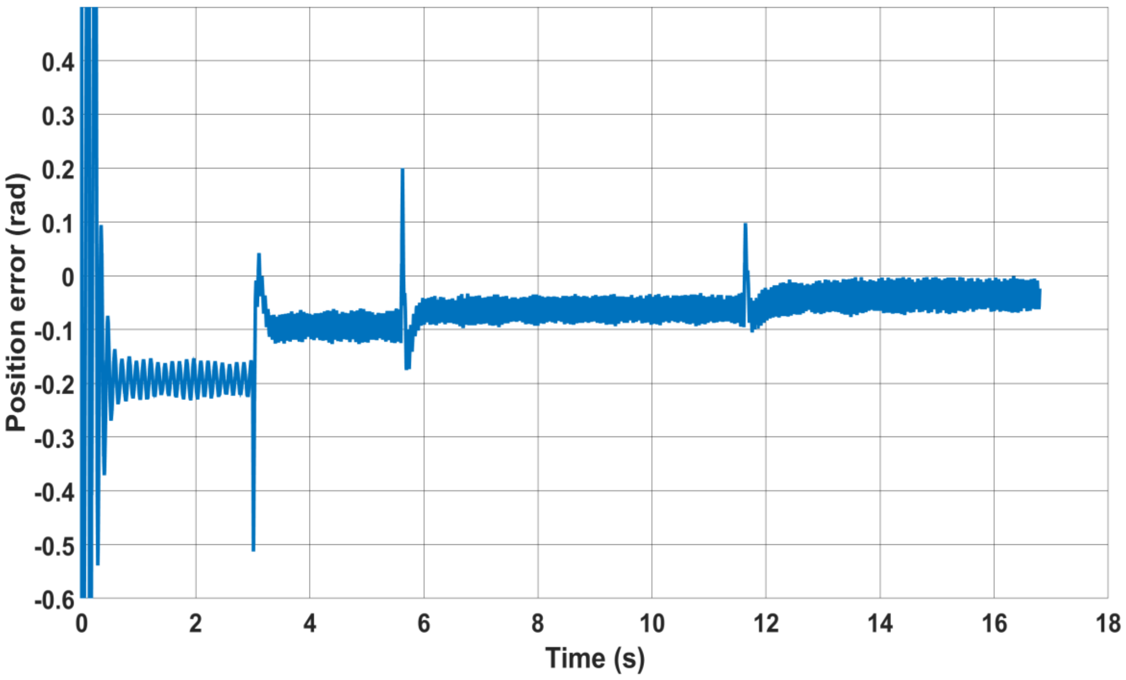

(b)

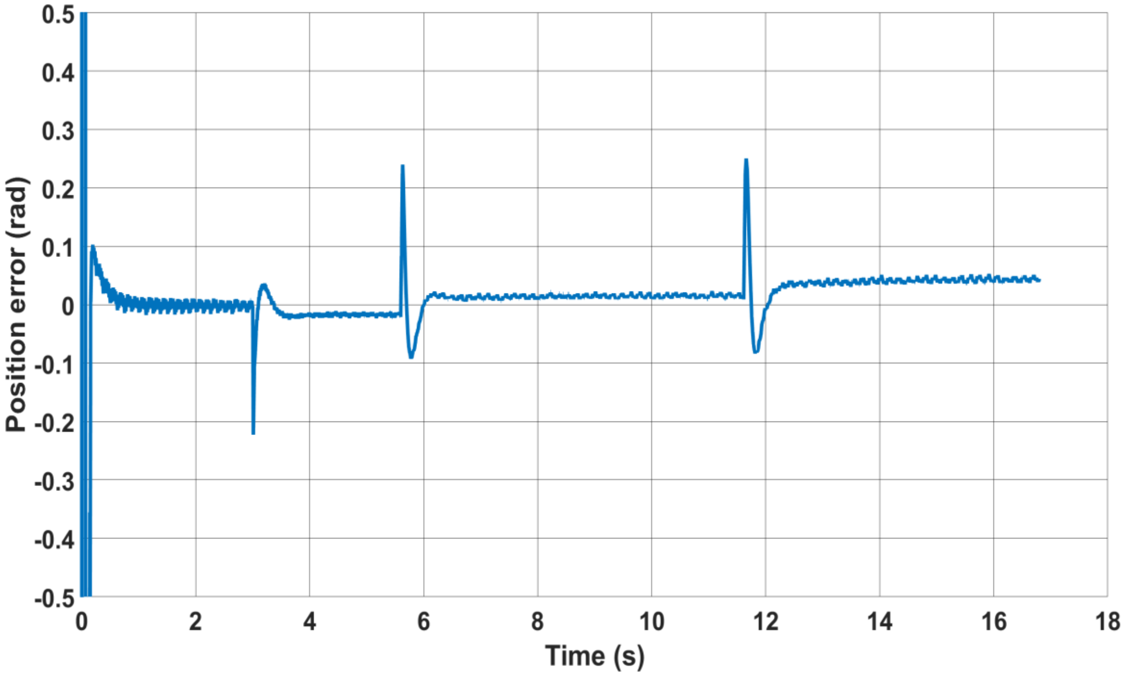

(c)

Figure 4.24 Open-loop response with regenerative operation, (a) Speed response for both methods, (b) position error for the classical MRAS, (c) position error for the novel MRAS

4.4.2.2 Sensorless Operation

To evaluate the performance of the proposed sensorless method, the dynamometer is first tested in torque mode and then in speed mode.

4.4.2.2.1 Torque mode

In this mode of operation, the dynamometer is set to torque mode and driven by the second Drive Unit at a constant speed of 300 rpm ≈ 95 rad/s to test the accuracy of the estimated position for the novel method. At 2 seconds, a reference torque of 2 N.m (30% of the rated torque) is applied, followed by an increase to 4 N.m (60% of the rated torque) at 4 seconds.

Figure 4.25(a) illustrates the corresponding phase currents for the different applied torques. These currents are obtained by dividing the given torque by the torque constant (1.6 N.m/A). From Figure 4.25(b), it is evident that the measured q-current accurately tracks the reference q-current, indicating that the estimated position closely aligns with the measured position, as depicted in Figure 4.25(c). Moreover, Figure 4.25(d) displays the position error, which is negligible at 0.03 rad.

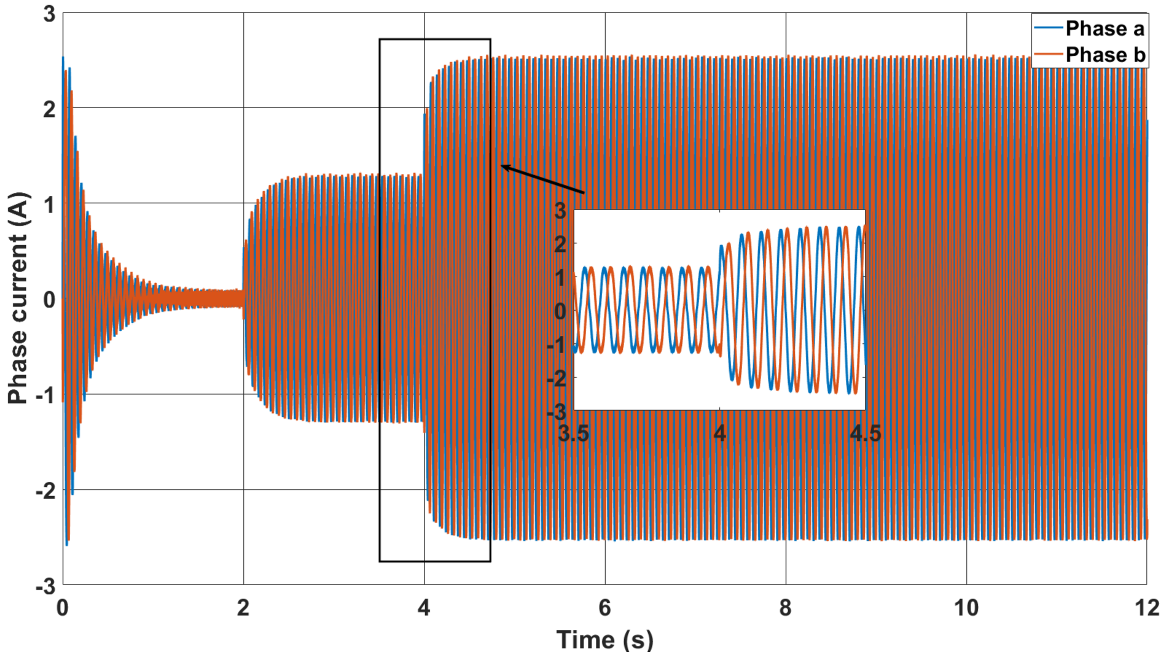
Phase current (A)
Time (s)
Phase a
Phase b
3
2
1
0
-1
-2
-3
0
2
4
6
8
10
12
3.5
4
4.5

(a)

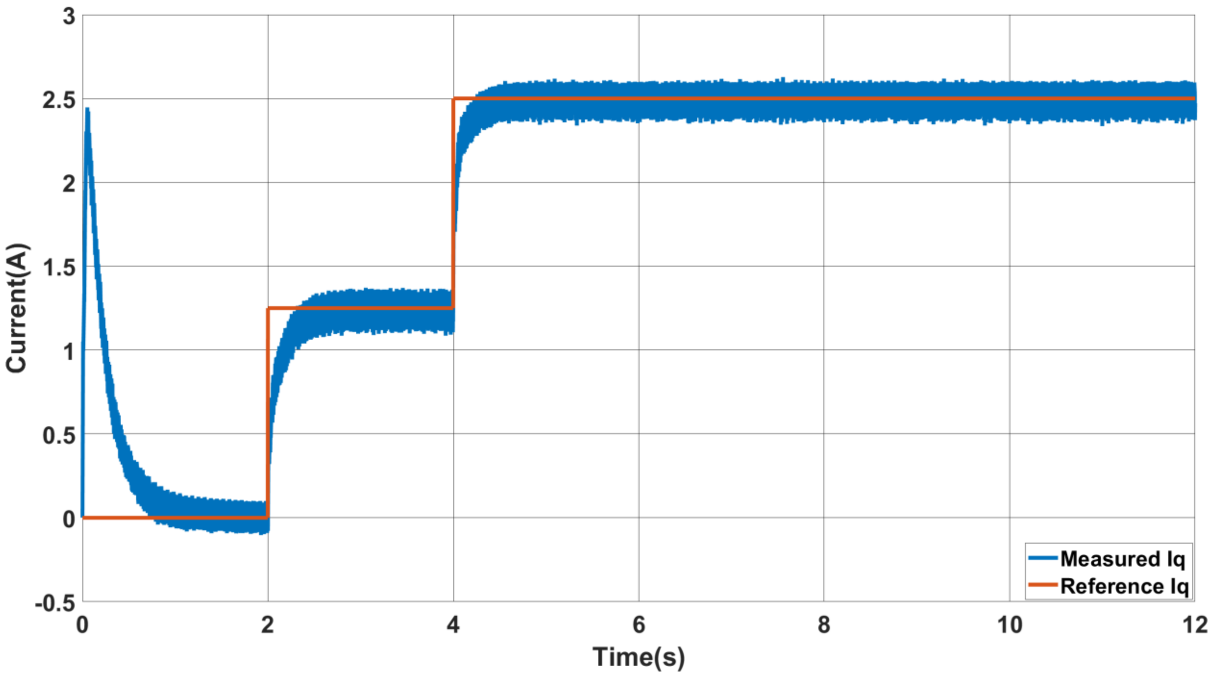
Current(A)
Time(s)
Measured Iq
Reference Iq
3
2.5
2
1.5
1
0.5
0
-0.5
0
2
4
6
8
10
12

(b)

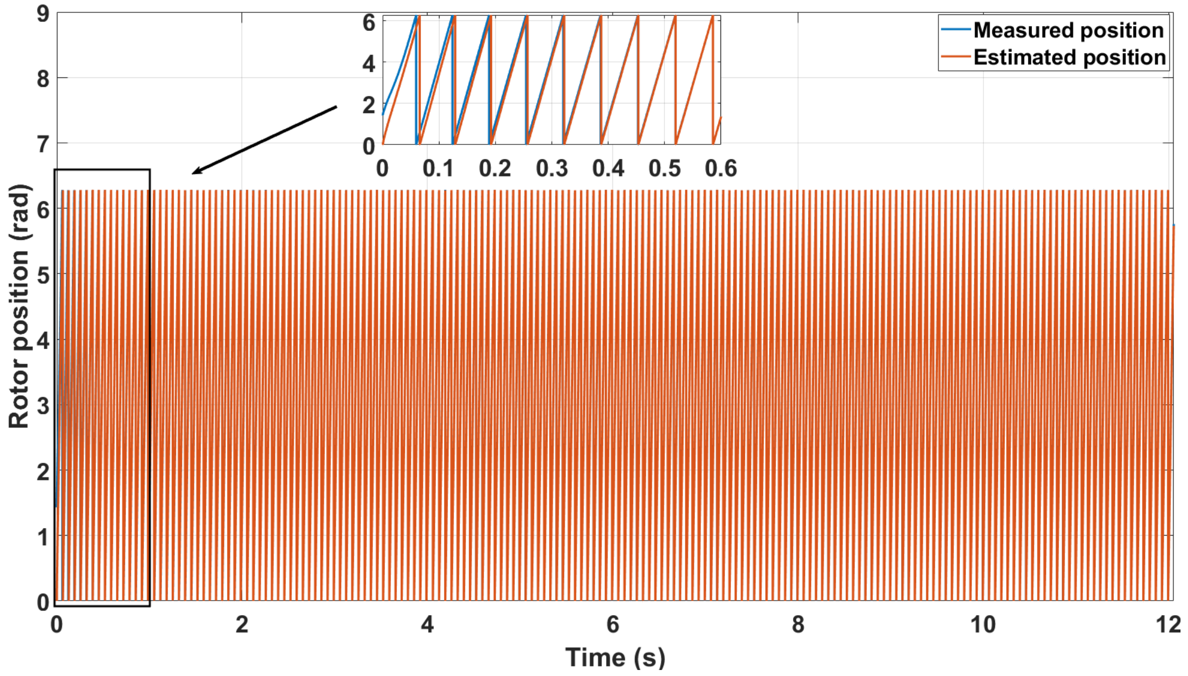
Measured position
Estimated position
Rotor position (rad)
Time (s)
0
1
2
3
4
5
6
7
8
9
0
2
4
6
8
10
12
0
0.1
0.2
0.3
0.4
0.5
0.6

(c)

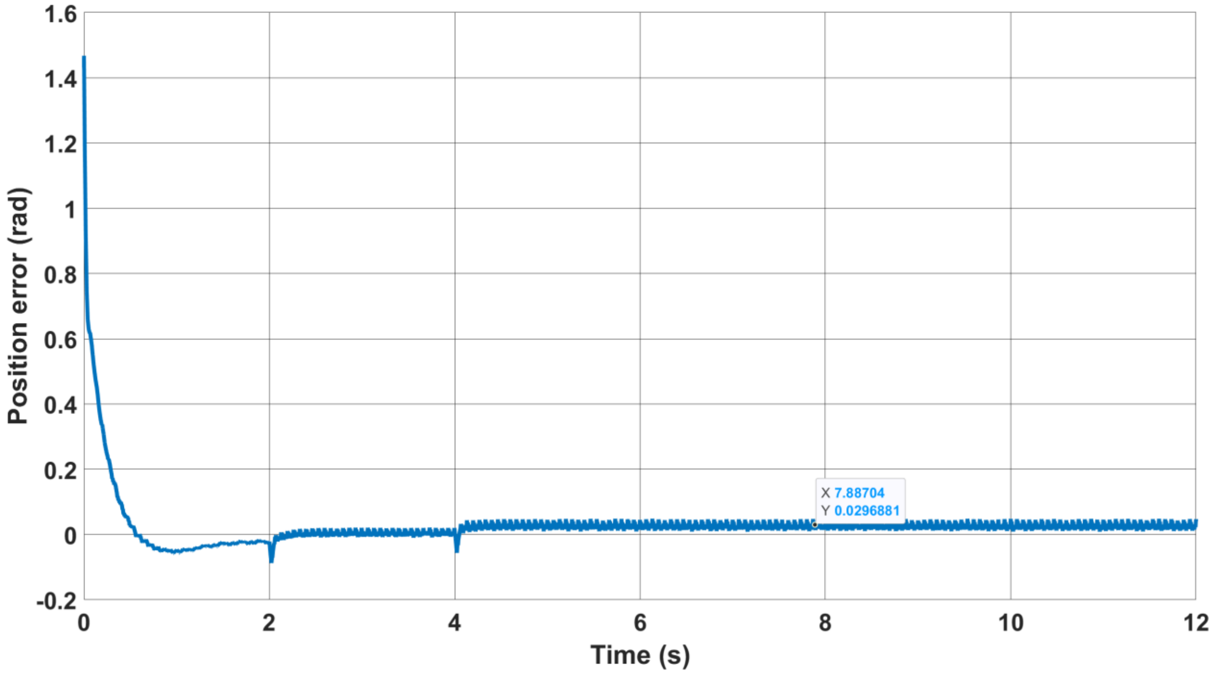
Position error (rad)
Time (s)
X 7.88704
Y 0.0296881
1.6
1.4
1.2
1
0.8
0.6
0.4
0.2
0
-0.2
0
2
4
6
8
10
12

(d)

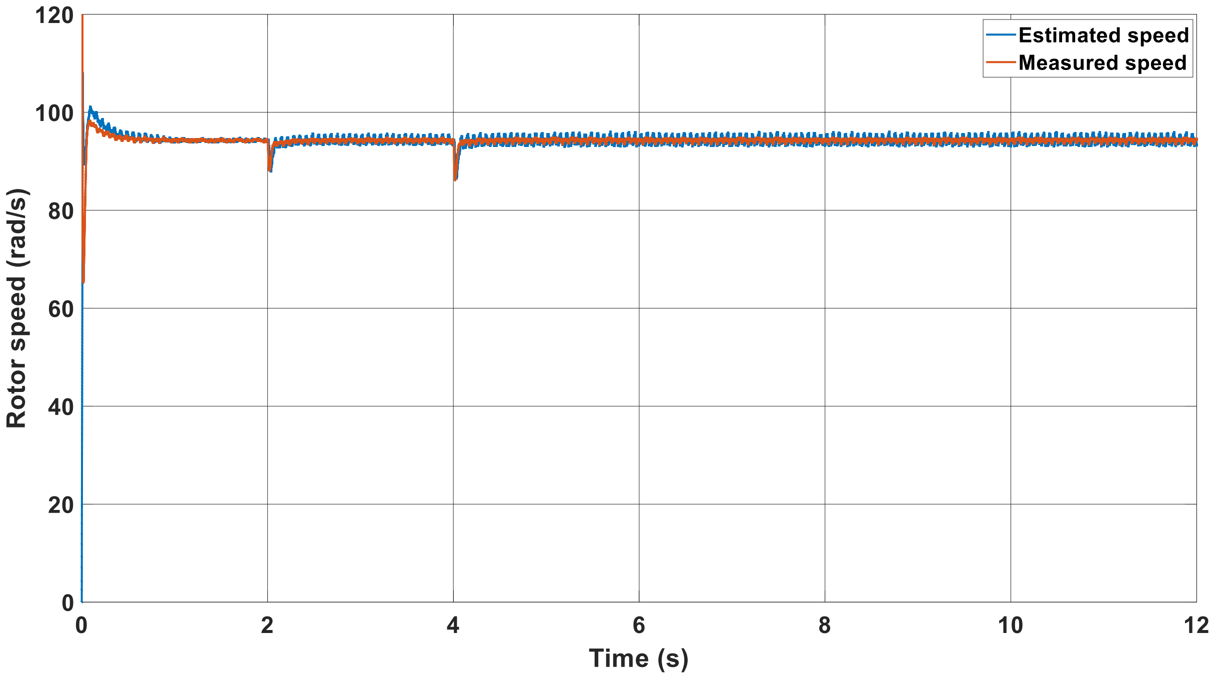

(e)

Figure 4.25 Sensorless response for torque mode, (a) phase currents, (b) measured and reference q-currents, (c) measured and estimated positions, (d) position error, (e) measured and estimated speeds.

4.4.2.2.2 Speed mode

In this mode, the FOC controller gets the speed and position signals from the estimator, and the second Drive Unit is set to torque mode. The performance of both estimators is evaluated under various load and speed conditions.

Figure 4.26 demonstrates the utilization of a rotating signal injection method for zero speed starting [74]. As back-EMF is unobservable at zero speed for both the conventional and proposed methods, this injection method is employed. The injection frequency and amplitude of the injected voltage are 40 volts and 800 Hz respectively. The figure shows the smooth operation of the drive during the gradual transition from 20 rad/s to 30 rad/s at 3 seconds. Additionally, the position error introduced by the injection method is reduced to zero once the proposed method is activated, as depicted in Figure 4.26(b).

In Figures 4.27 and 4.28, the performance of the novel and classical methods is tested at low speeds (1.6 Hz) with no load. It is evident from Figures 4.27(a) and 4.28(a) that the classical method exhibits higher speed oscillation compared to the novel method. Moreover, Figure 4.28(b) illustrates that as the speed decreases, the position error increases in the classical MRAS until it fails at a speed of 10 rad/s. However, the position accuracy remains nearly unaffected in the proposed method, as shown in Figure 4.27(b). This distinction is clearly observed in Figures 4.27(d) and 4.28(d), which depict the phase currents for both methods. Figure 4.27(d) demonstrates that the phase currents are not significantly impacted when switching from sensored mode to sensorless mode at 5 seconds using the novel method. Additionally, the current decreases as the speed decreases. Conversely, the classical method results in larger current transients due to the larger position error.

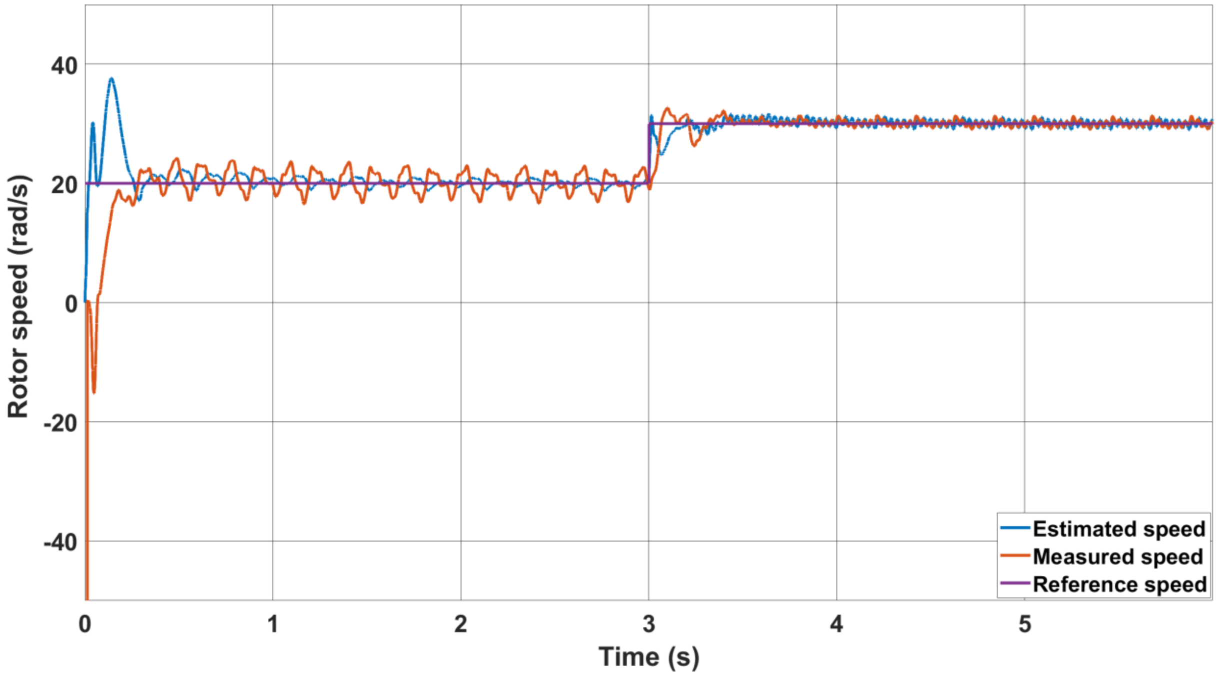

(a)

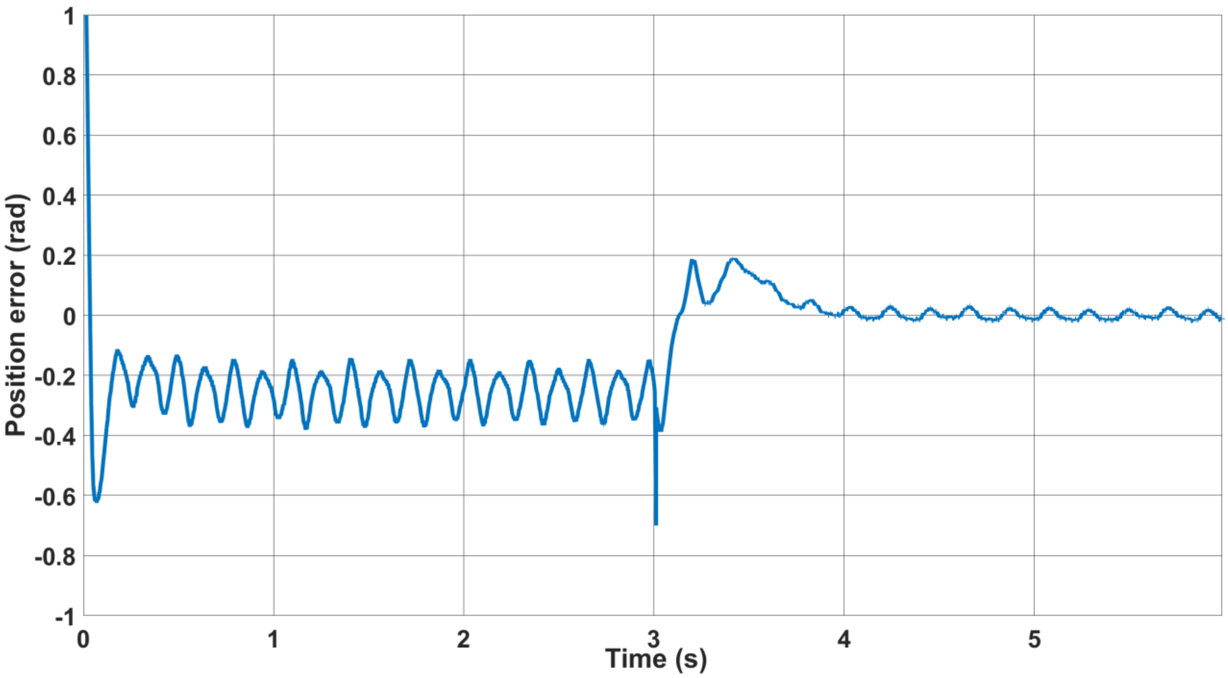
Position error (rad)
1
0.8
0.6
0.4
0.2
0
-0.2
-0.4
-0.6
-0.8
-1
0
1
2
3
4
5
Time (s)

(b)

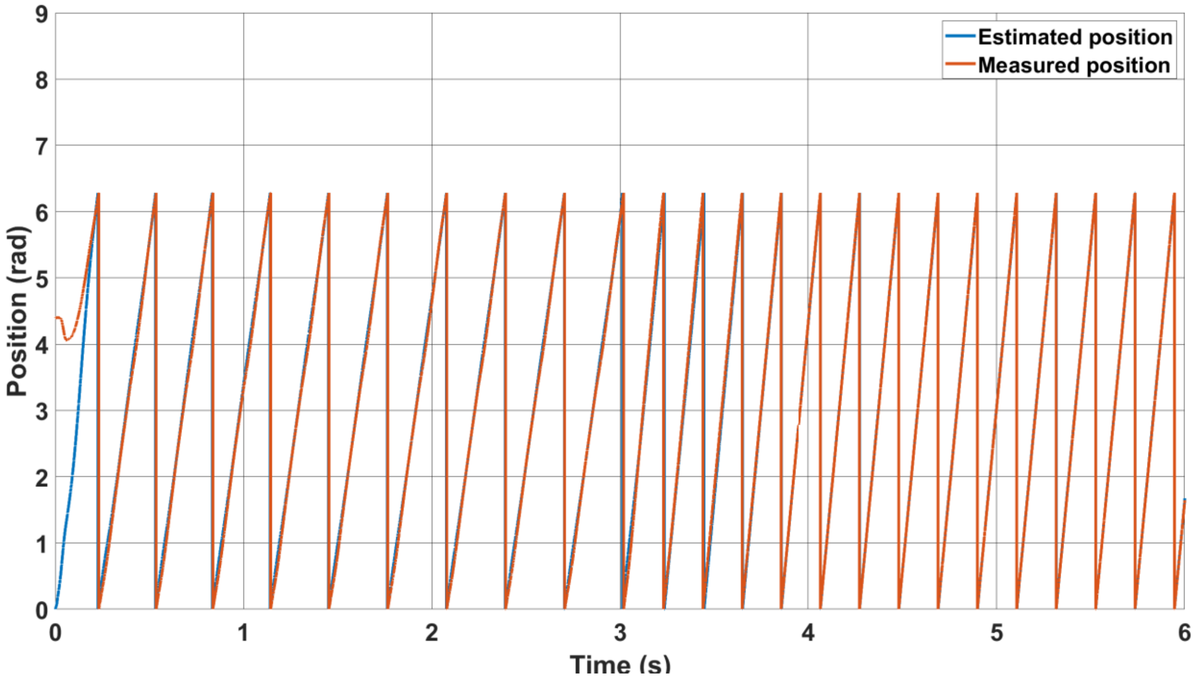
Estimated position
Measured position
Position (rad)
9
8
7
6
5
4
3
2
1
0
0
1
2
3
4
5
6
Time (s)

(c)

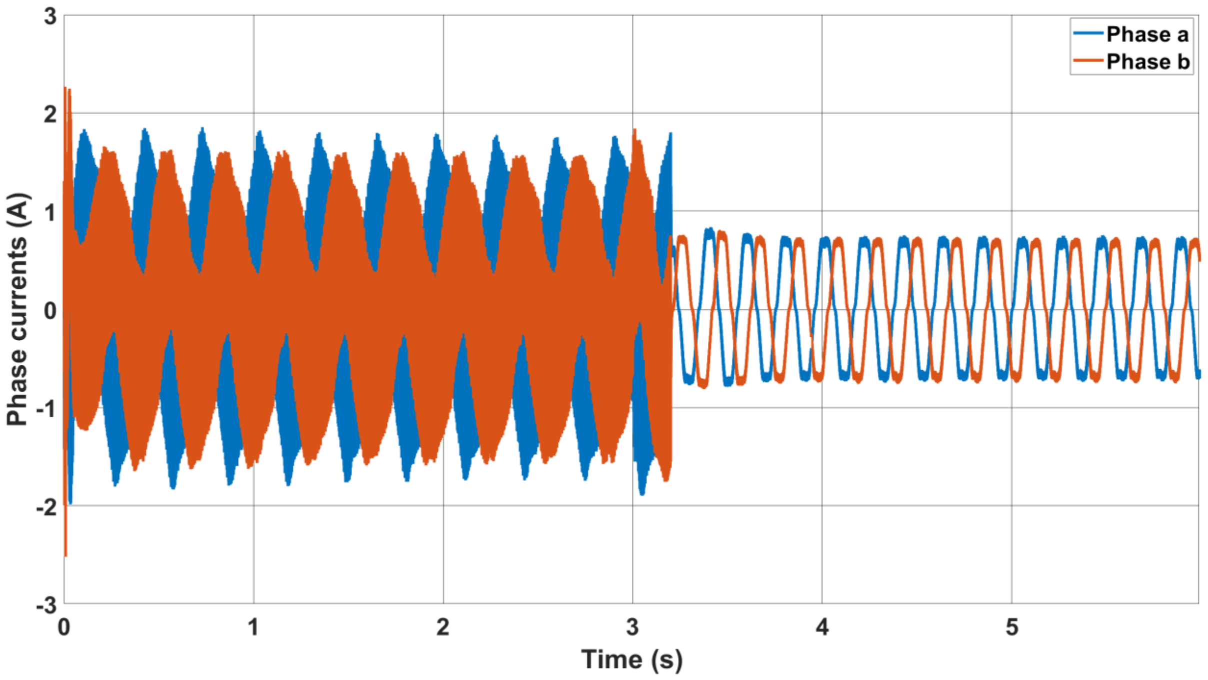

(d)

Figure 4.26 Signal injection method combined with the novel method, (a) Speed response, (b) Corresponding position error, (c) Novel estimated and measured positions, (d) Phase currents

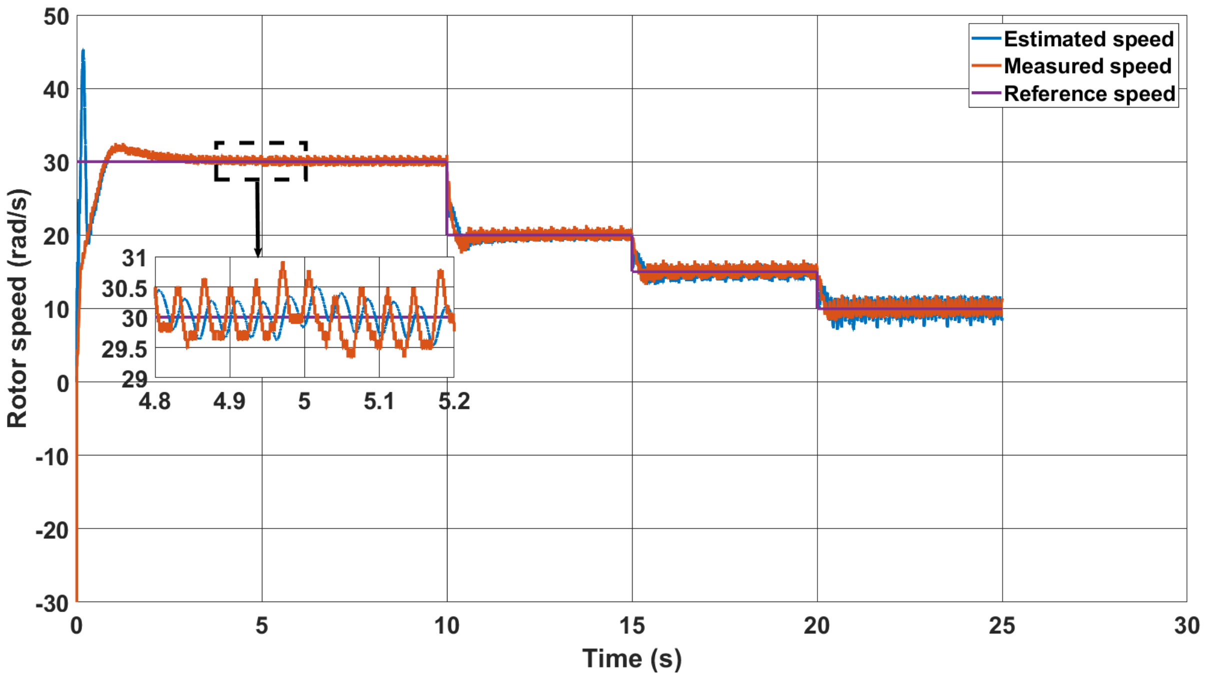

(a)

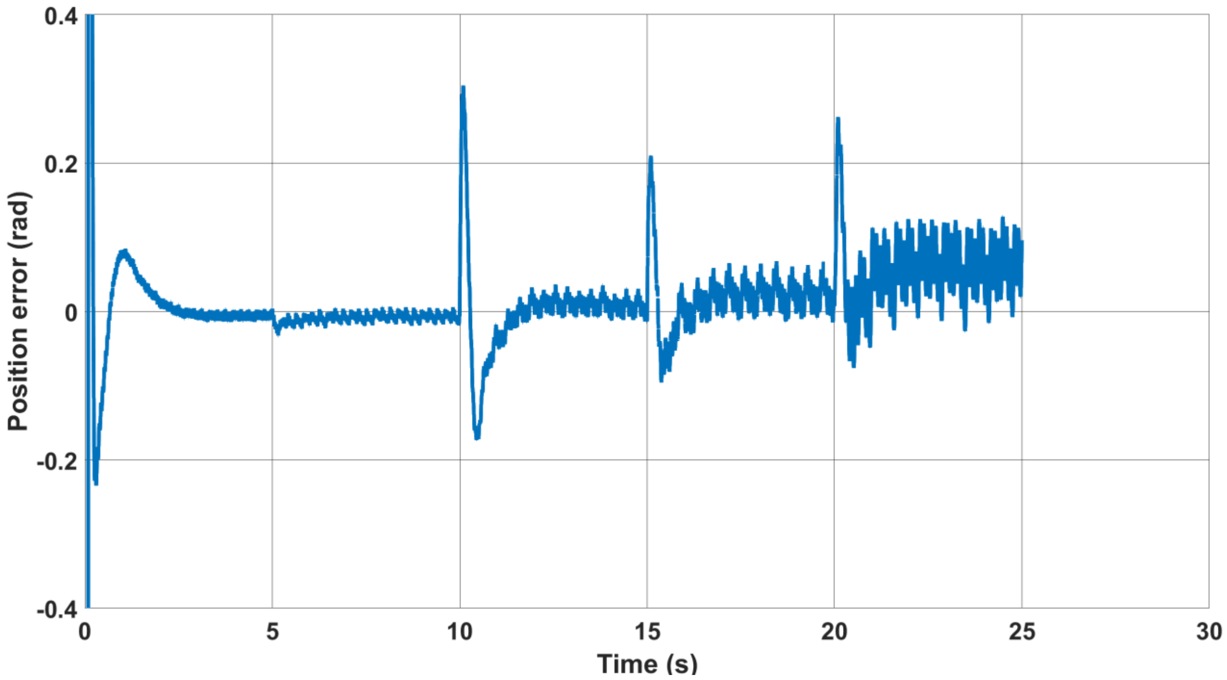

0.4
0.2
0
-0.2
-0.4
Position error (rad)
0
5
10
15
20
25
30
Time (s)

(b)

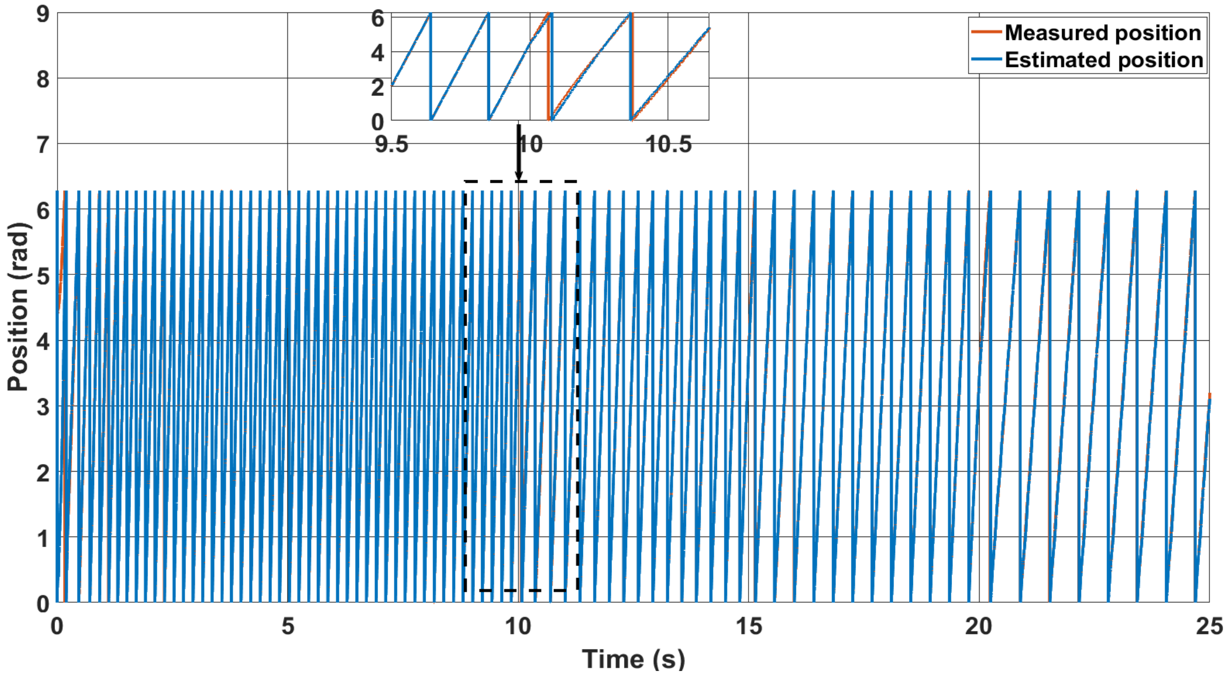

9
8
7
6
5
4
3
2
1
0
Position (rad)
0
5
10
15
20
25
Time (s)
Measured position
Estimated position
6
4
2
0
9.5
10
10.5

(c)

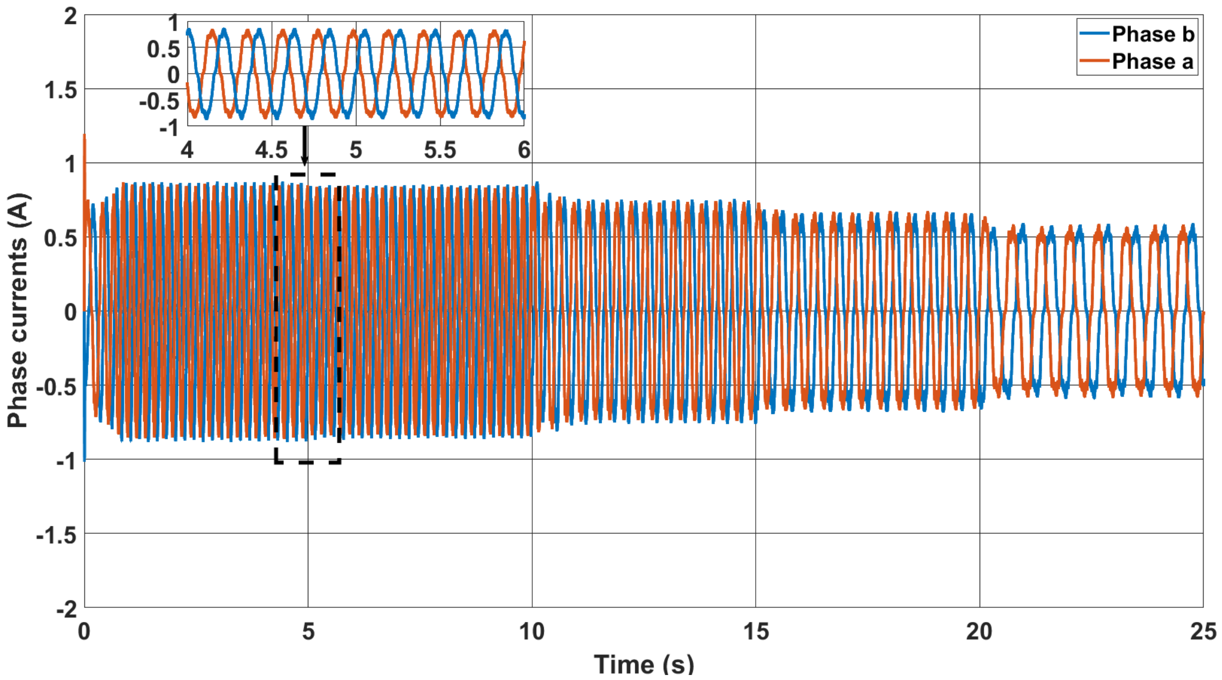

(d)

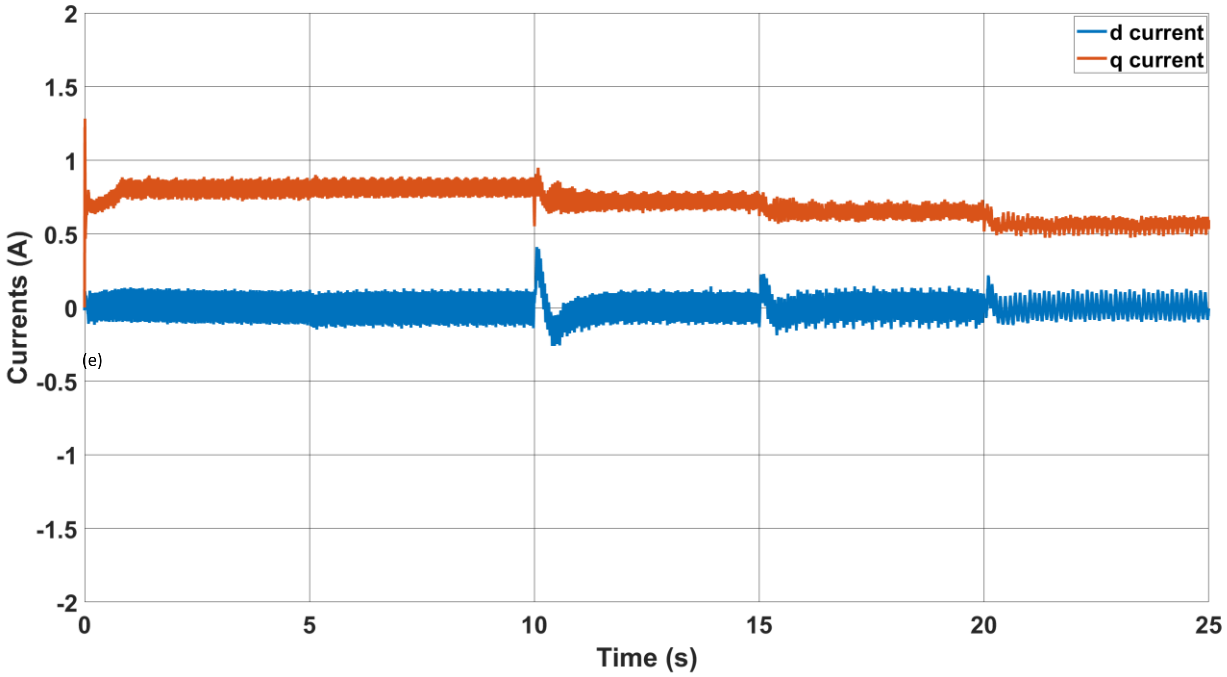

Figure 4.27 Novel method performance at low speeds, (a) Speed response, (b) Corresponding position error, (c) Estimated and measured positions, (d) Phase currents, (e) d-q currents

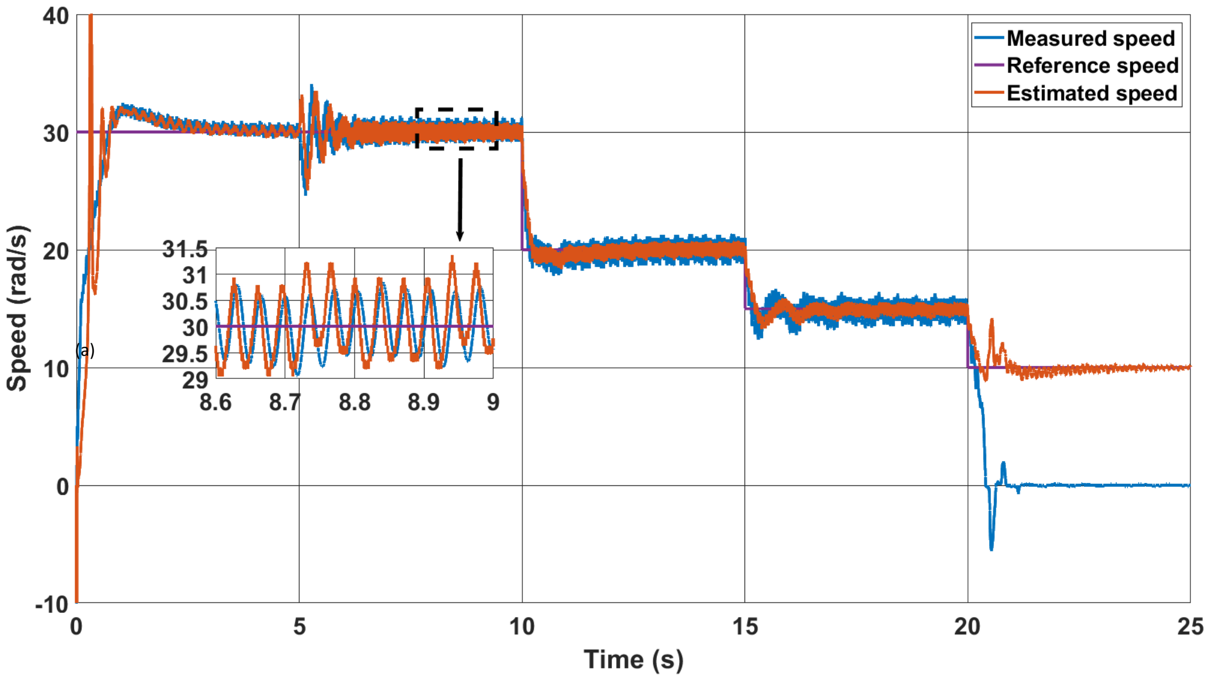
Measured speed
Reference speed
Estimated speed
Speed (rad/s)
Time (s)
40
30
20
10
0
-10
0
5
10
15
20
25
(a)
31.5
31
30.5
30
29.5
29
8.6
8.7
8.8
8.9
9

(a)

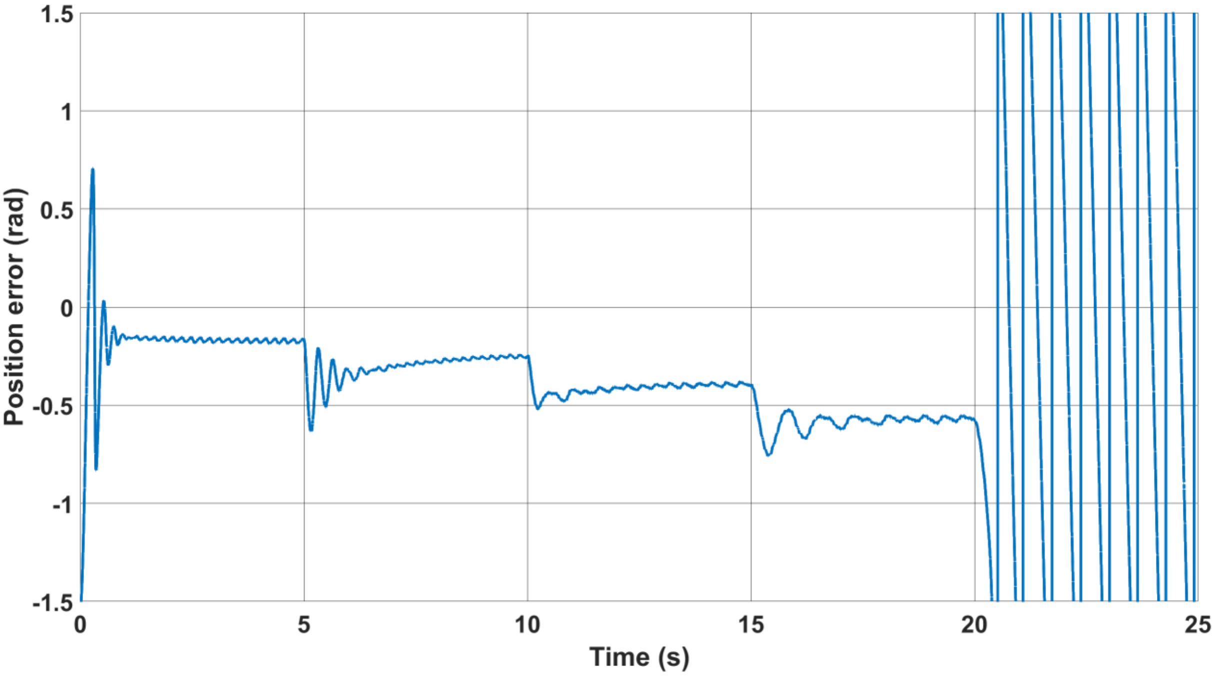
Position error (rad)
Time (s)
1.5
1
0.5
0
-0.5
-1
-1.5
0
5
10
15
20
25

(b)

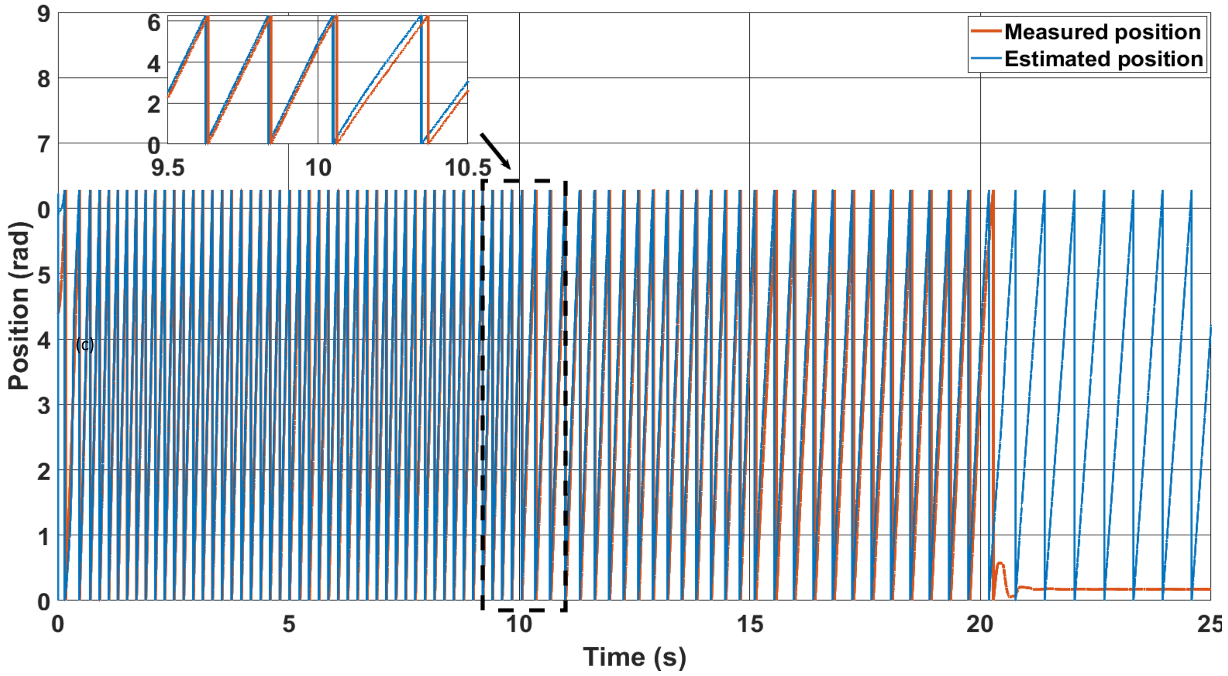
Measured position
Estimated position
Position (rad)
Time (s)
9
8
7
0
5
4
3
2
1
0
0
5
10
15
20
25
6
4
2
0
9.5
10
10.5
(c)

(c)

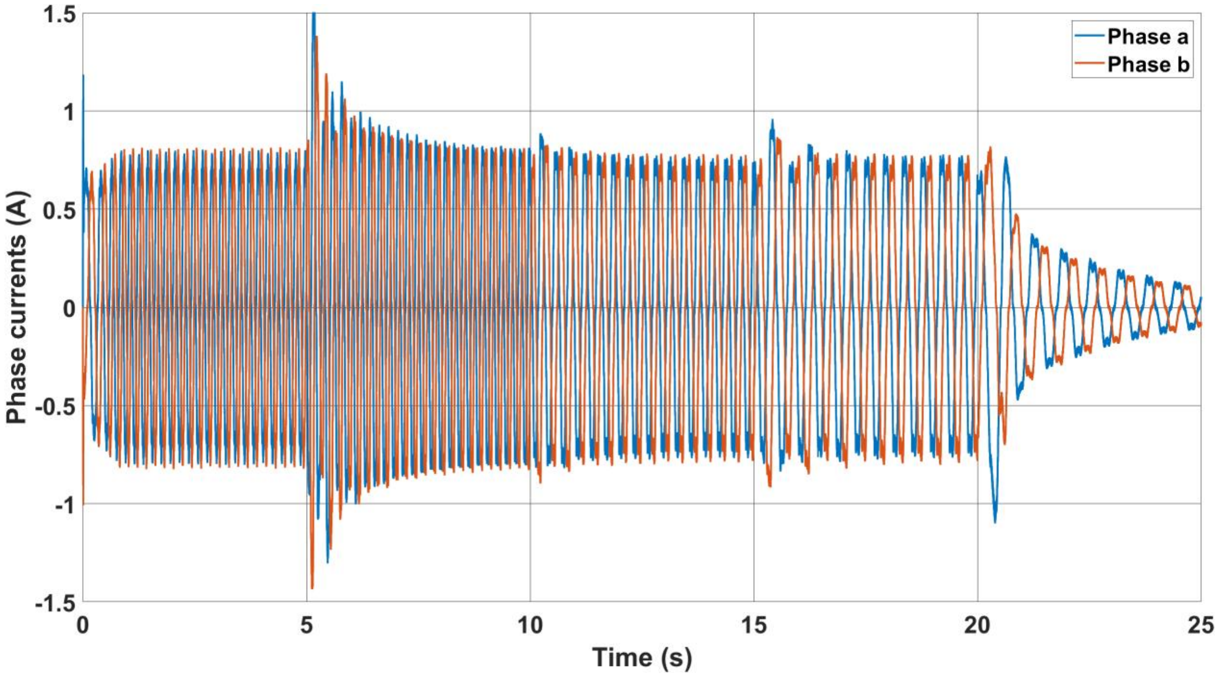
Phase a
Phase b
Phase currents (A)
Time (s)
1.5
1
0.5
0
-0.5
-1
-1.5
0
5
10
15
20
25

(d)

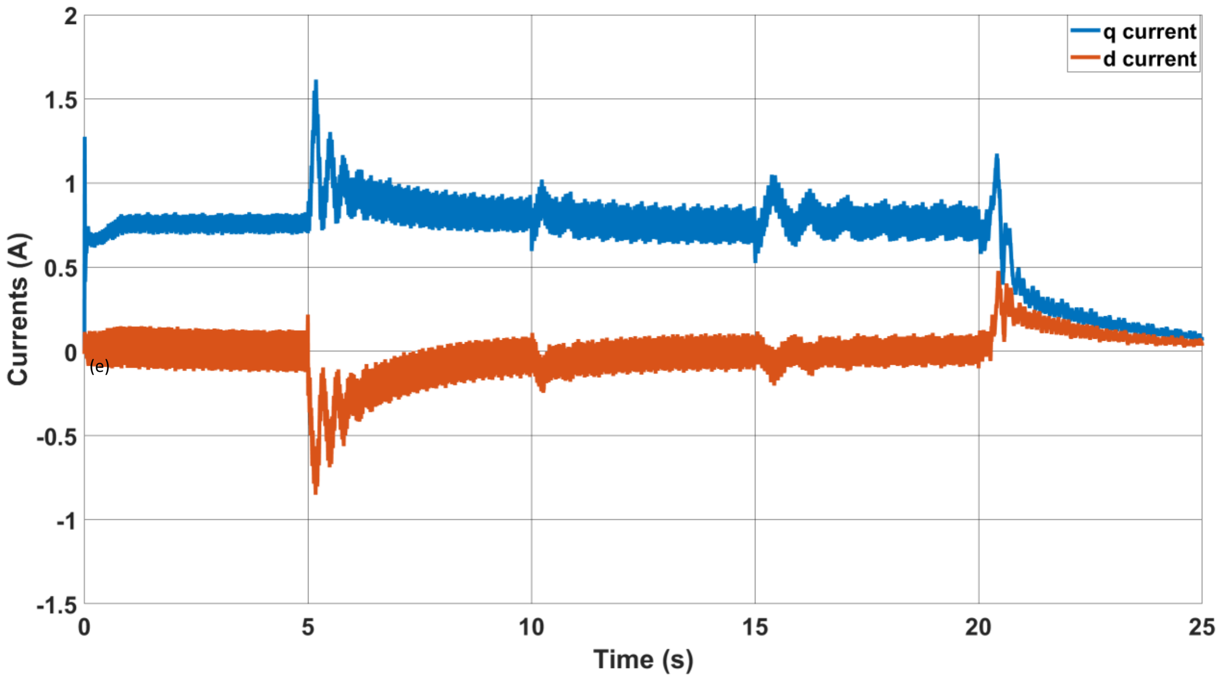

(e)

Figure 4.28 Classical method at low speeds, (a) Speed response, (b) Corresponding position error, (c) Estimated and measured positions, (d) Phase currents, (e) d-q currents

Figure 4.29 shows the performance of the two techniques at medium speeds with no load applied. They transition from open-loop mode to sensorless mode at 5 seconds. Figure 4.29(a) reveals that the estimated speed of the novel method exhibits more damping compared to the classical method.

Both methods are then tested in motoring and regenerative modes, as depicted in Figures 4.30 and 4.31, respectively. In both modes, the torque is initially set to 20% of the rated torque and then increased to 40% of the rated torque. The applied torque induces a slight oscillation in the estimated speed for both methods. Figure 4.30(b) illustrates that the position error in the novel method increases from -0.034 rad at no load to -0.053 rad at 20% of the rated load, further increasing to -0.072 rad at 40% of the rated torque. Similarly, in the regenerative mode, the error generated by the novel method ranges from -0.021 rad at no load to 0.032 rad at 20% of the rated torque, and finally to 0.079 rad at 40% of the rated torque, as shown in Figure 4.31(b). It can be observed that in the regenerative mode, the error in both methods increases with torque, while in the motoring mode, the error decreases.

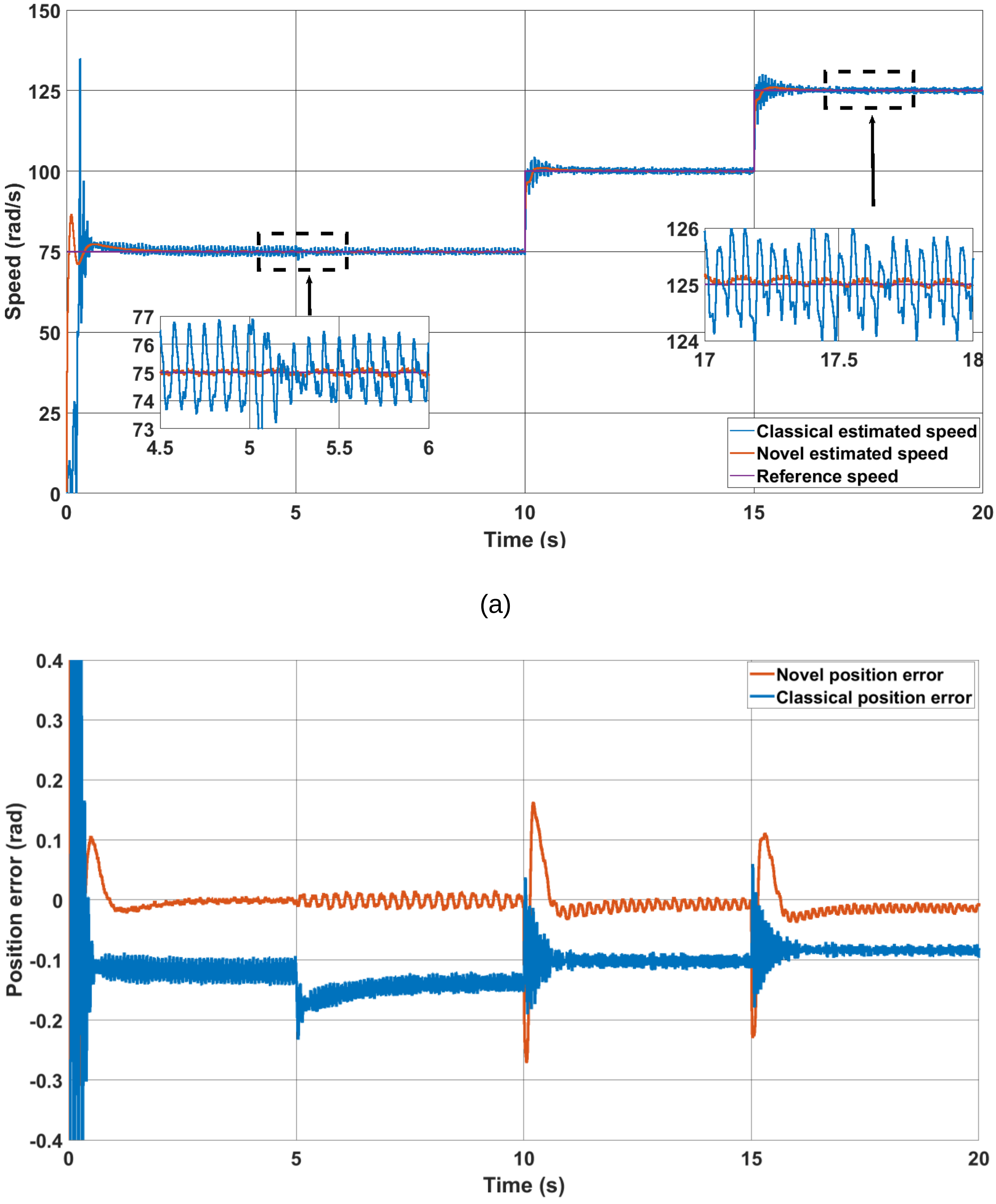

(a)

(b)

Figure 4.29 Medium speed response for both methods, (a) Estimated speed (b) position error.

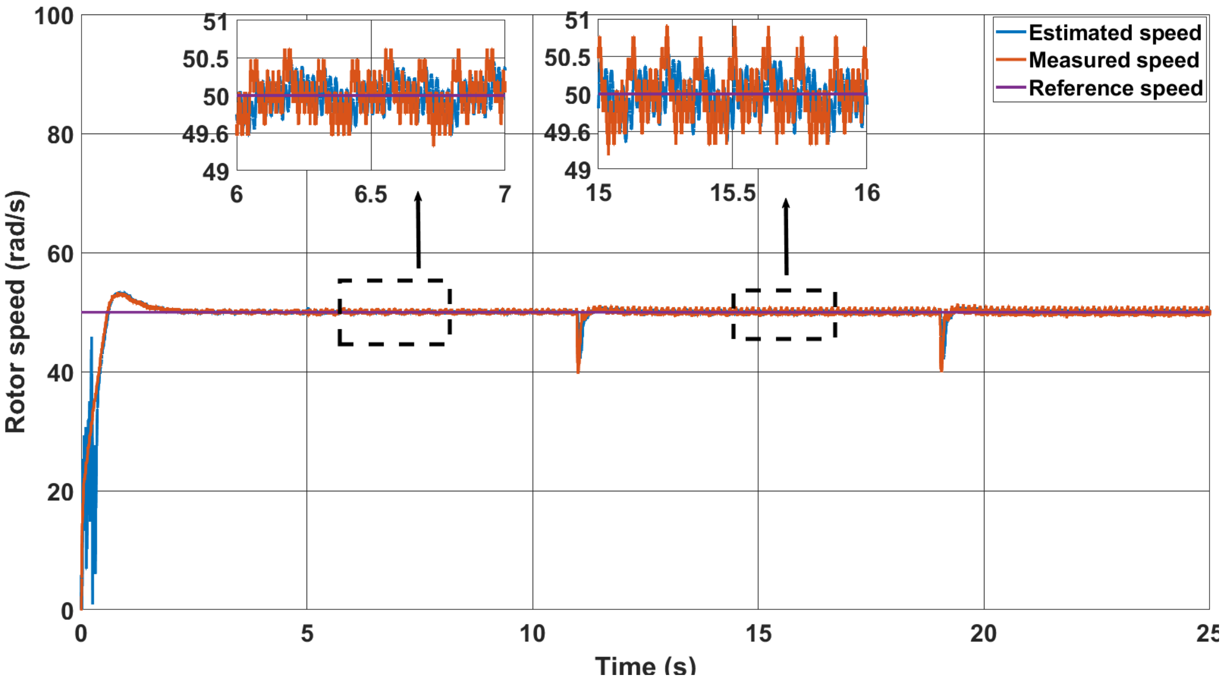
Rotor speed (rad/s)
Time (s)
100
80
60
40
20
0
0
5
10
15
20
25
51
50.5
50
49.6
49
6
6.5
7
51
50.5
50
49.6
49
15
15.5
16
Estimated speed
Measured speed
Reference speed

(a)

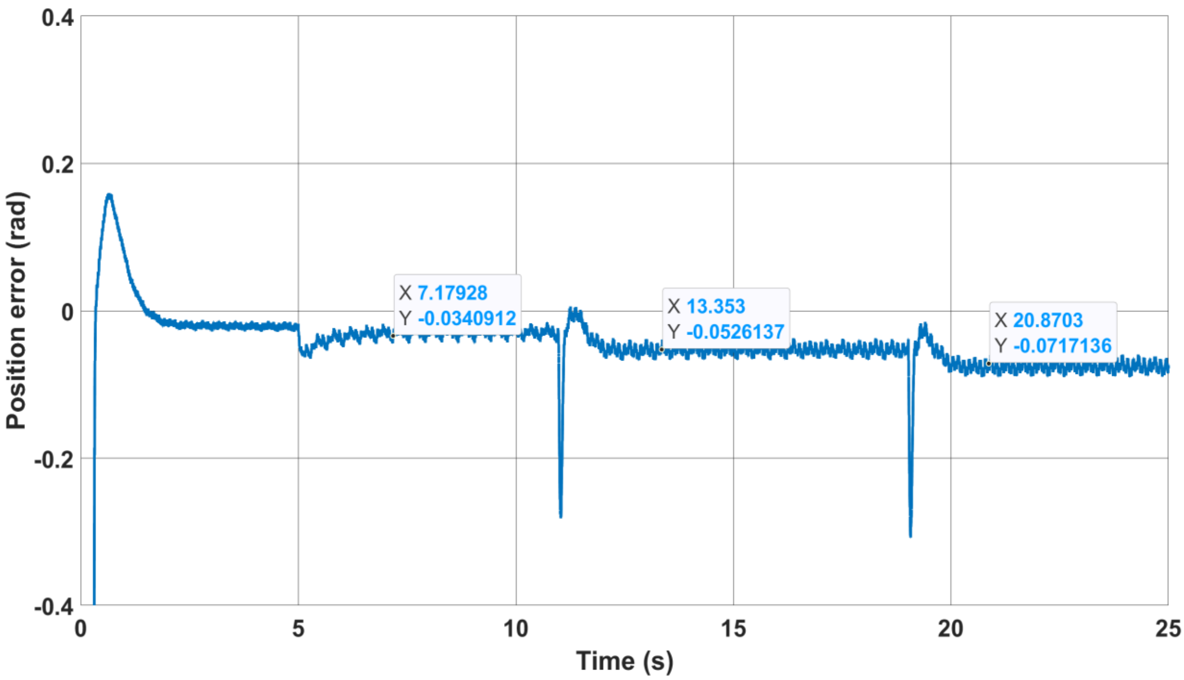
Position error (rad)
Time (s)
0.4
0.2
0
-0.2
-0.4
0
5
10
15
20
25
X 7.17928
Y -0.0340912
X 13.353
Y -0.0526137
X 20.8703
Y -0.0717136

(b)

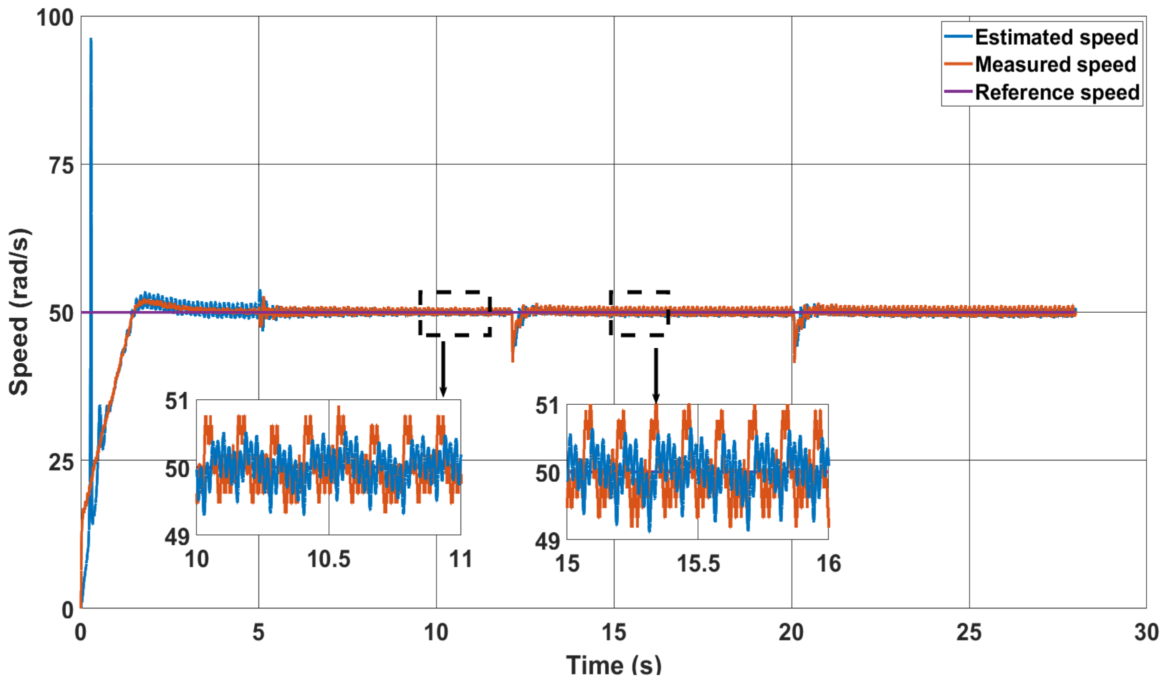

(c)

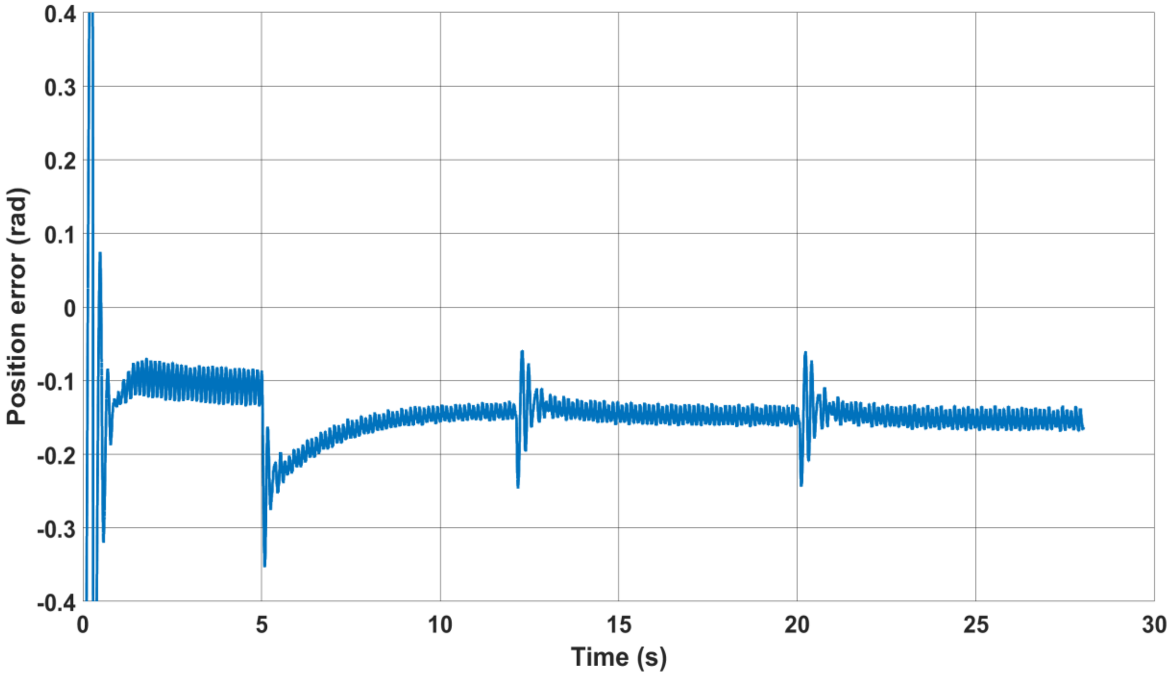

(d)

Figure 4.30 Sensorless operation with motoring mode, (a) Speed response for the novel, (b) Corresponding position error for the novel, (c) Speed response for the classical MRAS, (d) Corresponding position error for the classical MRAS.

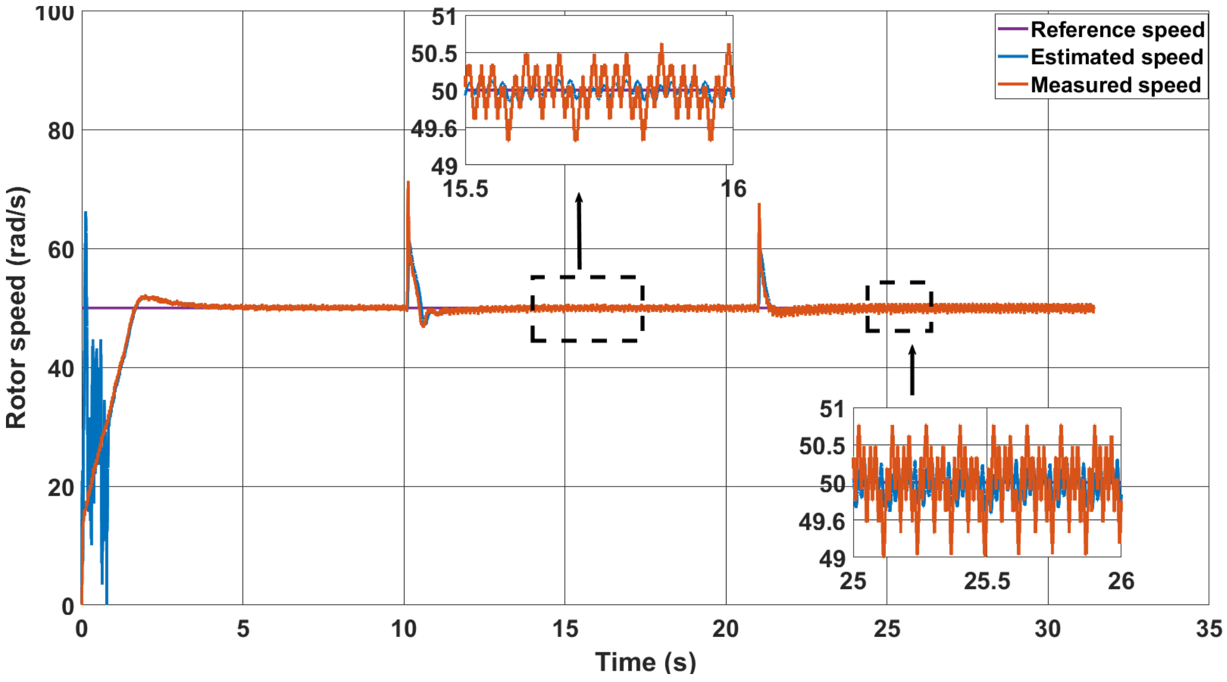
Reference speed
Estimated speed
Measured speed
Rotor speed (rad/s)
Time (s)
0
20
40
60
80
100
0
5
10
15
20
25
30
35
51
50.5
50
49.6
49
15.5
16
51
50.5
50
49.6
49
25
25.5
26

(a)

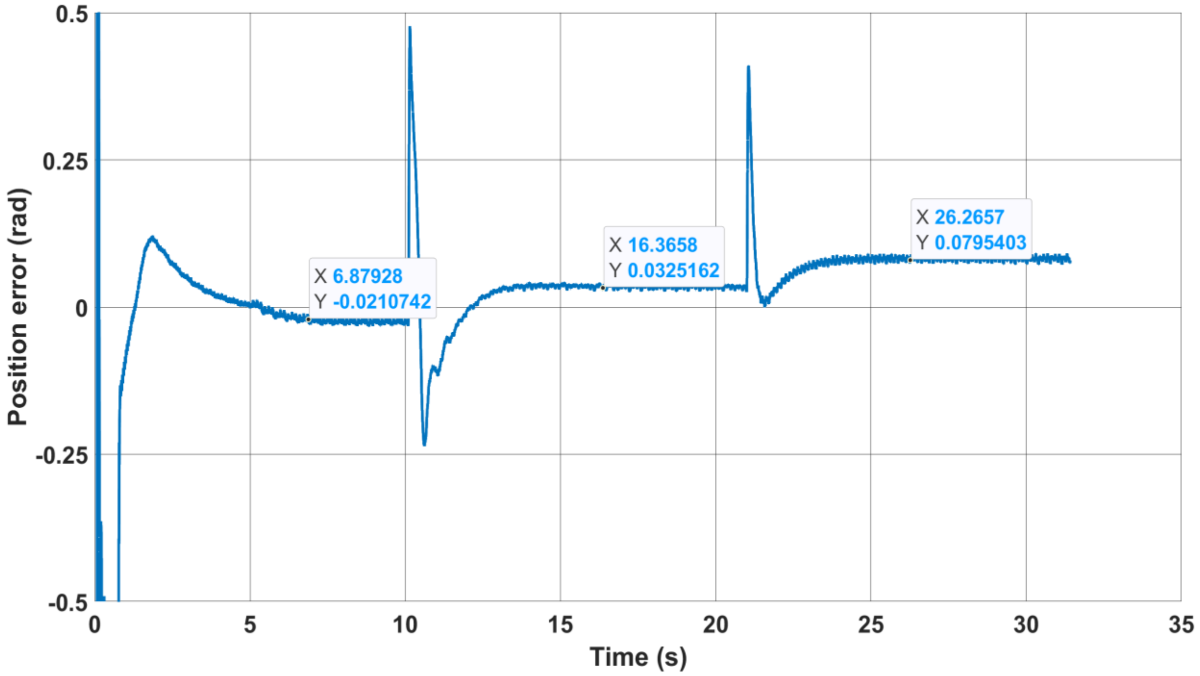
Position error (rad)
Time (s)
0.5
0.25
0
-0.25
-0.5
0
5
10
15
20
25
30
35
X 6.87928
Y -0.0210742
X 16.3658
Y 0.0325162
X 26.2657
Y 0.0795403

(b)

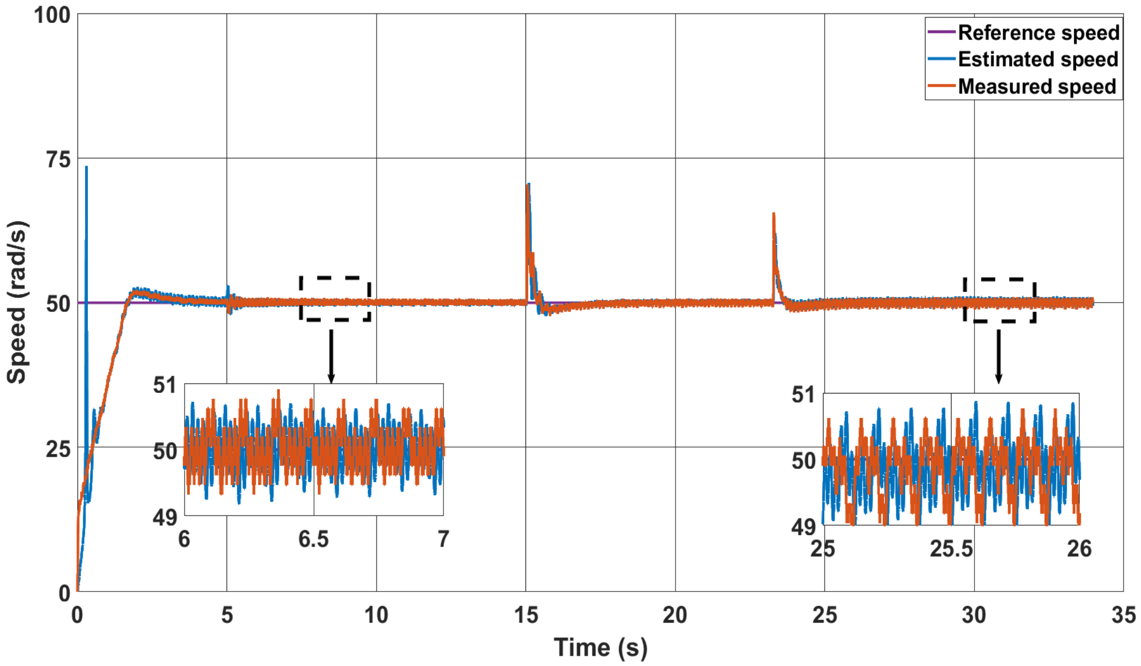

(c)

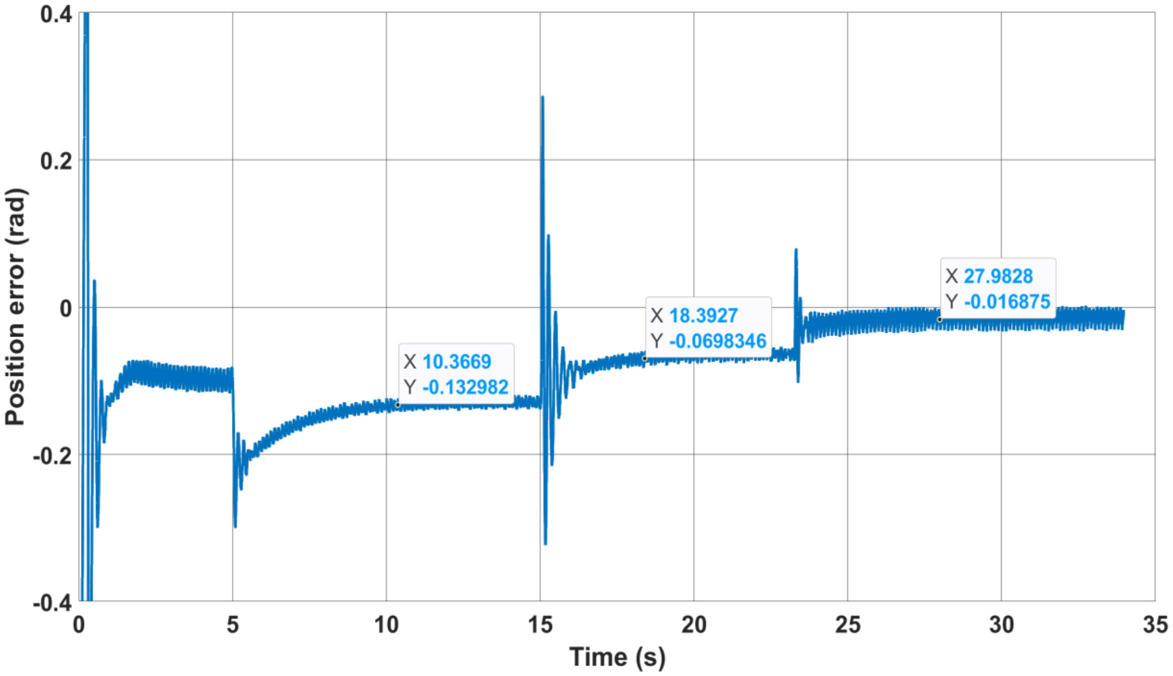

(d)

Figure 4.31 Sensorless operation with regenerative mode, (a) Speed response for the novel, (b) Corresponding position error for the novel, (c) Speed response for the classical MRAS, (d) Corresponding position error for the classical MRAS

To assess the robustness of the proposed scheme against variations in motor parameters and to compare it with the classical method, two experimental tests were conducted. In the first test (Figure 4.32), the sensorless mode was initiated at 2 seconds, followed by a 50% change in the stator resistance in the estimator models at 5 seconds, which was further increased to 100% at 8 seconds.

In the second test (Figure 4.33), the q-inductance in the estimator models was reduced by 20% at 5 seconds, and then to 40% at 8 seconds. It is evident that the novel method demonstrates robustness against motor parameter variations. This can be observed by comparing the estimated speed and position error produced by the novel method before and after the changes, as shown in Figure 4.32 and Figure 4.33. Both the error and speed oscillations remain unaffected. On the other hand, the classical method exhibits increased speed oscillation as the resistance increases, although it is less sensitive to changes in Lq.

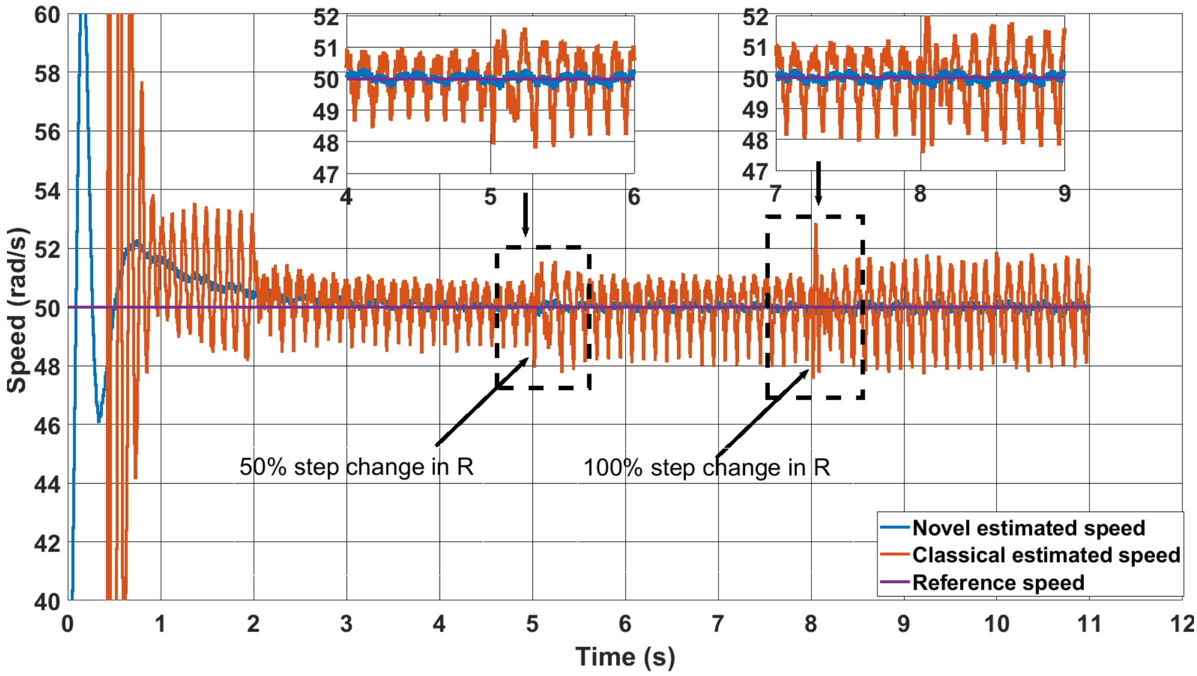

(a)

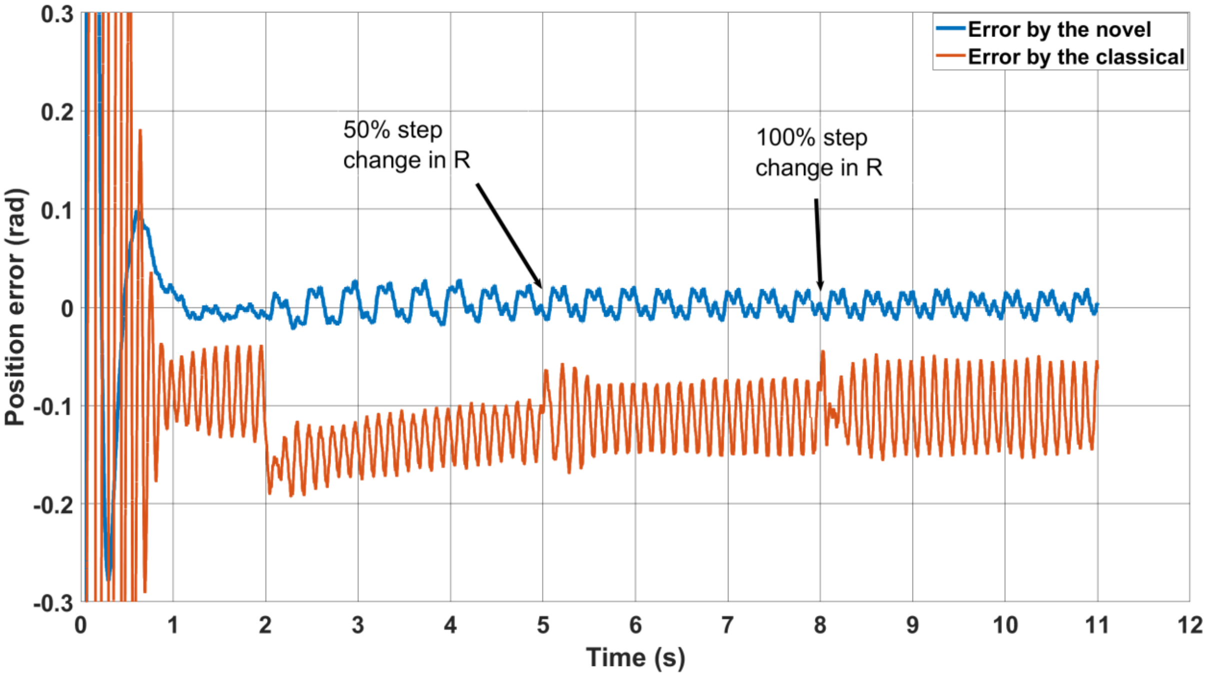

(b)

Figure 4.32 Effect of stator resistance change on both methods, (a) estimated speed response, (b) Corresponding position error.

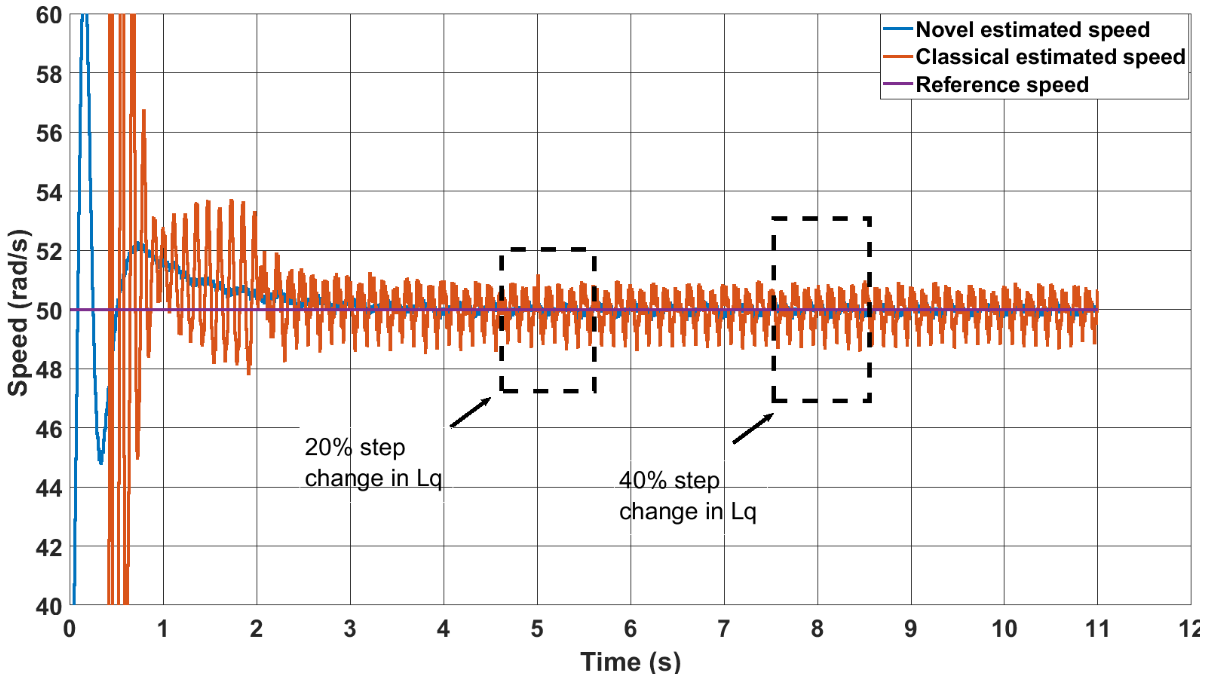

(a)

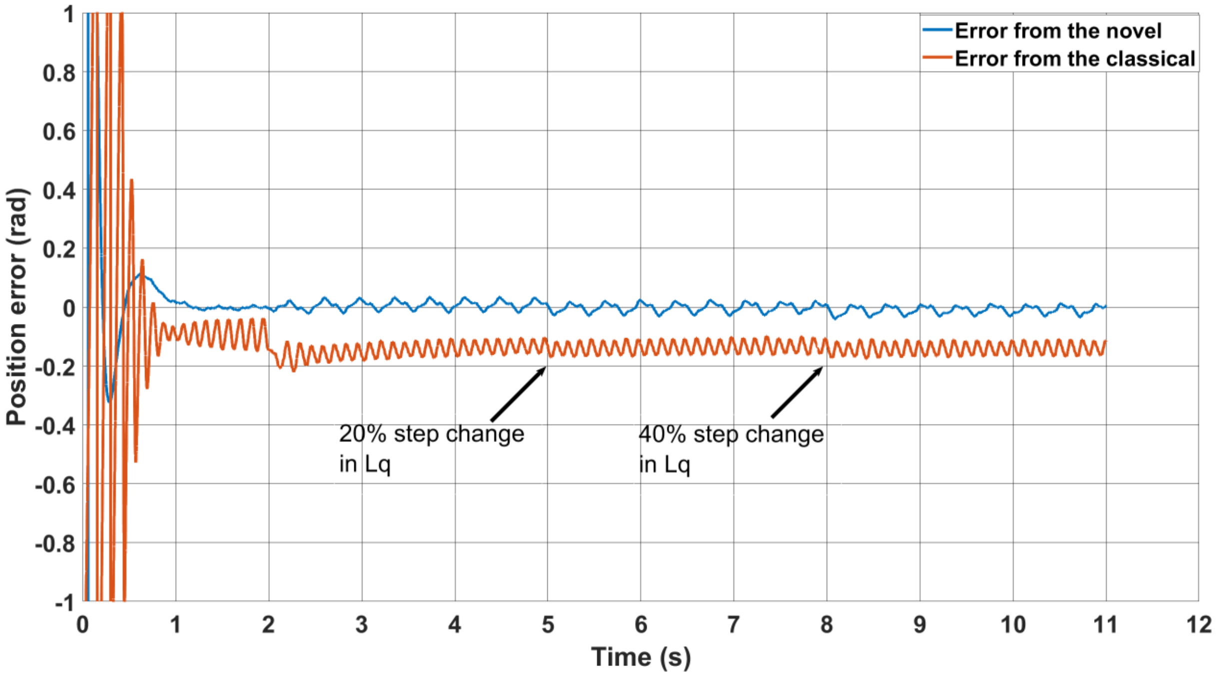

(b)

Figure 4.33 Effect of q-inductance change on both methods, (a) Estimated speed response, (b) Corresponding position error.

The position error for the novel method is also tested for $i_d \neq 0$ to investigate the effect of cancelling the terms $L_d d\hat{\imath}_d/dt$ and $R\hat{\imath}_d$ in (4.24) on the accuracy. Fig. 4.34 shows the error resulting from setting the d axis current reference to nonzero values. In this test, the d current is set to -0.5A and -1A at 7s and 10s respectively, and it is evident that the error is not substantially influenced when compared to the compensated error as shown in Fig. 4.34.

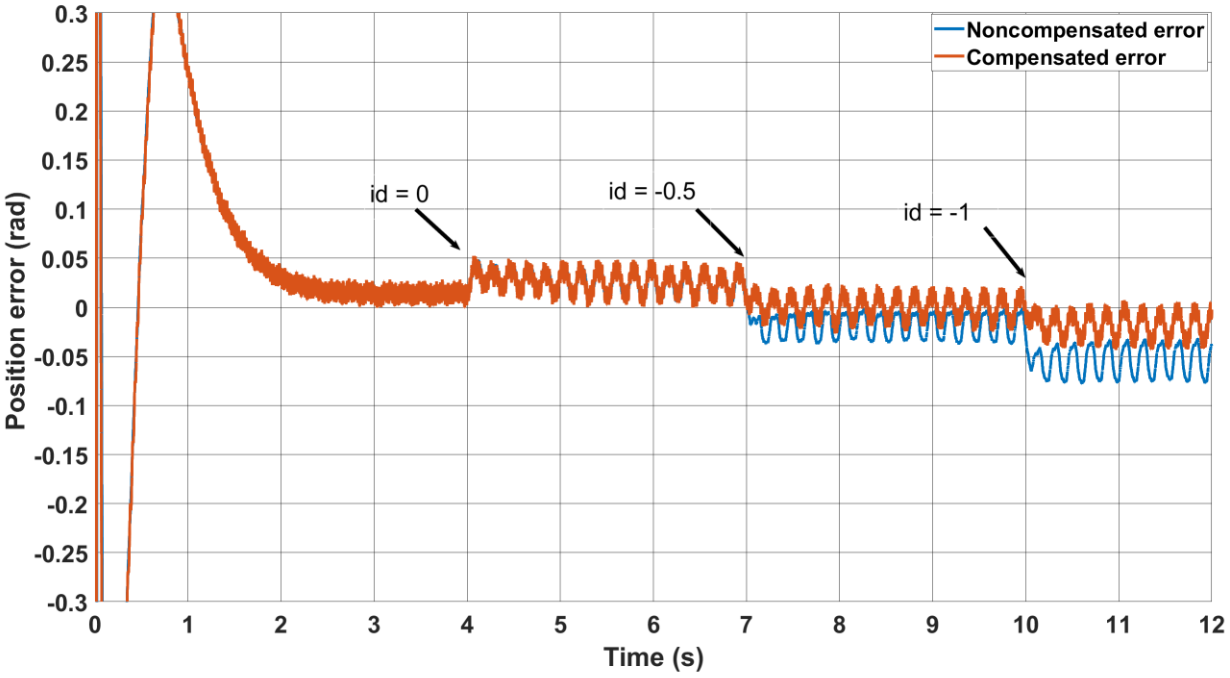

Figure 4.34 Effect of nonzero d-Axis Current on the estimated position accuracy for the novel method.

4.5 Conclusion

In this chapter, an innovative flux-based MRAS observer is introduced for sensorless PMSM drives. This method is based on oversampling and averaging over a switching period of the standards space-vector pulse-width modulation (SV-PWM) which allows the calculation of the rotor flux without integration. simulations , and experimental tests are presented to evaluate the performance of the proposed estimator. The results show good performance at various speeds and under various load circumstances. The performance at low speed is improved compared to the classical method. The proposed method also shows robustness to changes in motor parameters.

Chapter 5: Model Predictive MRAS Speed Estimator for Permanent Magnet Synchronous Machines

As mentioned in the previous chapters, the fixed Proportional-Integral (PI) controller is commonly used in MRAS schemes for speed estimation due to its simple design and good performance across a wide speed range. However, the fixed PI controller is unable to maintain optimal performance under all operating conditions. At low speeds, when variations in machine parameters and inverter nonlinearities become more noticeable, the PI gains need to be tuned to small values to prevent significant increases in speed oscillation. On the other hand, during transient operation conditions with sudden changes in load or speed, the PI gains need to be increased for smooth and satisfactory system operation. This necessitates the use of an adaptive PI controller, which poses a challenge and consumes a significant amount of time.

In this chapter, a novel (FCS-MPC) based speed estimator for PMSM is proposed. In this method, the adaptation process involves solving an optimization problem aimed at minimizing the speed error signal across a finite range of speeds. A speed search process is employed to guarantee optimal speed estimation at each sampling interval. The performance of the novel estimator is assessed, and a comparison is made with the PI-based flux MRAS estimator.

5.1 Finite Control Set Model Predictive Controller

Due to its user-friendly nature and capability to accommodate various performance specifications, Finite-Control-Structure Model Predictive Control (FCS-MPC) has found widespread application. FCS-MPC employs the system model to predict future states, considering all possible control actions. A cost function is then minimized to determine the optimal control action. To address the computational challenges associated with MPCs, the controller directly generates the switching state of the inverter to solve the optimization problem. This approach limits the system behaviour prediction to the switching states of the power converter [75].

Figure 5.1 depicts the General Control Scheme of (FCS-MPC) applied to motor control. In this scheme, the measured variables $x(k)$ (such as rotor speed, current, or voltage) are utilized to predict all possible variables $x_i(k+1)$ at the next sampling period for each of the n switching states $S(k)$. The reference values 〖$x^*{}_i(k+1)$ and constraints are considered, and a cost function is evaluated for each of the potential inputs (switching states). The cost function is usually based on the difference between the predicted state variables and the desired references. The switching state that corresponds to the minimum cost function is selected and applied to the inverter.

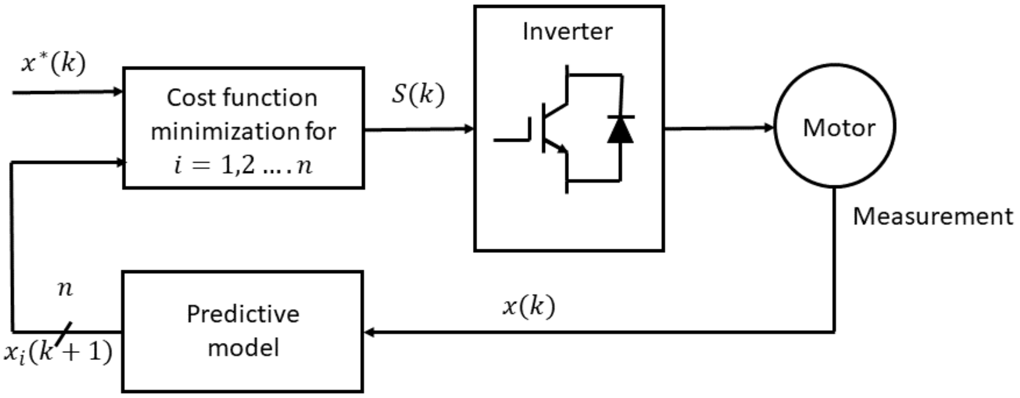

Figure 5.1 Block diagram of FCS-MPC

5.2 The Novel Model Predictive MRAS Estimator

This estimator is based on FCS-MPC concept to design the adaptation mechanism. The flowchart of the proposed algorithm is illustrated in Figure 5.2, while the block diagram of the predictive estimator is depicted in Figure 5.3. As discussed in the previous chapters and illustrated in Fig. 3.5, the traditional MRAS minimises the rotor flux error by utilising a PI controller whose output is the estimated speed $\widehat{\omega}$. Similarly, in the proposed FCS-MPC-MRAS method, the estimated speed is instead the output of a minimisation problem which consists of minimising a cost function, by selecting the estimated speed $\widehat{\omega}$ from a finite set of options which is iteratively narrowed down, until convergence is reached.

Since the rotor speed is a continuous signal, it is necessary to discretize it into a finite number of potential speeds to evaluate the cost function in a discrete number of steps as required by the finite control set MPC methodology. An algorithm is employed to discretize the rotor speed and calculate the cost function for each of these discrete speeds. The algorithm initiates by calculating the initial cost function at the starting speed ($w_{b,0} = 0\, rad/s$). The speed discretization process commences from this initial speed and progresses by displacing it with a calculated displacement (Δw_i) using the following formula:

$$\Delta w_i = 200 \cdot 2^{-i} \tag{5.1}$$

Where i represents the iteration order, and 200 is chosen because the rated speed of the tested machine is approximately 800 rad/s in electrical.

In each iteration, the adjustment of the base speed (w_b) is carried out to acquire nine discrete rotor speeds. This process is carried out as follows:

$$w_{i,j} = w_b + \Delta w_i . (j - 4) \tag{5.2}$$

Here, j represents the order of displacement, ranging from 0 to 8.

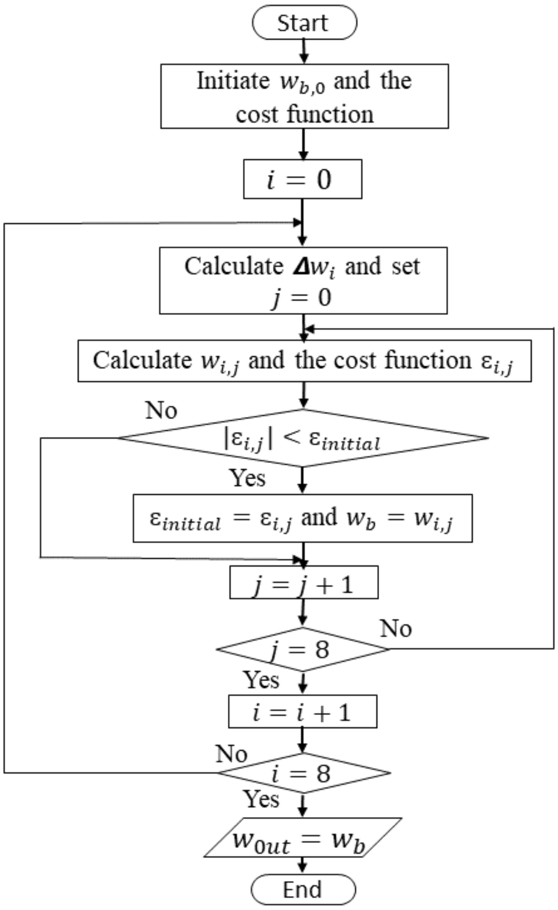

Figure 5.2 Flowchart of the proposed rotor speed search algorithm.

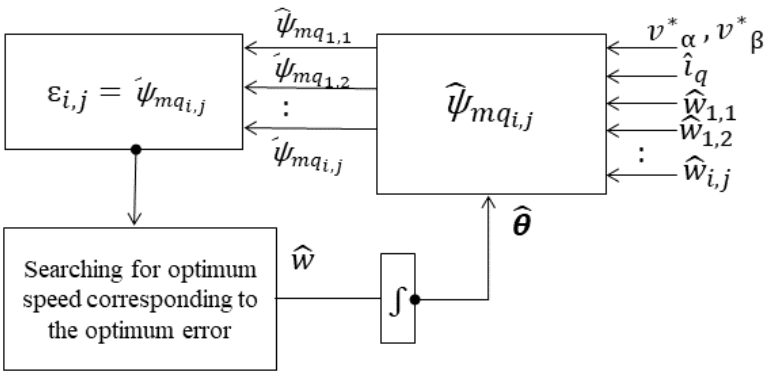

Figure 5.3 Block diagram of the proposed predictive estimator.

In the initial iteration ($i = 0$), a displacement value of 200 rad/s, denoted as Δw_0, is obtained. By applying equation (5.2), nine discrete speeds in electrical rad/s are generated: 800, 600, 400, 200, 0, -200, -400, -600, and -800. Each of these discrete speeds is utilized to calculate the fluxes on the estimated q-axis, denoted as $\hat{\psi}_{m_{qi,j}}$, as described in equation (4.24) for each individual speed. Subsequently, the cost function $\epsilon_{i,j}$ defined in equation (5.3) is computed for each speed. The speed that corresponds to the minimum error among the nine speeds is selected as the base speed for the next iteration.

$$\epsilon_{i,j} = \psi_m \cdot \hat{\psi}_{m_{qi,j}} \tag{5.3}$$

For ($i = 1$), the speed displacement is reduced to Δw_i = 235 $\cdot\ 2^{-1} = 100$, effectively doubling the search accuracy. The search process recommences from the new base speed, ($w_{b,1}$), to identify the speed that yields the minimum error in the second iteration. With each iteration, the search algorithm progressively converges towards the optimal speed. By the conclusion of the eighth iteration (Δw_8 = 0.78), the optimal speed can be determined with a precision of 0.78. Finally, the estimated position is calculated by integrating the estimated speed.

Due to the relatively slow mechanical dynamic, the rotor speed undergoes minimal changes between consecutive time samples, therefore the search algorithm can be initialized using the output speed from the previous sampling instant (previous output speed) instead of starting from zero speed. This adjustment does not compromise the accuracy of the estimation and significantly reduces the execution time.

In contrast to PI-based MRAS methods, the proposed method eliminates the need for gain tuning, making it simpler and ensuring optimal performance under various operating conditions. The iterative search algorithm consistently drives the cost function to its minimum within a single sample time.

5.3 Improved Speed Estimation Using an Adaptive LPF

Compared to traditional MRAS-based observers, the MP-MRAS observer exhibits superior performance under various operating conditions, particularly during the transient period, as discussed in the results section below. However, in the case of low speeds, experimental results reveal fluctuations in the speed during sensorless mode. To mitigate these fluctuations and improve the estimated speed, an adaptive low-pass filter is included in the design of the MP-MRAS estimator in this section.

Figures 5.4, 5.5 and 5.6 respectively present the block diagram, the adaptation mechanism and the Simulink model of an adaptive low-pass filter that can adjust its cut-off frequency based on the dynamic conditions of the system. The algorithm begins by measuring the speed error. In steady-state conditions, when the error is close to zero, the cut-off frequency gradually decreases (sudden decreases can lead to instability) from the maximum value to the minimum value for higher filtering. However, during transient conditions when a disturbance occurs and the error exceeds a predetermined threshold, the cut-off frequency is immediately set to the maximum value (e.g., 10Hz) to achieve a faster dynamic response.

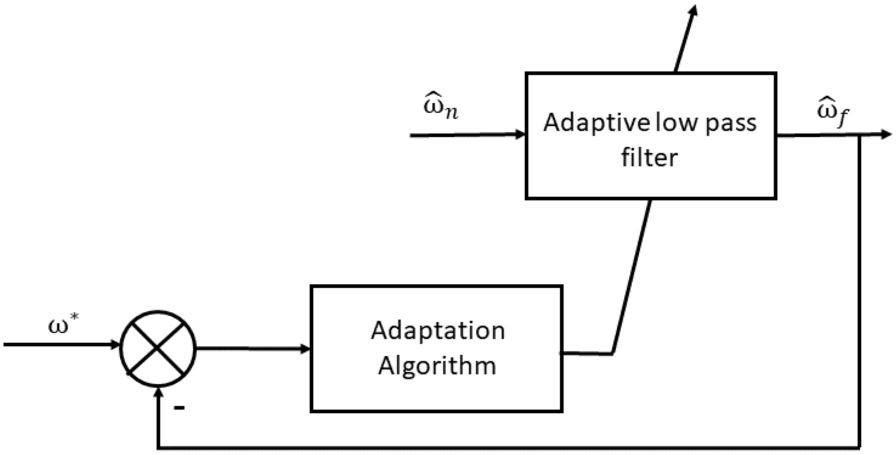

Figure 5.4 Block diagram of the adaptive low pass filter

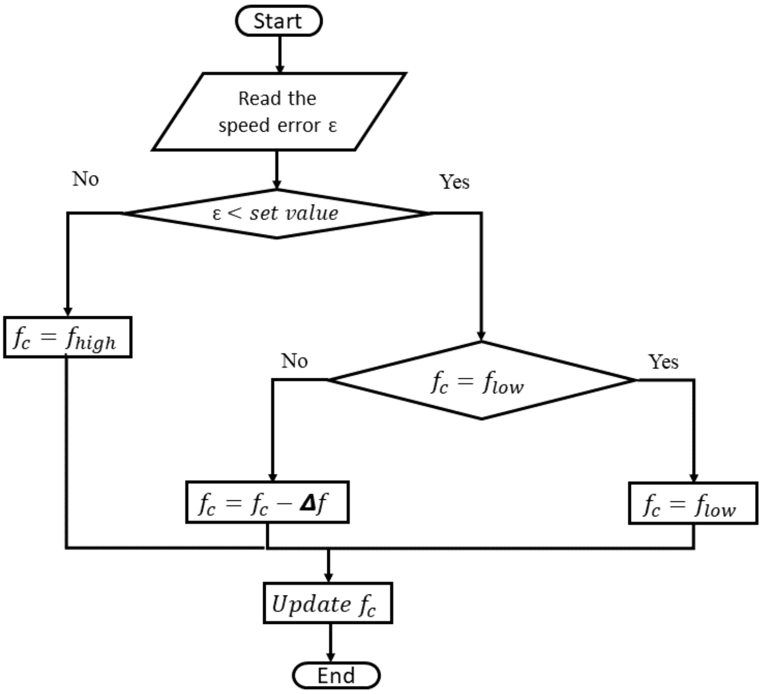

Figure 5.5 The flow chart of the LPF adaptation

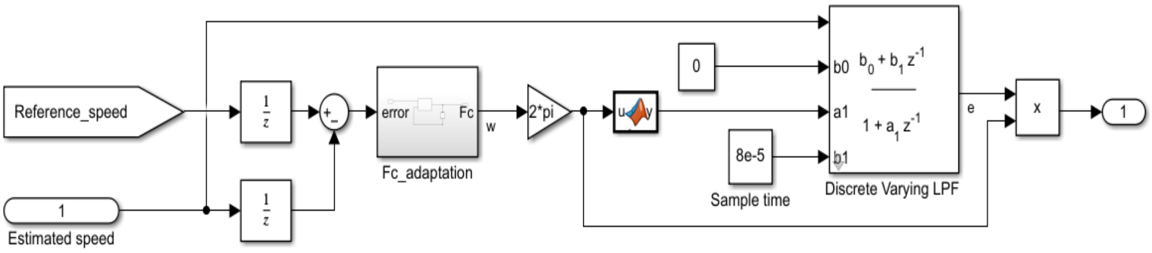

Figure 5.6 Simulink model of adaptive LPF

5.4 Simulation Results

The novel method is examined in MATLAB/Simulink as shown in figure 5.7, the control strategy FOC is implemented with sampling time of 80 µs to control a PMSM model with parameters listed in table 4.2.

Figure 5.8 shows the simulation results for system performance using a predictive estimator at low speed. The reference speed is established at 40 rad/s, and the torque is initially set to zero, and then the rated torque is applied at 1s. It can be noticed that when the torque is applied the estimated speed takes about 0.3s to track the reference speed. Moreover, the angle error during the transient period does not exceed 0.05 rad as depicted in Figure 5.8(b).

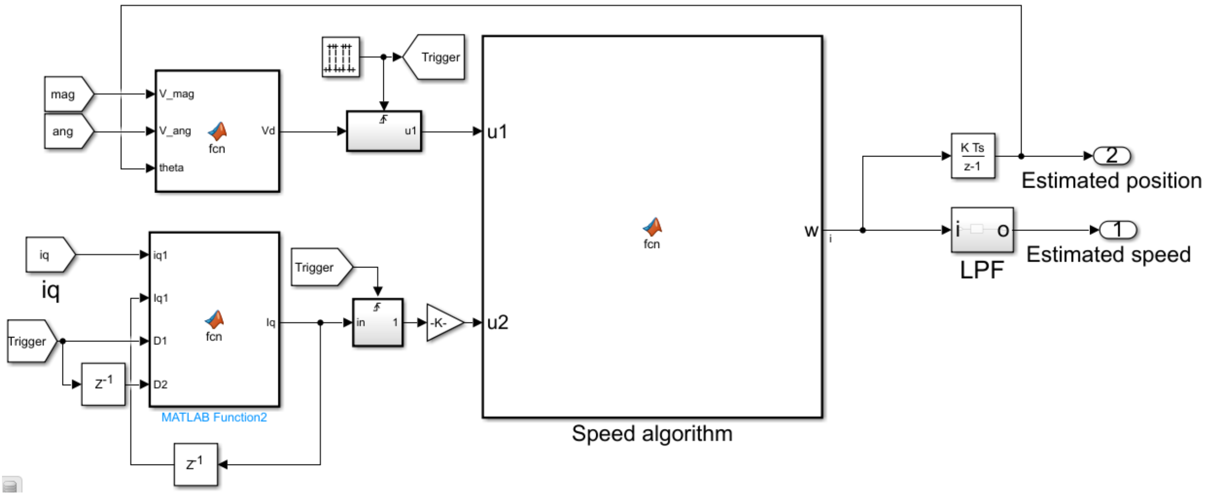

Figure 5.7 Simulink model of the novel predictive speed-based estimator.

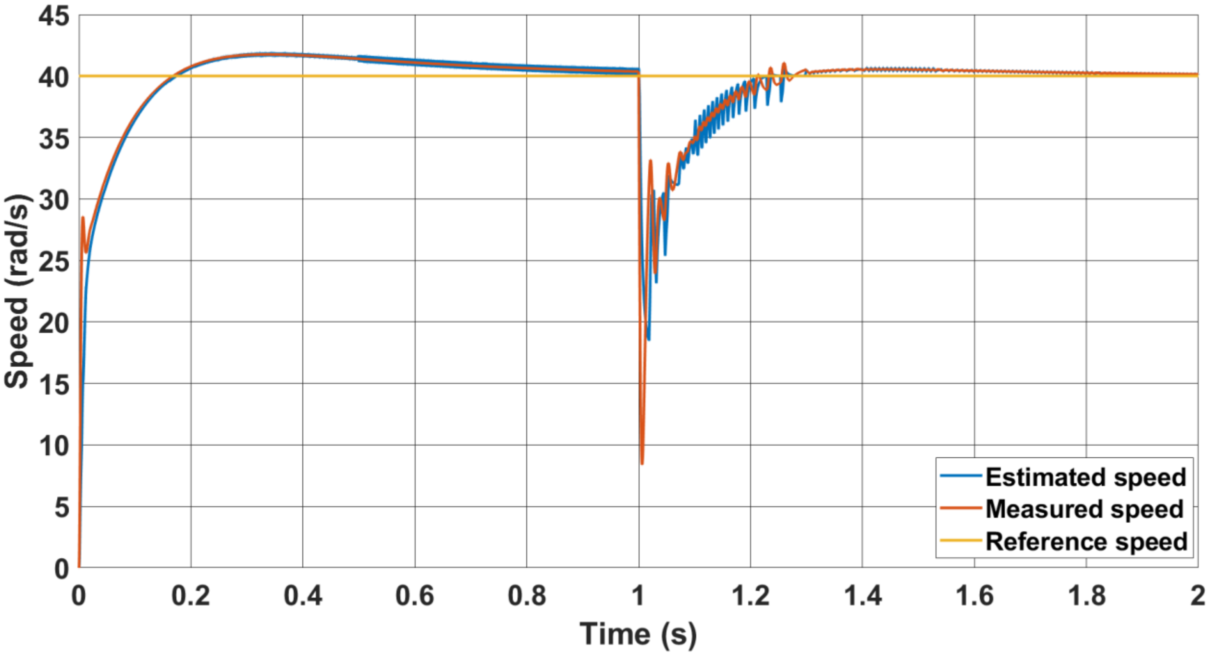

(a)

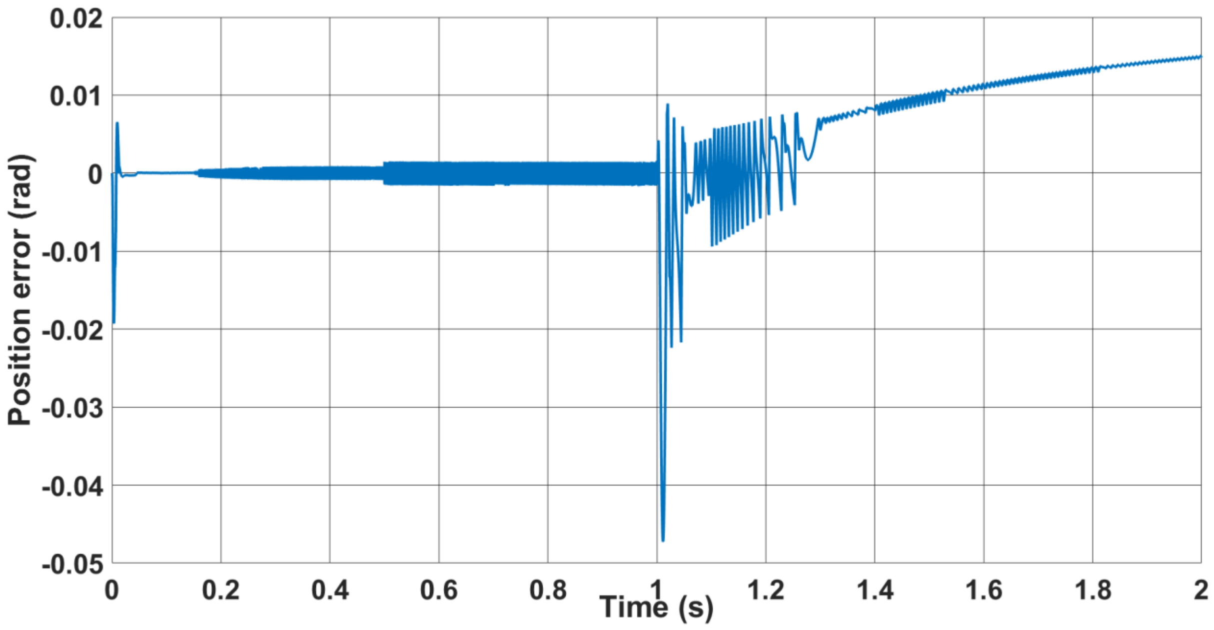

(b)

Figure 5.8 the system performance of the predictive estimator (a) speed response, (b) position error.

Figure 5.9 demonstrates the superiority of the predictive observer compared to the classical one. The reference speed is first set to 80 rad/s and the full rated load is applied, then the speed is increased to 160 rad/s. The predictive observer exhibits an error of 0.01 rad during the transient period, whereas the PI-based estimator resulted in error of -0.3 rad. Moreover, the transient period for the predictive estimated speed is shorter than the estimated speed produced by the PI-based method as shown in figure 5.9(a).

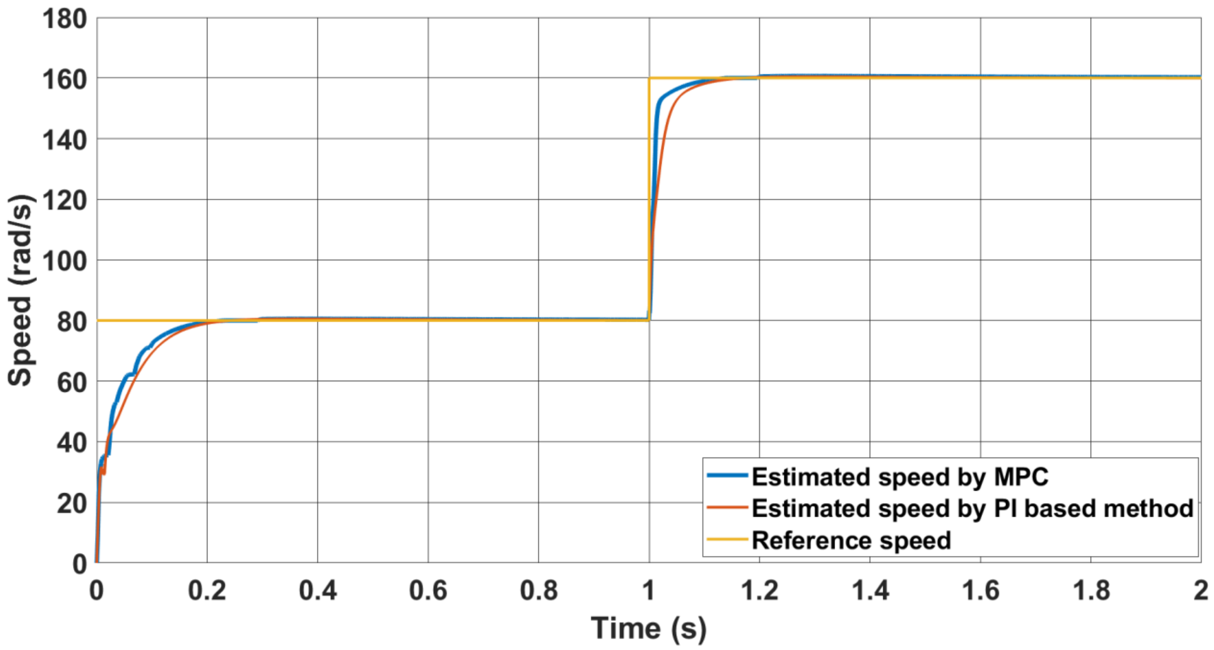

(a)

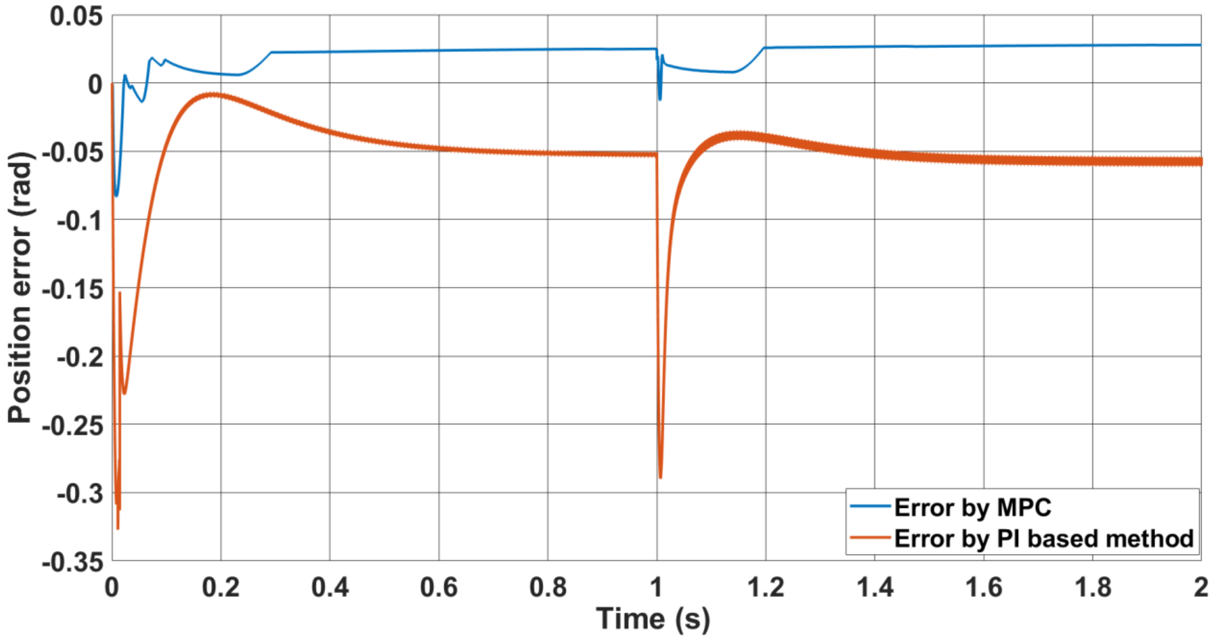

(b)

Figure 5.9 system performance for both the PI-based and predictive estimators (a) speed responses (b) corresponding position error

5.5 Experimental validation

The proposed estimator's performance is tested in both open-loop and close-loop (sensorless) operations and compared with the conventional MRAS scheme. Both estimators' performances are evaluated under various load and speed conditions. The inverter switching frequency is set to 3.125 kHz with a dead time of 0.5 μs, and the control strategy FOC is implemented with sampling time of 80 μs.

5.5.1 Open loop operation

The PI controller gains of the conventional MRAS are determined as Kp = 200 and Ki = 1000 using a trial-and-error method to achieve optimal dynamic performance. Figure 5.10 illustrates the performance of both the classical and predictive estimators under no load conditions. It can be observed from Figure 5.10(a) that the predictive method exhibits lower oscillation in the speed compared to the classical method. Furthermore, Figures 5.10(b) and 5.10(c) demonstrate that the position error, which represents the difference between the measured and estimated positions, is smaller in the predictive method than in the conventional method during the transient period.

Figure 5.11 illustrates the performance of both the classical and predictive MRAS methods under no load conditions, with the speed reference changing from 40 rad/s to -40 rad/s at 10s, and then from -40 rad/s to 40 rad/s at 20s. The predictive estimator demonstrates superiority over the classical MRAS method, as evidenced by the more damped oscillation in the estimated speed, as shown in Figure 5.11(a). Furthermore, during the transient period, the position error in the predictive method is significantly smaller (0.2 rad) compared to the classical method, which exhibits an error of approximately 0.7 rad, as depicted in Figure 5.11(c).

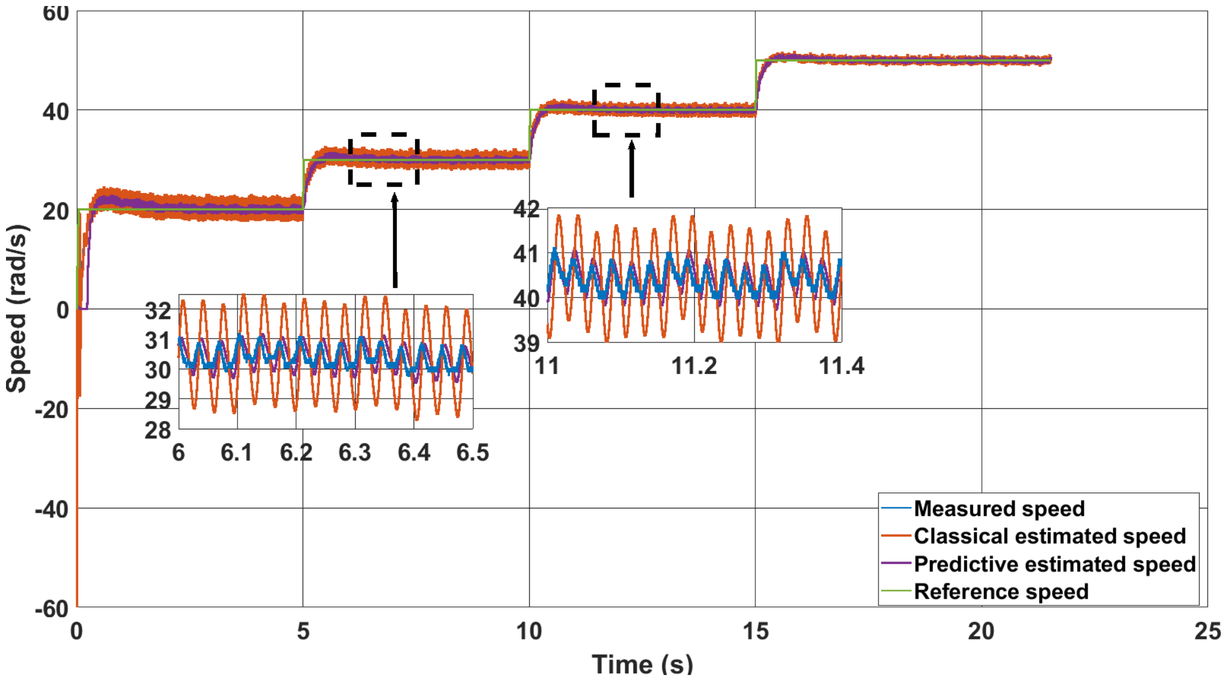

60
40
20
0
-20
-40
-60
Speed (rad/s)
0
5
10
15
20
25
Time (s)
32
31
30
29
28
6
6.1
6.2
6.3
6.4
6.5
42
41
40
39
11
11.2
11.4
Measured speed
Classical estimated speed
Predictive estimated speed
Reference speed

(a)

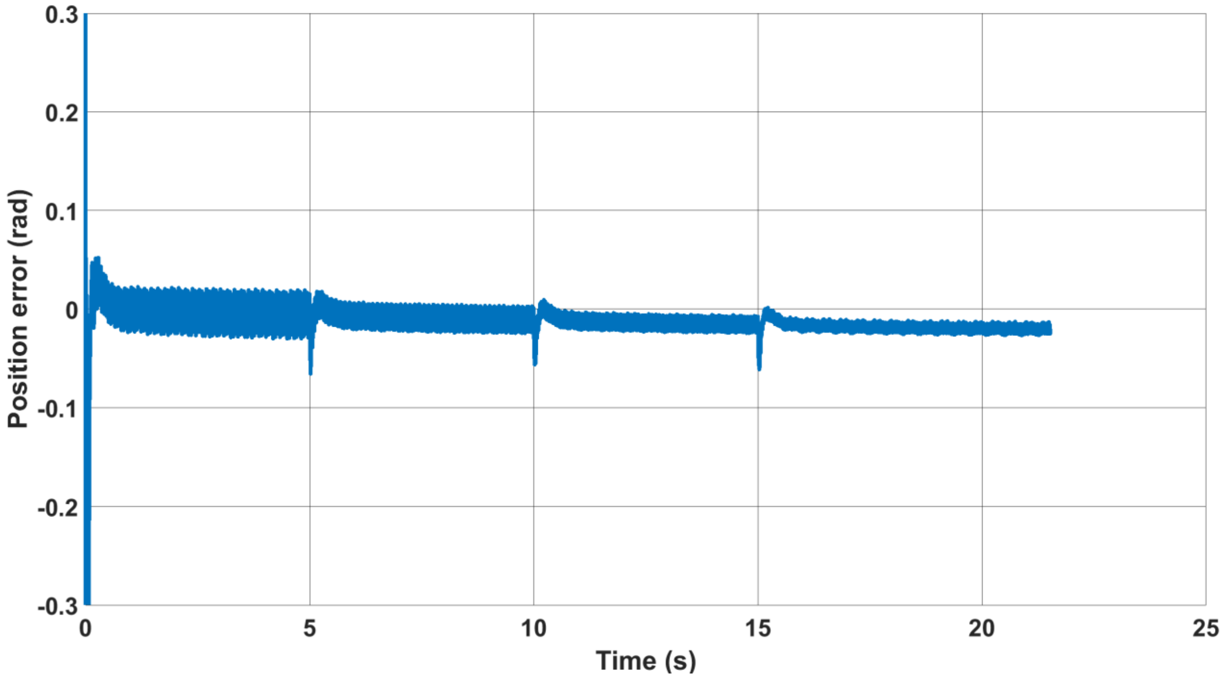

0.3
0.2
0.1
0
-0.1
-0.2
-0.3
Position error (rad)
0
5
10
15
20
25
Time (s)

(b)

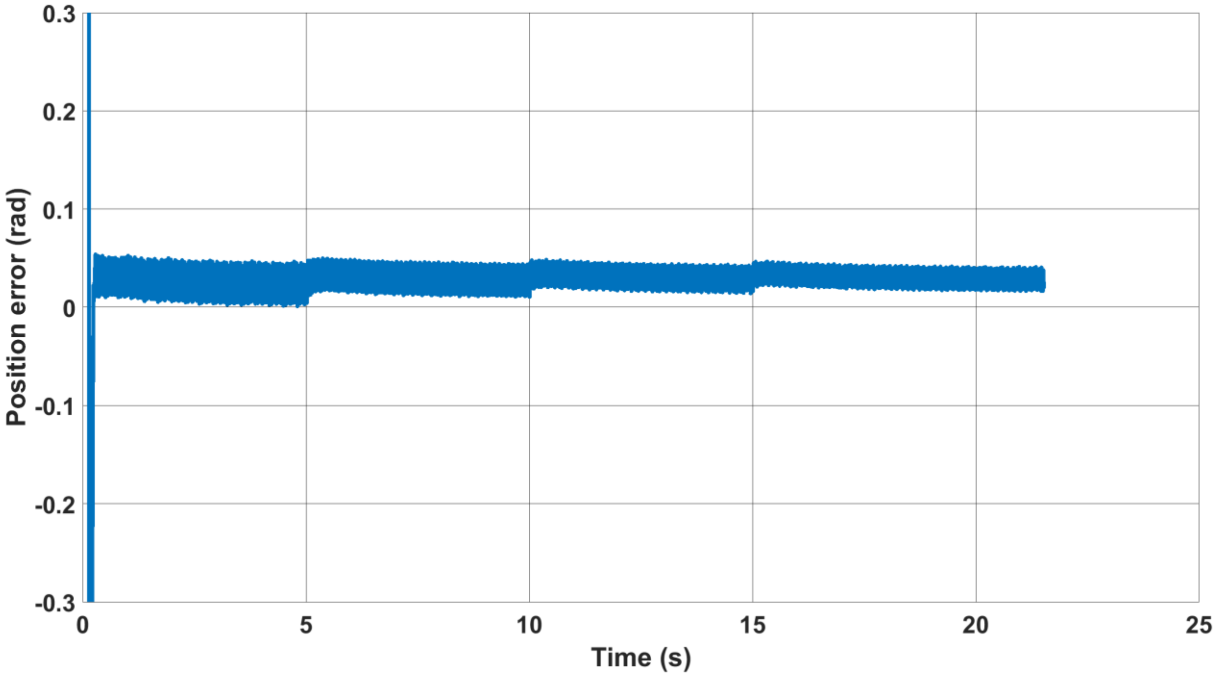

(c)

Figure 5.10 Low speed performance for open-loop mode, (a) Speed response, (b) Position error for the conventional method, (c) Position error for the predictive method.

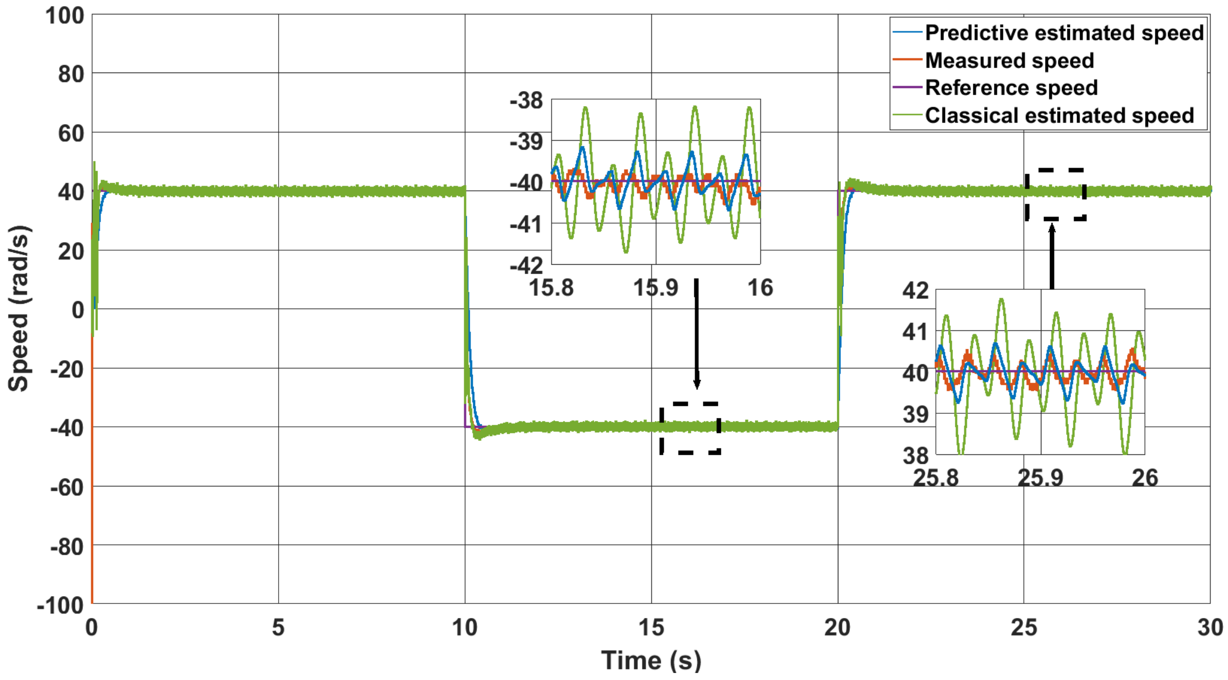

(a)

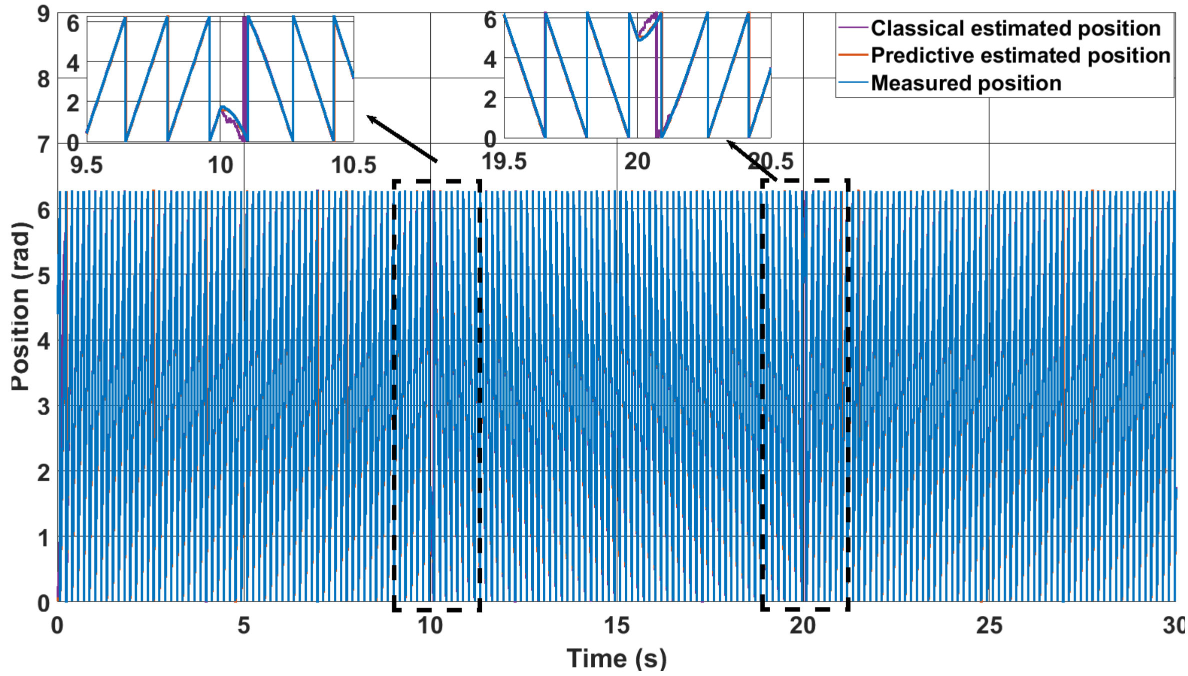
Classical estimated position
Predictive estimated position
Measured position
Position (rad)
Time (s)
0
1
2
3
4
5
6
7
8
9
0
5
10
15
20
25
30
9.5
10
10.5
19.5
20
20.5
0
2
4
6
0
2
4
6

(b)

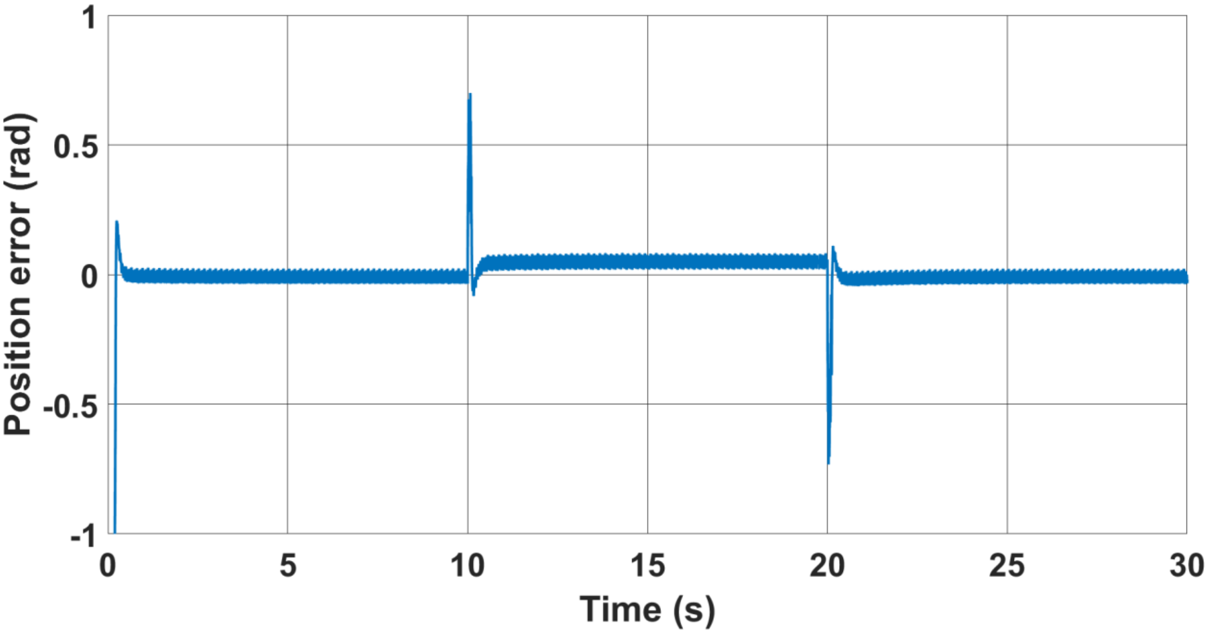
Position error (rad)
Time (s)
1
0.5
0
-0.5
-1
0
5
10
15
20
25
30

(c)

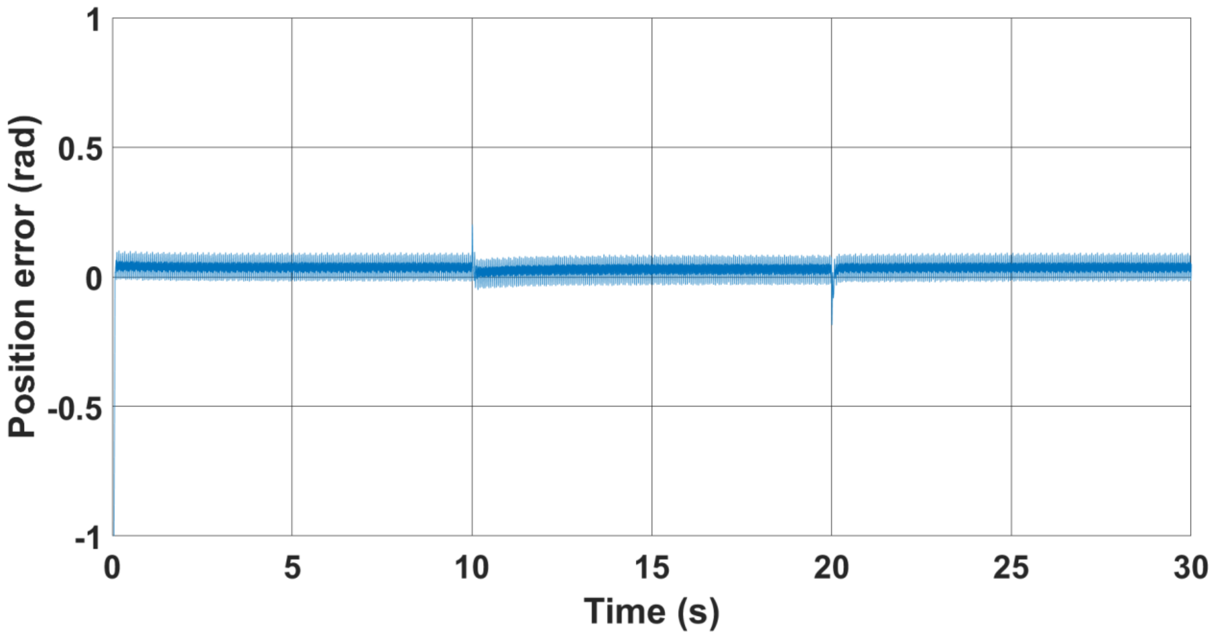

(c)

Figure 5.11 Zero crossing speed performance for open-loop mode at no load, (a) Estimated speed response, (b) Measured and estimated positions, (c) Position error for the conventional method (d) Position error for the predictive method

5.5.2 Sensorless Mode

Unlike the open-loop performance, the sensorless performance of the predictive observer exhibits oscillations in the estimated speed, particularly at low speeds. Interestingly, a 2-cut-off frequency low-pass filter is employed in conjunction with the predictive method successfully reduces the fluctuations in the estimated speed without affecting the operation of the drive, even when disturbances such as speed changes are introduced. This is in contrast to the conventional MRAS method, where the LPF fails to achieve the same result. Therefore, an adaptive low-pass filter can be utilized to gradually decrease the cut-off frequency to the minimum during steady-state operation for improved filtering quality, while setting it to 10 Hz for a faster dynamic response during transient operation.

Figures 5.12 and 5.13 demonstrate the performance of the two methods in sensorless mode at 2s when the reference speed is changed from 30 rad/s to 70 rad/s under no load conditions. The results indicate that the predictive estimator exhibits less oscillation in the estimated speed, particularly at low speeds. Moreover, the position error during the transient period is significantly lower in the predictive method, measuring approximately 0.21 rad, compared to approximately -0.7 rad in the conventional method. This distinction is evident when analysing the phase currents generated by the two methods during the transient period. The phase currents produced by the conventional method are higher than those produced by the predictive method, as depicted in Figures 5.12(d) and 5.13(d).

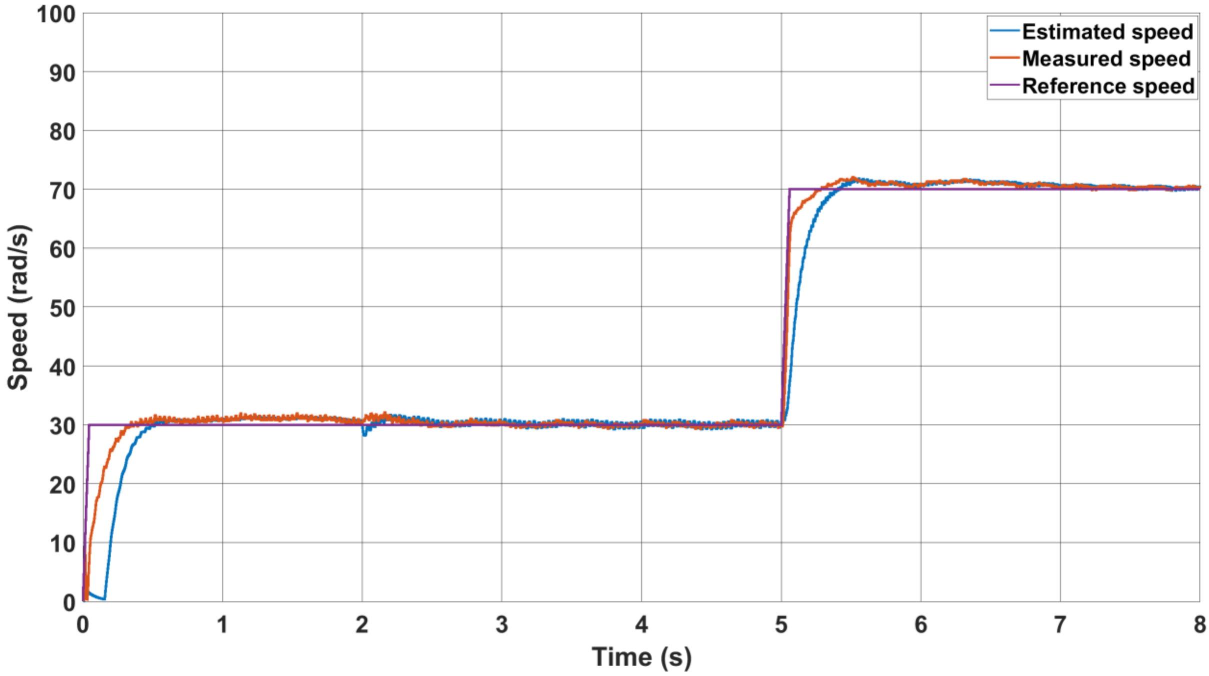

(a)

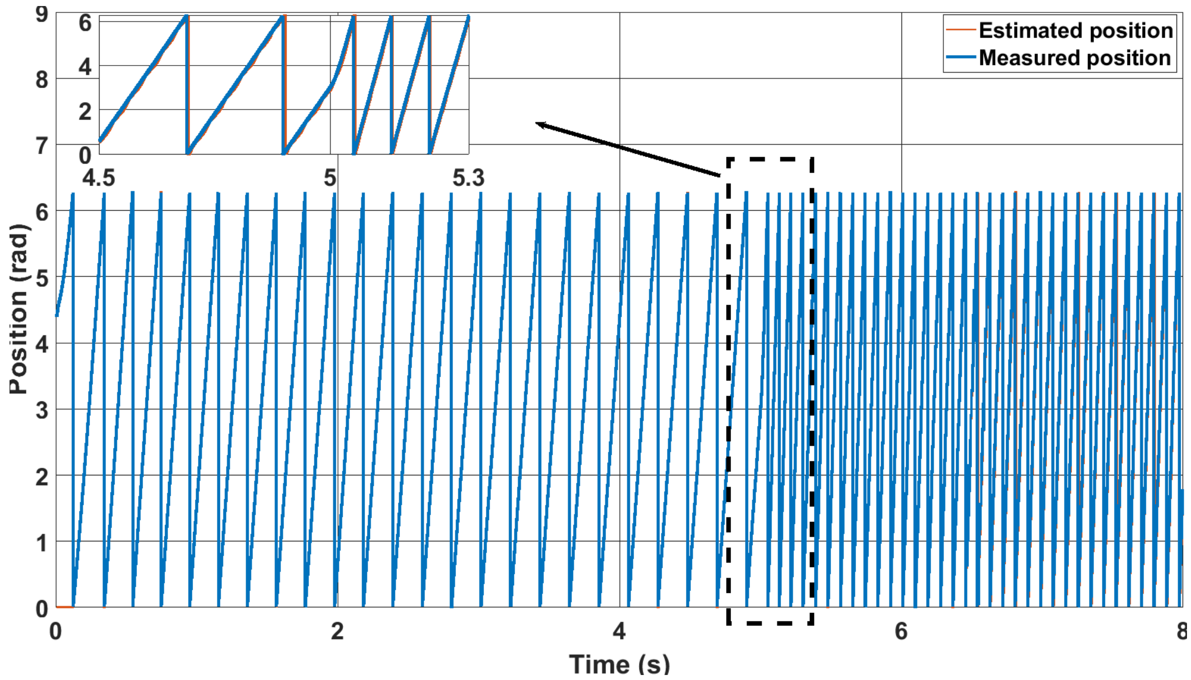
Estimated position
Measured position
Position (rad)
Time (s)
0
1
2
3
4
5
6
7
8
9
0
2
4
6
8
6
4
2
0
4.5
5
5.3

(b)

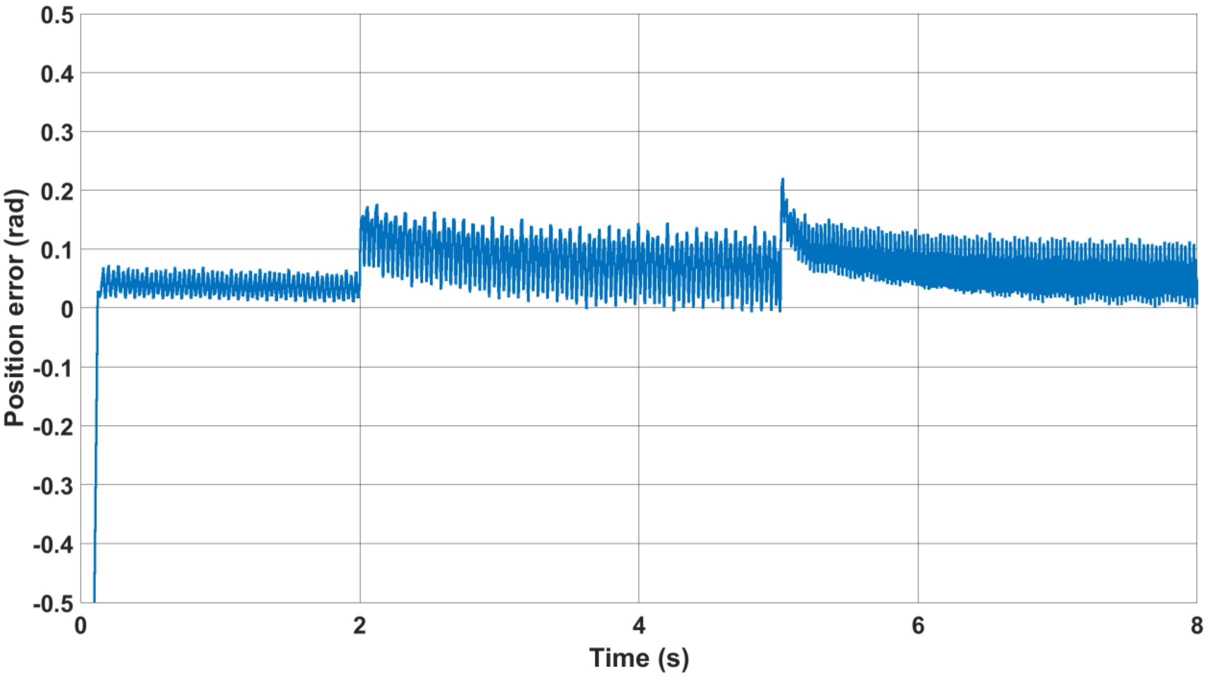
Position error (rad)
Time (s)
0.5
0.4
0.3
0.2
0.1
0
-0.1
-0.2
-0.3
-0.4
-0.5
0
2
4
6
8

(c)

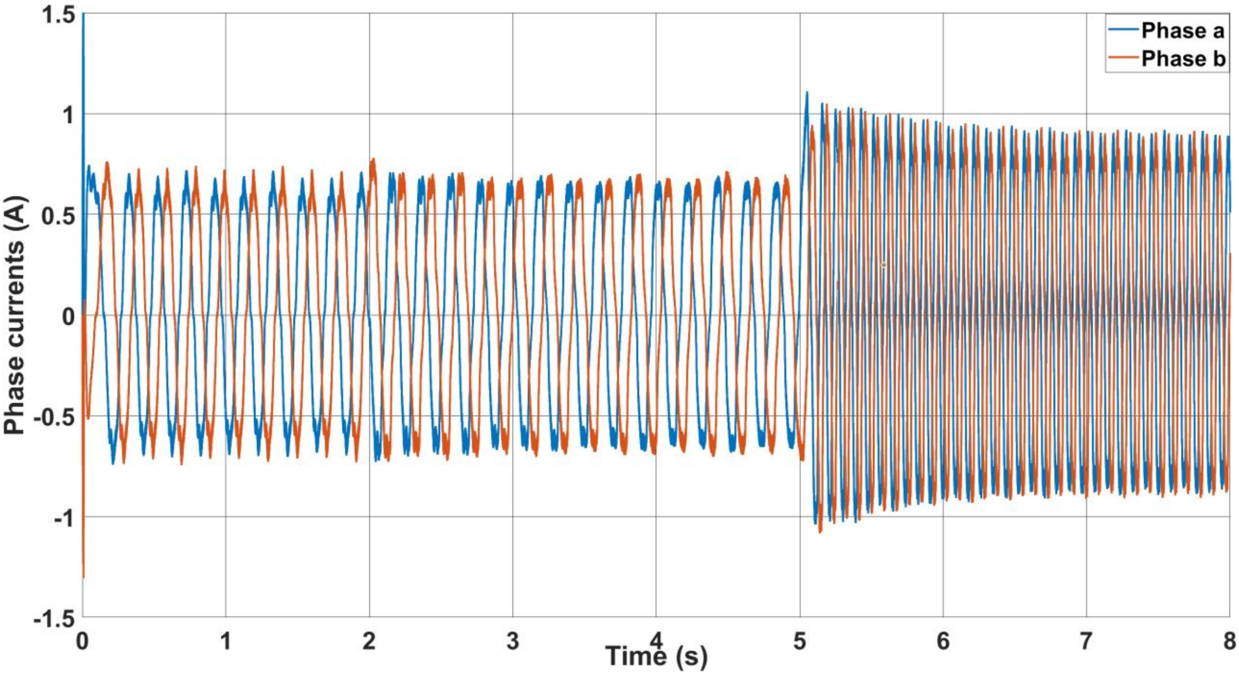
Phase a
Phase b
Phase currents (A)
Time (s)
1.5
1
0.5
0
-0.5
-1
-1.5
0
1
2
3
4
5
6
7
8

(d)

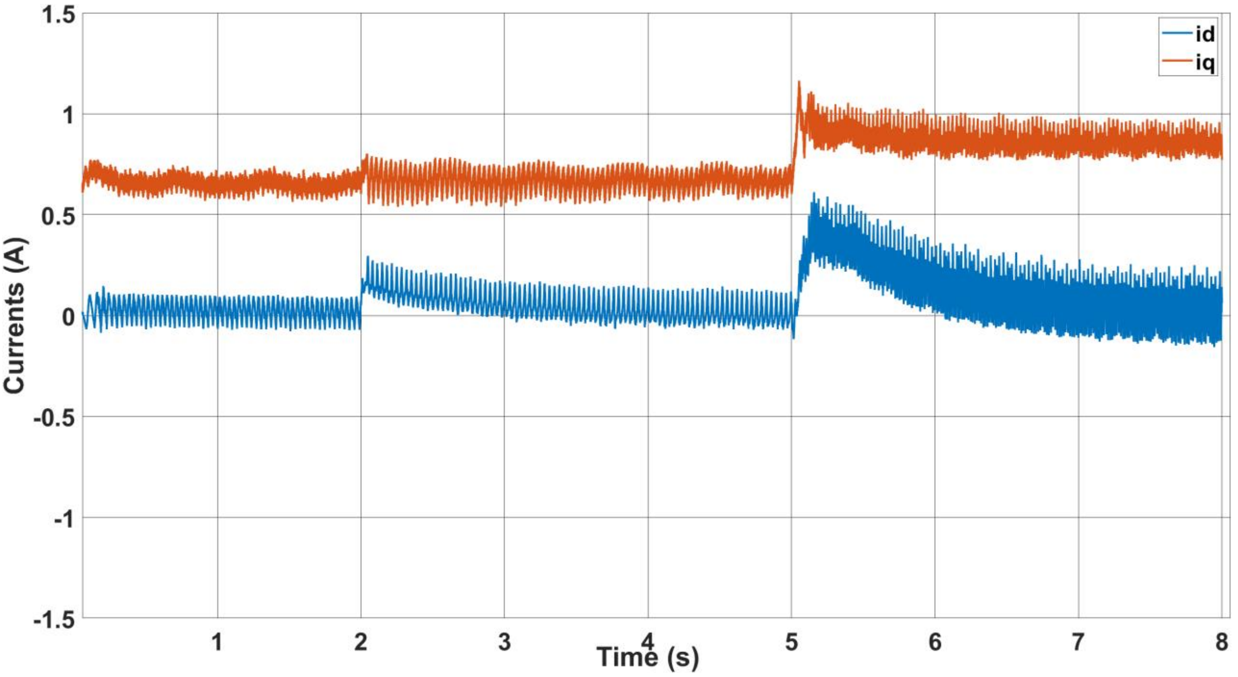
id
iq
Currents (A)
Time (s)
1.5
1
0.5
0
-0.5
-1
-1.5
1
2
3
4
5
6
7
8

(e)

Figure 5.12 Predictive method performance for sensorless mode, (a) Speed response, (b) Estimated and measured positions, (b) Position error, (d) Phase currents, (e) d-q current

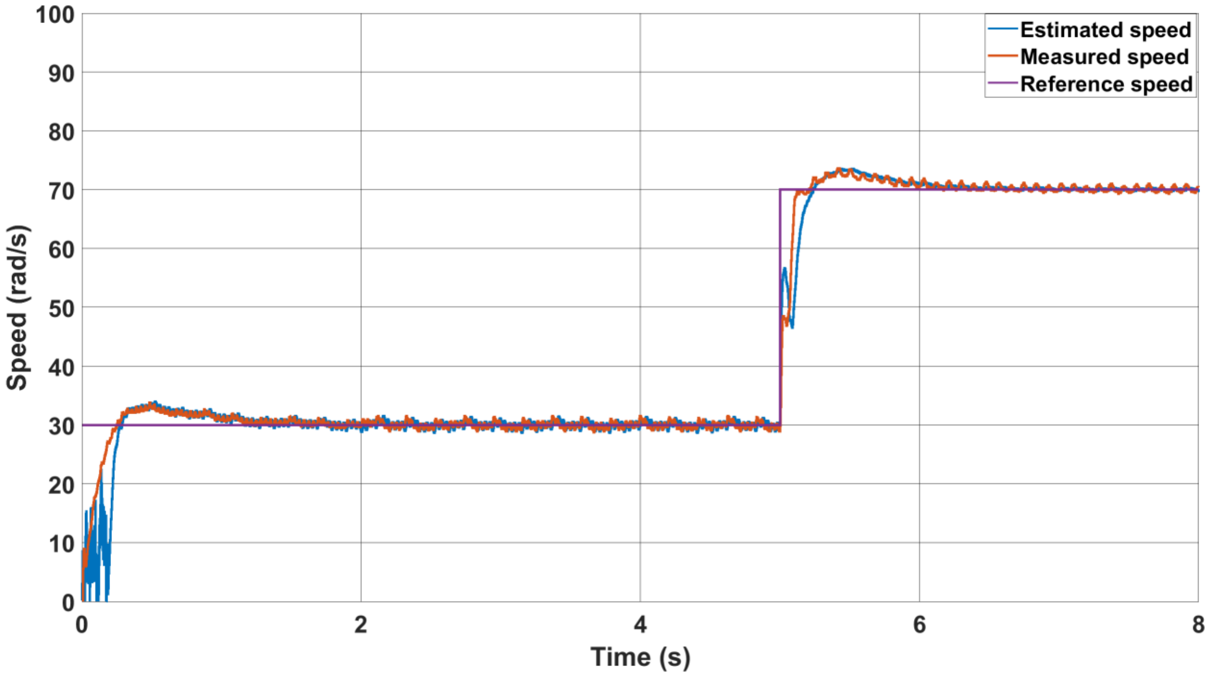

(a)

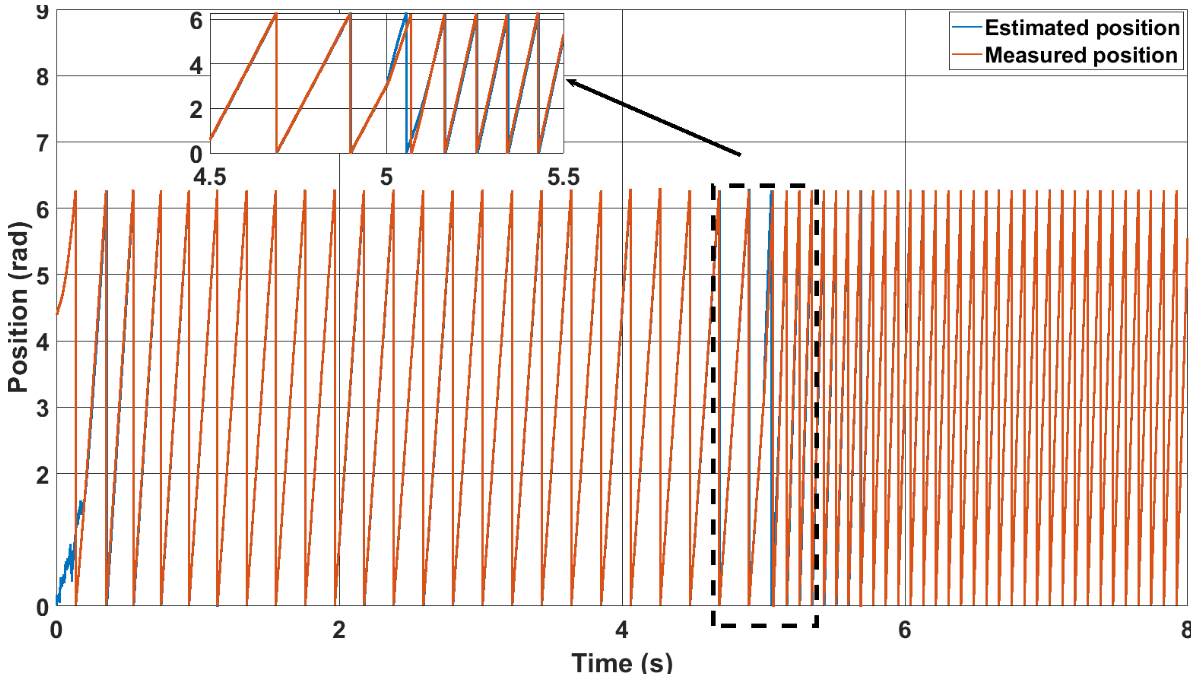

(b)

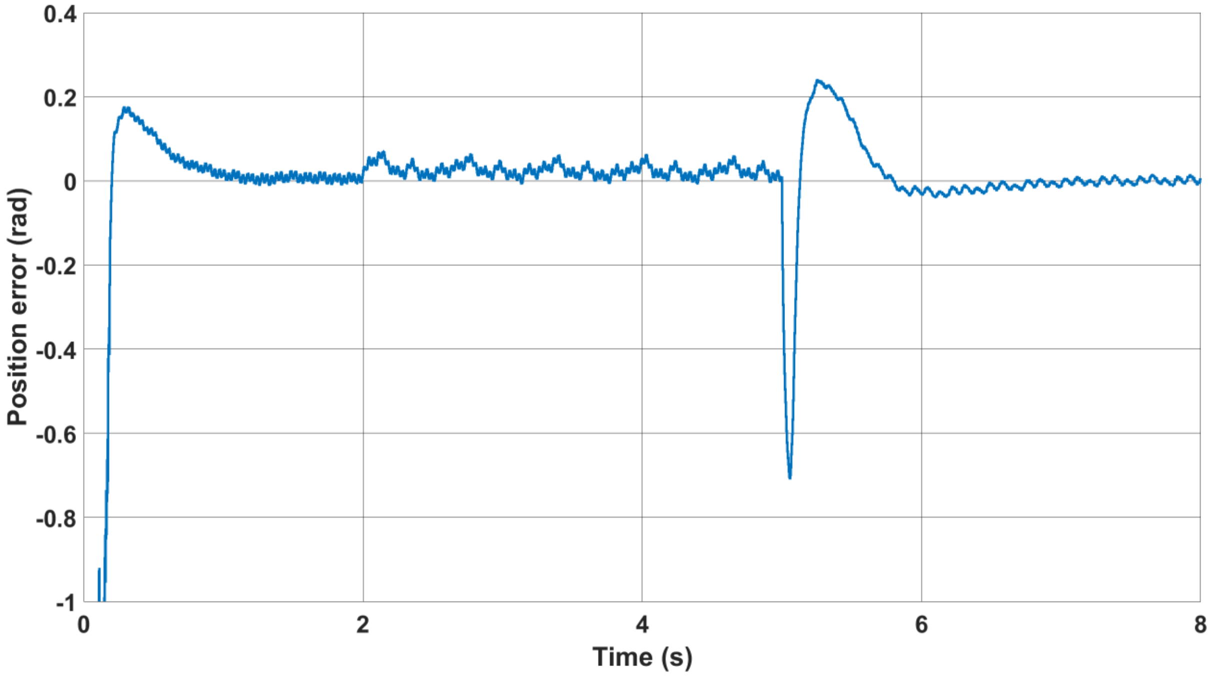
0.4
0.2
0
-0.2
-0.4
-0.6
-0.8
-1
Position error (rad)
0
2
4
6
8
Time (s)

(c)

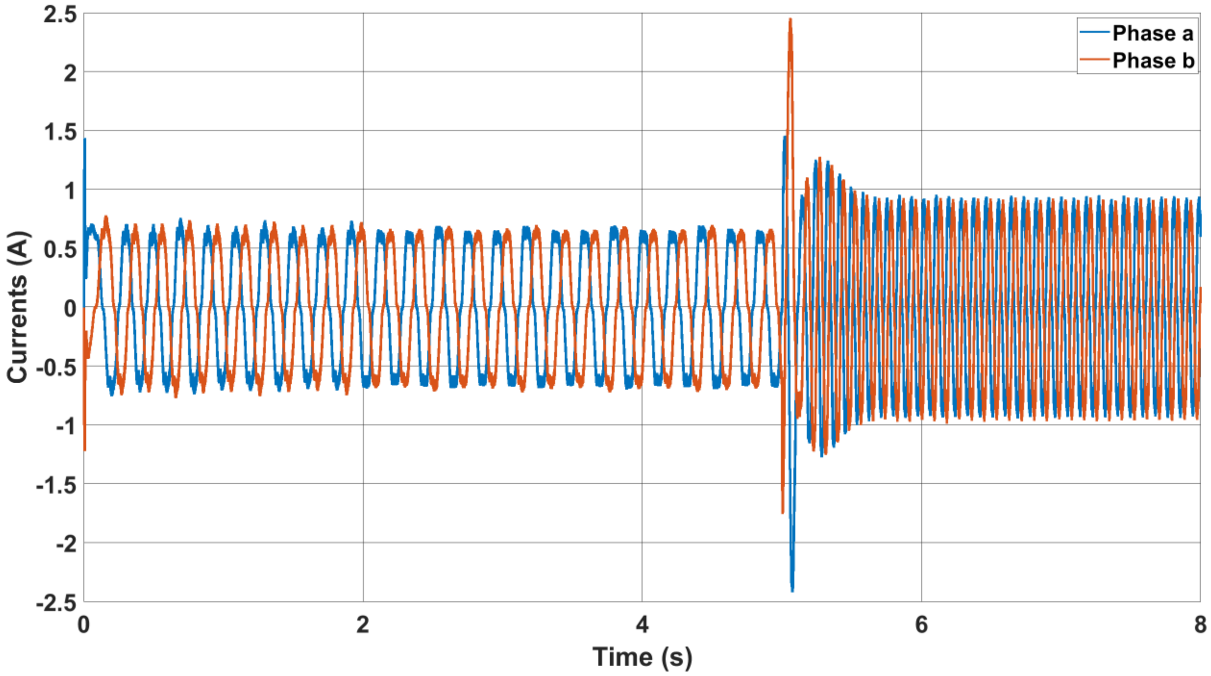
Phase a
Phase b
2.5
2
1.5
1
0.5
0
-0.5
-1
-1.5
-2
-2.5
Currents (A)
0
2
4
6
8
Time (s)

(d)

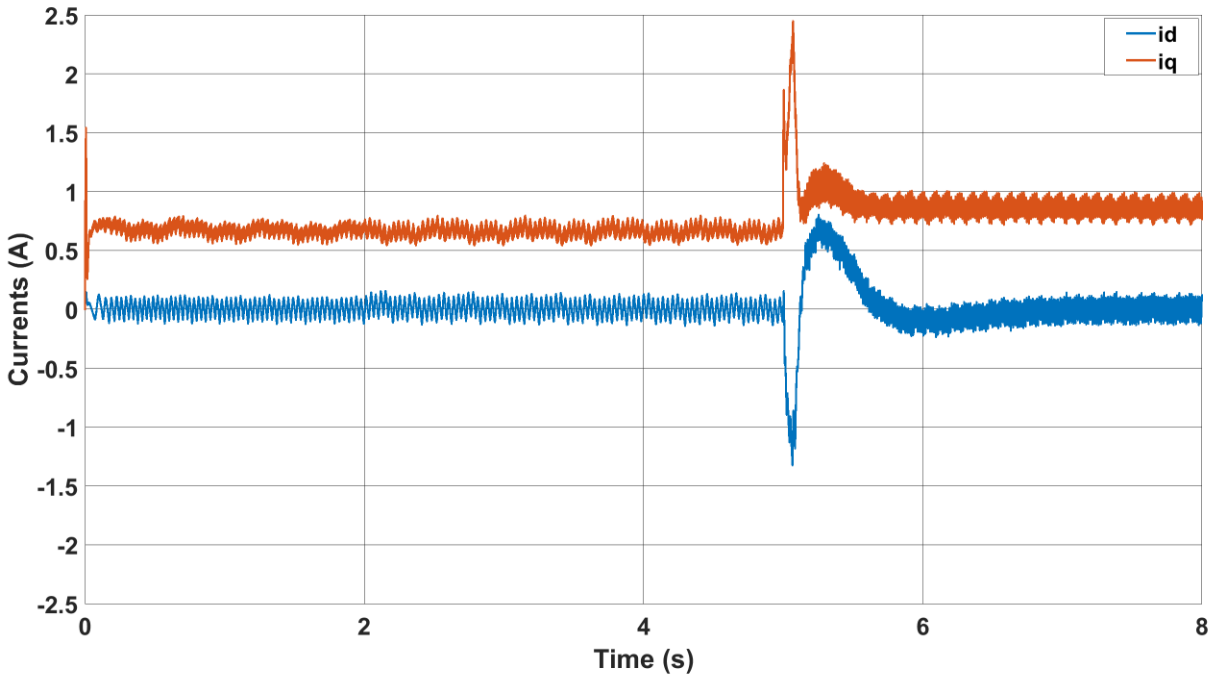

(e)

Figure 5.13 Conventional method performance for sensorless mode, (a) Speed response, (b) Estimated and measured positions, (b) Position error, (d) Phase currents, (e) d-q currents.

Figs 5.14 and 5.15 show the two methods performance for sensorless operation at 5s when the reference speed crossing zero at no load. It is shown that the drive can cross the zero speed with a smoother response at transient period compared to the conventional method. In the conventional method a speed rate limiter is needed for a smooth transient response as seen in Fig. 5.15(a). The position error produced by the predictive method during the transient period is about -0.3 rad compared to about -1.8 rad in the conventional method as shown in Figs. 5.14(c) and 5.15(c) respectively.

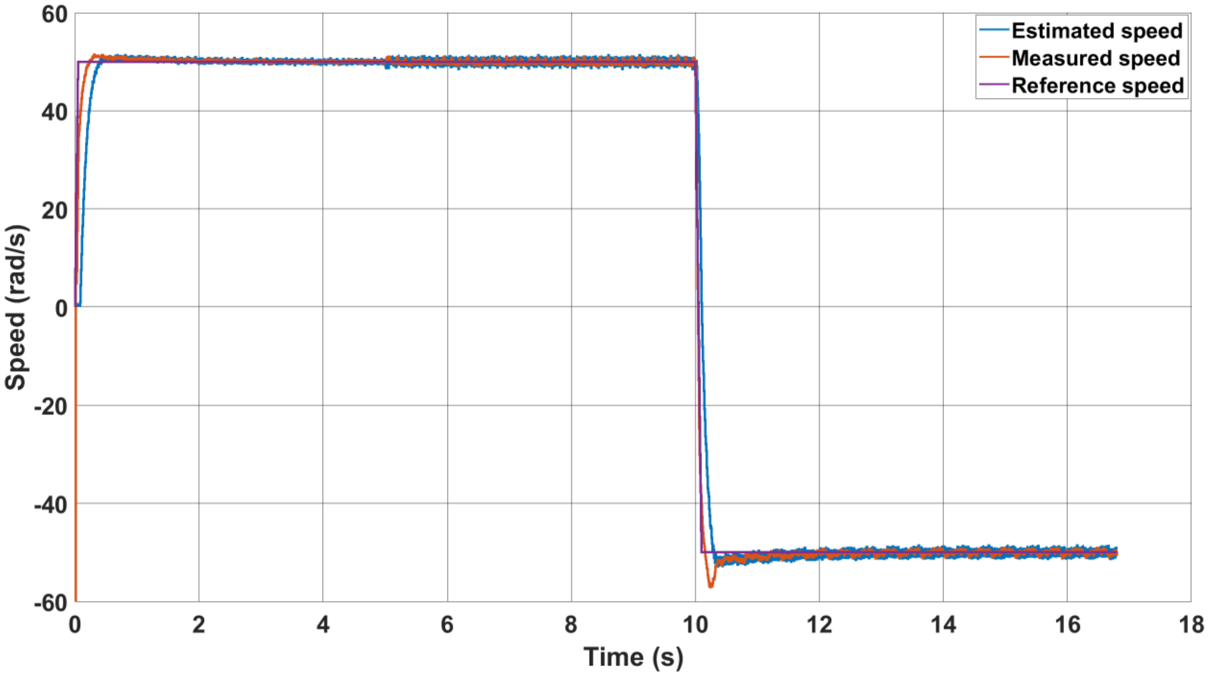

Estimated speed
Measured speed
Reference speed
Speed (rad/s)
60
40
20
0
-20
-40
-60
0
2
4
6
8
10
12
14
16
18
Time (s)

(a)

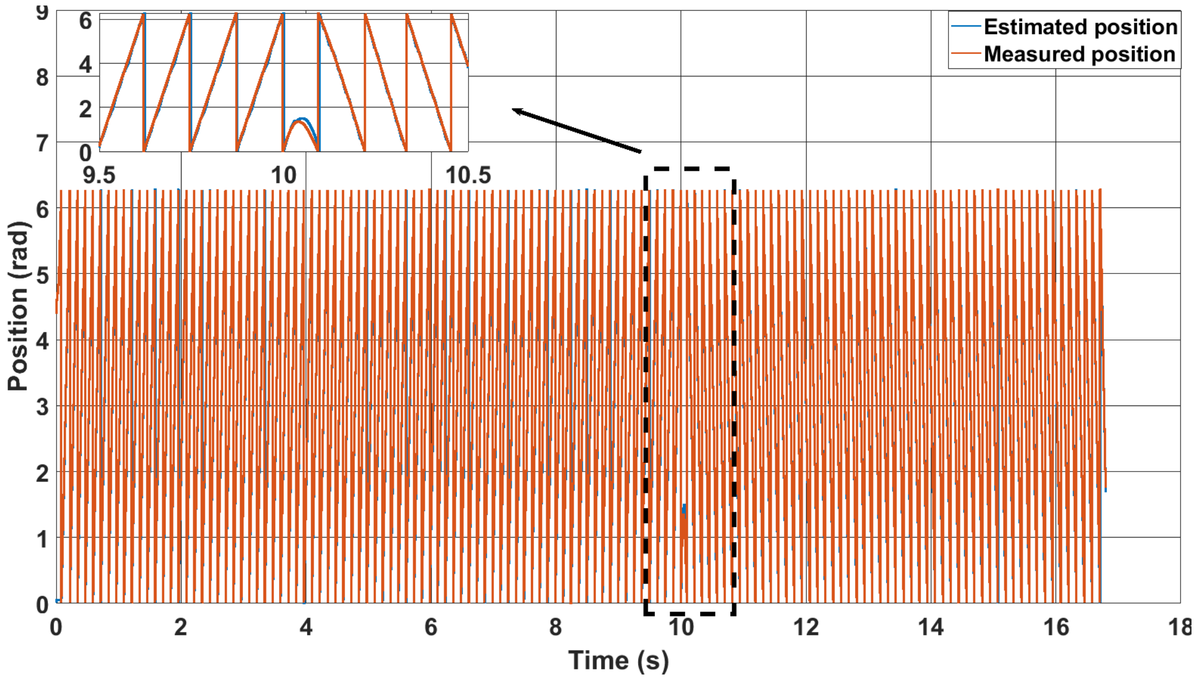

Estimated position
Measured position
Position (rad)
9
8
7
6
5
4
3
2
1
0
6
4
2
0
9.5
10
10.5
0
2
4
6
8
10
12
14
16
18
Time (s)

(b)

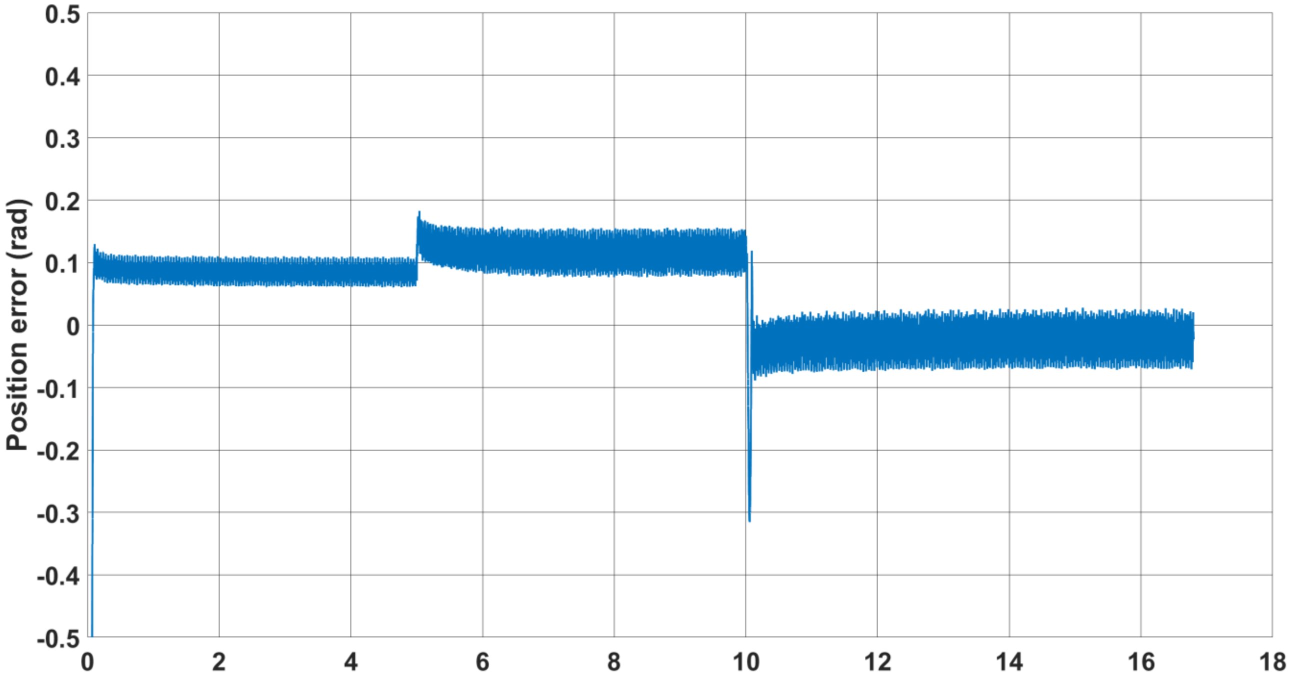

(c)

Figure 5.14 Zero crossing speed performance for sensorless mode of the predictive method at no load, (a) Speed response, (b) Measured and estimated positions, (c) position error.

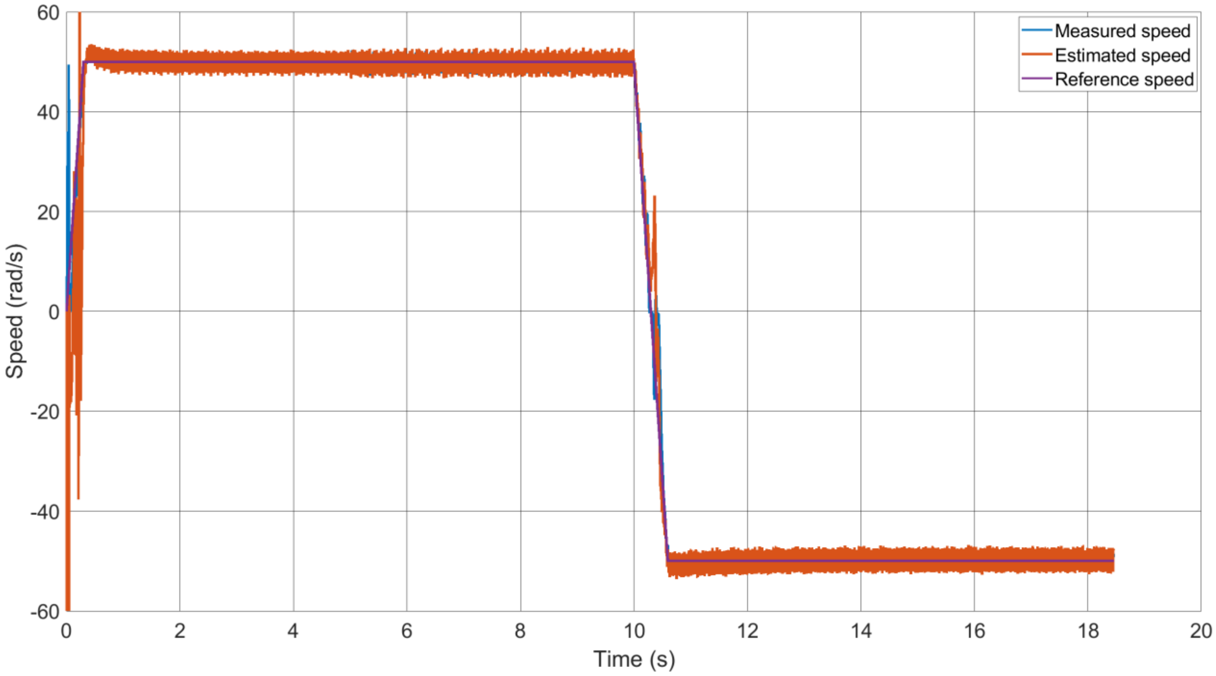

(a)

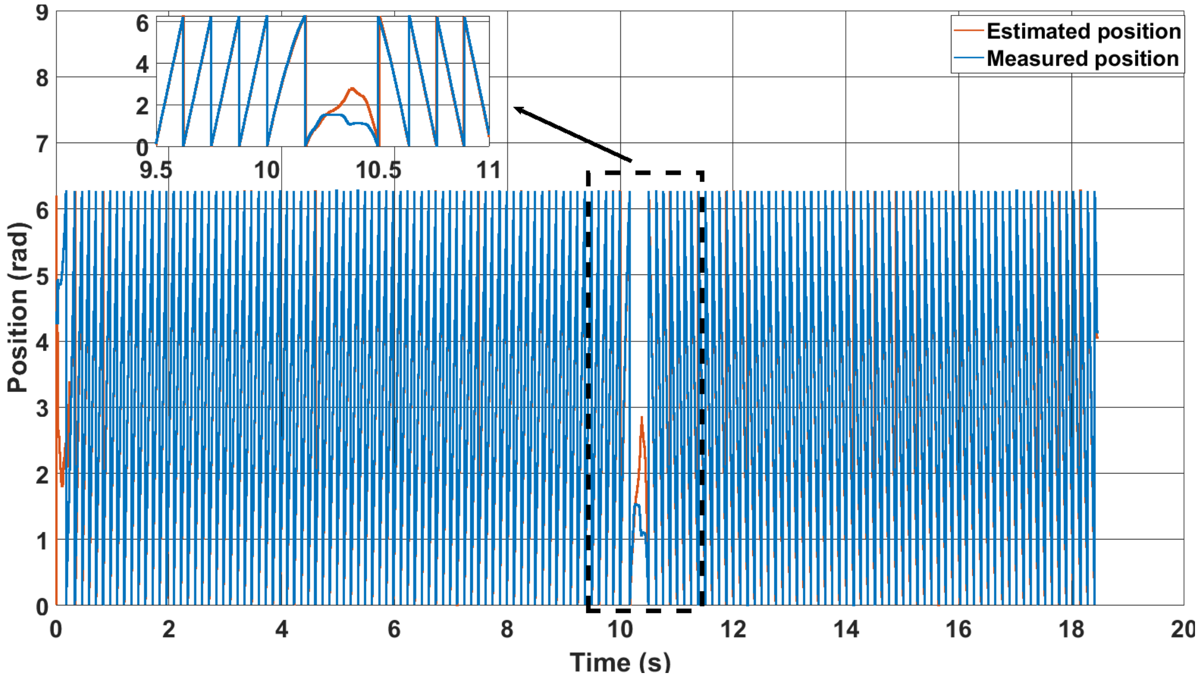
Estimated position
Measured position
Position (rad)
Time (s)
0
1
2
3
4
5
6
7
8
9
0
2
4
6
8
10
12
14
16
18
20
6
4
2
0
9.5
10
10.5
11

(b)

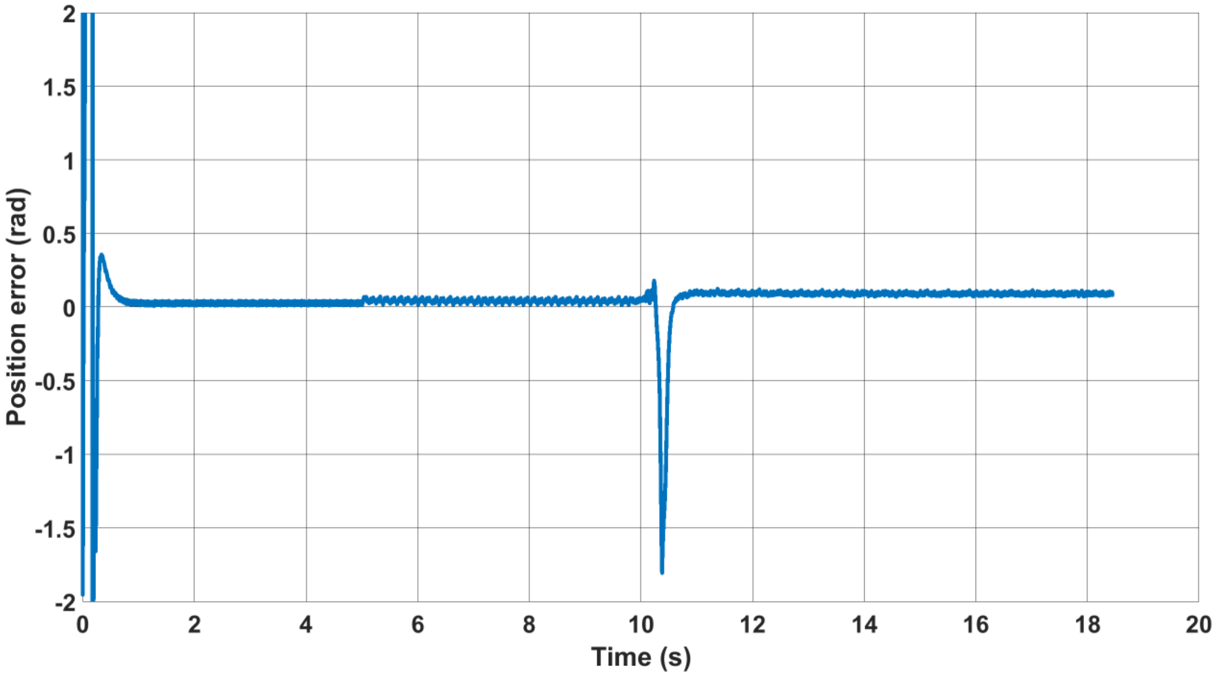
Position error (rad)
Time (s)
2
1.5
1
0.5
0
-0.5
-1
-1.5
-2
0
2
4
6
8
10
12
14
16
18
20

(c)

Figure 5.15 Zero crossing speed performance for sensorless mode of the conventional method at no load, (a) Speed response, (b) Measured and estimated positions, (c) Position error.

Figures 5.16 and 5.17 present the performance of both the classical and predictive methods in regenerative mode for sensorless operation at 5s. The experiments were conducted with a speed reference of 50 rad/s and load variations: initially, a load of 15% of the rated torque was applied, followed by an increase to 30% of the rated torque, and finally a decrease back to 15%. It can be observed that both methods exhibit a slight increase in speed oscillation and position error as the load changes. However, during the transient period, the position error significantly increases in the classical method when the load changes, whereas in the predictive scheme, the error only experiences a slight increase, as depicted in Figures 5.16(c) and 5.17(c). This distinction is further emphasized in Figures 5.16(d), 5.16(e), 5.17(d), and 5.17(e), which demonstrate that the current remains relatively unaffected during the transient period in the predictive method, while it exhibits a substantial increase in the classical method.

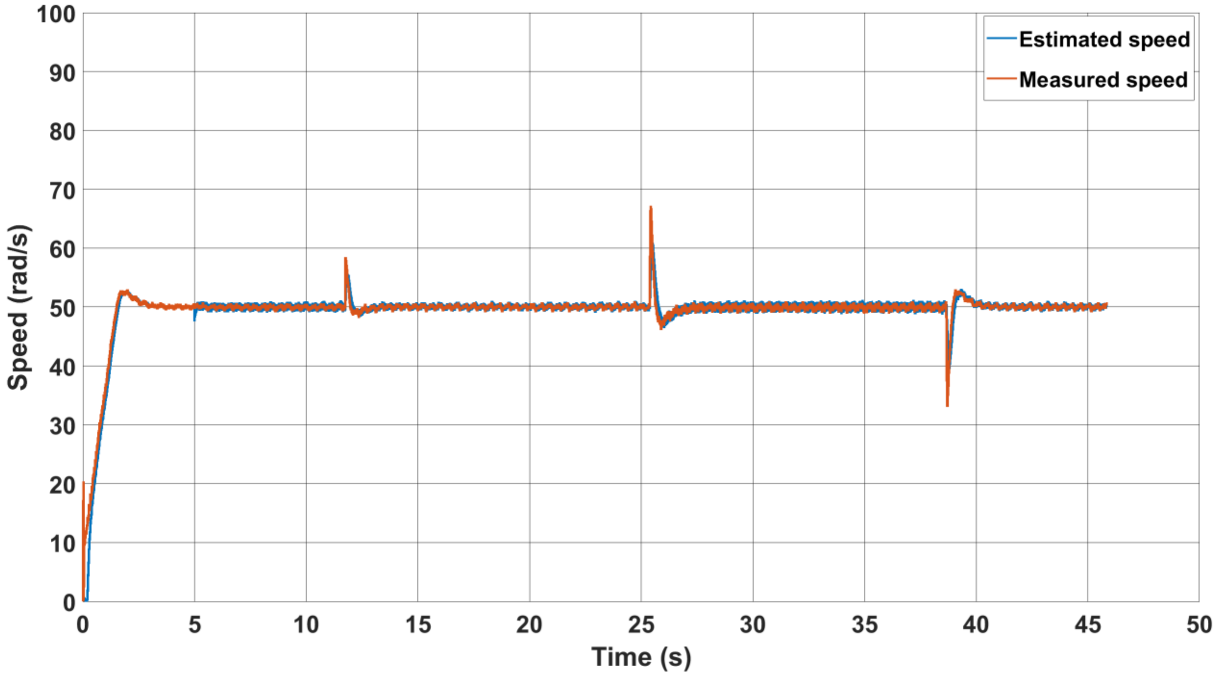

(a)

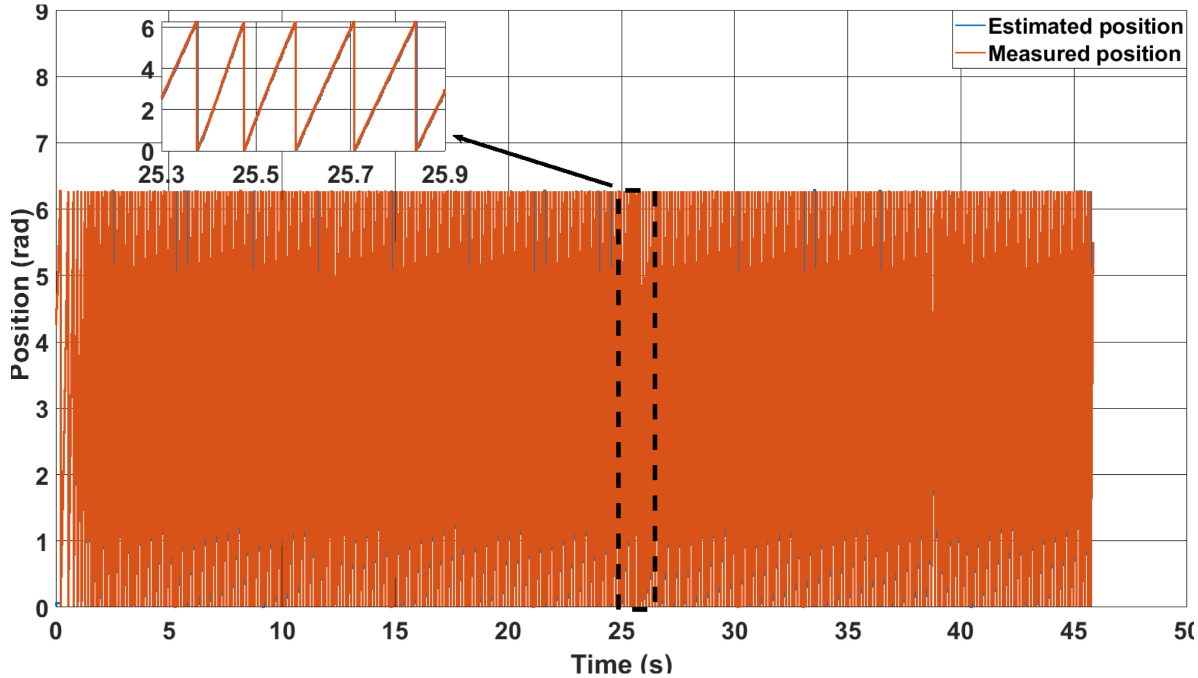
Estimated position
Measured position
Position (rad)
Time (s)
0
1
2
3
4
5
6
7
8
9
0
5
10
15
20
25
30
35
40
45
5(
0
2
4
6
25.3
25.5
25.7
25.9

(b)

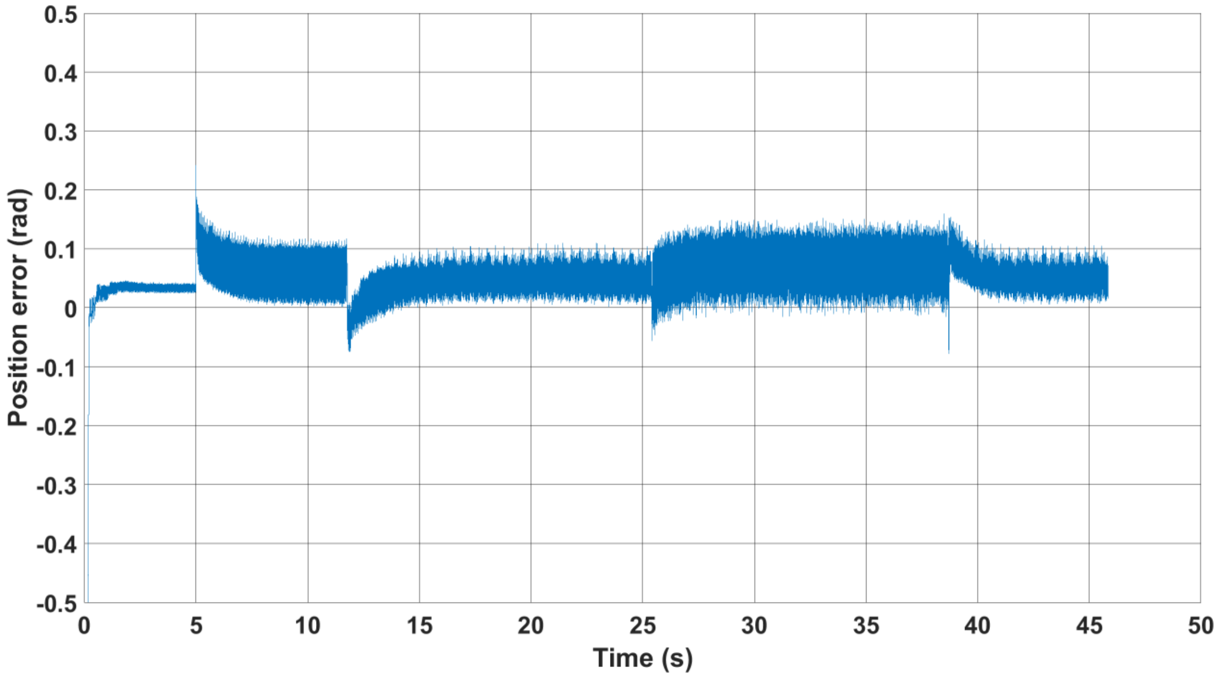
Position error (rad)
Time (s)
0.5
0.4
0.3
0.2
0.1
0
-0.1
-0.2
-0.3
-0.4
-0.5
0
5
10
15
20
25
30
35
40
45
50

(c)

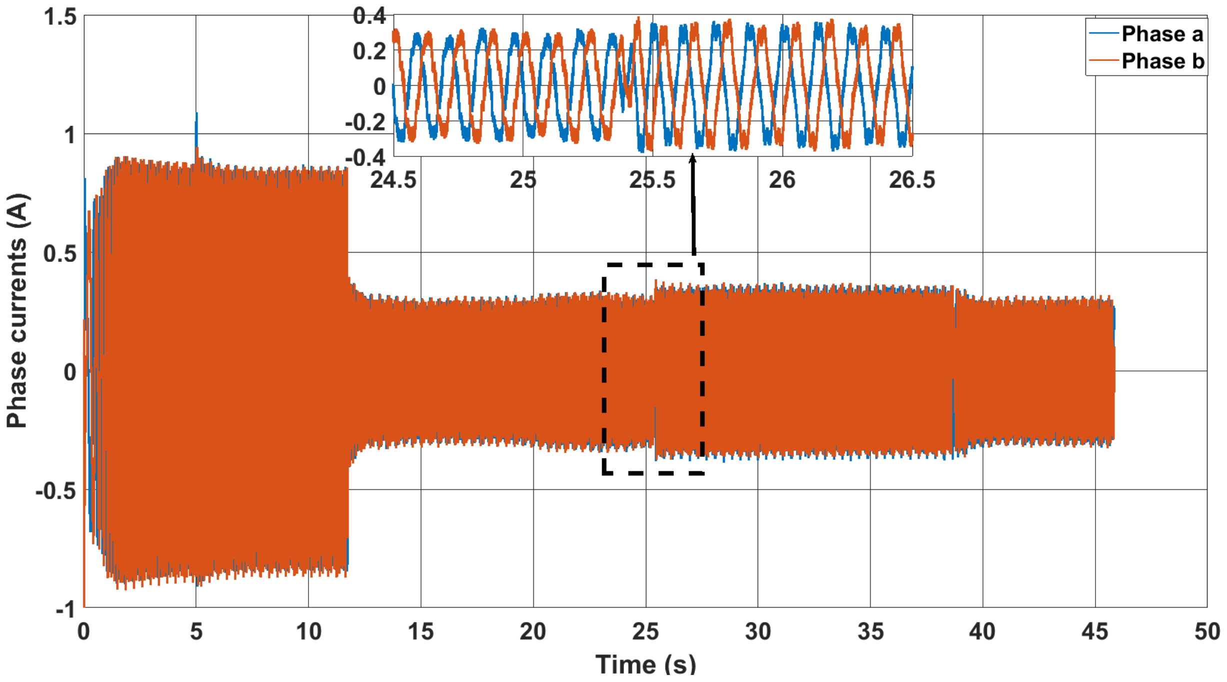
0.4
0.2
0
-0.2
-0.4
24.5
25
25.5
26
26.5
Phase a
Phase b
1.5
1
0.5
0
-0.5
-1
Phase currents (A)
0
5
10
15
20
25
30
35
40
45
50
Time (s)

(d)

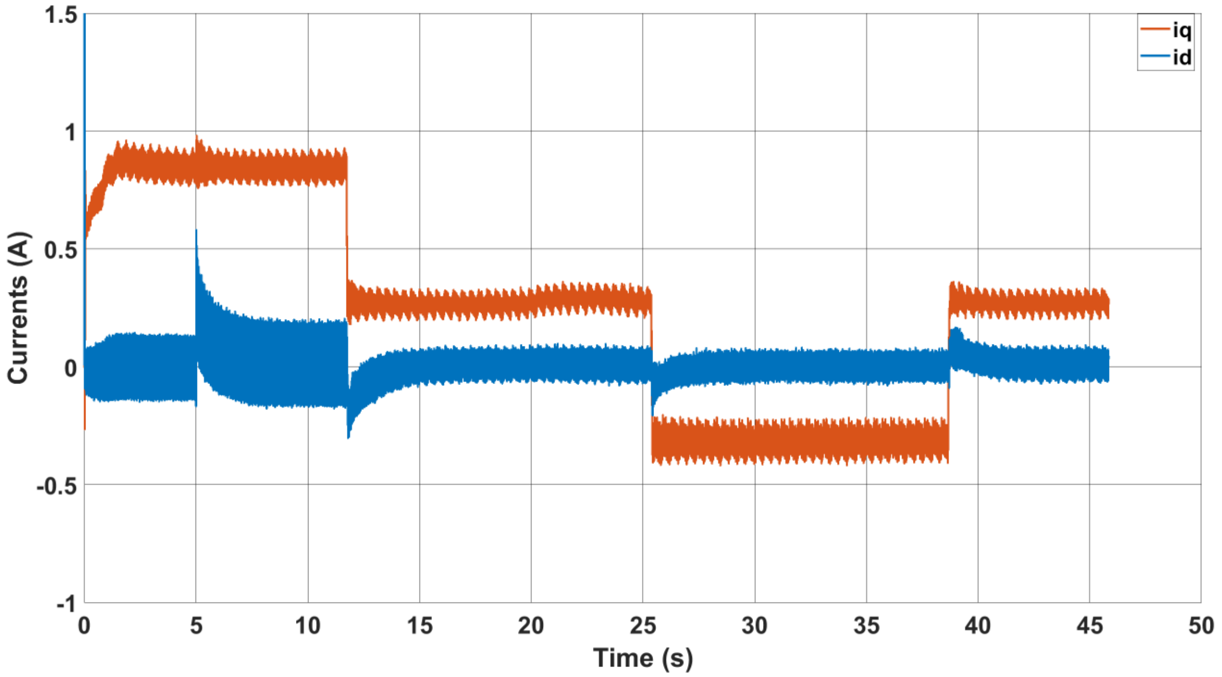
iq
id
1.5
1
0.5
0
-0.5
-1
Currents (A)
0
5
10
15
20
25
30
35
40
45
50
Time (s)

(e)

Figure 5.16 Sensorless operation for the predictive method with regenerative mode, (a) Speed response, (b) Estimated and measured positions, (c) Position error

.

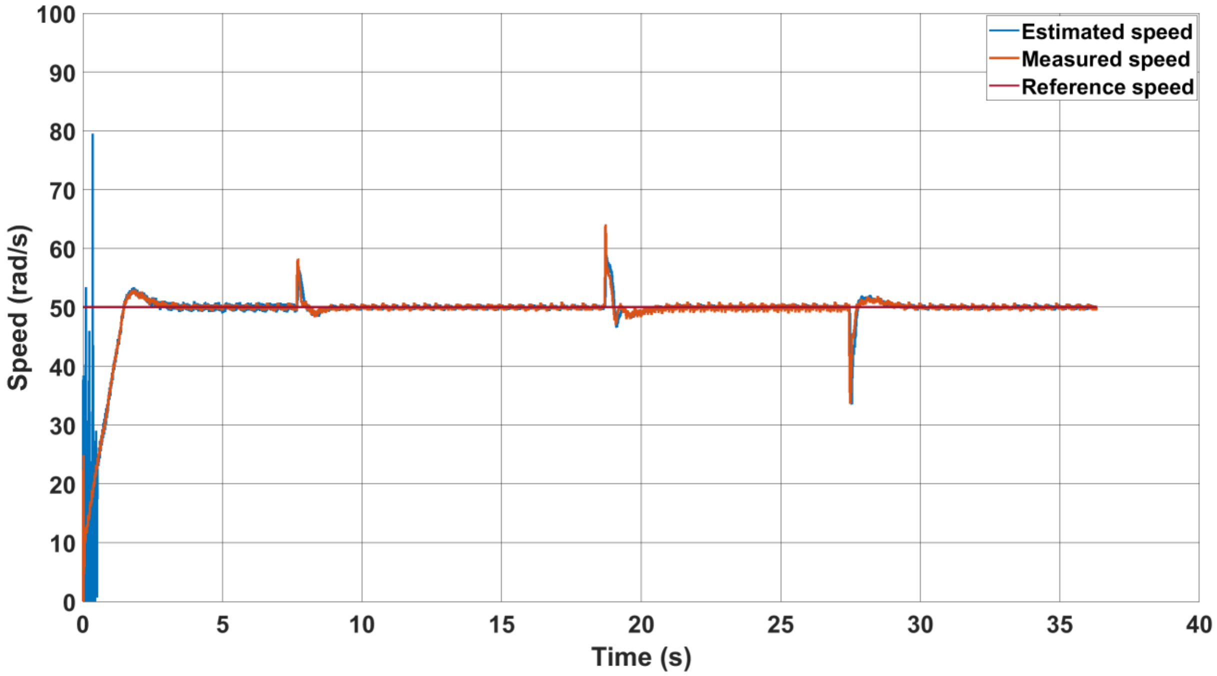

(a)

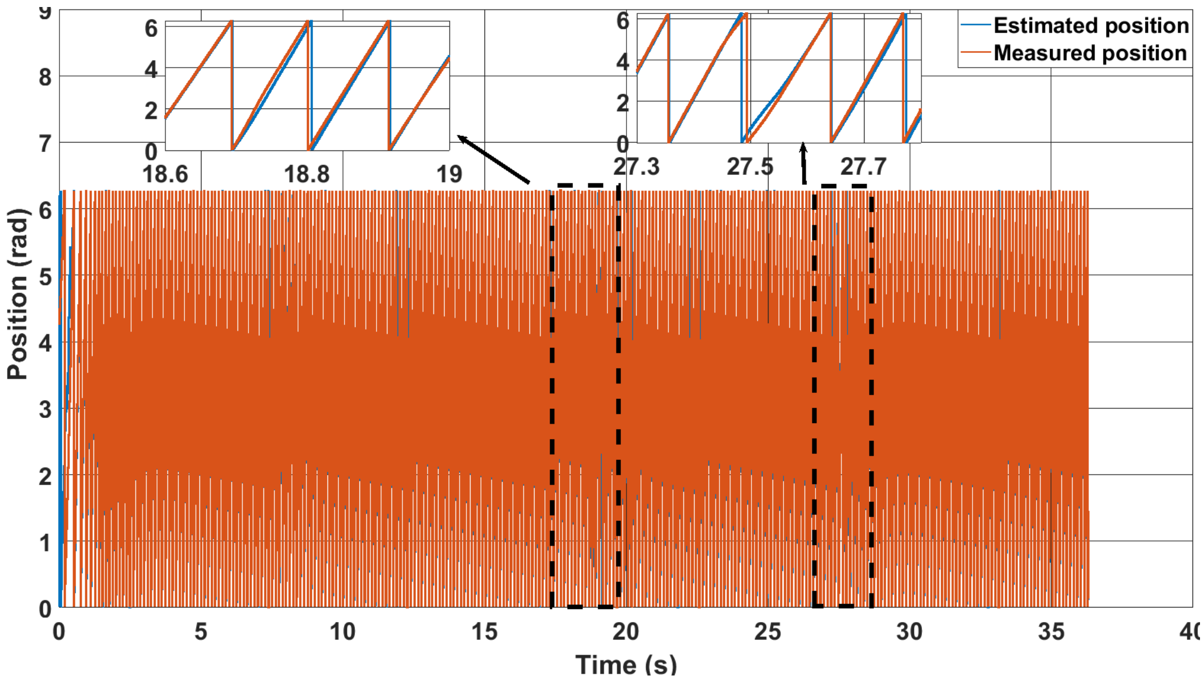

(b)

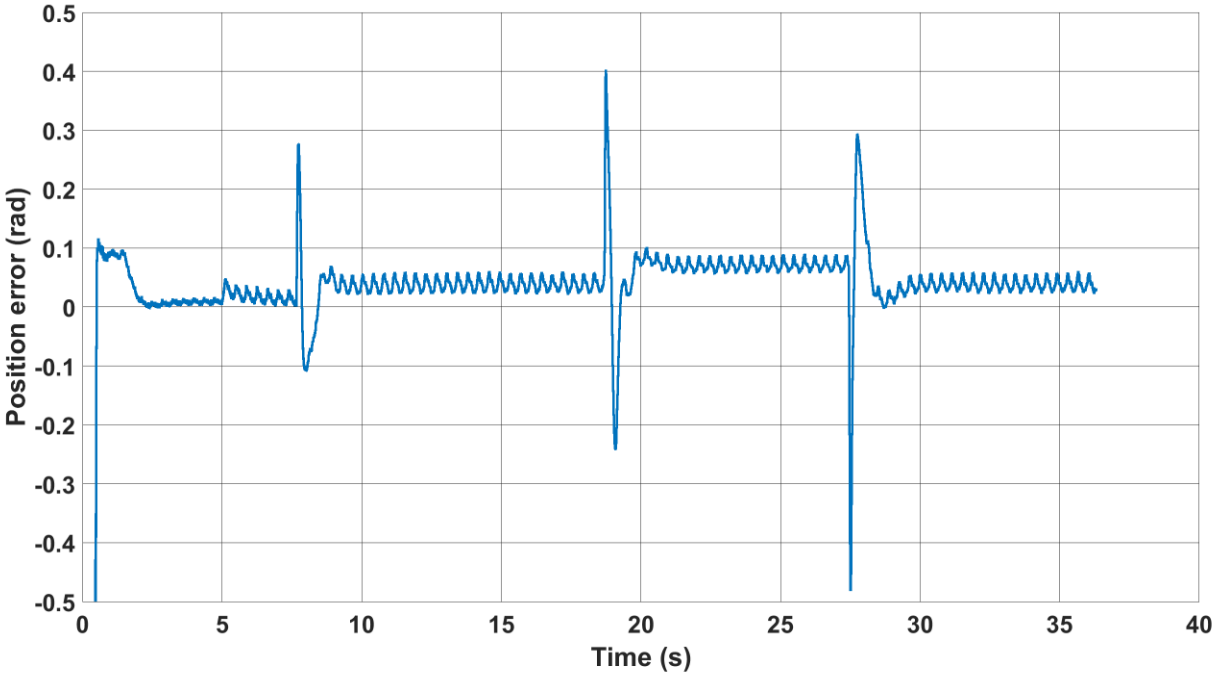
Position error (rad)
0.5
0.4
0.3
0.2
0.1
0
-0.1
-0.2
-0.3
-0.4
-0.5
0
5
10
15
20
25
30
35
40
Time (s)

(c)

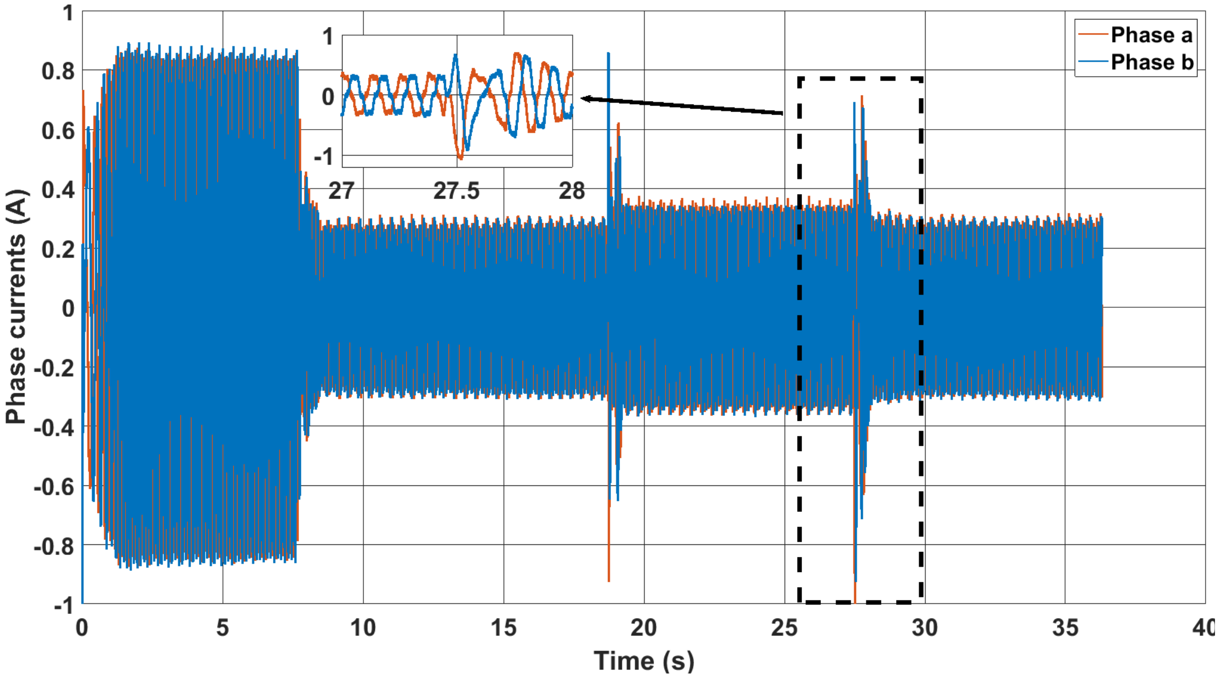
Phase currents (A)
1
0.8
0.6
0.4
0.2
0
-0.2
-0.4
-0.6
-0.8
-1
0
5
10
15
20
25
30
35
40
Time (s)
Phase a
Phase b
1
0
-1
27
27.5
28

(d)

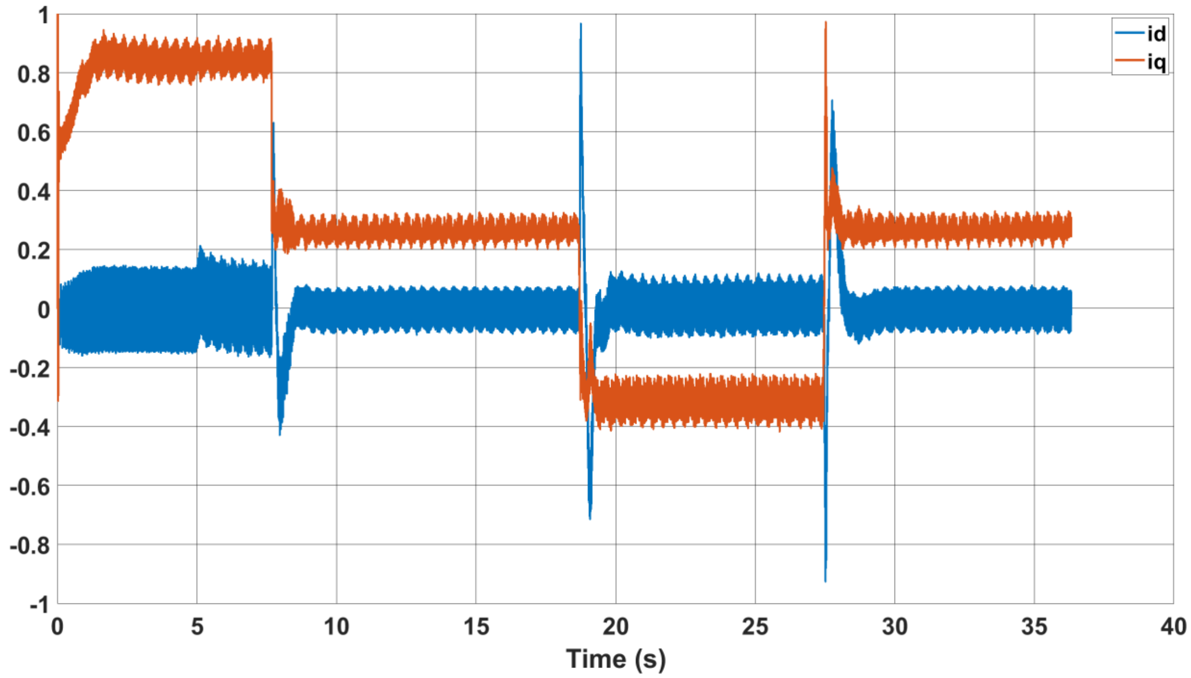

(e)

Figure 5.17 Sensorless operation for the conventional method with regenerative mode, (a) Speed response, (b) Estimated and measured positions, (c) Position error

5.6 Conclusion

A new (FCS-MPC) based estimator for PMSM is proposed. In this method, the adaptation process involves solving an optimization problem aimed at minimizing the speed error across a limited range of speeds. A speed search process is employed to guarantee optimal speed estimation at each sampling time. This removes the requirement for a PI controller in the adaptation process. Additionally, to decrease speed fluctuations at low speed, an adaptive low-pass filter is included to enhance performance. The performance of the proposed estimator is experimentally evaluated, and a comparison is made with the PI-based flux MRAS estimator.

The results show improved performance of the novel method compared to the PI-based MRAS method.

Chapter 6: Conclusion and further work

6.1 Conclusion

The use of permanent magnet synchronous machines (PMSM) is widespread in various applications, including industrial and high-performance sectors such as electric vehicle traction. PMSMs offer numerous advantages, including high efficiency and a simple structure. To achieve precise control of PMSMs, field-oriented control (FOC) is commonly employed due to its high accuracy and fast response.

In FOC, accurate measurement of the rotor position is crucial for achieving field orientation. Traditionally, position sensors such as encoders or resolvers have been utilized to provide the required rotor position data. However, in low-cost applications, the additional cost, size, weight, and complexity associated with position sensors are undesirable. This has led to a continuous interest in the development of sensorless control systems, where the rotor position is estimated without the need for additional sensors.

Sensorless control systems have gained significant attention in various applications, especially in high-performance scenarios like electric vehicle traction motors. In these applications, reliability is a critical requirement, and sensorless estimation serves as a backup solution in case of sensor failure. By incorporating sensorless control, the reliability and availability of the drive system can be enhanced, increasing its overall performance and robustness.

Model-Reference Adaptive Systems (MRAS) based methods are widely used in various applications due to their simplicity and performance. These methods aim to minimize the error between two estimations of rotor magnet flux using two alternative voltage and current models.

One commonly used MRAS technique is the flux-based MRAS, which calculates the stator flux by integrating the stator voltages in the voltage model.

However, the flux-based MRAS technique has a drawback. It relies on a pure integrator, which can cause performance degradation, particularly at low speeds. The integrator has infinite gain at zero frequency, which means it has the potential to amplify small offsets and initial conditions. To address this issue, integrators can be replaced with low-pass filters. By doing so, the performance at low speeds can be improved as the amplification of small offsets is mitigated.

Nevertheless, the introduction of low-pass filters comes with its own challenges. At low frequencies, these filters introduce additional phase delays, leading to errors in angle estimation. These errors can affect the overall performance of the MRAS-based method, especially in applications that require accurate angle estimation.

A novel estimator has been proposed for sensorless control of PMSM drives. The method uses oversampling of PWM voltages and currents during a switching cycle. The new method is proved to perform better than the classical MRAS method, with smaller position errors in most operating conditions. Unlike the classical flux-based MRAS method, the position accuracy is not affected in the novel method at low speeds due to the lack of integrator. Extensive experimental tests are conducted to evaluate the proposed estimator. The results of the experiments demonstrate good performance at various speeds and under various load circumstances, in both motoring and regenerating mode. The proposed method also shows robustness to changes in motor parameters.

The fixed PI controller is frequently utilized in the MRAS schemes' adaptation process to obtain the estimated speed as it showed a good performance over a large speed range. However, the problem with a fixed PI controller is that it is unable to maintain optimal performance under all different operation conditions. At low speeds the PI gains need to be tuned to small values to prevent a major increase in the estimated speed oscillation. However, for the system to operate smoothly and satisfactorily during the transient operation conditions when a sudden change occurs in load or speed, the PI gains need to be increased. Therefore, an adaptive PI controller is required for a satisfactory performance, however, this is a difficult process that takes time and effort.

The experimental testing of the PI gains' impact on the speed showed that employing higher PI gains leads to an increase in estimated speed oscillations, but implementing high gains improved the dynamic performance and shortened the settling time and reduced the angle error during the transient period compared to the response when low PI gains are applied.

A novel FCS-MPC-based speed estimator for PMSM is introduced in chapter 5. In this method, the adaptation process relies on solving an optimization problem to minimize the speed error signal across a finite range of rotor speed. Unlike PI-based MRAS methods the proposed technique does not need any gain tuning which make it simpler and guarantee the optimum performance. The performance of the novel FCS-MPC-based estimator is experimentally tested, and a comparison has been carried out between it and the PI-based flux MRAS estimator which is introduced in chapter 4.

The experimental results showed that the speed oscillation at low speeds can be significantly reduced in the predictive estimator by using a 2 Hz-cut-off frequency LPF without affecting the running system in comparison with the classical MRAS. In addition, during the transient period, the predictive scheme demonstrated a more accurate estimated position than the conventional scheme.

6.2 Future work

In Chapter 4, the estimation of rotor position and speed was based on using a fixed PI controller. However, this approach resulted in a significant increase in the estimated speed oscillation, particularly at low speeds. To address this issue and improve performance at low speeds, the use of an adaptive PI controller becomes necessary.

The adaptive PI controller is capable of dynamically adjusting its proportional and integral (PI) gains based on the system's dynamic condition. In steady-state operation, the controller gradually decreases the gains to prevent instability and minimize the estimated speed oscillation. On the other hand, during transient conditions, such as sudden changes in load or speed, the gains are instantly set to their maximum values to ensure a faster dynamic response and reduce the position error to a minimum.

The predictive flux MRAS speed estimator, introduced in Chapter 5, can be applied to different types of MRAS estimators that utilize PI controllers as an adaptation mechanism. Examples include reactive power-based MRAS and back EMF-based estimators. This demonstrates the versatility of the proposed method and its potential for broader application.

Moreover, the underlying principle of the novel method can be extended to other types of motors, such as induction motors (IM) and switched reluctance motors (SRM). By adapting the predictive estimator framework to these motor types, accurate and robust position estimation can be achieved.

It is worth noting that inverter non-linearity, especially at low speeds, can cause speed oscillation. To mitigate this effect, measurement of the stator terminal voltages is necessary. However, employing an inverter model compensator is a more practical approach, as it eliminates the need for voltage sensors while still compensating for inverter non-linearity.

Appendices

Appendix A: Average voltage calculation of the PWM-based speed and position estimations

The position of voltage reference vector is used to calculate the average PWM voltage at the starting of a PWM switching cycle, hence the voltage reference on $\alpha\beta$ frame (v^*_α, v^*_β) should be in a space vector form (V_mag, V_ang).

```
% Inputs are reference magnitude (V_mag), reference angle (V_ang), rotor
position (thet)
% Tsw = switching frequency/2, Vc = DC-link
function Vec_d = fcn(thet V_magnitude, V_angle)
tsw=0.00016;Vc=538;peak_phase= Vc/sqrt(3);
ma =( V_magnitude /peak_phase)*tsw;


%sector I
if (V_angle >=0) && (V_angle <pi/3)
t_a = ma * sin(pi/3- V_angle);
t_b = ma * sin(V_angle);
Sector_num = 1;
else
% Sector II
if (V_angle >= pi/3 && V_angle < 2*pi/3)
ad = V_angle - pi/3;
t_b = ma * sin(pi/3 - ad);
t_a = ma * sin(ad);
Sector_num = 2;
else
```

```
% Sector III
if (V_angle >= 2*pi/3 && V_angle < pi)
ad = V_angle - 2*pi/3;
t_a = ma * sin(pi/3 - ad);
t_b = ma * sin(ad);
Sector_num = 3;
else
% Sector IV
if (V_angle >= -pi && V_angle < -2*pi/3)
ad = V_angle + pi;
t_b = ma * sin(pi/3 - ad);
t_a = ma * sin(ad);
Sector_num = 4;
else
% Sector V
if (V_angle >= -2*pi/3 && V_angle < -pi/3)
ad = V_angle + 2*pi/3;
t_a = ma * sin(pi/3 - ad);
t_b = ma * sin(ad);
Sector_num = 5;
else
% Sector VI
if (V_angle >= -pi/3 && V_angle < 0)
ad = V_angle + pi/3;
t_b = ma * sin(pi/3 - ad);
t_a = ma * sin(ad);
Sector_num = 6;
else
Sector_num = nan;
t_a = 0;
t_b = 0;
```

```
end
end
end
end
end
end
% Calculation of q-components of state vectors
Vec1_a = 2*Vc/3;
Vec1_b = 0;
Vec1_d = cos(thet)*V1_a + sin(thet)*V1_b;
Vec2_a = 1*Vc/3;
Vec2_b = 1*Vc/sqrt(3);
Vec2_d = cos(thet)*V2_a + sin(thet)*V2_b;
Vec3_a = -1*Vc/3;
Vec3_b = 1*Vc/sqrt(3);
Vec3_d = cos(thet)*V3_a + sin(thet)*V3_b;
Vec4_a = -2*Vc/3;
Vec4_b = 0;
Vec4_d = cos(thet)*V4_a + sin(thet)*V4_b;
Vec5_a = -1*Vc/3;
Vec5_b = -1*Vc/sqrt(3);
Vec5_d = cos(thet)*V5_a + sin(thet)*V5_b;
Vec6_a = 1*Vc/3;
Vec6_b = -1*Vc/sqrt(3);
Vec6_d = cos(thet)*V6_a + sin(thet)*V6_b;
% Compute the average PWM output voltage of d component
if (Sector_num == 1)
Vec_d = 2*t_a*Vec1_d + 2*t_b*Vec2_d;
else
if (Sector_num == 2)
Vec_d = 2*t_a*Vec3_d + 2*t_b*Vec2_d;
```

```
else
if (Sector_num == 3)
Vec_d = 2*t_a*Vec3_d + 2*t_b*Vec4_d;
else
if (Sector_num == 4)
Vec_d = 2*t_a*Vec5_d + 2*t_b*Vec4_d;
else
if (Sector_num == 5)
Vec_d = 2*t_a*Vec5_d + 2*t_b*Vec6_d;
else
if (Sector_num == 6)
Vec_d = 2*t_a*Vec1_d + 2*t_b*Vec6_d;
else
Vec_d = 0;
end
end
end
end
end
end
```

Appendix B: Algorithm for model predictive MRAS speed estimator

```
% u1 is Average voltage calculation, u2 is summation of measured iq, u3 is
% summation of measured id, u4 is summation of id differences, wr is the
% reference speed and w_b is the initial speed.

function w = fcn(u1,u2,u3,u4,wr)

       persistent w_b
    firsttime = false;
    if isempty(w_b)
        w_b=0;
        firsttime = true;
    end
err_in=(-u1-u2*w_b+u3+u4)*3125/w_b;
if firsttime
for i=0:10

    w_delta=(wr)*2^-i;
    for j=0:13
        w_ij=w_b+w_delta*(4-j);

        % the cost function
        err=(-u1-u2*w_ij+u3+u4)*3125/w_ij;
        if (abs(err) < err_in)
            w_b=w_ij;
            err_in=err;
```

```
        end

    end

end

else

   w_delta=(wr)*2^-10;

    for j=0:13

        w_ij=w_b+w_delta*(4-j);


        % the cost function

        err=(-u1-u2*w_ij+u3+u4)*3125/w_ij;

        if (abs(err) < err_in)

            w_b=w_ij;

            err_in=err;

        end

    end

end

w=w_b*1/3;

end
```

Appendix C: Algorithm for adaptive LPF

```
% u is the difference between the reference and estimated speed


function y = fcn(u,y1)

set_value=5;

fc_low=4;

fc_high=10;

delta=0.0001;

if (abs(u)>set_value)
```

```
y=fc_high;

else

if (y1<=fc_low)

y=fc_low;

else

y=y1-delta;

end

end

end
```

Appendix D: Experimental equipment

D. 1 Voltage Source inverter

The inverter consists of six IGBT switches, and the outputs of the inverter are connected to the motor terminals via TA189 current sensors to measure the phase currents. As mentioned above, the three-phase two levels inverter is made by Semikron (figure 0.1), and the maximum voltage and current levels are 600 V_{dc} and 30A. The six switching signals (PWM signals) which are the output of the controller control the six power switches via 50 Ω coaxial cables as seen in the figure. The technique Space vector pulse width modulation (SVPWM) is implemented as it can have a higher voltage and lower total harmonic distortion (THD) compared to SPWM. The inverter is fed from a programable DC power supply shown in figure 0.2. The voltage should be gradually increased to the desired voltage to prevent high inrush currents, as there is no protection against overvoltage. The inverter switching frequency is set to 3.125 kHz with a dead time of 0.5 µs, and the control strategy FOC is implemented with sampling time of 80 µs.

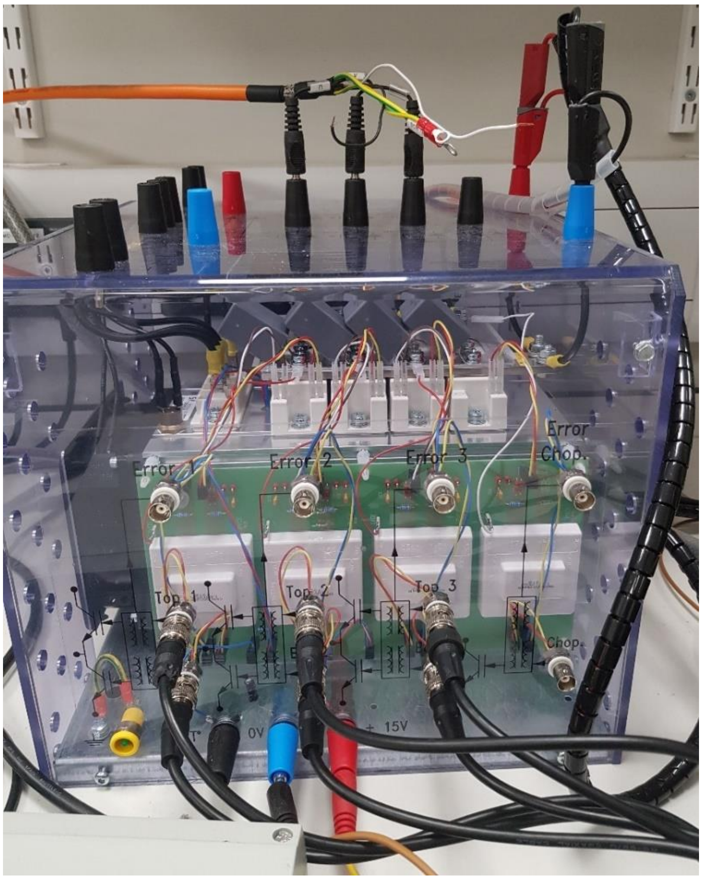

Figure 0.1 Laboratory photograph of the inverter

Figure 0.2 Laboratory photograph of the programable DC power supply

D.2 Interface Board

Figure. 0.3 shows an interface board designed at Sheffield university to interface the controller to the inverter. For the power switches to operate, the 5V PWM signals are required to be amplified to 15V. This is done by using six opto-isolated gate drivers to electrically isolate the controller from the power switches. Additionally, the interface board enables the controller to read the phase currents and rotor position from current sensors and the encoder, respectively.

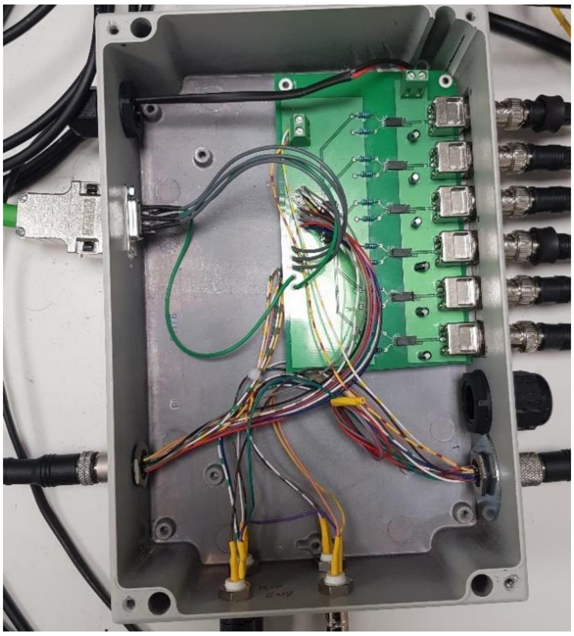

Figure 0.3 Laboratory photograph of the interface board

D.3 The Control Unit

The controller baseline real-time target machine shown in figure 0.4 manufactured by Speedgoat is used to run Simulink real-time applications and it has a built-in PWM generating circuit. A reconfigurable I/O 397 module is used for communication between the controller and plant hardware, actuator and sensors. The module supplies 4 analog inputs, 2 analog outputs and 7 digital channels, which can be configured independently as input or output.

Figure 0.4 Speedgoat target machine

D.4 Unidrive 700M

As mentioned above, the second Drive Unit is controlled by a Nidec Unidrive 700M drive (figure 0.5) which is manufactured by Control Techniques. It enables an individual control of the second motor for either torque or speed mode. For protection and safety purpose, the Unidrive is kept inside a cabinet with a protective system interfacing the drive and the 3-phase main supply. To prevent a direct contact with live parts, an interlock is installed so the main supply is disconnected in case the cabinet is open. 4 buttons are used in the cabinet to turn on the drive, turn off the drive, enable the motor and disenable the motor as shown in figure 0.6.

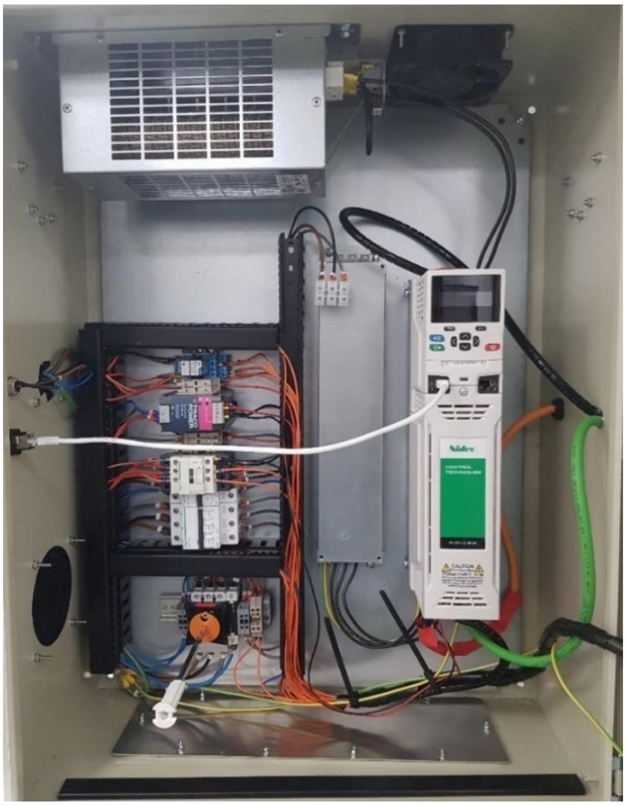

Figure 0.5 Nidec Unidrive 700M drive

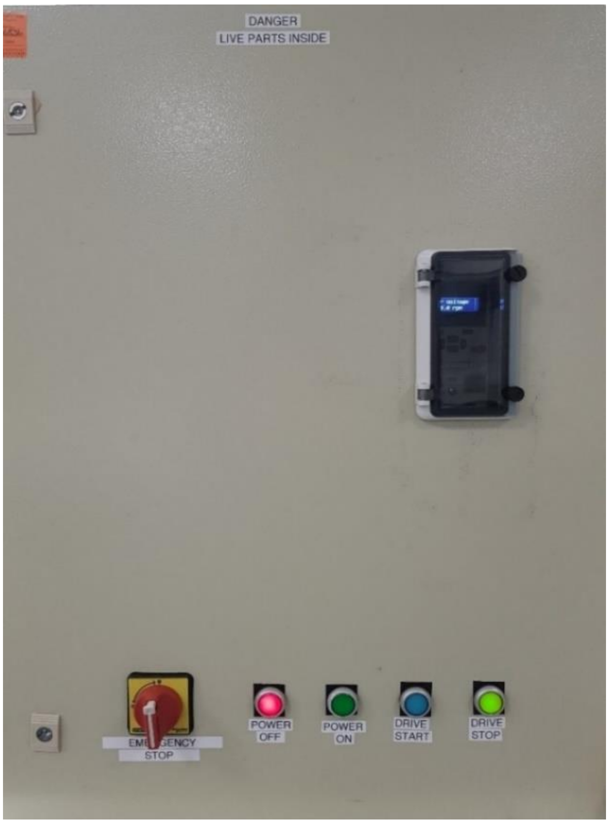

Figure 0.6 Drive cabinet.

References

1. Krishnan, R., Permanent Magnet Synchronous and Brushless DC Motor Drives. 2017: Cleveland, OH, USA.
2. Bose, B.K., Power Electronics and Variable Frequency Drives. 1996, Wiley: USA.
3. Yusivar, F., et al. Implementation of field oriented control for permanent magnet synchronous motor. IEEE.
4. Xiao, S., et al., On-line temperature monitoring of permanent magnet synchronous machines. 2019.
5. Heredia, J.R., F. Perez Hidalgo, and J.L. Duran Paz, Sensorless control of induction motors by artificial neural networks. IEEE Transactions on Industrial Electronics, 2001. **48**(5): p. 1038-1040.
6. Vas, P., Sensorless vector and direct torque control. Monographs in electrical and electronic engineering. 1998, Oxford ; New York: Oxford University Press. xxxi, 729 p.
7. Gabriel, R., W. Leonhard, and C.J. Nordby, Field-Oriented Control of a Standard AC Motor Using Microprocessors. IEEE Transactions on Industry Applications, 1980. **IA-16**(2): p. 186-192.
8. Harnefors, L., Design and analysis of general rotor-flux-oriented vector control systems. IEEE Transactions on Industrial Electronics, 2001. **48**(2): p. 383-390.
9. Schroedl, M. Sensorless control of AC machines at low speed and standstill based on the "INFORM" method. IEEE.
10. Jansen, P.L. and R.D. Lorenz, Transducerless position and velocity estimation in induction and salient AC machines. IEEE Transactions on Industry Applications, 1995. **31**(2): p. 240-247.
11. Finch, J.W. and D. Giaouris, Controlled AC Electrical Drives. IEEE Transactions on Industrial Electronics, 2008. **55**(2): p. 481-491.
12. Im, J.-H. and R.-Y. Kim, Improved Saliency-Based Position Sensorless Control of Interior Permanent-Magnet Synchronous Machines With Single DC-Link Current Sensor Using Current Prediction Method. IEEE Transactions on Industrial Electronics, 2018. **65**(7): p. 5335-5343.
13. Cao-Minh, T., T. Uchida, and Y. Hori. MRAS-based speed sensorless control for induction motor drives using instantaneous reactive power. *IECON'01. 27th Annual Conference of the IEEE Industrial Electronics Society (Cat. No.37243)*, Denver, CO, USA, 2001, pp. 1417-1422 vol.2
14. Maiti, S. and C. Chakraborty, A new instantaneous reactive power based MRAS for sensorless induction motor drive. Simulation Modelling Practice and Theory, 2010. **18**(9): p. 1314-1326.
15. Ravi Teja, A.V., V. Verma, and C. Chakraborty, A New Formulation of Reactive-Power-Based Model Reference Adaptive System for Sensorless Induction Motor Drive. IEEE Transactions on Industrial Electronics, 2015. **62**(11): p. 6797-6808.
16. Ravi Teja, A.V., et al., A New Model Reference Adaptive Controller for Four Quadrant Vector Controlled Induction Motor Drives. IEEE Transactions on Industrial Electronics, 2012. **59**(10): p. 3757-3767.
17. Rashed, M. and A.F. Stronach, A stable back-EMF MRAS-based sensorless low-speed induction motor drive insensitive to stator resistance variation. IEE Proceedings - Electric Power Applications, 2004. **151**(6): p. 685.

18. Zhang, X., et al., Speed Sensorless Control of a Surface-mounted Permanent Magnet Drive. 2019 10th International Conference on Power Electronics and Ecce Asia (Icpe 2019 - Ecce Asia), 2019.
19. Kang, J., Sensorless control of permanent magnet motors. Control Engineering,2010**41**(4): p. 1-4..
20. Holtz, J., Sensorless control of induction motor drives. Proceedings of the IEEE, 2002. **90**(8): p. 1359-1394.
21. Rehman, H., et al., A new current model flux observer for wide speed range sensorless control of an induction machine. IEEE Transactions on Power Electronics, 2002. **17**(6): p. 1041-1048.
22. Cortes, P., et al., Predictive Control in Power Electronics and Drives. IEEE Transactions on Industrial Electronics, 2008. **55**(12): p. 4312-4324.
23. Geyer, T., G. Papafotiou, and M. Morari, Model Predictive Direct Torque Control—Part I: Concept, Algorithm, and Analysis. IEEE Transactions on Industrial Electronics, 2009. **56**(6): p. 1894-1905.
24. Papafotiou, G., et al., Model Predictive Direct Torque Control—Part II: Implementation and Experimental Evaluation. IEEE Transactions on Industrial Electronics, 2009. **56**(6): p. 1906-1915.
25. Barrero, F., et al., A Proof of Concept Study of Predictive Current Control for VSI-Driven Asymmetrical Dual Three-Phase AC Machines. IEEE Transactions on Industrial Electronics, 2009. **56**(6): p. 1937-1954.
26. Morales-Caporal, R., et al., Transducerless Acquisition of the Rotor Position for Predictive Torque Controlled PM Synchronous Machines Based on a DSP-FPGA Digital System. IEEE Transactions on Industrial Informatics, 2013. **9**(2): p. 799-807.
27. Li, T., et al., An SRF-PLL-Based Sensorless Vector Control Using the Predictive Deadbeat Algorithm for the Direct-Driven Permanent Magnet Synchronous Generator. IEEE Transactions on Power Electronics, 2014. **29**(6): p. 2837-2849.
28. Morales-Caporal, R., et al., Sensorless Predictive DTC of a Surface-Mounted Permanent-Magnet Synchronous Machine Based on Its Magnetic Anisotropy. IEEE Transactions on Industrial Electronics, 2013. **60**(8): p. 3016-3024.
29. Chen, J.L. and T.H. Liu, Implementation of a predictive controller for a sensorless interior permanent-magnet synchronous motor drive system. Iet Electric Power Applications, 2012. **6**(8): p. 513-525.
30. Guzinski, J. and H. Abu-Rub, Speed Sensorless Induction Motor Drive With Predictive Current Controller. IEEE Transactions on Industrial Electronics, 2013. **60**(2): p. 699-709.
31. Catalailopez, J., et al., Novel Fuzzy Adaptive Sensorless Induction Motor Drive. IEEE Transactions on Industrial Electronics, 2006. **53**(4): p. 1170 uy66677788-1178.
32. Holtz, J., Sensorless Control of Induction Machines—With or Without Signal Injection? IEEE Transactions on Industrial Electronics, 2006. **53**(1): p. 7-30.
33. Guo, H., et al., Implementation of EKF for Vehicle Velocities Estimation on FPGA. IEEE Transactions on Industrial Electronics, 2013. **60**(9): p. 3823-3835.
34. Inan, R., M. Barut, and F. Karakaya. FPGA implementation of extended Kalman filter for speed-sensorless control of induction motors. Institution of Engineering and Technology.
35. Yoon-Seok, H., C. Jung-Soo, and K. Young-Seok, Sensorless PMSM drive with a sliding mode control based adaptive speed and stator resistance estimator. IEEE Transactions on Magnetics, 2000. **36**(5): p. 3588-3591.

36. Comanescu, M., An MRAS-Type Estimator for the Speed, Flux Magnitude and Rotor Flux Angle of the Induction Motor Using Sliding Mode. 2014 International Symposium on Power Electronics, Electrical Drives, Automation and Motion (Speedam), 2014: p. 719-724.
37. Gadoue, S.M., D. Giaouris, and J.W. Finch, MRAS Sensorless Vector Control of an Induction Motor Using New Sliding-Mode and Fuzzy-Logic Adaptation Mechanisms. IEEE Transactions on Energy Conversion, 2010. **25**(2): p. 394-402.
38. Comanescu, M. and L. Xu, Sliding-mode MRAS speed estimators for sensorless vector control of induction Machine. IEEE Transactions on Industrial Electronics, 2006. **53**(1): p. 146-153.
39. Maiti, S., et al., An Adaptive Speed Sensorless Induction Motor Drive With Artificial Neural Network for Stability Enhancement. IEEE Transactions on Industrial Informatics, 2012. **8**(4): p. 757-766.
40. Mohan Krishna, S. and J.L. Febin Daya, MRAS speed estimator with fuzzy and PI stator resistance adaptation for sensorless induction motor drives using RT-lab. Perspectives in Science, 2016. **8**: p. 121-126.
41. Westin, I., Sensorless Control of a PMSM, in mechanical engineering 2016, KTH Royal Institute of Technology/ School of Industrail Engineering and Managemen: Stockholm, Sweden. p.65
42. Bendjedia, B. and S. Chouireb. Comparative Study Between Sensorless Vector Control of PMSM Drives based on MRAS, SMO and EKF Observers. IEEE.

43. S. Singh and A. N. Tiwari, "Various techniques of sensorless speed control of PMSM: A review," *2017 Second International Conference on Electrical, Computer and Communication Technologies(ICECCT)*, Coimbatore, India, 2017, pp. 1-6.
44. Y. Zhao, C. Wei, Z. Zhang and W. Qiao, "A Review on Position/Speed Sensorless Control for Permanent-Magnet Synchronous Machine-Based Wind Energy Conversion Systems," in *IEEE Journal of Emerging and Selected Topics in Power Electronics*, vol. 1, no. 4, pp. 203-216, Dec. 2013.
45. Maiti, S. and C. Chakraborty. Reactive Power Based Speed Sensorless Controller for Permanent Magnet Synchronous Motor Drive. IEEE.
46. Jun Sung, P., et al. State observer with stator resistance and back-EMF constant estimation for sensorless PMSM. IEEE.
47. Schauder, C. Adaptive speed identification for vector control of induction motors without rotational transducers. in *IEEE Transactions on Industry Applications*, vol. 28, no. 5, pp. 1054-1061, Sept.-Oct. 1992
48. Saeidi, S. and R. Kennel. A novel algorithm for model predictive control of AC electric drives. *2nd International Electric Drives Production Conference (EDPC),* Nuremberg, Germany, 2012, pp. 1-7
49. Rodriguez, J., et al., Predictive current control of a voltage source inverter. Ieee Transactions on Industrial Electronics, 2007. **54**(1): p. 495-503.
50. Davari, S.A., et al., Using Full Order and Reduced Order Observers for Robust Sensorless Predictive Torque Control of Induction Motors. IEEE Transactions on Power Electronics, 2012. **27**(7): p. 3424-3433.
51. Nalakath, S., et al., Optimization-Based Position Sensorless Finite Control Set Model Predictive Control for IPMSMs. IEEE Transactions on Power Electronics, 2018. **33**(10): p. 8672-8682.
52. Kouro, S., et al., Model Predictive Control—A Simple and Powerful Method to Control Power Converters. IEEE Transactions on Industrial Electronics, 2009. **56**(6): p. 1826-1838.

53. Wang, F., et al., An Encoderless Predictive Torque Control for an Induction Machine With a Revised Prediction Model and EFOSMO. IEEE Transactions on Industrial Electronics, 2014. **61**(12): p. 6635-6644.
54. R. Vargas, J. Rodriguez, C. A. Rojas and M. Rivera, Predictive Control of an Induction Machine Fed by a Matrix Converter With Increased Efficiency and Reduced Common-Mode Voltage. IEEE Transactions on Energy Conversion, 2014. 29(2): p. 473-485.
55. Habibullah, M. and D.D.-C. Lu, A Speed-Sensorless FS-PTC of Induction Motors Using Extended Kalman Filters. IEEE Transactions on Industrial Electronics, 2015. **62**(11): p. 6765-6778.
56. Zbede, Y.B., S.M. Gadoue, and D.J. Atkinson, Model Predictive MRAS Estimator for Sensorless Induction Motor Drives. Ieee Transactions on Industrial Electronics, 2016. **63**(6): p. 3511-3521.
57. ZEWUDIE, A.T., Sensorless speed control of permanent magnet synchronous motor using model reference adaptive system, in department of electrical and computer engineering. 2019, Addis Ababa science and technology university: Addis Ababa.
58. Li, Y.M., Sensorless control of permanent magnet brushless AC motors accounting for cross-coupling magnetic saturation. 2009.
59. Peilin, X. and S. University of, Novel sensorless control for permanent magnet synchronous machines based on carrier signal injection. 2017.
60. Zhu, Z.Q. and D. Howe, Electrical Machines and Drives for Electric, Hybrid, and Fuel Cell Vehicles. Proceedings of the IEEE, 2007. **95**(4): p. 746-765.
61. Zbede, Y. and T. University of Newcastle upon, Model predictive MRAS estimator for sensorless induction motor drives. 2017.
62. Jun, H. and W. Bin, New integration algorithms for estimating motor flux over a wide speed range. IEEE Transactions on Power Electronics, 1998. 13(5): p. 969-977.
63. Myoung-Ho, S., et al., An improved stator flux estimation for speed sensorless stator flux orientation control of induction motors. IEEE Transactions on Power Electronics, 2000. 15(2): p. 312-318.
64. S. S. Badini and V. Verma, "A Novel MRAS Based Speed Sensorless Vector Controlled PMSM Drive," *2019 54th International Universities Power Engineering Conference (UPEC)*, Bucharest, Romania, 2019, pp. 1-6.
65. Young Ahn Kwon and Dae Won Jin, "A novel MRAS based speed sensorless control of induction motor," *IECON'99. Conference Proceedings. 25th Annual Conference of the IEEE Industrial Electronics Society (Cat. No.99CH37029)*, San Jose, CA, USA, 1999, pp. 933-938 vol.2.
66. K. Huang, W. Li, S. Huang, L. Xiao, L. Zheng and Z. Xu, "Sensorless control of direct-driven permanent magnet wind power generation system based on improved MRAS," *2011 International Conference on Electrical Machines and Systems*, Beijing, China, 2011, pp. 1-5.
67. A. Matsumoto, M. Hasegawa, M. Tomita and K. Matsui, "Algebraic design of full-order flux observer for IPMSM position sensorless control," *2011 IEEE International Electric Machines & Drives Conference (IEMDC)*, Niagara Falls, ON, Canada, 2011, pp. 1276-1281.
68. K. -G. Lee, J. -S. Lee and K. -B. Lee, "SPMSM sensorless control for wide speed range using full-order flux observer," *2014 IEEE International Conference on Industrial Technology (ICIT)*, Busan, Korea (South), 2014, pp. 164-168
69. A. Rattanaudompisut and S. Po-Ngam, "The practical and simple feedback gains design of an adaptive full-order observer for speed-sensorless induction motor drives," *2015 12th International Conference on Electrical Engineering/Electronics, Computer,*

Telecommunications and Information Technology (ECTI-CON), Hua Hin, Thailand, 2015, pp. 1-6.

70. B. Chen, W. Yao, K. Wang, K. Lee and Z. Lu, "Comparative analysis of feedback gains for adaptive full-order observers in sensorless induction motor drives," 2013 IEEE Energy Conversion Congress and Exposition, Denver, CO, USA, 2013, pp. 3481-3487.
71. Shiref, M., Investigation into PI controller output ripple in MRAS based electrical drives. 2013, Newcastle University: Newcastle.
72. Abu-Rub, H. (2012). High-Performance Control of AC Drives with MATLAB/Simulink Models. Texas A&M University at Qatar, Qatar.
73. Xiao, S. and A. Griffo, PWM-based Flux linkage estimation for permanent magnet synchronous machines. Journal of Engineering-Joe, 2019(17): p. 4045-4049.
74. Peilin, X. and S. University of Sheffield, Novel sensorless control for permanent magnet synchronous machines based on carrier signal injection. 2017
75. L. Rovere, A.F., A. Gaeta, P. Zanchetta and M. Marcheson, Sensorless Finite-Control Set Model Predictive Control for IPMSM Drives. IEEE Transactions on Industrial Electronics, 2016. **63**(9): p. 5921-5931.